

**Physics of Nickel Oxide Hole Transport Layer for Organic
Photovoltaics Application**

by

Nicodemus Edwin Widjonarko

M.S., University of Colorado, Boulder, 2009

B.A., University of California, Berkeley, 2007

A thesis submitted to the
Faculty of the Graduate School of the
University of Colorado in partial fulfillment
of the requirements for the degree of
Doctor of Philosophy
Department of Physics

2013

This thesis entitled:
Physics of Nickel Oxide Hole Transport Layer for Organic Photovoltaics Application
written by Nicodemus Edwin Widjonarko
has been approved for the Department of Physics

Joseph J. Berry

Prof. Charles Rogers

Date _____

The final copy of this thesis has been examined by the signatories, and we find that both the content and the form meet acceptable presentation standards of scholarly work in the above mentioned discipline.

Widjonarko, Nicodemus Edwin (Ph.D., Physics)

Physics of Nickel Oxide Hole Transport Layer for Organic Photovoltaics Application

Thesis directed by Doctor Joseph J. Berry

Titular Chair: Prof. Charles Rogers

Organic photovoltaics (OPV) offers a potential for solar-electric power generation to be affordable. Crucial to OPV device performance is the incorporation of interlayers, ultra-thin films deposited between the photoactive material and the electrical contacts. These interlayers have various, targeted functionalities: optical window, encapsulation, or electronic bridge. The last category is known as “transport layers”, and is the focus of this thesis.

In this thesis, we explore and investigate the physics that leads to improvements in OPV device performance when a transport layer is employed. We focus on the use of non-stoichiometric nickel oxide (NiO_x) as a hole transport layer (HTL) in poly(3-hexylthiophene):phenyl- C_{61} -butyric acid methyl ester (P3HT:PCBM) solar cells. NiO_x deposited by physical vapor deposition is chosen for this study because of its successful use as HTL, the ease to engineer its electronic properties by varying deposition parameters, and it leading to improved device lifetime.

Our initial studies indicate that the well-known “high work-function” rule is not adequate to explain the trends observed in the devices. The series of investigations discussed in this thesis reveal that band-offsets at the NiO_x / P3HT:PCBM interface need to be taken into account in order to explain the observed trends. Non-optimal band-offsets lead to either sigmoidal current-voltage characteristics or reduced photocurrent.

The optimal energy level alignment depends on the energy levels of the photo-active material, which are measurable. This means that an HTL material must be optimized for different photoactive material. A simple and practical set of rules are proposed to achieve this optimal energy level alignment for a given photoactive material. The rules not only include the pervasively-used “high work-function” rule, but also the impacts of band-offsets investigated in this work.

Dedication

To my parents and brother.

To past and current teachers.

To those whom I hold dear in my heart.

To Daughter of Elysium.

Acknowledgements

As I reflect upon the meandering path that I have taken to reach this day, I cannot help but to realize that this journey has been possible only because many people have lend their hand in various ways. My research advisor, Joe Berry, undoubtedly earns the first mention in this list. He is an inspirational figure and his contributions to my education has been unparalleled. I also extend my utmost gratitude to Prof. Charles Rogers, to Dave Ginley, and to John Perkins who have made this remarkable NREL experience possible. Dave Ginley have provided me with various enriching opportunities, including my first invited paper. Dave Ginley, Chen Hsiang Yu, and Sovannary Phok have also picked me up at times when I was most in need; without them, this journey would have never seen this end.

Prof. Tom deGrand and Steve Pollock have set the bar high early in my graduate study. In-depth discussions with Phil Parilla, Jian Li, Mike Toney, Jao van de Lagemaat, Brian Gregg, Erin Ratcliff, Antoine Kahn, Prof. Ivan Smalyukh, Neal Armstrong, Garry Rumbles, and Alex Miedaner have also helped calcify my understanding of various aspects of device physics. These people are like mentors to me.

Ajaya Sigdel and Paul Ndione have been together with me in making this work possible. The following people have also contributed, in their own unique way, to the whole experience at NREL: Dana Olson, Andres Garcia, Philip Schulz, Craig Perkins, Andriy Zakutayev, Dane Gillaspie, Matthew Dabney, Prakash Periasamy and Archana Subramaniyan, Sarah Cowan, Brad MacLeod, Stefan Oosterhout, Sanjini Nanayakkara, Matthew White, Alex Nardes, Andrew Ferguson, Tavi Semonin, Brandon Reese, Xerxes Steirer, Yi Ke, Feng Lin, Robert Pasquarelli, Petr

Zvolsky, Anna Trendewicz, Matthew Reese, Robin Richards, Maikel van Hest, Arrelaine Dameron, Josh Martin, Jeff Alleman, Steve Christensen, Vince Bollinger, Joel Pankow, Jennifer Leisch, Calvin Curtis, Susan Habas, Heather Platte.

I will dearly miss the company of fellow CU physics graduate students and also Jeanne Nijhowne, Kristen Kennedy, Diane Willey, and Carol Allman.

Thank you also to the extended Indonesian and Singaporean community, including Zilong Chen, Wee Kiat Lim, Bu Menuk, and Tante Chandra, who have made Boulder a home far way from home. Lastly and most importantly, I would like to specially thank my family, whom I hold closest to my heart, for the gift of love and for supporting me all the way to this day. None of this is possible without you.

The work that is described here is done at the National Renewable Energy Laboratory (NREL) in Golden, CO and is supported by Center for Interface Science: Solar-Electric Materials (CIS:SEM), an Energy Frontier Research Center Funded by the U.S. Department of Energy, Office of Basic Sciences, under Award No. DE- SC0001084.

Contents

Chapter

1	Introduction	1
1.1	On Sustainability	1
1.2	The Case for Photovoltaics	2
1.3	Organic Photovoltaics	6
1.4	Thesis Focus and Organization	11
2	Physics Specific to Bulk-Heterojunction Organic Photovoltaics	13
2.1	Carrier Transport in Organic Materials	13
2.2	Photocarrier Generation and Bulk Heterojunctions	15
2.3	Interlayers	17
2.4	Heterojunction Nature of OPV Devices	18
3	Characterizations of Organic Photovoltaic Cells and Their Components	20
3.1	Solar Cell Performance	20
3.2	Energy Levels in a Material	23
3.2.1	Ultraviolet Photoemission Spectroscopy and Inverse Photoemission Spectroscopy	23
3.2.2	The Kelvin Probe	25
3.3	Optical Properties	26
3.3.1	UV-Visible Optical Reflection / Transmission Spectroscopy	26

3.3.2	Spectroscopic Ellipsometry	28
3.4	Material Composition	28
3.4.1	X-ray Photoemission Spectroscopy	28
3.4.2	X-ray Diffraction	30
3.4.3	X-Ray Fluorescence	30
3.4.4	Laser-Induced Breakdown Spectroscopy	30
3.4.5	Inductively Coupled Plasma Atomic Emission Spectroscopy	31
3.5	Structural Properties	31
3.5.1	Atomic Force Microscopy	31
3.5.2	X-ray Diffraction	33
3.5.3	Surface Energy	45
4	Materials and Nickel Oxide Development	48
4.1	Deposition Methods	48
4.1.1	Pulsed Laser Deposition (PLD)	48
4.1.2	Other Deposition Methods	54
4.2	Materials	58
4.2.1	Nickel Oxide	58
4.2.2	P3HT, PCBM and P3HT:PCBM	77
4.2.3	PEDOT:PSS	82
4.2.4	Indium Tin Oxide	83
5	Sputtered Nickel Oxide as an Efficient Hole Transport Layer in P3HT:PCBM Organic Solar Cell	84
5.1	Experimental	85
5.2	Results and Discussions	87
5.3	Summary	94

6	The Impact of Substrate Surface Properties on the Morphology of Polymer-Fullerene Bulk Heterojunction	96
6.1	Vertical Phase Segregation of P3HT:PCBM	97
6.1.1	Assessing Vertical Phase Segregation by Depth-Profile XPS	98
6.1.2	Understanding the Physical Origin of Vertical Phase Segregation by 2-Component Surface Energy Measurement and XPS	98
6.2	Crystallographic Order and Texture	107
6.3	The Overall Picture	113
6.4	Summary	115
7	The Impact of Band Offsets at Nickel Oxide - Bulk-Heterojunction Interface on OPV Performance	117
7.1	Band Offsets and Kinetic Barriers: An Analogy	118
7.2	Theory	119
7.3	Experimental Results and Discussions	131
7.3.1	Band Alignment at the NiO _x / BHJ Interface	131
7.4	Summary	138
8	Development of Laser-Induced Breakdown Spectroscopy for Stoichiometric Analysis of Compositionally-Graded Combinatorial Amorphous Thin Film Oxides	140
8.1	Experimental Set Up	141
8.1.1	Equipment	141
8.1.2	Sample Description	145
8.1.3	Signal-to-Noise Optimizations	149
8.2	Assumptions and Mathematical Model for Analysis	153
8.3	Selecting Spectral Peaks for Analysis	156
8.4	Calibration and Combinatorial Mapping	157
8.5	Results and Discussions	160

8.6	Summary	163
9	Closing Remarks	165
9.1	Summary of Main Results	165
9.1.1	On Energy Level Alignment at HTL / BHJ Interface	165
9.1.2	On The Impact of HTL Surface Properties on BHJ Morphology	168
9.2	Where Do We Go From Here	170
9.2.1	Optimization Process of Contact Materials for Photovoltaics by Physics- Driven Designs	170
9.2.2	A High-Throughput Approach to Contact Optimizations for OPV	173
9.2.3	Studies on Material Disorders of Various Length Scales and Their Impact on Opto-Electronic Properties	177
	Bibliography	183
	Appendix	
A	Symbols	203
A.1	Physical constants	203
A.2	Energy levels and statistics of electron-hole population	204
A.3	Solar cell characterization	205
A.4	Charge transport	205
A.5	Photoelectric effect	206
A.6	Deposition parameters	206
A.7	X-ray diffraction	207
B	The Physics of Photovoltaic Conversion	208
B.1	The Need for Semiconductors	208

B.2	The ultimate efficiency of a photovoltaic cell	210
B.3	Non-radiative recombination, losses during carrier transport	216
C	Electrons and Holes in Semiconducting Materials	217
C.1	Statistics of Electrons and Holes in Semiconductors at Thermodynamic Equilibrium	217
C.1.1	Intrinsic Semiconductor	220
C.1.2	Extrinsic Semiconductor	221
C.1.3	Carrier Population in Non-Equilibrium Steady State	223
C.1.4	On Fermi Level, Quasi-Fermi Levels, Chemical Potential, and Electrochemical Potential	224
C.2	Drift-Diffusion Model of Carrier Dynamics	227
C.2.1	Drift current	228
C.2.2	Diffusion current	230
C.2.3	Total drift-diffusion current	230
D	Junctions	234
D.1	Junctions	235
D.1.1	Band Alignment at an Ideal Heterojunction	236
D.1.2	Current Transport Across a Heterojunction	240
D.1.3	Band-Offsets, Non-Ideal Interfaces, and Interfacial Dipoles	242

Tables

Table

3.1	Probe liquids in contact angle measurements for 2-component surface energy calculation.	47
4.1	Electrical properties of NiO _x films with different Ar:O ₂ ratio during deposition. . . .	72
4.2	Work-function of sputtered NiO _x films with different Ar:O ₂ ratio during deposition. O ₂ plasma clean done at 155 W, 0.80 torr for 5 minutes.	72
5.1	Summary of NiO _x HTL deposition condition, surface treatment, work-function, and their corresponding average device performance indicators.	87
6.1	Polar and non-polar components of surface energies of the substrates and organics as calculated from contact angle measurement results.	101
8.1	LIBS system specifications	144
8.2	Energy levels and transition probabilities of In-271 nm and Zn-277 nm lines.	157

Figures

Figure

1.1	Deviation of average, annual global temperatures from the 1961-1990 period. An increase of one degree Celcius equals to two degree Fahrenheit. Reproduced from Ref. [108]	3
1.2	(a) The abundance of renewable power relative to current average global power consumption. Also indicated is the projected global power consumption if the whole world income increases to equal that of the US. (b) Global reserves of non-renewable energy sources. Also shown is the current annual consumption.	4
1.3	Molecular nature of OPV material make it possible for the device to absorb certain colors only (a), lending it the colorful nature (b).	8
1.4	Lightweight, flexible, and colorful, OPV offers a versatile deployment, for example on everyday objects or in building integration as a semi-transparent photovoltaic window.	8
1.5	Record photovoltaic cell efficiency by year and technology.	9
1.6	Typical OPV device architecture.	10
2.1	Illustration of photo-generation process in OPV. Adapted from Ref. [50]	15
2.2	OPV device architectures, indicating the different layers and the direction of charge collection in standard (blue) and inverted (red) architecture. Also shown are the different types of active layer architectures: planar bilayer, ordered heterojunction, and bulk-heterojunction.	16

3.1	Illustration of JV- characteristic of a solar cell and the important performance parameters. Sub-figure (a) is the zoomed-in version of (b). Note that the resistances are measured from the dark JV characteristics.	21
3.2	Terrestrial solar spectrum. Source: NIST.	21
3.3	Examples of UPS and IPES spectra, showing the extraction of the energy levels.	24
3.4	The Kelvin contact potential method for measuring workfunction (adapted from KP Technology manual).	25
3.5	(a) UV-Visible reflection / transmission set up.	27
3.6	Illustration of the XPS. Image credit: Wikipedia commons.	29
3.7	Basic elements of an AFM.	32
3.8	Illustration of Bragg's Law in XRD. In general, α is the incidence angle, and δ is the exit angle perpendicular to the sample.	35
3.9	Illustration for diffraction condition by two scatterers.	35
3.10	(a) Sample texture. (b) Orientation sensitivity of X-ray diffraction.	37
3.11	Pole figure of Si (111) planes from a single crystal. Image credit: Bruker Inc.	38
3.12	Illustration for XRD done at grazing incidence (GIXD).	39
3.13	(a) The two extreme direction of \vec{q} at a fixed incoming angle. (b) \vec{q} oriented inside this cone defined by $\omega = \theta - \alpha$ cannot be detected.	40
3.14	Illustration of XRD with 2D detector, showing the measurement geometry and examples of image data from samples with different textures.	42
3.15	Contact angle measurement.	46
4.1	Essential features of PLD-1.	49
4.2	Typical PLD-1 laser fluence calibration data.	51
4.3	(a) PLD-1 sample / heater stage. (b)-(c) Typical PLD-1 heater calibration data.	53
4.4	Typical PLD-1 deposition rate for NiO	55

4.5	Illustration of sputter deposition process. AC power ionizes inert gas (e.g. Ar), which are subsequently attracted and confined by the magnetic field. The magnetic field is such that the ions are accelerated towards target surface, ejecting target particles by momentum transfer.	55
4.6	Spin casting process.	57
4.7	(a) Nickel oxide powder. NiO has greenish hue when close to stoichiometry and black when oxidized. (b) The cubic rock-salt structure of stoichiometric NiO.	60
4.8	Work-function of the PLD NiO films as measured using the Kelvin method and UPS. Precision of KP data is less than 5 <i>meV</i> , UPS is 0.1 <i>eV</i>	64
4.9	Optical absorbance of PLD NiO _x films. Dotted line indicates <i>E_g</i> from photoemission.	66
4.10	UPS / IPES spectra of select PLD NiO _x films and the extracted energy levels.	66
4.11	GIXD of select PLD NiO _x films, showing the different structural property. Also shown for comparison is the data for solution-processed NiO _x and the data for the ITO substrate. The data for ITO is taken in $\theta - 2\theta$ geometry.	67
4.12	XPS (a) O1s and (b) Ni2p spectra of select PLD NiO _x films.	69
4.13	TEM of sputtered NiO films on ITO. (a) <i>t</i> = 5 nm, (b) <i>t</i> = 150 nm.	71
4.14	XRD of sputtered NiO _x grown at different Ar:O ₂ ratio: (a) 1:2, (b) 1:10, and (c) 1:45. Also shown in (d) is the XRD data taken with the same instrument and measurement geometry for a crystalline NiO film grown by PLD. Data are background-subtracted	72
4.15	Absorbance of sputtered NiO _x films grown at different oxygen condition.	74
4.16	Work-function decay of sputtered NiO grown at Ar:O ₂ = 1:2.	74
4.17	Photoemission study of sputtered NiO ₂ , set 1. <i>WF</i> and <i>E_v</i> of the sputtered NiO _x as a function of Ar:O ₂ ratio.	75
4.18	Photoemission study of sputtered NiO ₂ , set 2. (a) Photoemission onset, showing similar <i>WF</i> = 5.0 <i>eV</i> , (b) near gap structure, showing <i>E_v</i> = 5.4 <i>eV</i> , (c) changes in photoemission onset of the Ar:O ₂ =1:45 sample, (d) O1s XPS spectra, (e) Ni2p XPS spectra.	76

4.19	Illustration of P3HT, its lamellar structure in crystallites, and its optical absorbance.	78
4.20	UPS and IPES spectra of (a)-(b) neat P3HT and PCBM films, (c)-(d) P3HT:PCBM bulk heterojunction film. From Ref. [82].	79
4.21	C ₆₀ and C ₆₀ -PCBM	80
4.22	PEDOT:PSS	82
5.1	(a) TEM data of the sputtered NiO _x film, showing the lack of crystallinity and the 5 nm thickness. (b) Transmittance of sputtered NiO _x films with different deposition atmosphere.	88
5.2	J-V characteristics of the best P3HT:PCBM devices employing as-deposited NiO _x HTLs and PEDOT:PSS.	88
5.3	(a) XPS survey data of a sputtered NiO _x film, showing peaks from the various elements. (b) Comparison of the O 1s peaks of the different NiO _x films, showing the presence of Ni(OH) and hydrous oxides at different amounts. The “fresh” sample has been briefly exposed to air during sample transport.	90
5.4	UPS data on different blends of P3HT:PCBM on NiO _x HTL.	91
5.5	The energy level alignments of the OPV layers used in this study: (a) before equilibration (Vacuum level aligned), and (b) after equilibration (Fermi level aligned) showing vacuum level shifts. The valence bands (LUMO) levels are taken from Ref. [82].	93
6.1	(a) Device structure. (b) P3HT concentration as a function of argon sputtering time, suggesting vertical phase segregation of the BHJ. Calibration data are displayed as-is, while sample data are normalized to the P3HT sputter calibration. Dot-dash line marks 50% P3HT by weight.	99
6.2	AFM images of nickel oxide (S, R, H) and PEDOT:PSS (P) substrates, all deposited on ITO. PEDOT:PSS surface roughness is lower due to its thickness.	103

6.3	XPS (a) O1s and (b) Ni2p of the nickel oxide substrates, indicating the P0, P1, and P2 peaks. Spectra are offset for clarity.	104
6.4	GIXD of the nickel oxide substrates. Also shown is the $\theta - 2\theta$ XRD of ITO for comparison.	105
6.5	Illustration of the XRD data processing: (a) P3HT and its crystallite, (b) measurement geometry and principal axes, (c) specular Q-scan, equivalent to $\theta/2\theta$, (d) X-scan. Note that instead of taking a slice of the 2D scan, we took a high-resolution $\theta/2\theta$ scan	108
6.6	Fit results of the XRD data as a function of film thickness for P3HT:PCBM deposited on different NiO _x HTL. See text for details.	109
6.7	Pseudo-Voigt mixing parameter describing the XRD peak shape as a function of thickness. Also shown for comparison are the corresponding crystallite sizes.	112
6.8	Illustration of P3HT:PCBM film formation process	114
7.1	Energy levels of a heterojunction (a) before contact and (b) after contact, with an illustration of kinetic barrier experienced by an electron traveling along the conduction band edge.	118
7.2	Energy levels in ideal heterojunctions with various band-offsets (Case 1 – 3) and reduced V_{bi} (Case 4). The devices are under illumination, resulting in splitting of E_{Fn} from E_F . For simplicity, only electron transport is considered. The corresponding JV curves are shown below each diagram, where the black curve is the best device. See text for details.	120
7.3	Case 1 under increasing illumination and forward bias. The calculated J-V characteristics using typical values from fits of actual devices is also shown.	122
7.4	Case 3 under increasing forward bias. The calculated J-V characteristics under increasing ΔE_c are also shown.	126

7.5	(a) Case 2 under illumination, illustrating the reduction in φ_n across the interface. (b) The calculated J-V characteristics with increasing ΔE_c	127
7.6	Calculated J-V characteristics for Case 4. The arrow indicates the direction for reduced V_{bi}	130
7.7	Energy levels of P3HT and PCBM from Ref. [82].	130
7.8	(a) WF of PLD NiO_x as a function of $p(\text{O}_2)$. (b) Energy levels for 4 samples in the set, together with the final band-alignment with P3HT:PCBM following Anderson's rules.	131
7.9	NiO_x film absorbances as a function of deposition parameters.	133
7.10	JV characteristics of P3HT:PCBM devices on NiO_x HTL's deposited under varying parameters. Black curve is the best device. (a) Blue curves uses NiO_x grown at higher $p(\text{O}_2)$, while (b) orange curves employ NiO_x grown at elevated temperature.	133
7.11	(a) Numerically simulated J-V characteristics for devices containing an injection barrier at an organic HTL / organic BHJ interface (dashed). The solid lines are for flat heterojunctions and are not relevant for our studies. (b) Experimentally measured J-V characteristics. Our analytical treatment is able to explain these observations by Tress et al. Reproduced from Ref. [244]	135
7.12	An illustration of the proposed optimal energy levels for HTL and ETL in a photovoltaic device after contact. Below, an illustration of the rules on how to achieve the final band alignment assuming the validity of Anderson's rules.	137
8.1	Diagrammatic representation of the LIBS system.	143
8.2	LIBS raw data and the position of Zn and In peaks. (A) is the zoom-in of the raw spectra between wavelengths = 268 and 280 nm, showing the data, and the positions of In and Zn lines, including the ones that we analyze. (B) is the full spectra that we obtain from the LIBS. (C) and (D) respectively shows the relative position of In and Zn peaks with normalized relative intensity.	146

8.3	Microscope image of the laser-ablated spots on an a-IZO sample. The film was completely ablated after 3 laser shots.	147
8.4	Cross section profile of LIBS laser-ablated spot on a 200 nm-thick a-IZO sample. Data was taken using stylus profilometer across the diameter of a spot created by 3 laser shots. Spot diameter was about 800 μm	148
8.5	Signal count as a function of camera focus position relative to the sample surface. $D = 0 \mu\text{m}$ corresponds to camera focus on the sample surface, while negative value corresponds to camera focus below the sample surface. Based on the intensity of the Zn line, $D = -400 \mu\text{m}$ was used as the optimum position.	150
8.6	Figure 6(A) shows the LIBS spectra as a function of time delay between the start of data acquisition and the laser fire, t_d . $t_d = 0$ corresponds to starting data acquisition when the laser fires, while positive and negative t_d corresponds to starting data acquisition after and before the laser fires. Figure 6(B) shows the signal to noise ratio of Zn-277 nm and In-271 nm lines as a function of t_d as given in Equation 8.1. The optimum time delay is 5 μs after the laser fires.	152
8.7	LIBS calibration curve. The ratios of the Zn-277nm to In-271nm characteristic lines against indium atomic percent from ICP-AES analysis. Equation 8.4 was fitted to the data and the calibration coefficient extracted. The uncertainty of the calibration coefficient is from orthogonal distance regression (ODR = 2) fit.	159
8.8	LIBS and ICP-AES combinatorial compositional analysis results as a function of position across the sample. Data is taken from 3 combinatorial libraries with different expected indium content. L2, L3 and L4 are expected to have indium content of 15-50 at%, 35-70 at%, and 70-95 at% respectively.	161
8.9	2D Mapping of indium atomic percent in a combinatorial a-IZO sample using (A) ICP-AES, (B) LIBS, and (C) XRF. Note that LIBS mapping consists of 1 less column than the XRF.	162

9.1	An illustration of the proposed optimal energy levels for HTL and ETL in a photovoltaic device after contact. Below, rules on how to achieve the final band alignment assuming the validity of Anderson's rule.	166
9.2	Illustration of P3HT:PCBM film formation process	169
9.3	Proposed design phase flow for contact optimization.	171
9.4	Illustration of the processes involved in a combinatorial device study. In the illustrated case, we vary the interlayer property.	174
9.5	Preliminary combinatorial OPV device data. See text for details.	175
9.6	(a) Illustration of the various distances in a material and the disorders related to them. (b) Building blocks of short-range disorders.	179
9.7	Spano fit of P3HT:PCBM data.	180
B.1	Work-functions of select metals.	209
B.2	The Shockley-Queisser thermodynamic limit for single E_g photovoltaic material. . .	215
C.1	n and p and their dependence on E_F and $g(E)$. (a) shows the e^- density of states as a function of energy. (b) is the Fermi-Dirac function describing the probability of such states being occupied by an e^- . (c) shows the actual e^- population, which is the product of $g_e(E)$ and $f(E)$. In an n-doped material, the dopant effectively raises the equilibrium Fermi level (d), resulting in an increased e^- population at the expense of h^+ population (e) as dictated by Eqn. C.6.	219
C.2	Illustration of the doping process and carrier injection.	221
C.3	n and p in the presence of external work, illustrating the quasi-Fermi level splitting. In non-equilibrium, the external energy supplied excites e^- into E_c , leaving h^+ in E_v . This increases n and p and, equivalently, splitting E_{Fn} and E_{Fp} away from E_F . Compare with Fig C.1.	225

C.4	Examples of energy levels for drift and diffusion currents. The last figure is for Dember effect in non-uniform illumination of photoactive layer at flat band, in this case the photons arrive from the left. The net current is zero.	229
C.5	Sketch of energy levels across a junction at thermodynamic equilibrium.	232
D.1	Energy levels in a homojunction and heterojunctions. The top figures illustrate the materials before contact. The bottom figures depict the final band alignment following Anderson's rule. Arrows indicate the band-offsets.	237
D.2	Energy levels in a staggered n-p heterojunction before (a) and after (b) contact. . .	237
D.3	Depletion, inversion, and accumulation	239
D.4	Energy levels in a staggered n-p heterojunction at (a) equilibrium, (b) low forward bias, and (c) high forward bias. Positive current at forward bias is defined to flow from material 2 to 1 (e^- current from material 1 to 2)	241

Chapter 1

Introduction

1.1 On Sustainability

Any discussions on renewable energy inevitably touch upon the broad concept of sustainability. At TED 2009, Prof. Louise Fresco, ex- assistant director-general for research at United Nations Food and Agriculture Organization, in relation to her research on world famine, warned that never before has humanity become so detached from their food source; that despite its importance to the continuity of human life. This has led to, for example, the greatest irony that some drives for “sustainable” farming practices have led to not enough quantity of food being produced to feed the communities they are supposed to support. Or that “organic” eating habits in some parts of the developed world have led to famine in poorer parts of the globe. Often, the global drive for famine eradication are reduced to efforts based on narrow-minded interpretation of sustainability.

A similar case can be argued for energy. It is the author’s opinion that it is not the case that the general public is apathetic to living sustainably, nor do some segments of the society conspire to scuttle sustainability efforts to keep their socio-economic privileges. It is not the case either that “normal folks” are not mentally gifted enough to understand the importance of data such as shown in Fig. 1.1. Perhaps we are simply so detached from our energy cycle that a holistic view of energy sustainability is hard to comprehend. For example, very few energy consumers notice that a typical power usage in a developed country of 10 kW per person [262, 15] is roughly equivalent to ridiculously having 10 horses or 100 servants per person¹. Literally, everybody is a king. Is this

¹ 1 horse power = 750 W , man-power assumes daily diet of $2000\text{ Cal} = 8.4\text{ kJ}$ and 8 work hours.

sustainable? How do we define sustainability?

Here's a picture of being globally sustainable offered by Mr. Albert Rose, a respected physicist most renowned as the man behind video camera tubes. **A sustainable development is one that allows the global population reach the standard of living currently enjoyed by the developed world without permanently rising average global temperature by one or two degree [201]².**

The co-dependence of energy supply and economic development is obvious and do not need further explanation. The need to keep global temperature constant to within one or two degree, however, might be shocking to a lot of people. We shall see that this sets a very stringent limit to global prosperity.

The reason for this limit is simple: one's body cannot function well when the body's temperature is raised by a mere few degree (one gets fever or heat shock). In summer days, wind breeze helps regulate our body temperature. However, if the temperature of the whole world increases, then the winds will also be hotter, and our body's will necessarily increase its temperature by as much. If global temperature increases, the whole world will be affected, and a world with most of its population on sickbed is definitely not a picture of a sustainable future.

So never mind the debate whether global warming is real. The case to be made is a permanent one degree increase in global temperature is definitely not a risk worth flirting around with. This should be an absolute upper limit in defining a sustainable development.

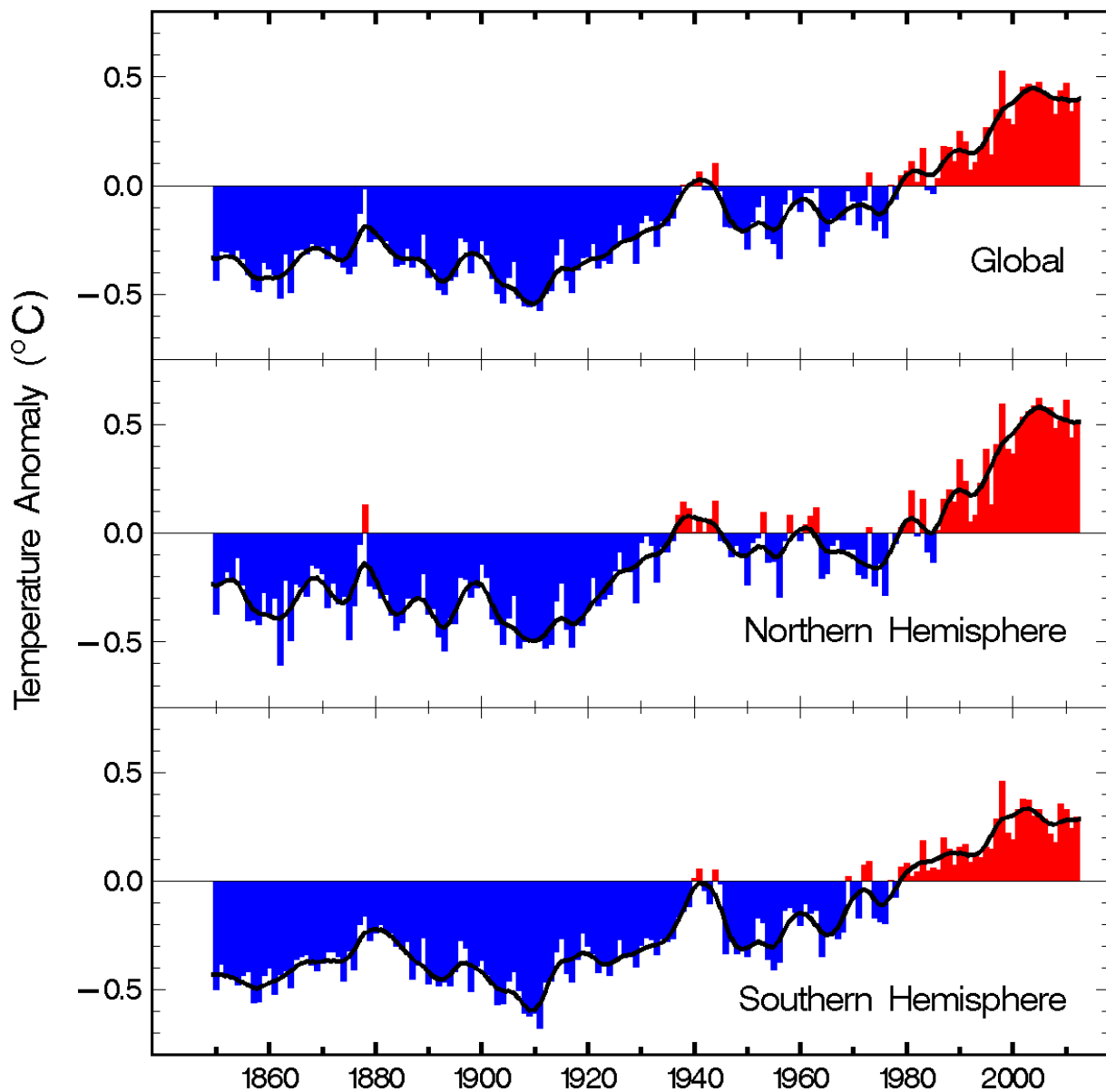
1.2 The Case for Photovoltaics

So how much do we energy currently consume? Average world consumption is about 0.6 ZJ at 15 TW . If the rest of the world reaches the standard of living of that of the US, energy consumption will increase by roughly 120-fold³. Fig. 1.2a compares the world energy consumption against how much renewable energy is available and how much non-renewable energy reserves are

² A very recommended reading targeted towards both technical and non-technical readers.

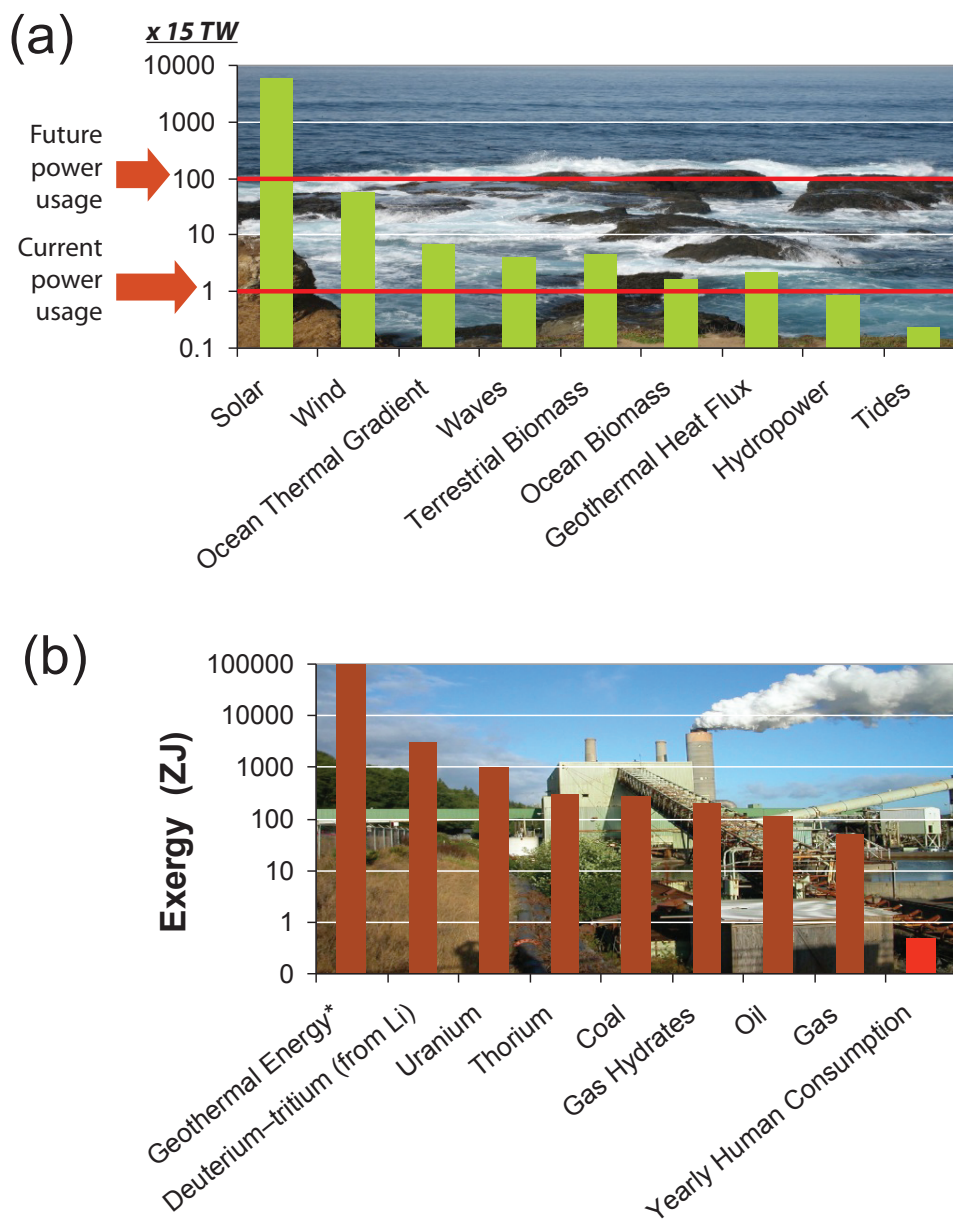
³ Assuming GDP per capita of \$12k for world average and \$48k for the US, world population of 7 billion, US population of 250 million. This is a conservative figure considering the rapid increase in global population.

Global and Hemispheric Annual Temperature Anomalies 1850–2012



Source: P. D. Jones, T. J. Osborn, and K. R. Briffa
 University of East Anglia, Norwich, UK
 D. E. Parker, Met. Office, Bracknell, Berkshire, UK

Figure 1.1: Deviation of average, annual global temperatures from the 1961-1990 period. An increase of one degree Celcius equals to two degree Fahrenheit. Reproduced from Ref. [108]



From Hermann, 2006: Quantifying Global Exergy Resources, Energy 31 (2006) 1349–1366

Figure 1.2: (a) The abundance of renewable power relative to current average global power consumption. Also indicated is the projected global power consumption if the whole world income increases to equal that of the US. (b) Global reserves of non-renewable energy sources. Also shown is the current annual consumption.

available. Note that renewable energy is measured in the unit of power while non-renewables in energy. This reflects that renewable energy sources cannot be depleted, but is ultimately limited in terms of the generated power (energy per unit time). In contrast, non-renewables can be depleted, but it can generate more power for shorter period of time.

Most of current energy generation systems involve fossil fuel burning, whether it is coal, natural gas, or oil. Fig. 1.2b already highlights one of the most imminent problem of continued reliance on fossil fuel: the world reserve will only last for another century or so. It is not sustainable.

In direct contrast, renewable energy sources are more than enough to sustain a “good life” of 10 *kW* consumption per capita for the whole world. In fact, **solar energy alone is enough to feed more than 10 times the amount of the projected energy demand.**

Another problem with burning fossil fuel is its waste product: dust particles, acidic gas, and of course greenhouse gases. Dust particles, acidic gases, and some greenhouse gases impose health hazard and reduces quality of life. Recent appalling news on the Chinese air quality is a sobering reminder of this.

The **greenhouse gases**, on the other hand, **imposes the most imminent and stringent limit to sustainable development.** The “normal” temperature of the Earth is dictated by the balance of heat we receive from the sun and the heat that is re-radiated by the Earth. Greenhouse gases in the atmosphere prevent heat from being re-radiated from the Earth, effectively trapping it near Earth’s surface leading to an increase in surface temperature.

The current level of CO₂ traps an equivalent of roughly 0.5% of the solar radiation close to Earth’s surface. This is a miniscule fraction. However, as shown in Fig. 1.2a, it is easily ten times the current global energy usage. Worse, this corresponds to about 0.5°C increase in temperature since 1980 (Fig. 1.1), close to the maximum limit of 1°C increase in temperature that were discussed earlier. If we would continue producing the greenhouse gas as by-products of energy generation, the world power production is limited to increase by maximum a factor of 2 in order to keep temperature change below 1°C. At this point, a careful reader might challenge that we might

be able to add another factor of 2, or 3, or even 10 due to various reasons⁴. The case to be made is that this is very far short of the 120-fold increase necessary to improve standard of living of the whole world. Again, this is not sustainable.

From this point of view, photovoltaic is the ultimate way for energy generation. Due to the abundance of solar energy, it is also probably the only one that has the potential to completely satisfy the world's thirst for energy while being environmentally friendly. Additionally, it does not generate any hazardous byproduct during operation. It also is the only one that has the chance of being modular enough to be deployed almost anywhere, which will allow energy generation to be more integrated with our lives.

Answering the question: "is our current way of life sustainable?" We believe that such good life can be sustainable. However, **the use of renewable energy is a necessary pre-requisite such high standard of living in a global level**. Photovoltaic is perhaps one of the most serious contender to be a big energy player in the future due to its sheer potential and the possibility for modular deployment. One of the main challenges for photovoltaic is of course related to their high initial cost relative to other energy sources⁵. It is the purpose of this work to be part of the effort to make photovoltaic more accessible to most economies.

1.3 Organic Photovoltaics

Organic photovoltaic (OPV) is one of the photovoltaic technologies championed by Mr. Rose more than three decades ago, back when "organic electronics" was almost unheard of outside a small fraction of the scientific community. It refers to a class of photovoltaic technologies that incorporate organic materials, such as small molecules or polymers as the photoactive material, i.e. the part that is responsible to convert light into electricity. Many of these organic materials are very good light absorbers with optical absorption coefficient above $10^7 m^{-1}$ in the visible range [50]. This is very high, allowing efficient light absorption with mere 100 *nm* of film thickness, a

⁴ For example, greenhouse gases are generated not only from power plants, but also from other carbon burning: cars, engines, forest clearing, etc.

⁵ Note that price for fossil fuel is subsidized in many nations.

factor of ten thinner than the few μm of CuInSe_2 . It is even a factor of 1000 thinner than the several hundred μm of the leading terrestrial solar cell technology, monocrystalline Si. On top of this, organic materials are abundant and do not naturally contain harmful elements. Further, most of the technology required for processing these types of materials are already mature: organic materials are used profusely in the form of plastics, coatings, and additives to name a few. This leads to the possibility of producing a highly cost-effective photovoltaic systems, in contrast to the relatively more expensive inorganic modules that dominate the market [28].

Economic sense is not the sole OPV strength. Tunable color and mechanical flexibility of these materials also give OPV a unique edge over other photovoltaic systems. Imagine a photovoltaic converter that has characteristics of a plastic sheet: lightweight, foldable, and possibly colorful! This allows for a very versatile deployment. For example, due to their molecular nature, thinner-than-usual OPV device may selectively absorb certain colors, resulting in colorful devices (Fig. 1.3). Combined with its lightweight character and low cost, OPV has attracted architects for potential artful building-integrated applications. Integration may not stop at buildings. Being flexible, OPV modules may eventually be incorporated into everyday objects: umbrellas, bags, cellphone cover to name a few (Fig. 1.4). In other words, OPV is perhaps the photovoltaic technology that may become pervasively used in consumer products.

A relatively new solar energy conversion technology, OPV has been stigmatized with low device efficiencies and short lifetime until recently. However, development has been dramatic: power conversion efficiency for laboratory cells have improved with rapidly from 2% in year 2001 to 8.3% in year 2010 (Fig. 1.5), and the latest figure reached 12.0%. Arguably, such rapid progress can only be matched by that of multi-junction III-V technology (top purple curve of Fig. 1.5). On another front, innovation in device architectures and novel photoactive materials have resulted in a significant improvement in device lifetime [218, 269, 142, 141]. Understanding of device physics have also progressed significantly [50].

The richness of carbon chemistry make the material choice for OPV almost limitless, and arguably this gives OPV a potentially unique advantage over other photovoltaic technologies. Nat-

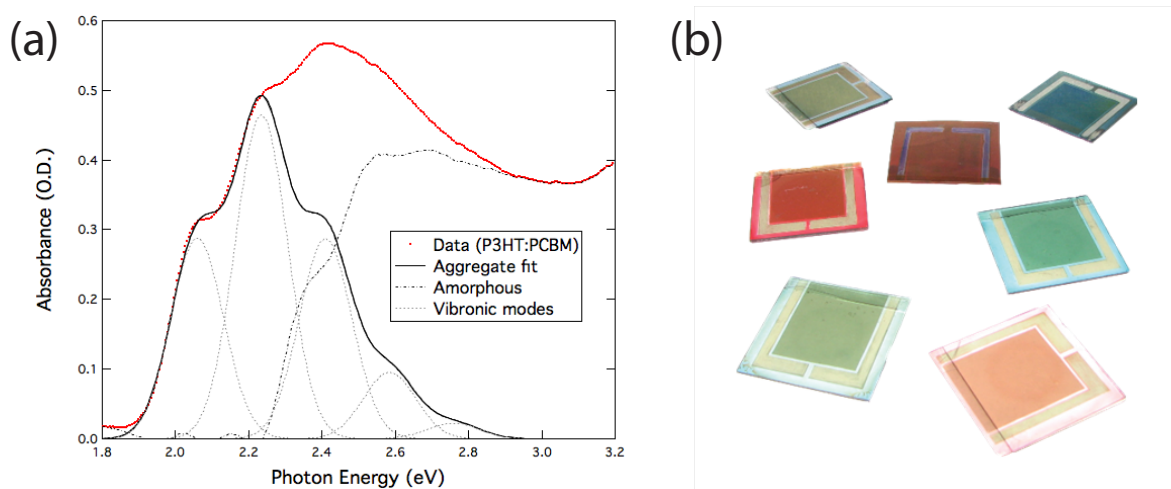


Figure 1.3: Molecular nature of OPV material make it possible for the device to absorb certain colors only (a), lending it the colorful nature (b).

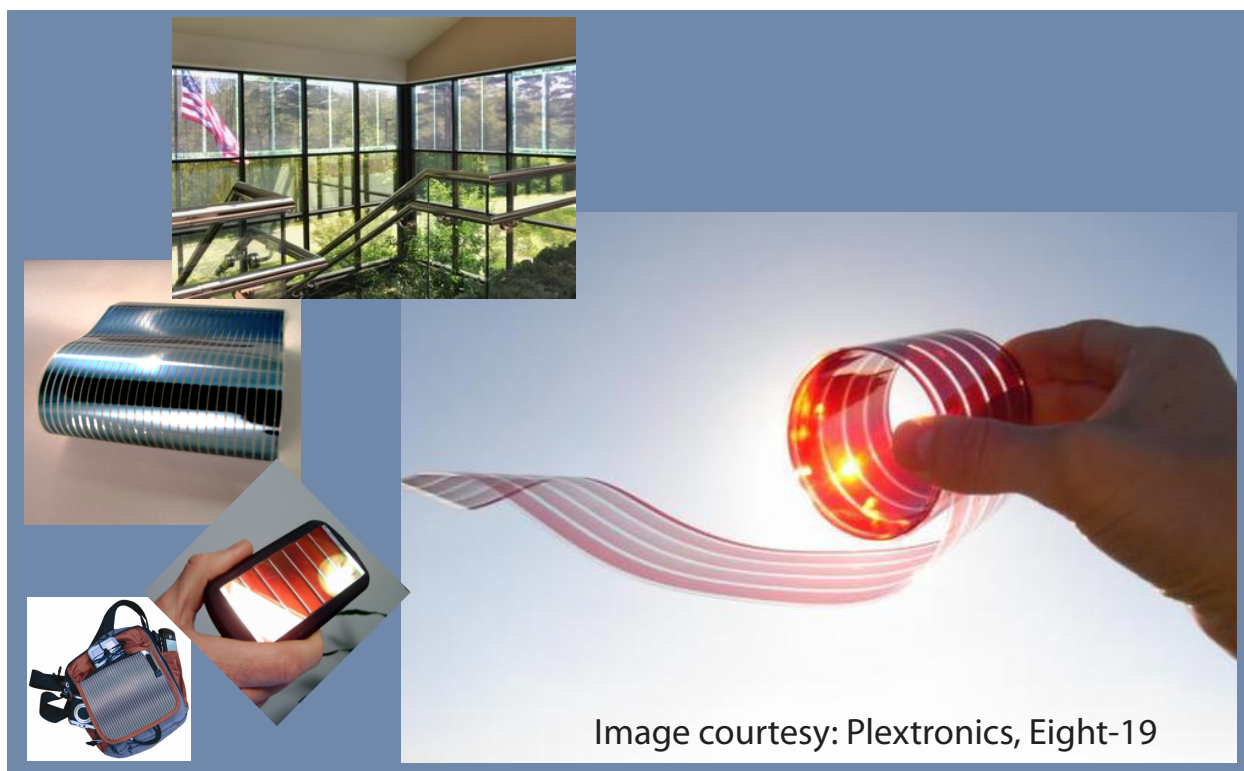


Figure 1.4: Lightweight, flexible, and colorful, OPV offers a versatile deployment, for example on everyday objects or in building integration as a semi-transparent photovoltaic window.

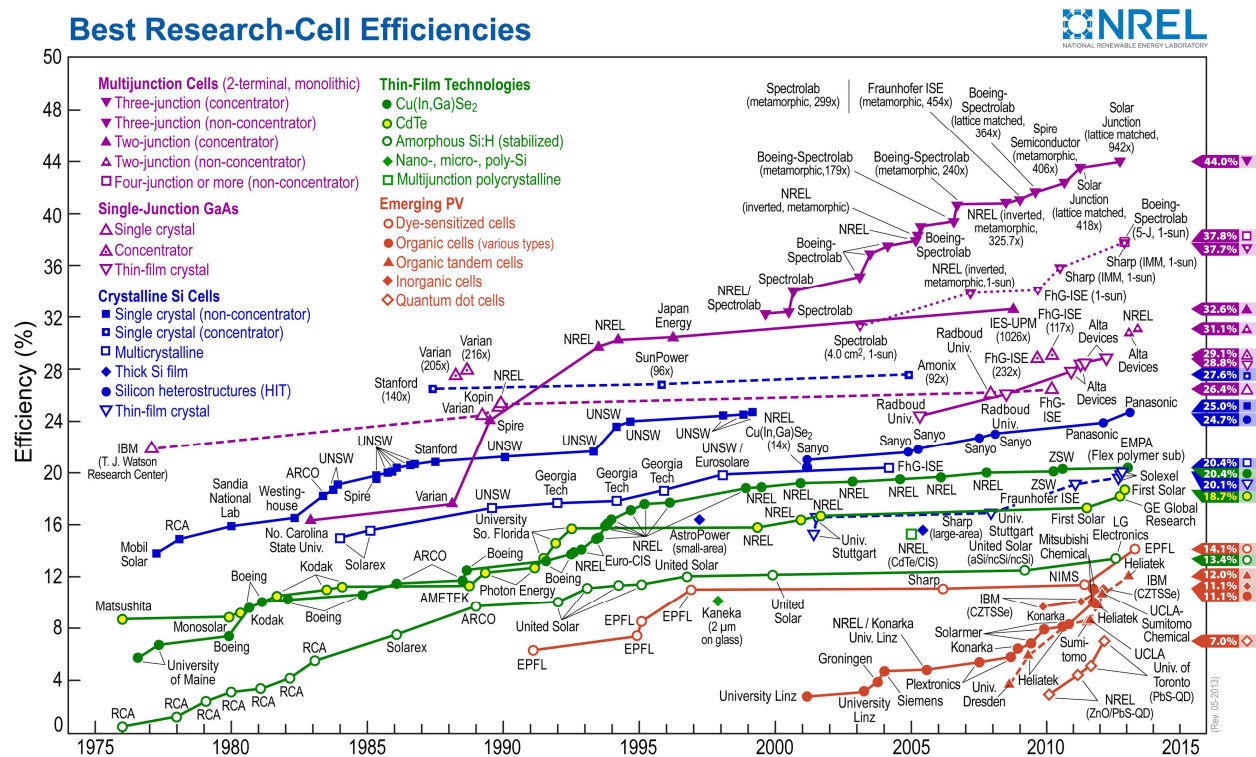


Figure 1.5: Record photovoltaic cell efficiency by year and technology.

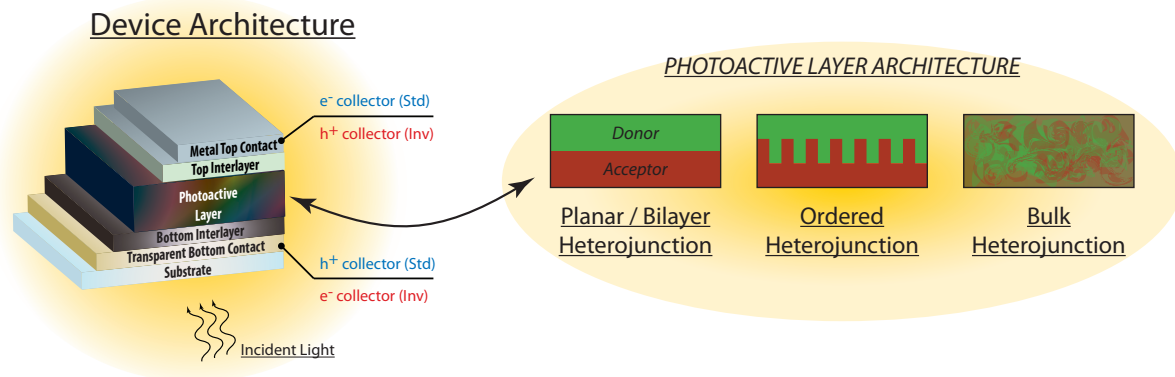


Figure 1.6: Typical OPV device architecture.

usually, the most dramatic advances in power conversion efficiency for OPV devices have resulted from developments of more efficient photo-active materials [134, 213, 25]. However, photoactive materials are just one building block of an efficient device (Fig. 1.6). Contact materials and device architecture also play crucial roles in achieving higher efficiency, and are expected to rise in importance as OPV technology drives to maturity.

Indium tin oxide (ITO) currently still reigns as the most commonly used transparent conductive oxide (TCO) [72, 129, 219]. ITO, being polycrystalline and typically deposited at high temperatures, is not the best match to the desire of using flexible substrates, low-temperature deposition, and organic materials. The last decade have seen replacement candidates, many of which are ZnO-based materials, emerging with various degree of success [57]. Of particular interest, Ga:ZnO_x, In:ZnO_x, and Al:ZnO_x have been demonstrated as compatible with organic photovoltaic [9, 238, 77, 20]. The use of highly conductive poly(3,4-thylenedioxythiophene)poly: (styrenesulfonate) (PEDOT:PSS), a polymer mixture, as a flexible TCO has also been demonstrated [164].

Closer to the focus of this work is the prevalent use of interlayers. Their important function can be likened to a gate for charges that divides the photovoltaic cell and the external world: it allows for an efficient charge extraction. From one perspective, interlayers such as PEDOT:PSS or ultra-thin NiO_x improves device performance by directing electronic paths in the device [104].

From another equally important point of view, they also “bridge” the contact material and the photoactive material, allowing cross-compatibility among the myriad novel photoactive materials and the more limited choice of TCO’s. There are also other ways that such functional layer can improve device performance. For example, it has been shown that TiO₂ **optical spacer** improves device performance by increasing light intensity, leading to increased current extraction [206].

1.4 Thesis Focus and Organization

It is the focus of this work to improve our understanding of the physics of the interlayers in OPV. Why does it improve device performance? In particular, we are interested in investigating how an interlayer’s electronic properties impact photovoltaic performance.

So far, there is only one design rule for an interlayer: that its work-function has to be as high as possible. The ultimate goal is to utilize the knowledge gained from this study to synthesize a more comprehensive list of design rules that connect the electronic properties of the organic photoactive material and that of the interlayer.

This work can be divided into 3 large sections:

Background information that serves to familiarize the readers to the details of the experiments.

This includes the current chapter, an overview to the physics involved in OPV §2, a chapter dedicated to explaining general aspects of important characterization techniques (§3), and the materials (§4) involved in the study.

Experimental results and discussions begins with discussions on the development of sputtered NiO_x interlayers (§5). This series of experiments underscore the need of a more thorough understanding of the physics of interlayers than the mere work function rule. We also learn from this study the subtleties that need to be addressed in order to perform a careful investigation on these OPV devices. The most challenging issue to tackle is assessing and ensuring that the photoactive layer remain unaltered upon changing interlayer. The result of our investigation on the photoactive layer morphology is discussed (§6). We then discuss

the central results of our study on the band alignment at the oxide / organic interface and how it impacts device performance (§7). Based upon this study and the literatures available recently, we propose a set of design rules for the electrical contact material. Lastly, to match the rapid discoveries of novel photoactive materials, we need a high-throughput scientific investigation approach⁶. Here we present our work on optimization a combinatorial composition analysis system (§8) as an effort to develop such high-throughput scientific investigation approach.

Closing remarks (§9) concludes this work by first giving a summary of the main results presented in this thesis. It is then followed by future outlooks on experiments that might be of interest or that is in progress.

Lastly, a short review of device physics is presented in the appendices.

⁶ The “old” high-throughput approach is to employ a throng of graduate students.

Chapter 2

Physics Specific to Bulk-Heterojunction Organic Photovoltaics

OPV works based on the same basic physics that governed all photovoltaics technologies. The energy harvest starts with a photogeneration of charged carriers in the material. By tailoring the device structure appropriately, these photogenerated carriers flow in an ordered way, giving rise to the electrical current that can be used to do work. A short review of these topics are covered in the appendices (photovoltaic effect in §B, transport of charged particles inside a material in §C, and junctions in §D). However, there always exist details unique to each specific photo conversion technologies. OPV is not special in this respect. Therefore, before we move on to discuss the experiments, we would like to briefly touch upon some of the unique characteristics of OPV.

2.1 Carrier Transport in Organic Materials

The first characteristic that is rather unique to OPV is the low carrier mobility in the organic materials due to the hopping nature of carrier conduction, understandable from its largely disordered nature. Carrier mobility is typically in the range of $10^{-7} - 10^{-3} \text{ cm}^2 \text{ V}^{-1} \text{ s}^{-1}$, easily 10 orders of magnitude lower than that of Si. Carrier concentration, on the other hand, is still respectable at $10^{15} - 10^{16} \text{ cm}^{-3}$ [67, 24, 74, 151, 139]. Combined, this leads to conductivity of $\lesssim 10^{-6} \Omega^{-1} \text{ cm}^{-1}$ or resistivity of $\gtrsim 10^6 \Omega^1 \text{ cm}^1$.

The low carrier mobility is commonly thought as one of the main drawback of OPV. However, this is not entirely true. For a typical device area of 0.11 cm^2 , the series resistance of the device increases by, at best, $\sim 1 \Omega / 100 \text{ nm}$. Therefore, an OPV device is limited in terms of active layer

thickness to a few hundred nanometers. However, the high optical absorptivity of the organic absorber actually allows us to use very thin films. Typical active layer thickness is less than 0.5 μm and as low as 100 nm , resulting in a respectable $\sim 10 \Omega$ series resistance¹.

More importantly, however, the hopping nature of conduction in organic materials raises a critical question: are the results of drift-diffusion model, used profusely in the semiconductor community, applicable to these materials? In particular, the validity of this model for practical device thicknesses, which are greater than the mean hopping distance, is unclear. If application of drift-diffusion and the band transport model are justified, then we have at our disposal the established yet simple tools available in the semiconductor physics arsenal. Of particular interest is the use of the energy level diagrams, drawing the analogies between the HOMO (LUMO) of the organic material with E_v (E_c) in crystals.

Stallinga defends its use, with the addition of trap states, to describe conduction in semiconducting organic materials based on the simple argument that if the material is conductive enough then the electronic wavefunction is delocalized enough to justify the drift-diffusion / band transport picture [231]. This is not at all a new concept. In fact, the use of the concept “effective transport energy”, which bears strong parallels with the concept of “mobility edge” and “band tail” in amorphous semiconductors, has been gaining momentum [50]. The relationship between hopping time and the distribution of the tail states have also been derived [241]. Perhaps the most convincing demonstration is Tress’ thorough work on testing the applicability of the drift-diffusion model for OPV devices [245]. Through comparison of a multitude of simulation and experimental results, it is concluded that the model is consistent with macroscopic observations in device performance. However, the limits of the physical depth of the model is still unclear, and caution must be used.

In this light, throughout this work, we assume that the drift-diffusion model is applicable for describing carrier transport in the organic material. The 3D nature of the bulk-heterojunction layer obviously cannot be taken into account in the simple 1D picture. Instead, we follow the approach of Kirchartz et al. in modeling the active layer as an effectively quasi-homogenous material with

¹ Not taking into account contact resistance and cable resistance.

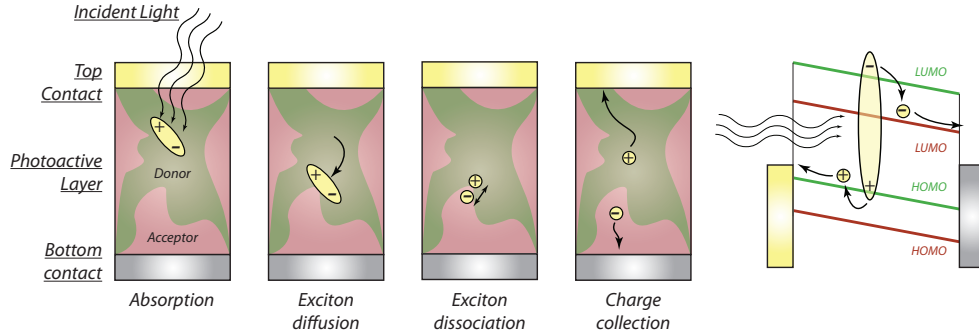


Figure 2.1: Illustration of photo-generation process in OPV. Adapted from Ref. [50]

an effective $E_c = LUMO_A$, $E_v = HOMO_D$, and $E_g = E_c - E_v$ [147, 115].

2.2 Photocarrier Generation and Bulk Heterojunctions

The second, but more important limitation for OPV is related to the charge generation process in the photoactive material (Fig. 2.1). Due to the low dielectric constant ($\epsilon_r \sim 3-4$) of the organic materials, an absorbed photon does not readily yield free carriers, but typically results in a tightly-bound excitons with binding energy usually in the order of 100 meV , which is much greater than the thermal energy at typical operating condition ($kT \sim 27\text{ meV}$) [79]. Dissociations of these excitons is generally understood to happen at the interface between the donor and absorber material [83, 69, 70]. Fundamentally, this process is very efficient, and does not constitute a rate-limiter for photogeneration [215]. However, this indirectly leads to the performance of OPV photoactive materials to be characteristically limited by the exciton diffusion length, typically on the order of $3-10\text{ nm}$ [83, 151].

The requirement that excitons diffuse to the donor / acceptor heterojunction places a stringent constraint on device architecture (Fig. 2.2 a-c). The typical bilayer, planar heterostructure is thus not the best architecture for OPV in general. Nano-scale engineering of the active layer morphology to produce nano-structures with sizes less than this characteristic length (widely known as an “ordered heterojunction”) has been shown to effectively improve device performance [151].

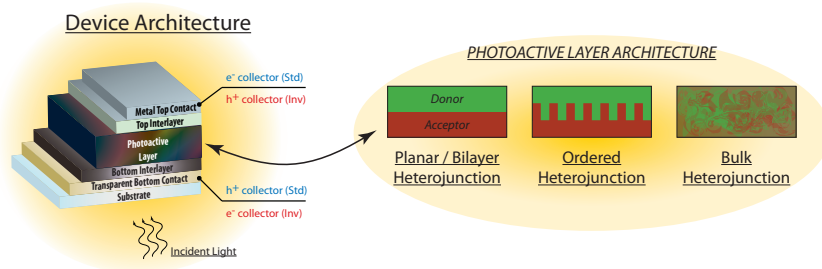


Figure 2.2: OPV device architectures, indicating the different layers and the direction of charge collection in standard (blue) and inverted (red) architecture. Also shown are the different types of active layer architectures: planar bilayer, ordered heterojunction, and bulk-heterojunction.

However, fabrication of an ordered heterojunction is arguably not cost-efficient, effectively reducing the economic advantage of OPV. Instead, the highly folded BHJ architecture has been widely utilized as a cost-efficient and effective solution to this problem [52], and is now almost exclusively used in best-performing OPV cells ².

BHJ active layers are solution deposited from a mixture solution of the (donor and acceptor) constituents. As the quasi-homogenous solution dries, the dissolved constituents phase segregate into nano-scale domains which form the heterojunctions. This effectively reduces the exciton diffusion distance while increasing the donor-acceptor interfacial area, leading to high **internal quantum efficiencies** (number of carrier produced per incident photon). An internal quantum efficiency of nearly 100% has been reported with this architecture [215, 178]. Needless to say, the ease of fabrication and the effectiveness of the BHJ architecture in improving the quantum efficiency of the device have led it to become the de-facto active-layer architecture for OPV devices, even in tandem OPV cells [233, 113].

Does this extra step in photo-carrier generation, namely the exciton dissociation, render invalid the discussions on thermodynamic limit of efficiency? The answer is no. The Shockley-Queisser limit is still the thermodynamic limit of photo conversion efficiency. This is because the Shockley-Queisser treatment bypasses any assumption of specific photo-generation path by

² Excluding tandem cells.

postulating that all photons with quantum energy greater than E_g produces exactly one e^-h^+ pair in the external circuit [116]. In fact, it can be argued that the extra energy expended to dissociate the exciton can be grouped in the non-radiative loss that reduces device efficiency.

2.3 Interlayers

Unfortunately, the use of BHJ architecture is not without its own set of disadvantages. First, the complexity of the device structure dramatically increases, and the final nano-structure of the solution-processed layer is strongly influenced by the drying kinetics, solvent properties, and the substrate properties [84]. This greatly elevates the challenge for performing highly controlled scientific investigations. For example, studies involving changes of the substrate surface must also take into account any possible changes in the details of the BHJ structure that are caused by differences in the surface properties of the substrate³. Often, basic scientific studies revert back to using planar heterojunction architectures before exploring the BHJ.

Second, due to its quasi-homogenous nature, BHJ architecture of the photo-active material leads to a loss in the asymmetry in the built-in potential that helps carrier extraction and reduces charge recombination in traditional bilayer or ordered heterojunction architecture [259]. The built-in potential plays a tremendous role in charge extraction in OPV since carrier lifetime is significantly lower than that typically found in inorganic technologies (this is due to the inherently disordered nature of the material). Device contacts modifiers, generically termed **interlayers** have been typically used to make up for this loss in various ways. For example, poly(3,4-thylenedioxythiophene)poly:(styrenesulfonate) (PEDOT:PSS) is an organic layer that has been successfully and widely used as a **hole transport layer** (HTL) in many OPV devices. Its high WF , when used in conjunction with metal anode that has lower WF , recreates the built-in potential for carrier extraction. Similarly, MoO_3 interlayer has also been shown to improve hole extraction from the device [153, 85, 94, 110]. There are also other ways that such functional layer can improve device performance. For example, it has been shown that TiO_2 **optical spacer** improves

³ We shall see an example of its importance in §6-7

device performance by increasing light intensity in the absorber layer, leading to increased current generation [206].

There are a few important properties about materials for such contact modifications regardless of the details of their function in a photovoltaic device:

- Compatibility with both the contact and the photo-active material
- Tuneability in the functional property, whether it is optical, chemical, or electronic, to cater to the myriad photo-active materials,
- Transparency, especially when employed at the bottom (window) contact
- Chemical and physical durability, especially when employed at the top contact
- Ease of deposition and scalability
- Material abundance and low cost

Many oxide thin films are easily deposited either by physical and chemical vapor deposition or from solution, have high chemical stability, and are transparent in the optical regime. More importantly, their energy levels, doping concentration, and morphology can be systematically tuned by varying the deposition parameters or composition. These characteristics, when complemented by the high repeatability of PVD methods, make oxide thin films very attractive as contact modifiers for OPV cells.

2.4 Heterojunction Nature of OPV Devices

Lastly, we would like to underscore the heterojunction nature (as opposed to homojunction) of OPV devices. From the preceding discussions, it is clear that an OPV device is generally made of multiple materials. This, by definition, makes it a heterojunction, not a homojunction. Three important implications are [119, 234, 173]:

- Band-offsets, i.e. discontinuities of electronic energy levels, may occur at interfaces

- Interfacial states are more likely to develop at interfaces
- Fermi-level pinning may happen at interfaces

This can be a double edged sword. On one hand, it adds to the complexity of the device, and the use of homojunction-related formulae must be accompanied with great care. On the other hand, it add extra degrees of freedom to the device design, possibly allowing for characteristics that are otherwise not obtainable by homojunction devices [127, 5].

The central theme of this thesis is the exploration and investigation of NiO_x/BHJ heterointerface. We shall see in later chapters that all of the implications listed above will play a role in OPV device performance.

Chapter 3

Characterizations of Organic Photovoltaic Cells and Their Components

In this section, we shall briefly explain some of the main characterization methods that are used in the studies. The aim of this chapter is far from covering all of the details of the measurements. Instead, only the basic principles are discussed. Nevertheless, some techniques, such as the XRD, will be covered in more details than others because the technique development is a major part of the study.

3.1 Solar Cell Performance

The most important measurement done on any photovoltaic cell [58, 222] is the characterization of its current-voltage measurement which tells us its performance. A typical J-V characteristic of a photovoltaic cell is shown in Fig. 7.10. We note that by “current” and “power”, the community actually means “current density” and “power density”.

The **maximum power conversion efficiency** (*PCE*) of a solar cell is defined as the maximum power it can generate as a fraction of the incident power from the sun:

$$PCE = \frac{\text{max power generated}}{\text{incident power}} = \frac{V \times J}{100 \text{ mW cm}^{-2}} \quad (3.1)$$

The last equation above assumes incident solar irradiance of 100 mW cm^{-2} for A.M. 1.5 solar irradiance spectrum, which is valid for most sub-tropical geographies and shown in Fig. 3.2. For tropical countries, A.M. 1.0 spectrum should be used. Only the part of JV curve that lies in the fourth quadrant in the JV plot corresponds to power production. Consequently, this is commonly referred to as the **power-producing quadrant**.

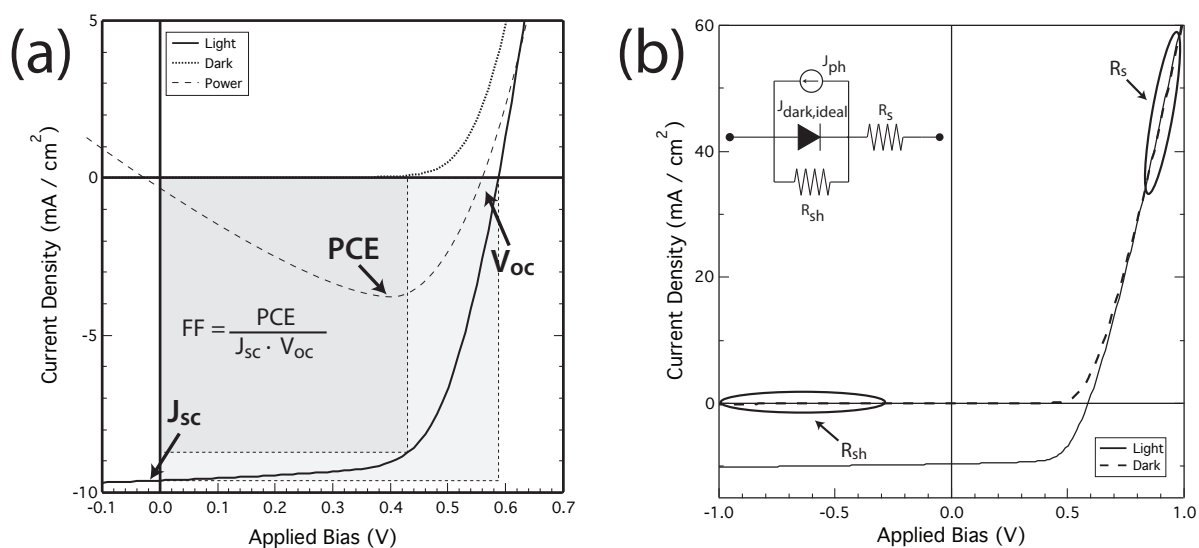


Figure 3.1: Illustration of JV- characteristic of a solar cell and the important performance parameters. Sub-figure (a) is the zoomed-in version of (b). Note that the resistances are measured from the dark JV characteristics.

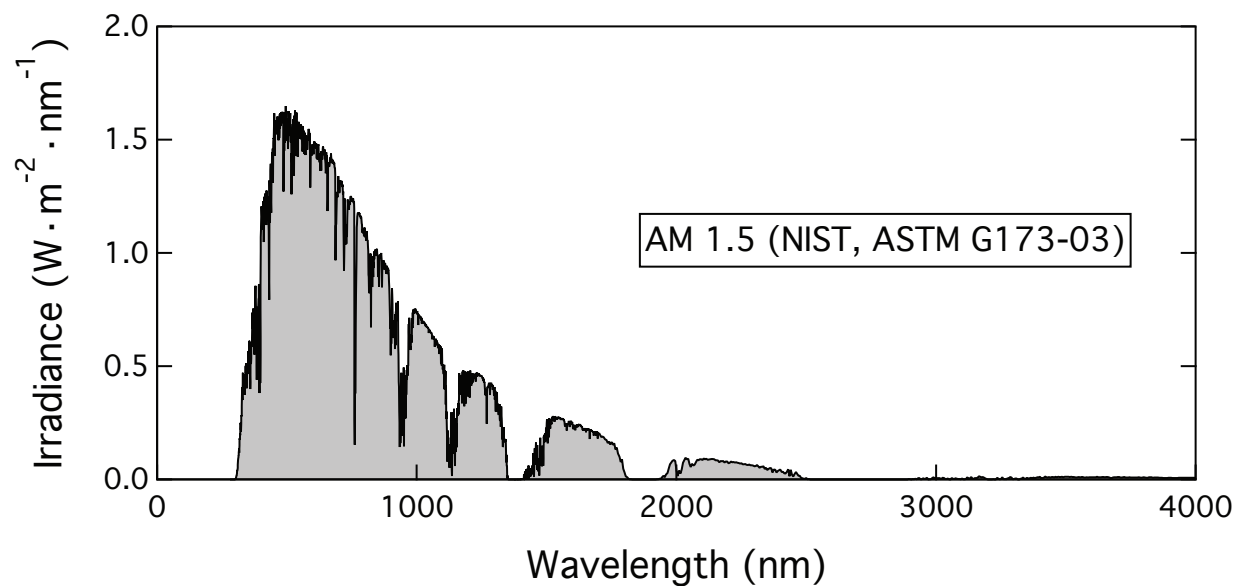


Figure 3.2: Terrestrial solar spectrum. Source: NIST.

The **short-circuit current**, J_{sc} , is the maximum current the cell can produce. When charge extraction efficiency from the cell is unity, this equals the total rate of photogeneration of charges in the cell. Photogeneration of mobile charges increases the electrochemical potential of charged carriers inside the cell. V_{oc} is the maximum voltage that the cell may develop due to this increase in the electrochemical potential inside the cell. PCE can then be empirically expressed as:

$$PCE = FF \frac{V_{oc} \times J_{sc}}{\text{incident power}} \quad (3.2)$$

where the empirical parameter FF is called the **fill factor** of the cell. Improving the cell performance can therefore be thought of as improving J_{sc} , V_{oc} , and FF . They are, however, not independent of each other.

J_{sc} in an ideal case is determined by the number of photons that are absorbed in the material, essentially those whose energy $h\nu$ is greater than the bandgap of the absorber, E_g . However, in conventional solar cells, V_{oc} is limited by E_g . Therefore, there must be an optimal E_g for power production below which photocurrent yield is high but voltage is low, and above which voltage is high but current is low. $E_g = 1.4\text{ eV}$ has been identified as optimal for a single E_g cell with maximum theoretical $PCE = 33.0\%$ [199, 221, 202, 203].

An ideal cell should have PCE that approaches $\frac{V_{oc} \times J_{sc}}{\text{incident power}}$, or $FF \rightarrow 1$ ¹. Fill factor, therefore, is an empirical measure of losses inside the cell. These losses may incur during photocarrier extraction to the terminals or due to increased radiative recombination beyond what is required by black-body thermodynamics. Most of the work done here will be related to improving carrier extraction by means of improving the heterojunction at the contact. Consequentially, improvement in PCE will visibly be related mostly to improvement in FF .

Two other empirical quantities are often used to describe losses in a photovoltaic cell: the **series resistance** R_s and the **shunt** or **parallel resistance** R_{sh} or R_p . These are empirical quantities corresponding to an idealization of the photovoltaic device as a circuit shown in Fig. 7.10b. R_s can be related to, for example, the resistivity of any part of the device. Physical

¹ FF can never equal 1 due to thermodynamic considerations [202, 203].

interpretation of low R_p , on the other hand, tend to not be straight-forward. It can be, for example, related to increased interfacial recombination [269]. R_p and R_s can be approximated from the slope of the dark JV curves at far reverse and far forward bias, respectively.

3.2 Energy Levels in a Material

Electronic energy level alignment at the heterojunction, crucial to carrier transport in the cell, is a topic of immense complexity [126, 119, 252]. In this work, we focus on a heterojunction between a metal oxide and an organic molecule, which has been shown to largely follow Anderson's rules [7]. Although we reserve some cautions on the universal applicability of these set of rules to oxide / organic heterointerfaces, we shall see in §7 that our device results largely agree with it. This will allow us to formulate a more comprehensive list of design rules for an efficient HTL, which forms the main result of this work.

3.2.1 Ultraviolet Photoemission Spectroscopy and Inverse Photoemission Spectroscopy

Regardless of the details on how they align, the final energy level alignment at a heterojunction must be governed in part by the energy levels of the constituent materials, which we can directly measure. The most direct and informative measurement comes in the form of photoemission measurements [31, 45, 44]. Two main photoemission measurements involved in this study are the Ultraviolet Photoemission Spectroscopy (UPS) and the Inverse Photoemission Spectroscopy (IPES)². An example of a combined UPS and IPES data are shown in Fig. 3.3.

UPS provides information about the electronic density of states near the valence band, E_v . In this experiment, ultraviolet light is shone upon the sample inside a vacuum chamber. The energy of the ultraviolet light, a few tens of eV , is suitable for exciting the valence electrons near the sample surface, which escapes the material, travels through the vacuum chamber, and detected by

² Photoemission measurements are credited to our collaborators at NREL Measurement and Characterization group, at Princeton University, and at University of Arizona.

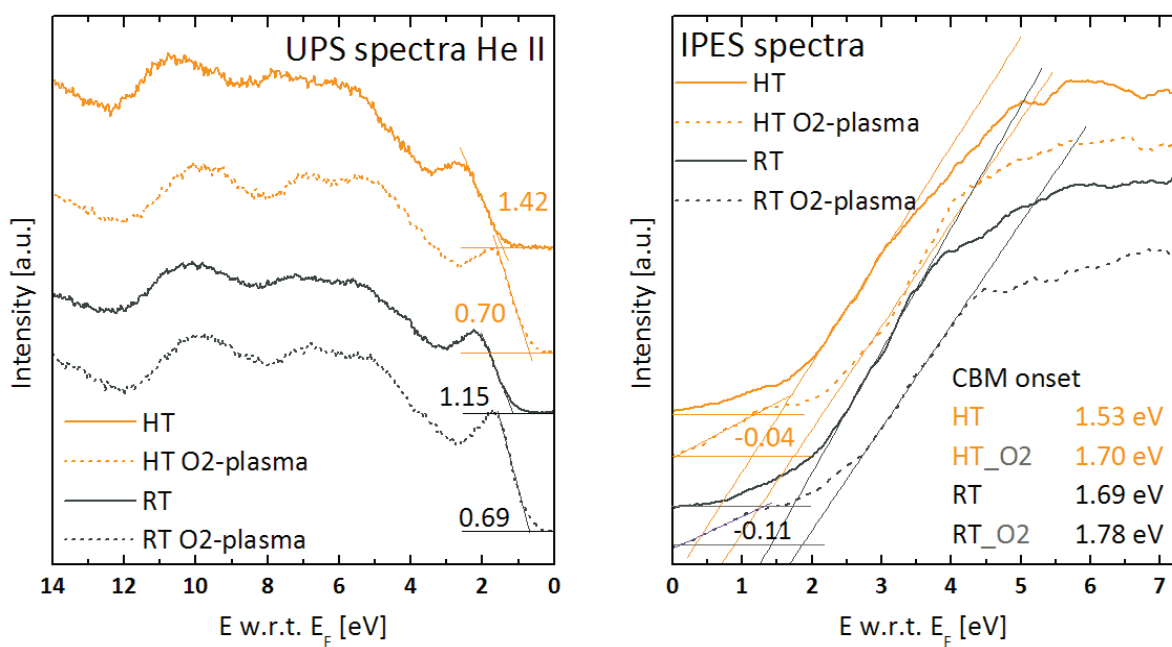


Figure 3.3: Examples of UPS and IPES spectra, showing the extraction of the energy levels.

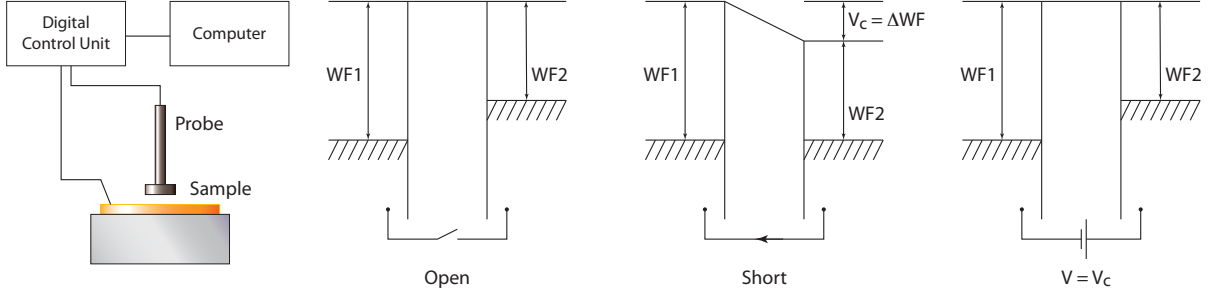


Figure 3.4: The Kelvin contact potential method for measuring workfunction (adapted from KP Technology manual).

energy-selective detector. The kinetic energy of the photon is related to the original binding energy of the electron by:

$$E_{kin} = h\nu - E_{bin} \quad (3.3)$$

The counts of photoexcited electrons as a function of E_{bin} therefore correspond to the electronic density of states at that energy. Additionally, the onset of photoemission is, by definition, equal the material's WF, which is also of utmost interest.

In IPES, electron beam of known energy is directed to the sample, coupling with the unoccupied electronic states in the material. Some of these electrons radiatively relax, and the emitted photons counted as a function of E_{bin} :

$$h\nu = E_{kin} - E_{bin} \quad (3.4)$$

where E_{kin} is the kinetic energy of the electrons. Therefore, IPES lends us insights on the density of states near the conduction band, E_c , of the material.

3.2.2 The Kelvin Probe

WF may also be measured by the Kelvin method (also known as the “contact potential method”), the essential features of which are illustrated with the help of Fig.3.4. In this method, two conductive materials, the probe and the sample, are arranged in a parallel-plate capacitor

configuration and connected electrically through an external voltage source and meter. Due to WF difference of the two materials, a potential difference develop between the two terminals of the voltage meter. The measured potential difference is nulled when an external bias equals to the WF difference is applied to the system. Therefore, if the probe WF is known, the sample WF may also be calculated.

3.3 Optical Properties

Also essential to the performance of the cell is the optical properties of each layer. This is done by two methods: optical reflection / transmission spectroscopy and spectroscopic ellipsometry.

3.3.1 UV-Visible Optical Reflection / Transmission Spectroscopy

Fig. 3.5 illustrates the basics of this measurement. Light from the UV and visible spectrum is passed through a dichroic mirror, and the reflected beam directed perpendicularly towards the sample. The fraction of the light transmitted through the sample is captured by another fiber optic and directed towards a spectrometer, where the number of photons are counted as a function of wavelength. Similarly, part of the light reflected by the sample is reflected by the dichroic mirror to the spectrometer. An integrating sphere may be used to capture the diffusely scattered light from the sample. A dark calibration is applied to correct for instrumental noise. Air or user's substrate can be used as a transmission calibration sample. An Al mirror of known reflectance is used as the reflectance calibration sample.

The film's absorbance may then be calculated from T , R , and the Beer-Lambert's Law:

$$\begin{aligned} I^T &= I_0 (1 - R) 10^{-A} \\ \Rightarrow A &= \text{Log} \left| \frac{1 - R}{T} \right| \end{aligned} \quad (3.5)$$

where the logarithm is in base-10, and the unit of absorbance is in **optical density** (O.D.).

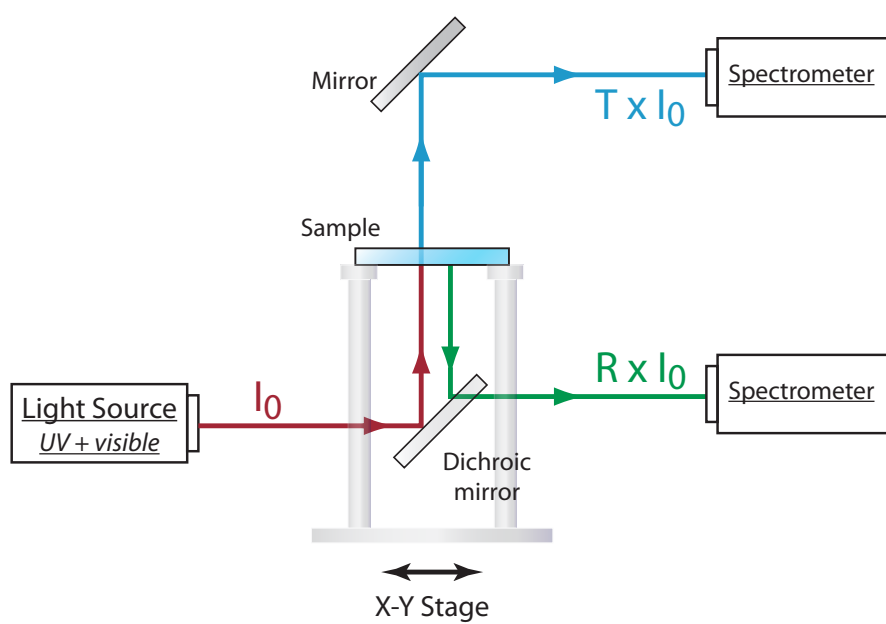


Figure 3.5: (a) UV-Visible reflection / transmission set up.

3.3.2 Spectroscopic Ellipsometry

Spectroscopic ellipsometry is an analytical technique based on the changes in polarization of a polarized light after it is reflected from a sample surface³. It measures both the intensity and phase change of the reflected beam, and therefore contains more information than normal optical reflection spectroscopy. Further, because it measures the ratio of the reflected intensity to the incident intensity and the phase change of the light, it is inherently much more precise and accurate than techniques that measure absolute intensity. Data fitting to theoretical models is part of the analysis. When done properly, it may provide information on film thickness and the index of refraction as a function of wavelength. Models may also take into account multilayers of thin films and rough surfaces.

3.4 Material Composition

Material composition can be examined by a few experiments, each has its own merits and disadvantages. A few methods that are commonly used at NREL are X-ray Photoemission Spectroscopy, X-ray Diffraction, X-ray Fluorescence, ICP, and Laser-Induced Breakdown Spectroscopy.

3.4.1 X-ray Photoemission Spectroscopy

X-ray Photoemission Spectroscopy (XPS) is a quantitative surface composition analysis technique⁴. The set-up and physics of XPS is similar to UPS, with the main difference being the photon wavelength and the orbitals that are being excited. In a typical commercial XPS system, an X-ray of $\sim 1.5 \text{ keV}$ is employed. This high energy is enough to ionize core-level electrons, producing free electrons with a set of characteristic binding energies (Eq. 3.3). Identifying the E_b fingerprint and their relative intensities, a quantitative analysis of the sample composition can be done (Fig. 5.3). Like other characterization methods that involve free electrons, XPS is only sensitive to surface composition.

³ Spectroscopic ellipsometry fitting is mostly credited to Dr. Paul F. Ndione.

⁴ Photoemission measurements are credited to our collaborators at NREL Measurement and Characterization group, at Princeton University, and at University of Arizona.

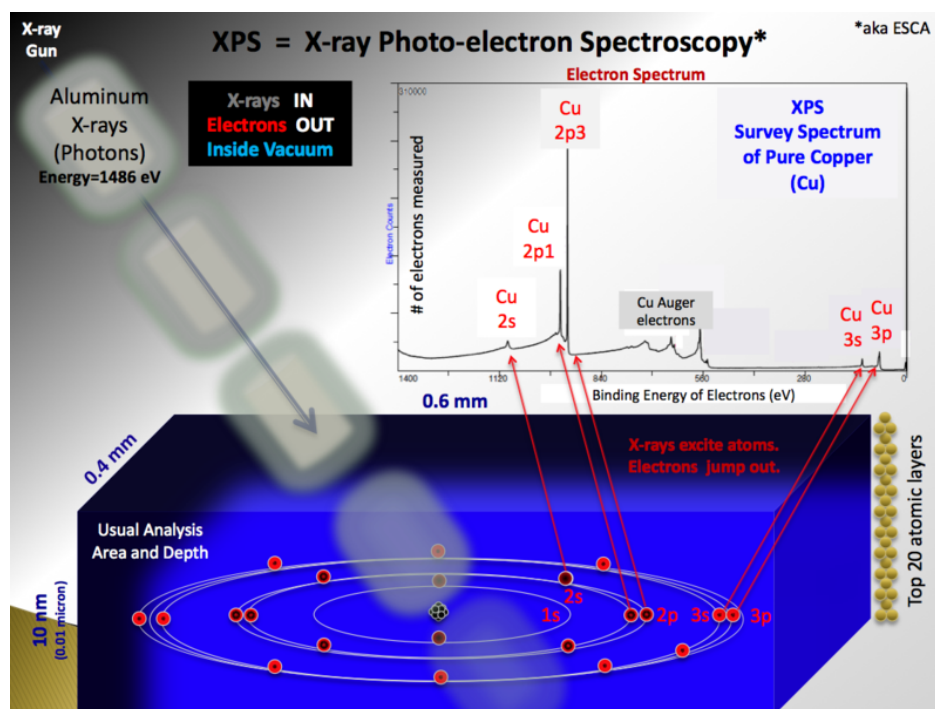


Figure 3.6: Illustration of the XPS. Image credit: Wikipedia commons.

3.4.2 X-ray Diffraction

X-ray diffraction (XRD) can be used as a tool for composition analysis. The information given is much more rich than simply elemental analysis. However, it can only give a positive identification: it cannot identify if a material is absent. XRD will be discussed in details in §3.5.2.

3.4.3 X-Ray Fluorescence

The physics of X-ray Fluorescence (XRF) measurement is similar to that of XPS. The main advantage over XPS is that can be done in air because it yields photons instead of free electrons. In XRF, the sample is bombarded with a flux of X-ray, ionizing some of the core electrons. This renders the atoms unstable, and electrons at higher orbital energies may fall into the emptied state, emitting a photon of lower energy. This is called fluorescence. Since energy levels are characteristics of atomic species, so is the fluorescence spectra. Hence, the fluorescence spectra can be used to uniquely identify chemical composition.

Our XRF instrument employs a fundamental parameter - based fit routine to enable the user to get the relative elemental abundance in the sample. However, analysis of light element ($Z < 20$) is challenging due to low X-ray cross-section. Additionally, the use of nickel in the X-ray optics renders compositional analysis of nickel element inaccurate.

3.4.4 Laser-Induced Breakdown Spectroscopy

Laser induced breakdown spectroscopy (LIBS) is a recently developed locally destructive elemental analysis technique that can be used to analyze solid, liquid, and gaseous samples. In LIBS, an Nd:YAG laser ablates a small amount of the sample and spectral emission from the plume is analyzed using a set of synchronized spectrometers. The intensity of the characteristic photon flux emitted from the plume is proportional to the number of atoms in the plume, which makes it possible to calculate the relative amount of constituent elements in the sample. LIBS offers several appealing features for compositional analysis in general: it does only local damage, data taking is very fast, it is sensitive to light elements, analysis is independent of the physical state

of the sample, and no special sample preparation is needed. LIBS is employed in the Mars Rover mission to remotely analyze the composition of Martial soil and rock samples. The fast nature of LIBS data taking and analysis also makes it suitable for high-throughput and combinatorial investigations. This will be covered in greater details in §8

3.4.5 Inductively Coupled Plasma Atomic Emission Spectroscopy

Inductively Coupled Plasma Atomic Emission Spectroscopy (ICP-AES or simply ICP) is a destructive trace elemental analysis technique. In ICP, the sample is dissolved in appropriate solvent and introduced in a mist form into a plasma flame. This ionizes the sample mist, and the characteristic photon flux from the plume can be used for elemental analysis similar to LIBS. Inductively coupled plasma is used to avoid contamination from the surrounding. ICP is a well-established chemical analysis technique. Its main drawbacks lie in its destructive nature and the need for sample preparation. ICP is also lacking good spatial resolution. In this work, ICP is used as a calibration technique and compared with the performance of LIBS and XRF (§8).

3.5 Structural Properties

Structural properties of a material are tied to its optoelectronic properties. For example, a crystalline material will have optical absorption profile and electrical conductivity that is different from its amorphous counterpart. Here at NREL, structural properties can be investigated using a few techniques, most prominently X-ray diffraction and atomic force microscopy. Structural order of the organic molecules can also be assessed from its absorption profile.

3.5.1 Atomic Force Microscopy

Atomic Force Microscopy (AFM) is a very high-resolution scanning probe microscopy ⁵ . The microscopic probe in AFM sits on a macroscopic cantilever with piezoelectric tube (Fig. 3.7). When the probe is brought close to a sample surface, the cantilever deflect according to Hooke's

⁵ Atomic force microscopy is mostly credited to Dr. Ajaya K. Sigdel.

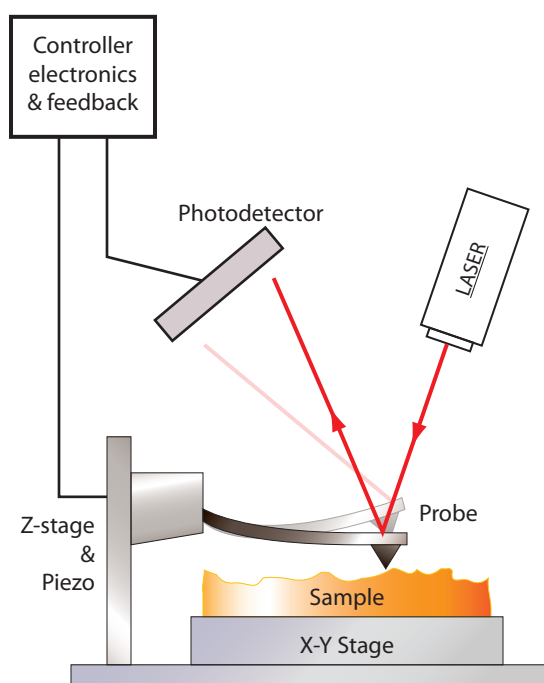


Figure 3.7: Basic elements of an AFM.

Law due to various surface effects. The cantilever deflection is precisely monitored, typically using a combination of laser beam and photodiodes, providing the topographical information of the sample surface when scanned in the X-Y direction. The piezoelectric tube of the cantilever moves it up and down to maintain constant force by the probe to the sample, thus preventing any probe-sample collision which may result in sample and equipment damage.

3.5.2 X-ray Diffraction

Structural analysis of organic materials by XRD forms a major part in this study (§6) and will be explained in more details than other characterization methods. XRD work in this project is done both with lab-scale diffractometer and at Stanford Synchrotron Radiation Laboratory (SSRL). Both conventional 1D and 2D detectors are used. Here we shall discuss the general aspects of XRD done in different geometries. Details specific to pole figures done using 2D detector is presented in §6.

Investigation of structural properties using X-ray diffraction (XRD) has a few advantages. First is the high penetration depth of X-ray enabling analysis on the sample volume instead of only on sample surface. It is also more compatible with soft materials, such as the organics, compared to electron-based characterization methods. XRD also provides some degree of compositional information, making use of the signature of lattice parameters and point-group symmetry. Additionally, when done properly, XRD may provide a rich information on structural disorders in the film.

Main challenges in XRD of organic materials are low X-ray scattering cross-section by carbon atoms and possible sample degradation during experiment. Additionally, the use of thin film samples greatly exacerbate the situation (we employed samples as thin as 10 *nm*). The use of synchrotron-based X-ray diffraction has allowed us to overcome these difficulties: a combination of bright X-ray source, grazing-incidence measurement geometry, 2D detector, and He chamber allows for extremely rapid data taking without sacrificing much of data quality nor giving in to sample degradation.

3.5.2.1 XRD basics

XRD signal is a result of an elastic scattering of monochromatic X-ray by core electrons of atoms in a crystal. The discrete symmetry of the crystal lattice causes the X-rays to be diffracted, producing the well-known XRD patterns, analogous to diffraction of visible light by gratings⁶. It is most well-known to follow Bragg's Law for constructive interference (Fig. 3.8). The scatterers in XRD are core electrons of atoms inside a crystal lattice and the Bragg planes are imaginary planes that comprise of these constructively diffracting atoms. However, instead of deriving the Bragg condition directly, we will take an analogous approach and derive the condition for interference vectorially as this will greatly help us when we discuss diffraction at grazing incidence and diffraction with 2D detector.

Consider two scatterers separated by a displacement vector \vec{d} (Fig. 3.9a). A monochromatic light of wavelength λ is incident on them along the direction \hat{k} . Its wavevector is $\vec{k} = 2\pi\hat{k}/\lambda$. The lights are scattered by the scatterer in the direction \hat{k}' . Because the scattering is elastic, the magnitude of the outgoing wavevector and its wavelength remain constant. The condition for constructive interference is that the phase difference of the two light paths is an integral multiply of 2π . From Fig. 3.9a, the condition for constructive interference is:

$$\begin{aligned} m\lambda &= \vec{d} \cdot \hat{k} + \vec{d} \cdot \hat{k}' \\ &= \vec{d} \cdot (\hat{k} - \hat{k}') \\ 2\pi m &= \vec{d} \cdot (\vec{k} - \vec{k}') \end{aligned} \tag{3.6}$$

where the integer m is called the diffraction order. When $m = 1$, the quantity $(\vec{k} - \vec{k}')$ is exactly the shortest reciprocal lattice vector, \vec{q} , of the diffracting crystallographic planes, and its magnitude is simply:

$$q := \|\vec{k} - \vec{k}'\| = \frac{2\pi}{d} \tag{3.7}$$

⁶ The analogy is actually very precise: from the perspective of scattering theory, XRD from a crystal is simply a Fraunhofer diffraction of light from a 3-dimensional "grating". The diffraction pattern, proportional to the Fourier transform of the grating, is proportional to the reciprocal lattice.

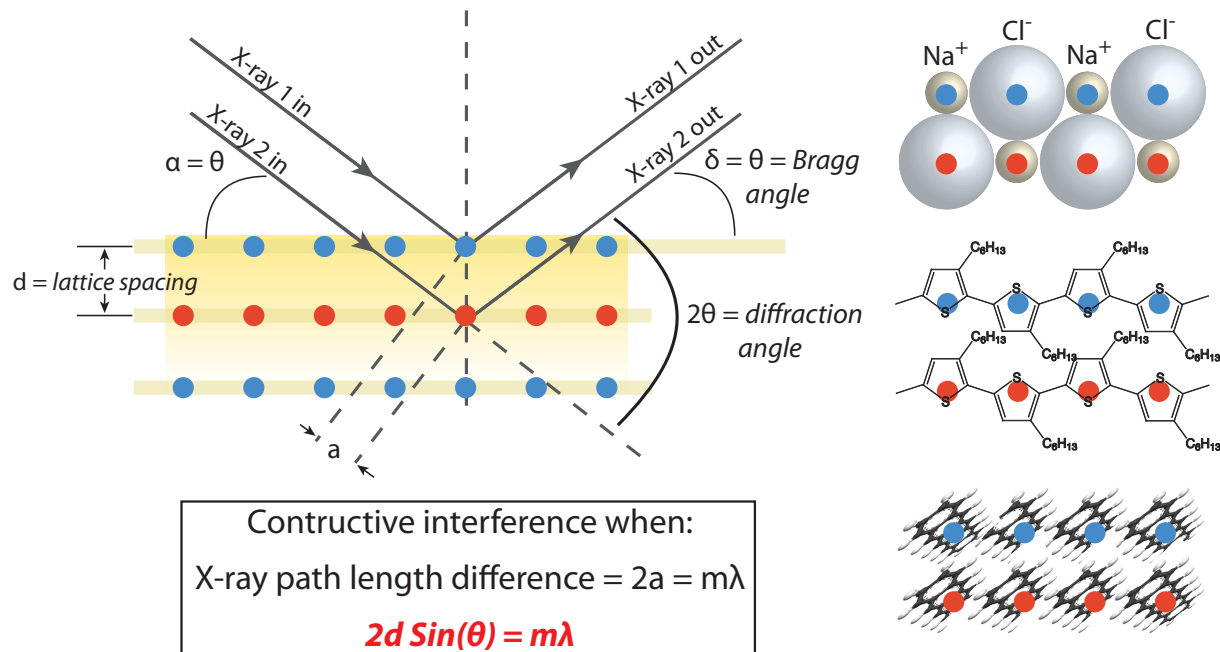


Figure 3.8: Illustration of Bragg's Law in XRD. In general, α is the incidence angle, and δ is the exit angle perpendicular to the sample.

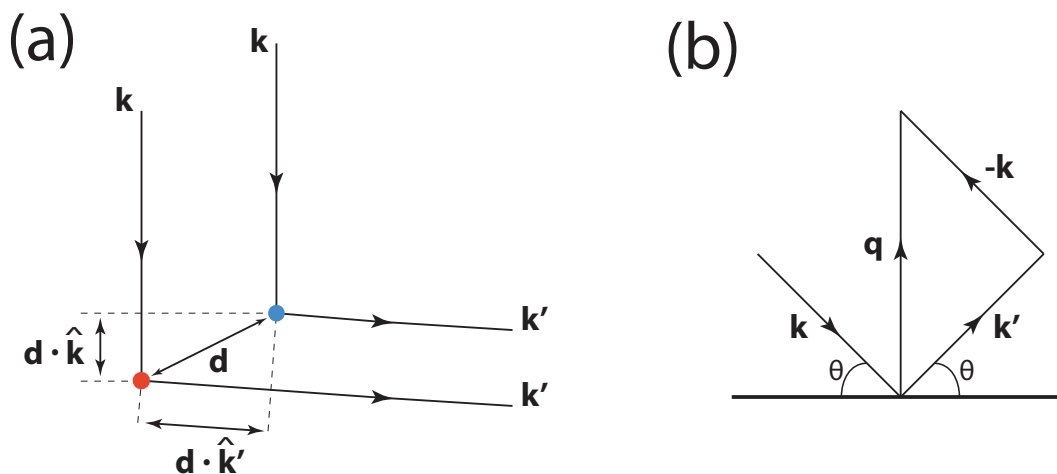


Figure 3.9: Illustration for diffraction condition by two scatterers.

and the condition for diffraction (Eqn. 3.6) can be re-written as:

$$\begin{aligned}
 2\pi &= \vec{d} \cdot \vec{q} \\
 &\text{or} \\
 1 &= \hat{d} \cdot \hat{q}
 \end{aligned} \tag{3.8}$$

The connection with Bragg's Law (Fig. 3.8) can be made with the help of Fig. 3.9b. Since the magnitudes of \vec{k} and \vec{k}' are the same, $(\vec{k} - \vec{k}')$ is simply the bisector of the angle subtended by them. It follows that \vec{k} and \vec{k}' must make the same angle θ to a plane perpendicular to $(\vec{k} - \vec{k}')$. Therefore the scattering event can be seen as a Bragg reflection off this plane with Bragg angle θ . From Fig. 3.9b, the magnitude of $(\vec{k} - \vec{k}')$ is simply $2k \sin\theta$. From Eqn. 3.6 and 3.7, this also equals $2\pi m/d$. Using the definition of wavevectors, we finally arrive at the usual formulation for Bragg's condition:

$$\begin{aligned}
 2k \sin\theta &= \frac{2\pi m}{d} \\
 \frac{2\pi}{\lambda} \sin\theta &= \frac{\pi m}{d} \\
 2d \sin\theta &= m\lambda
 \end{aligned} \tag{3.9}$$

Likewise, the magnitude of \vec{q} is related to θ by:

$$q = \frac{4\pi}{d} \sin\theta \tag{3.10}$$

Fig. 3.9b will be helpful in illustrating a subtlety related to XRD done at fixed incidence angle.

3.5.2.2 Intensity corrections

The following two intensity corrections are important for XRD done in traditional specular configuration ⁷ [43]. Additional corrections for special configurations will be discussed in the appropriate subsections. Ref. [43] discusses these corrections in great details and touches upon a few other corrections which may be important for other material systems. Most of the corrections done throughout this chapter are readily implemented in WxDiff analysis program.

⁷ Intensity data are to be divided by the correction factors.

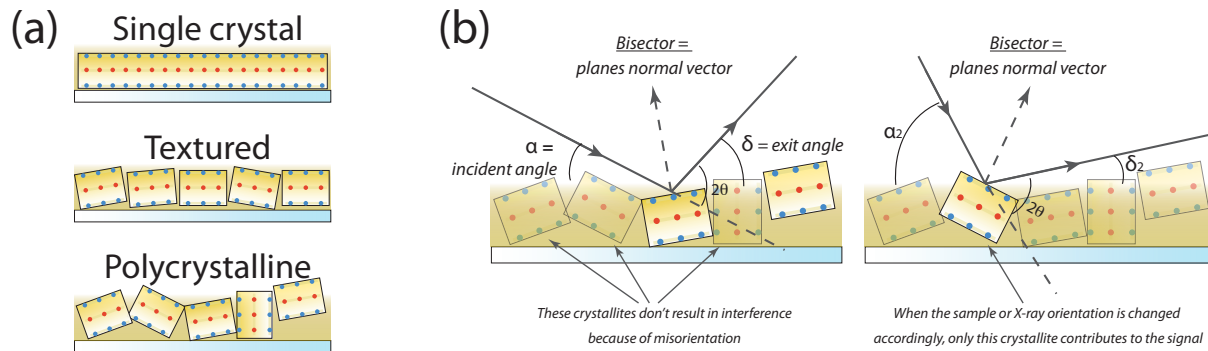


Figure 3.10: (a) Sample texture. (b) Orientation sensitivity of X-ray diffraction.

When the X-ray source is partially polarized, the following polarization correction need to be applied:

$$C_p = p_{\parallel}(1 - \cos^2\delta \cdot \sin^2\gamma) + (1 - p_{\parallel})(1 - \sin^2\delta) \quad (3.11)$$

where p_{\parallel} is the fraction of light that is polarized parallel to the sample surface, δ is the exit angle perpendicular to the sample surface, and γ is the exit angle parallel to the sample surface (Figs. 3.8, 3.12). Lab-scale sources tend to be randomly polarized, while synchrotron radiation tends to be highly polarized. We assume $p_{\parallel} \approx 95\%$ for SSRL light.

When analyzing XRD data involving a scan in θ , the Lorentz correction need to be applied:

$$C_L = \frac{1}{4 \sin^2\theta \cos\theta} \quad (3.12)$$

This correction takes into account the amount of time each diffracting crystallites remain in the diffracting position, thus correct for the different integration time of different Bragg angle [43, 30]. This correction is usually combined with the polarization correction and known as the **Lorentz-polarization factor**. However, it is important to note that, unlike the polarization correction, the Lorentz correction will change the shape of diffraction peaks due to its θ -dependence. Therefore, it is important to apply this correction in peak shape analyses.

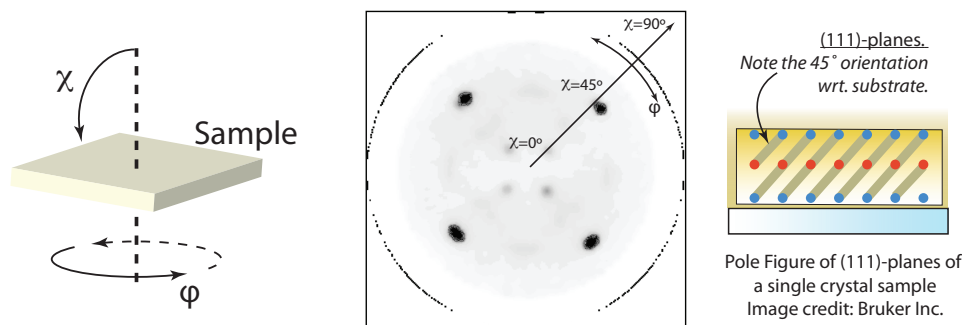


Figure 3.11: Pole figure of Si (111) planes from a single crystal. Image credit: Bruker Inc.

3.5.2.3 Material texture and pole figures

A sample **texture** refers to the orientation of crystallites in it (Fig. 3.10a). At one end of the spectrum is a single crystal sample, where the crystal is oriented in only one direction. On the other extreme is a poly-crystalline material, where the crystallites in the film are randomly oriented. In between, there are, for example, uni-axially textured samples in which crystallites are oriented only in one direction.

As evident from the vectorial nature of Eqn. 3.8, X-ray diffraction is sensitive to the orientation of the diffracting crystallites. For example, one of the most common XRD measurement geometry is the $\theta - 2\theta$ geometry. This refers to the fact that the θ and 2θ axes of the goniometer are simultaneously moved such that the 2θ angle is precisely twice of θ at all times. From Fig. 3.8b and 3.8c, this consequently results in any diffraction planes must lie parallel to the sample surface. Similarly, by rotating the sample relative to the direction of the beam, diffraction peaks must result from different crystallites in the sample (Fig. 3.10b). It is also possible, in the case of a highly textured sample, to entirely miss the XRD signal simply due to sample (crystallite) misorientation.

XRD can therefore be employed to investigate the texture of a sample. This is done by producing a **pole figure**. A pole figure is a visualization of the distribution of crystallite orientations in the sample. Using conventional diffractometers with 1D detector, it is made by rotating the sample axes (χ and ϕ) while fixing θ and 2θ corresponding to the Bragg reflection of interest. Fig.

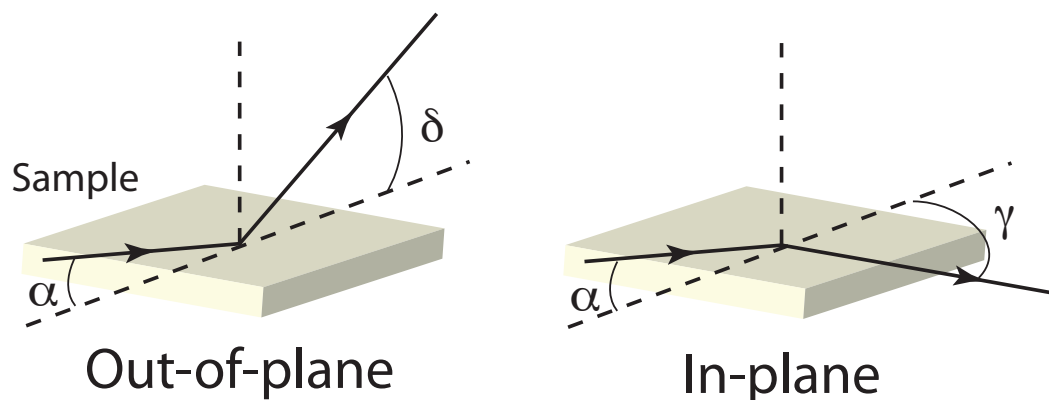


Figure 3.12: Illustration for XRD done at grazing incidence (GIXD).

3.11 shows an example of such plot. Note that it reflects both the 45° tilt of the reflecting (111) planes with respect to the substrate and the cubic (4-rotation) symmetry of the cubic single-crystal sample.

3.5.2.4 Grazing incidence XRD

Grazing Incidence XRD, or **Glancing Incidence XRD** (GIXD) refers to an XRD measurement done with a fixed, very low incidence angle α . In the case of measurements with 1D detector, the detector arm may be scanned out of the sample plane or in the sample plane (Fig. 3.12). This measurement geometry is particularly useful for increasing signal yield by increasing the irradiated volume especially in the case of thin film samples. It also has the added benefit of reducing irradiated substrate volume. However, there are a few additional subtleties related to GIXD that needs to be addressed [90, 242]:

- Due to the fixed incidence angle, the orientation of the Bragg planes are necessarily different for different \vec{q} (Fig. 3.9b).
- Blind area due to forbidden Bragg reflection
- Absorption correction which depends on film thickness, increased irradiated area, and the position of the sample

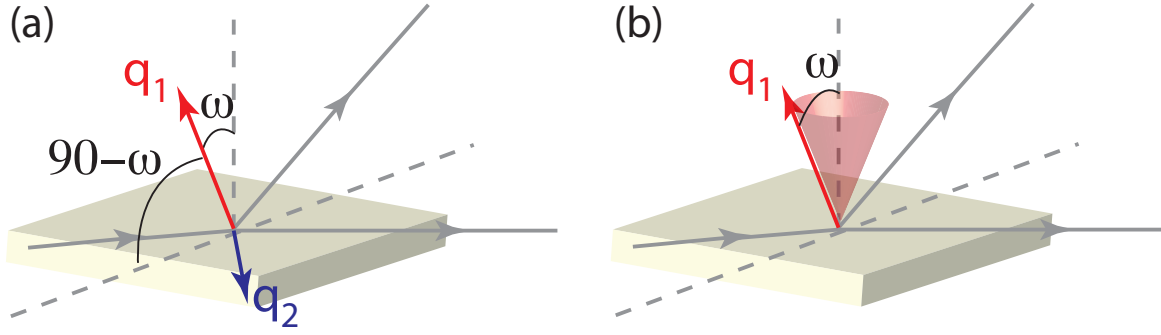


Figure 3.13: (a) The two extreme direction of \vec{q} at a fixed incoming angle. (b) \vec{q} oriented inside this cone defined by $\omega = \theta - \alpha$ cannot be detected.

- Shift in measured 2θ due to refraction

The first point is obvious from examining Fig. 3.9b while restricting the incoming angle fixed. The second point is related, but important only when investigating texture of the film. Suppose that we restrict the incoming angle at a low angle, and investigate a fixed \vec{q} (Fig. 3.13. Eqn. 3.8 dictates that a diffraction spot will only be produced when orientation of the crystallite is parallel to \vec{q} . The extreme orientation that can be sampled at a fixed α are defined by \vec{q}_1 and \vec{q}_2 as shown in Fig. 3.13a. The angle between \vec{q}_1 and the sample surface is $90^\circ - \omega$, while that between \vec{q}_2 and the surface is essentially zero because α is small. Any crystallite whose tilt angle is closer to the normal than $90^\circ - \omega$ will never satisfy 3.8 and gives no diffraction peak. In other words, those orientation inside the cone ω from the normal is not observed. In the limit that $\alpha \rightarrow 0^\circ$, $\omega \rightarrow \theta$ [12].

The absorption correction ⁸ depends on film thickness and is important for thin films:

$$C_A = \frac{1}{\mu' \sin(\alpha)} \frac{1}{\frac{1}{\sin(\alpha)} + \frac{1}{\sin(\delta)}} \left(1 - e^{-\mu' t \left(\frac{1}{\sin(\alpha)} + \frac{1}{\sin(\delta)} \right)} \right) \quad (3.13)$$

where α and δ are the incidence and exit angles (Fig. 3.8), t is the film thickness, and μ' is the extinction coefficient of the X-ray in the material (the apostrophe is to avoid confusion with mobility, chemical potential, or electrochemical potential which share similar notations). In the

⁸ Intensity data are to be divided by the correction factors.

case where the sample size is finite, the beam may spill over and diffraction intensity is limited by the sample size. Intensity might also be limited by the effective detector size, which is set by the X-ray optics.

The last correction, although not important for our analysis, is worth mentioning. At incidence angle close to the critical angle for total external reflection of the X-ray, the position of the measured Bragg angle shifts by a few tenths of a degree to smaller angle due to refraction [242]:

$$\begin{aligned}\Delta\theta &\approx \frac{1}{2} \left[\alpha - \frac{1}{\sqrt{2}} \sqrt{\sqrt{(\alpha^2 - \theta_c^2)^2 + 4\beta^2} - \theta_c^2 + \alpha^2} \right] \\ &\approx \frac{1}{2} \left[\theta_c - \sqrt{\beta} \right] \text{ for } \alpha \text{ near } \theta_c\end{aligned}\tag{3.14}$$

where θ_c is the critical angle for total external reflection of X-ray, and β is the imaginary part of the material's index of refraction.

3.5.2.5 XRD with 2D detectors

In this measurement technique, the point detector is replaced by a 2D image detector as illustrated in Fig. 3.14. XRD with 2D detector offers much more information in expense of resolution:

- The usual \vec{q} -scan information can be obtained as a slice in the radial direction.
- Sample texture is readily assessed (Fig. 3.14). The usual $\vec{\chi}$ -scan can be obtained as a slice in the azimuthal direction.
- If one is interested in only an equivalent of, for example, \vec{q} -scan, this can be obtained by integrating in the $\vec{\chi}$ -direction. Hence, measurement time can be immensely reduced.

Three points are worth mentioning about this measurement geometry. First, like in the case of GIXD, since the incidence angle is fixed, the different Bragg reflections (different 2θ or \vec{q}) must necessarily come from Bragg planes with different orientation. Additionally, since the image detectors are usually flat while diffraction is spherically symmetric, there is a non-linear relationship

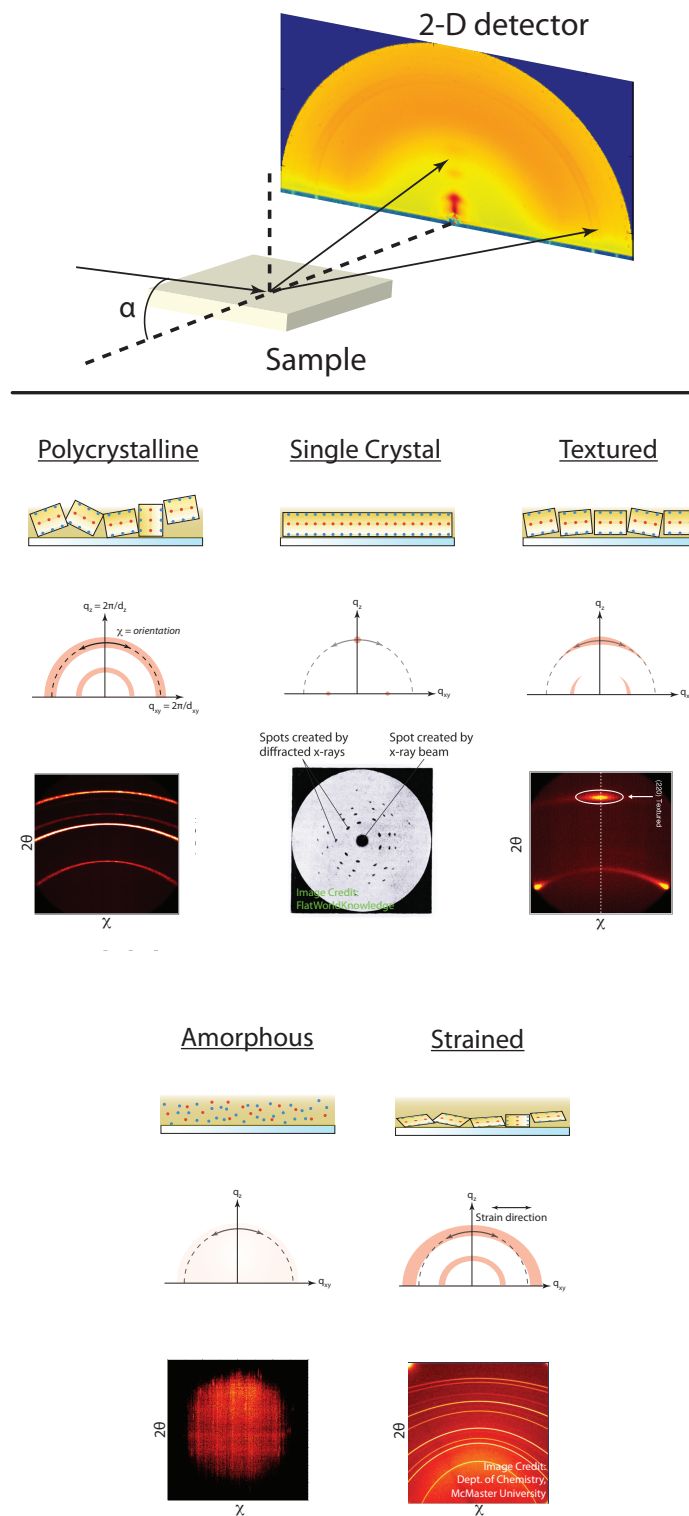


Figure 3.14: Illustration of XRD with 2D detector, showing the measurement geometry and examples of image data from samples with different textures.

between \vec{q} (or 2θ) and pixel position on the detector [149] which can be corrected in WxDiff when proper calibration is done. Lastly, this also means that \vec{q} (or 2θ) resolution of the detector also changes radially, with highest resolution achieved at the positions furthest from the detector origin. Consequently, the sample-detector distance can be adjusted to get the optimum resolution for the \vec{q} -range of interest.

3.5.2.6 Pole figure with 2D detectors

Similarly, pole figures can be made by patching several 2D XRD images [87]. For our purposes, however, it is sufficient to make a slice with constant ϕ due to the azimuthal symmetry of the spin-coating process. If such azimuthal symmetry is present, the sample is called to have a **fiber texture**. Under normal specular measurement condition, one 2D XRD image would have been sufficient to fully describe the film texture. However, the nature of organic thin film samples in this study necessitates a maximal use of grazing incidence geometry. As discussed earlier, this will result in Bragg reflections near $\chi = 90^\circ$ being forbidden, essentially creating a hole in the pole figure.

In this study, we follow the method outlined in Refs. [106, 12], where 2 images and a specular data are patched to obtain the full pole figure for the fiber-textured film: the GIXD, a **local specular** data taken with 2D detector to fill most of the forbidden area, and a high-resolution rocking curve for orientations close to $\chi = 90^\circ$. The “local” in local specular refers to the measurement geometry ($\alpha = \theta$) where the condition for specular reflection is satisfied for the Bragg reflection of interest. The rocking curve data is also important for normalizing the data intensities, allowing for inter-sample comparisons.

This method rests on the following assumptions:

- The sample has an isotropic crystallite orientation distribution in the plane of the substrate.
A spin-coated sample artificially inherits this texture
- The image detector sensitivity is not polarization dependent.

- Film thickness does not exceed the penetration depth of the X-ray, otherwise the obtained information only reflects the physical properties of the near-surface region of the sample.

2D GIXD for this experiment are done at Stanford Synchrotron Radiation Laboratory, beamline 11-3. Optimum incidence angle is found between 0.10° and 0.12° . 2D local specular data are taken with the same equipment, but with incidence angle around 2.0° , corresponding to q of the P3HT[100] peak at X-ray energy of 11.0 keV (the actual q used is determined from the measured location of the peak from the GIXD data). Additionally, the sample is rocked to ensure that all crystallites, including those that are slightly misoriented, are sampled [107].

The GIXD image is valid everywhere, except for the blind region between $(90^\circ - \theta) < \chi < (90^\circ + \theta)$. The validity range of the local specular data is $(\chi = 30^\circ \text{ to } 150^\circ)$, outside which the diffracted beams are blocked by the substrate.

Data from an annular region spanning the Bragg reflection of interest are properly background-subtracted and integrated in the radial (\hat{q}) direction to obtain the orientation distribution density as a function of χ . The two data are patched by increasing the arbitrary intensity of the local specular data such that it matches with the GIXD data at the overlapping region of validity. Systematically, the multiplicative constant is determined by linearly fitting point-by-point the local specular intensity at the patch region against the corresponding GIXD intensities. It is crucial that an offset is not applied to the GIXD intensity as non-zero baseline of the GIXD data, assuming good background subtraction, is an indication of the presence of polycrystalline phase. A small offset may be applied to the local specular data to account for slight differences in the measurement condition, but this should not be necessary. Instead, a large offset from the fit is used as an indicator for bad background subtraction.

Specular rocking curve data were taken at Stanford Synchrotron Radiation Laboratory, beamline 7-2. In this experiment, 2θ is set to correspond to P3HT[100] peak. χ is then rocked, measuring the orientation of the P3HT lamellae close to perpendicular from sample surface. Background subtraction and absorption correction are applied to the data. Additionally, the intensity of the

rocking curves data are also multiplied by the full-width at half-max (FWHM) of the peak in q , which is different among samples. The data are then patched to the rest of the data by scaling the combined data from the 2D images.

3.5.2.7 Relative degree of crystallinity

The area under an XRD peak is dependent on the number of diffracting crystallites⁹, and therefore can be used to compare the degree of crystallinity of different samples. The orientation sensitivity of XRD, however, needs to be taken into account: for example, one may incorrectly conclude that a single crystal sample is not-so-crystalline simply because of sample misorientation which result in apparent low peak area. Therefore, it is more accurate to use the area under a pole figure to assess degree of crystallinity.

For the pole figure of the organic materials above, the relative **degree of crystallinity** (DoC) of different samples may be compared via:

$$DoC \propto 2\pi \int_{-\frac{\pi}{2}}^{\frac{\pi}{2}} \sin(\chi)I(\chi)d\chi + \text{single crystal terms} \quad (3.15)$$

where by “single crystal terms” we refer to reflections from crystallites that are extremely oriented such that the lineshape is not fully resolved by the detector. This is simply the product of the intensity of the peak and the resolution of the detector.

3.5.3 Surface Energy

Surface energy is a quantity of interest in the physics of interfacial formation and catalysis¹⁰. We are interested in this quantity because it is related to film wetting, which is crucial for spin-coating process.

Surface energy of a solid sample is calculated from the result of contact angle measurement. In this experiment, a droplet of “probe liquid” is delivered using a digitally controlled syringe onto the surface. A 50 fps-video is taken to capture the drop injection, delivery onto the substrate, and

⁹ In contrast, the peak height is highly affected by measurement geometry, and is often unreliable for analysis.

¹⁰ Surface tension is the same with surface energy

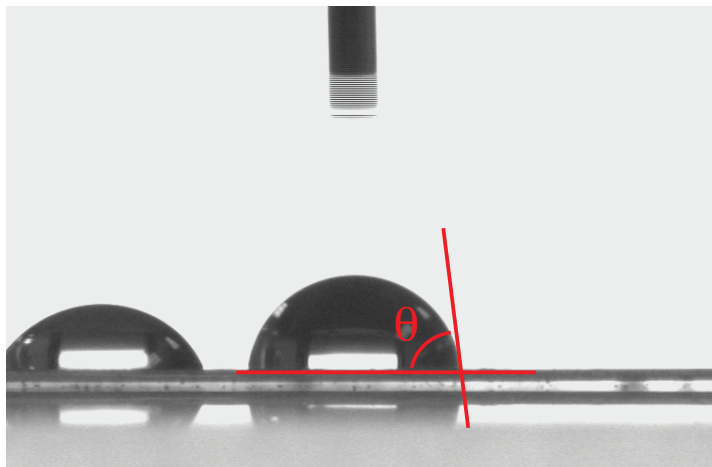


Figure 3.15: Contact angle measurement.

evolution on the substrate. The contact angle the drop makes with the solid is then obtained by fitting the drop images (Fig. 3.15).

For the works done here, we are mostly interested in obtaining the polarity of the surface which can be calculated from the polar and non-polar components of surface energy:

$$Polarity = \frac{\gamma^p}{\gamma^p + \gamma^{np}} \times 100\% \quad (3.16)$$

We largely follow the method of Owens and Wendt [176]. The surface energy and its components can be obtained from contact angles of two probe liquids with different known polarities by simultaneously solve two Owens-Wendt Equations:

$$\sqrt{\gamma_s^{np} \times \gamma_l^{np}} + \sqrt{\gamma_s^p \times \gamma_l^p} = \gamma_l^{tot} \frac{\cos \theta + 1}{2} \quad (3.17)$$

where the subscripts l, s refer to the probe liquid or the solid.

Probe liquids that have been used throughout this study are listed in Table 3.1. Diiodomethane is commonly used as a non-polar test liquid. However, due to health hazard, it is not used as a probe liquid. Liquids are dropped using teflon-coated needles to minimize the effect of surface tension of the needles. Even so, we still had problems with volatile liquids crawling up the side of the needle instead of deposited onto the substrate. These solvents, e.g. xylene, chloroform, and

Table 3.1: Probe liquids in contact angle measurements for 2-component surface energy calculation.

Probe Liquid	γ^p (mJ/m ²)	γ^{np} (mJ/m ²)	γ^{tot} (mJ/m ²)	Polarity (%)	ρ_m (kg/m ³)	l_{cap} (mm)
Water	46.4	26.4	72.8	63.7	1000.0	2.72
Ethylene glycol	21.3	26.4	47.7	44.7	1113.2	66.1
o-dichlorobenzene	0.07	26.77	26.84	0.27	1300.0	45.9
chlorobenzene	0.08	33.2	33.28	0.27	1110.0	55.3

hexane, are consequently disqualified as potential probe liquids.

The sample stage is shielded to prevent local air flows from disturbing the drop shape. Additionally, camera magnification calibration is done at the beginning of every run in order to be able to measure drop sizes properly. This is important since to minimize changes in drop shape due to liquid's weight, liquid volume has to be maintained such that the drop diameter is less than the liquid capillary length (l_{cap}):

$$l_{cap} = \sqrt{\frac{\gamma^{tot}}{\rho_m g}} \quad (3.18)$$

where ρ_m is the mass density of the liquid and $g = 9.8 \text{ m s}^{-2}$ is the gravitational acceleration on Earth's surface. The list of l_{cap} can be found in Table 3.1. Eqn. 3.18 can be obtained by equating static pressure due to gravity and Laplace pressure due to surface tension:

$$P_G = P_{surf}$$

$$\rho_m g l_{cap} = \frac{\gamma^{tot}}{l_{cap}}$$

Lastly, In the case of relatively volatile liquids, a decreasing contact angle as a function of time may be observed, in which case the highest contact angle (earliest time) is used for surface energy calculation.

Chapter 4

Materials and Nickel Oxide Development

We shall start the discussion of the experiments that have been taking place by describing the materials involved. Deposition methods and basic material properties will be touched upon. Since the investigations described in this work revolve around the use of nickel oxide as a hole transport layer in organic photovoltaic devices, a greater emphasis will be put to the nickel oxide development that has been undertaken.

4.1 Deposition Methods

4.1.1 Pulsed Laser Deposition (PLD)

PLD, a physical vapor deposition technique, is the main deposition method used in this study; hence, we will describe this process in a more detailed manner than the other deposition techniques. In the PLD process, a high-power, short-pulsed¹ Kr:F excimer laser (248 *nm*) is fired onto the target (source) material. Upon delivery of high photon energy density, the target material is ablated, the generated plasma travels through the chamber, and finally condensed onto the substrate that has been positioned across the target [253]. Fig. 4.1 details the PLD system at NREL that is being used for this study (PLD-1) and illustrates the deposition process.

PLD allows incredibly precise control of the deposition parameters, and hence film properties. During the deposition process, only the top surface of the target is ablated while maintaining its temperature. This and the confined plume produced by laser ablation makes it considered less

¹ Laser pulse specification is 50 *ns*

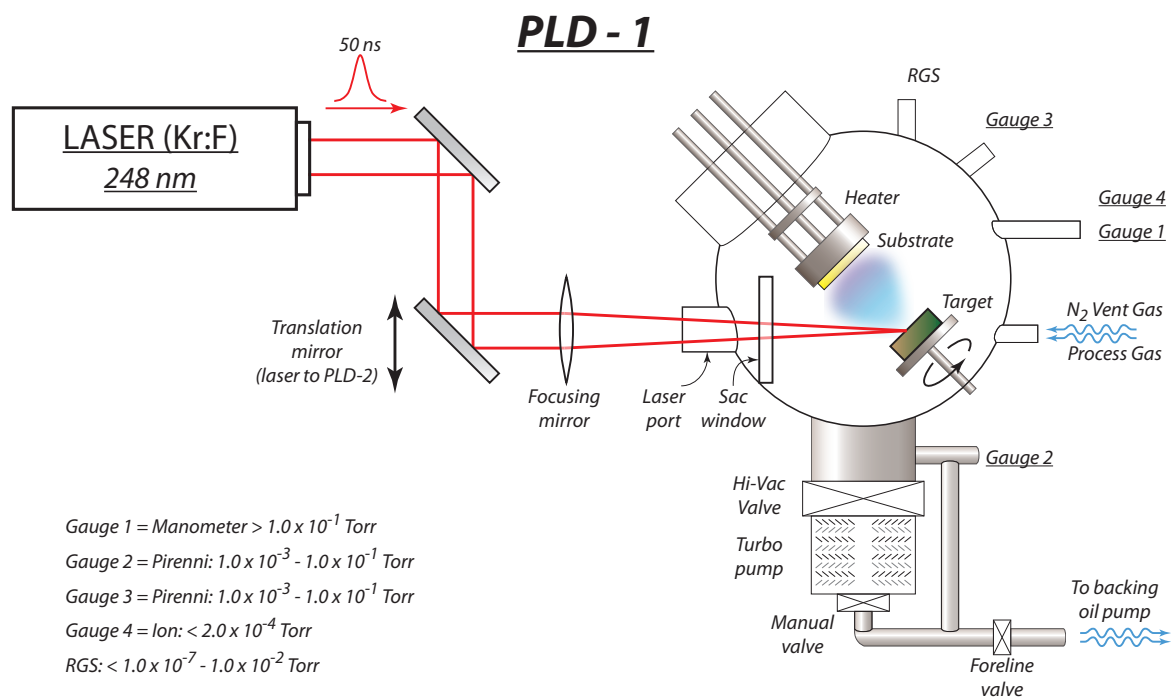


Figure 4.1: Essential features of PLD-1.

prone to contamination than processes involving unconfined plasma such as those found in sputter deposition or those involving source heating such as evaporation. PLD is also operable under a very wide range of deposition atmosphere, from 10^{-10} Torr to 1 Torr.

The two main disadvantages of PLD are “bouldering” – production of fine chunks of particles ranging from nanometer to microns in size – and scalability. The first can be overcome by using high-quality targets and a smooth target surface. To keep the target surface smooth, we polish the target after every use. Target is also rotated to reduce uneven ablated surface during deposition. Alternately, rastering the target is also commonly done. We also found that reducing laser fluence also helps prevent bouldering in some target materials such as MoO. On the other hand, the issue of scalability is not of a particular concern for this work. It has, however, also been partially addressed by the use of commercial excimer laser which is able to deposit a thin film on an 8”-wafer at $1\ \mu\text{m}/\text{min}$.

Commonly controlled PLD parameters are target composition, deposition atmosphere, laser fluence, position of the substrate relative to the target, substrate temperature, and deposition rate. Film composition is most strongly affected by the target composition. PLD process usually yield films that have almost the same cation stoichiometry as the target material ². This not essential in our study, but is extremely advantageous in cases where multi-cation targets are used. Therefore, the use of high-quality target materials is thus of utmost importance. For our experiments, a 99.9%-pure NiO target (Cerac) is used. Unfortunately, homogeneity of target composition is still a concern and, although it is usually trivial to test by using commercial XRF system, we are unable to do so due to the incompatibility of our XRF system with nickel and light elements. Visual inspection is also reliable for **positive** detection of problem. For example, after we have used about half of the target thickness, we observed that the work-function of the NiO_x films reduce by $\sim 0.1 - 0.2\ \text{eV}$ when the laser ablates the target further away from the center. We hypothesize that this is an indication of inhomogeneities in target composition. Although we have no means to conclusively test this hypothesis without sacrificing the target, dark spots soon start to become

² Here we emphasize **cation** stoichiometry instead of overall stoichiometry.

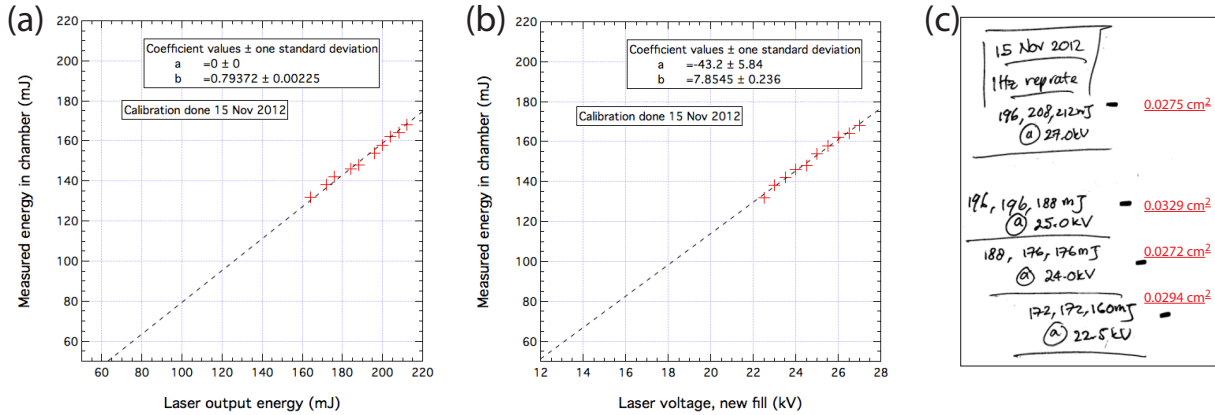


Figure 4.2: Typical PLD-1 laser fluence calibration data.

clearly visible on the target at $r \gtrsim 5 \text{ mm}$, corroborating this claim. Consequently, we started to restrain the location of laser ablation on the target to near the center.

Oxygen composition in the film is mostly controlled through the chamber oxygen partial pressure ($p(\text{O}_2)$). PLD-1 is evacuated by a rough oil pump and a turbo-molecular pump. Pressure in the chamber is monitored by five vacuum gauges: one Pirani gauge to monitor the foreline, one manometer for low vacuum in the chamber, one Pirani gauge for typical deposition pressure in the chamber ($m\text{Torr}$), and one ion gauge for high vacuum. A residual gas analyzer with a built-in vacuum gauge is a later addition. Whenever possible, pressure readings from all gauges are recorded at every deposition. Typical pressure observed after an overnight evacuation is $3.0 - 7.0 \times 10^{-7} \text{ Torr}$; however, base pressure for typical deposition is $1.0 - 6.0 \times 10^{-6} \text{ Torr}$. PLD-1 supports the use of a combination of 3 process gases: O_2 , Ar, and forming gas. Gas flows are controlled by mass flow controllers. Ultra-high purity process gases (99.999%) are used. Additionally, pumping efficiency of the turbo-molecular pump can be controlled by partially closing the vane valves at the mouth of the pump.

Laser fluence is affected by two factors: the total energy delivered by the laser unit onto the target and the illuminated area on the target. The first of these is set largely by the voltage of

the laser unit and is measured in the chamber using a thermal energy meter³. Fig. 4.2b shows a linear relationship between the measured energy per pulse in the chamber and the laser voltage. The relationship between the output laser energy per pulse, which is measured internally in the laser unit, and the actual measured energy per pulse in the chamber is also linear, as expected, with typically about 20.0% of the energy lost to optics (Fig. 4.2a). Fluctuations in laser energy per pulse is typically $\pm 4 \text{ mJ}$ between laser voltage = 18.0 – 26.0 *kV*. Outside this range, laser energy tend to be less stable and is avoided. So far, we found no evidence that laser repetition rate affects the deposition of NiO_x in any significant way.

The illuminated target area can be tuned by moving the focusing lens along the direction of the laser path. Laser spot area is then measured using thermal paper that is pasted on the target and placed on the target holder. The spot produced is then scanned and the area is accurately calculated from the number of colored pixels and the scan resolution (Fig. 4.2c). Laser fluence per pulse is kept constant at 3 J/cm^2 for all of our NiO_x depositions.

Another subtle but important factor determining the laser fluence on the target is material deposition on the laser port (Fig.4.1). Under normal circumstances, some material is deposited on the window at the laser port, reducing its transparency [258]. Further, due to the invisible wavelength of the laser, visual inspection of the window transparency is often misleading. Therefore, we cover the laser port with a sacrificial quartz window (transparent to $\lambda = 248 \text{ nm}$ light). Windows are replaced for every deposition and etched in appropriate dilute acid when not in use to regain its transparency. Optical transmission spectroscopy is done on the cleaned windows before use, and any small differences in optical transmittance is taken into account when calculating the number of laser shots. Typical window transmittance is $\sim 89.5\%$ at 248 nm and $\sim 94.0\%$ at 550 nm .

The substrates for the thin films are mounted on an inconel heater / sample stage by either Kapton tape or Ag paste. The heater / sample stage can be moved in all three directions. The position in the X-Y (parallel to sample / target surface) directions is optimized such that the plume is centered on the sample and is very rarely changed. The Z-position may be changed to either

³ Laser pulse is measured to be in the μs instead of 50ns due to slow response of the thermal energy meter.

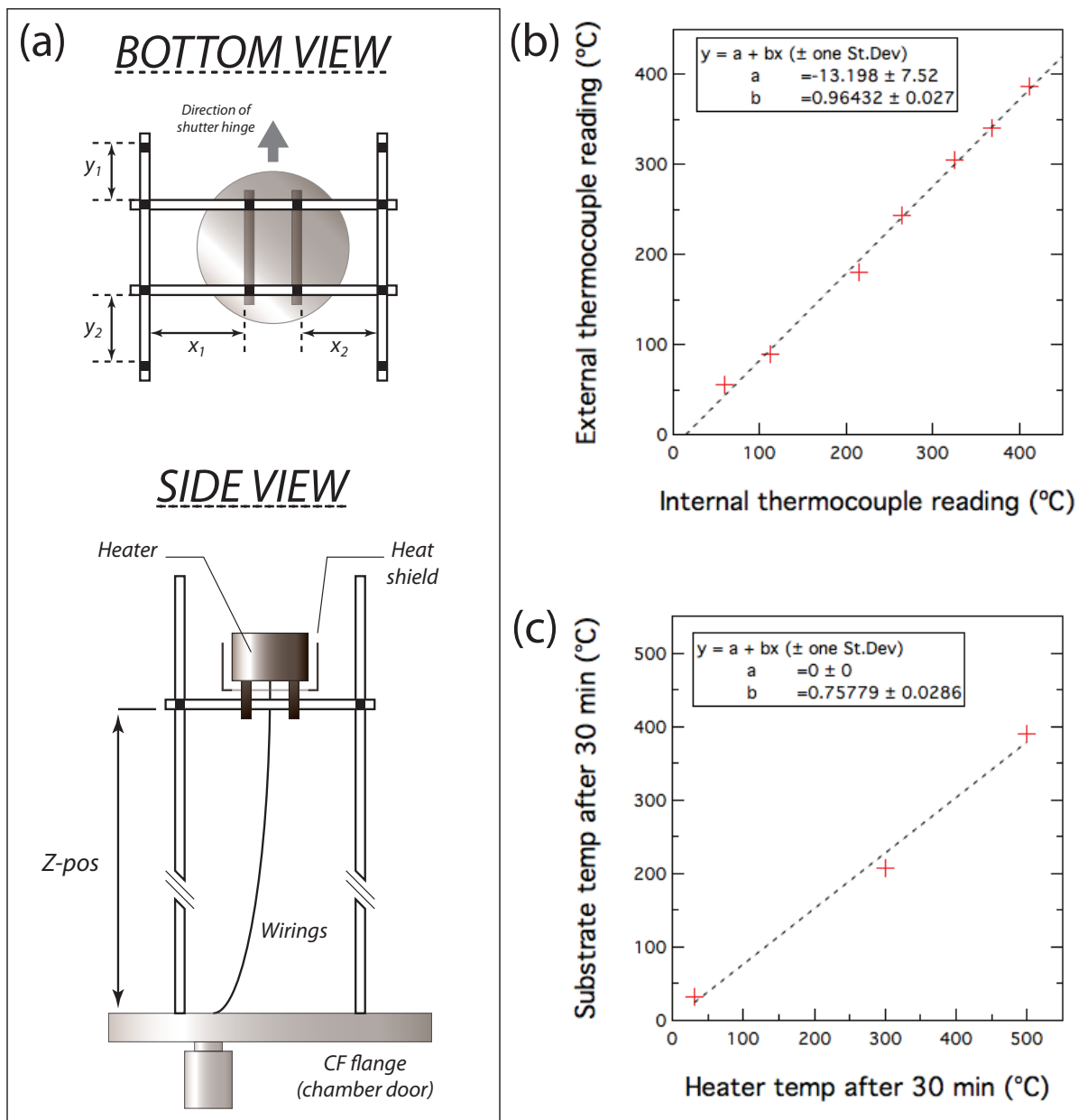


Figure 4.3: (a) PLD-1 sample / heater stage. (b)-(c) Typical PLD-1 heater calibration data.

obtain greater thickness uniformity or to alter the plume and sample condensation kinetics. The target to sample distance for PLD-1 is related to the Z-position by:

$$Z_{s-t} = (230 - Z_{pos}) \pm 5 \text{ mm} \quad (4.1)$$

The heater supports temperatures of up to 900°C , and is otherwise constantly kept at 32°C . The heater temperature (T_h) is monitored by a K-type thermocouple. During routine calibration (Fig. 4.3b-c), the value read by the system thermocouple is typically within 20°C of a test thermocouple. T_h at the heater edge is also $\sim 10^\circ\text{C}$ lower than at the center. This is not a concern because sample sizes are $< 1'' \times 1''$, substantially smaller than the heater. Measured substrate temperature (T_{sub}), when using 1 mm-thick glass or ITO, rises much more slowly compared to the heater. After 30 min of soaking, $T_{sub} \approx 0.76 T_h$ and its rate of change is $< 1^\circ\text{C}/\text{min}$, constant enough for typical deposition time of $< 30 \text{ min}$.

Film thickness by PLD can be very precise, owing to the digital nature of the pulsed laser. Control over film thickness can be achieved by a thickness calibration sample and confirmed post-production. In the case of ultra-thin films ($t < 50 \text{ nm}$), post-production thickness measurement is done by optical ellipsometry. The deposition rate is affected by target material, chamber atmosphere, laser fluence, T_{sub} , and Z_{s-t} . Deposition from ceramic targets ($\sim 1 \text{ nm}/1000 \text{ pulses}$) are typically much faster ($\sim 10\times$) than from metallic targets due to the high thermal conductivity of metals. In the case of deposition from NiO target, the typical deposition rate is roughly constant at $3 \text{ nm}/1000 \text{ pulses}$ up to $p_{tot} = 10 \text{ mTorr}$, after which deposition rate decays almost linearly (Fig. 4.4). The data in Fig. 4.4 is for $Z_{s-t} = 52 \text{ mm}$ and laser fluence of $3 \text{ mJ}/\text{cm}^2$.

4.1.2 Other Deposition Methods

4.1.2.1 Radio-frequency (RF) magnetron sputtering

Naturally, to overcome the difficulty of scaling up PLD technique, a great deal of interest has emerged on alternative deposition methods for the oxides. Magnetron sputtering process is one of the prevailing deposition methods for industrial-scale transparent conducting oxides. The method

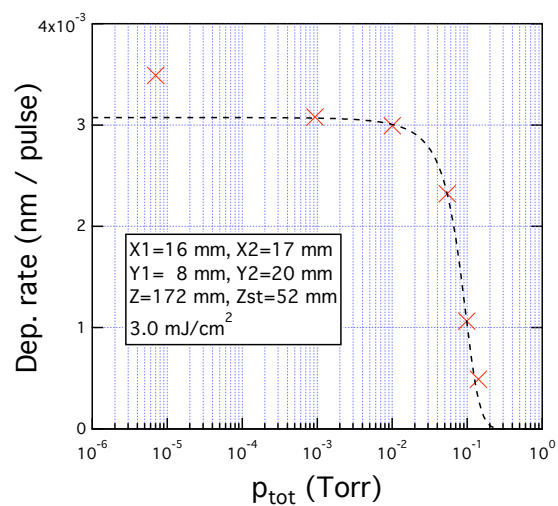


Figure 4.4: Typical PLD-1 deposition rate for NiO

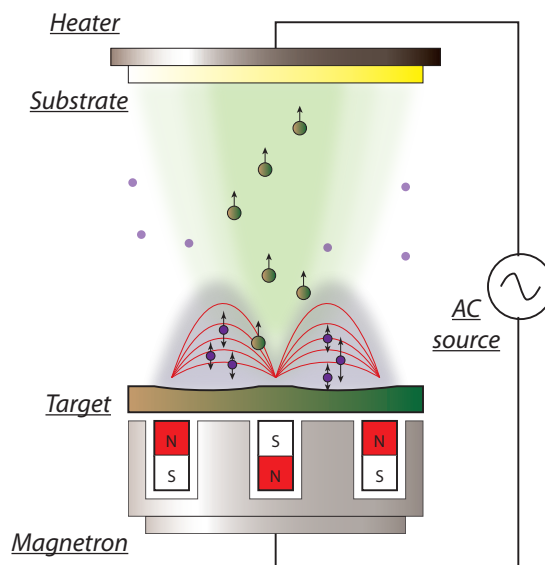


Figure 4.5: Illustration of sputter deposition process. AC power ionizes inert gas (e.g. Ar), which are subsequently attracted and confined by the magnetic field. The magnetic field is such that the ions are accelerated towards target surface, ejecting target particles by momentum transfer.

is preferred due to its ability to produce high quality films, large area, medium deposition rate (up to several hundred nm / min), low thermal generation, and its capability for low-pressure operation [86, 159].

Fig. 4.5 illustrates the sputter deposition process. Sputtering involves a creation of plasma of inert gas (in our case, Ar) between a cathode and an anode in an otherwise vacuum chamber. The substrate is placed on the cathode, while the source material (the target) is placed on the anode. Upon ionization, the positively charged Ar ions are accelerated towards and bombard the target at the anode. Target particles are then ejected by momentum transfer and diffuse towards the substrate across it. The substrate is often rotated for a more uniform film thickness and its temperature may be elevated. Other process gases may also be introduced to the chamber.

High power DC or RF (or both) source may be used to create the plasma. The first often results in faster deposition rate, but is limited for use in conducting targets. On the other hand, RF sputtering (13.56 MHz) is suitable for both conducting and insulating targets. A magnetron, placed behind the target, is also often employed in RF sputtering to assist ion bombardment. The magnetic field above the target confines charged Ar ions close to the target surface, thus plasma can be maintained at lower pressure. Additionally, since charged particles inside a magnetic field travel in a helical path, the magnetron has an additional benefit of accelerating the ions towards the target, greatly increasing the sputter rate. The sputtered materials, often have neutral charge, are not affected by the magnetic trap and are free to diffuse towards the substrate.

In our deposition system (EVO-Vac), sputtering is done using a stoichiometric 3"-diameter targets at RF (13.9 MHz) power of up to 150 Watt. Ar is used as the sputter gas, and O₂ is available as process gas. In a typical run, gas flow is controlled by the mass flow controller, and experimenter has control over the chamber total pressure and the gas mixing ratio. Chamber atmosphere is monitored using an RGA unit with built-in vacuum gauge. Substrate size of up to 4" × 4" can be accommodated, ~ 30 cm above the target. Substrate heating is provided by infrared heating element, and substrate is rotated at 6 rev / min by default. Film thickness is estimated from stylus profilometry of calibration samples deposited on glass, and close monitoring of the

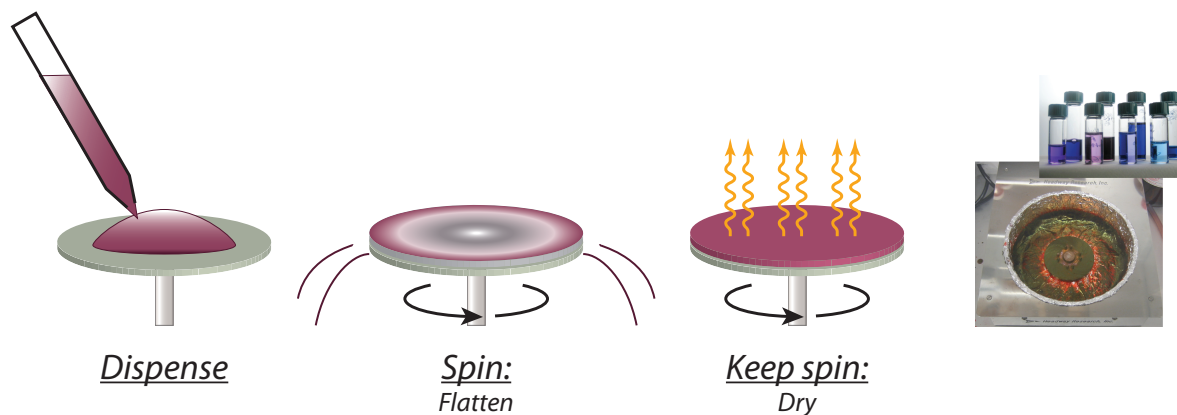


Figure 4.6: Spin casting process.

deposition rate using a quartz crystal microbalance. The deposition chamber is positioned inside an Ar glovebox, allowing for a controlled atmosphere during substrate preparation.

4.1.2.2 Spin-casting

Spin-casting is one method of thin-film deposition from a solution precursor. In this method, the substrate is placed on a digitally-controlled spinner. The precursor solution is then dropped onto the substrate, and the substrate is spun at a predetermined rate and acceleration for a set time. The sample is held onto the spinner by vacuum. Upon spinning, the solvent in the precursor dries, leaving a mostly dried thin film. Chemical reaction from the precursor compounds into the final compounds may happen during spinning or during post-production treatment, such as thermal annealing.

The film formation process is driven by solvent evaporation kinetics [84] and film quality is essentially affected by almost every available parameter: spin acceleration and speed, precursor viscosity, precursor temperature, and substrate surface energy to name a few. Spin parameters are trivially controlled through the digital control unit. All of our deposition are done at room temperature. Therefore, in order to keep precursor solution temperature the same for every batch, the solution is cooled down at ambient temperature for at least 30 minutes prior to deposition.

Variation in substrate surface energy is reduced by oxygen-plasma cleaning the substrates right before deposition. Because the effect of plasma cleaning is temporary, deposition is also done in small batches of at most 4 substrates.

In this study, spin-casting is employed to deposit metal oxides, organic films including the photoactive layer, and for depositing photoresist layer during photo-lithography process.

4.1.2.3 Thermal evaporation

Thermal evaporation is done almost exclusively for the deposition of metal top contacts in the OPV devices. In this physical vapor deposition method, ultra-high purity sources (usually pellets or wires) are placed inside a crucible of appropriate composition. The samples with appropriate shadow masks are placed upside-down above the source. The chamber is brought to a base pressure of ($\sim 10^{-8}$ Torr). High-voltage radio-frequency current is then passed through the crucible, elevating its temperature and evaporating the source material in it. Film deposition rate and thickness is tightly controlled by using PID algorithm coupled with a quartz crystal microbalance. The thermal evaporation chamber used in this study is located inside a N₂ glovebox, for a controlled atmosphere even in-between device processing and measurement.

4.2 Materials

4.2.1 Nickel Oxide

Nickel oxide (NiO_x) is arguably the most widely-studied p-type, wide band-gap oxide; nevertheless, it seems that understanding of the electronic properties of this material has not converged to a common conclusion yet [216, 214]. Stoichiometric NiO is considered a classic Mott-Hubbard type insulator [102], but is a p-type conductor when it is oxidized [133]. Various conflicting investigation results is a clear indicator that the electronic structure and the nature of conduction in this material is more complicated than has been suggested [214, 145, 152, 211, 229, 27, 225, 157, 161, 264]. Conduction mechanism in NiO_x as been described as percolative [225, 145], small-polaronic [27],

or grain-boundary dominated [265, 2, 27, 161]. Reports on the observation of Hall effect in nickel oxide are also conflicting [264, 161] and there is even a report indicating that NiO can be both p- and n-type [225]. Exotic spin-related anomalies in conductivity above the Néel temperature have also been reported [254].

However, the disagreements might have arisen from deviations of sample composition from stoichiometry, due to unintentional doping, or due to the presence of grain boundaries, none of which are mutually exclusive. Bosman showed that reports of band-transport from before ca. 1963 must be taken with extreme caution due to the high sensitivity to sample imperfections related to differences in the details of sample preparations [27]. Combined with the difficulties related in measuring oxygen content accurately, these might have led to these inconsistencies in the experimental results [211, 214, 172, 39, 61, 51]. Although naturally unstable at standard room temperature and atmosphere, oxidized form of nickel oxide (e.g. Ni_2O_3 , or equivalently can be seen as Ni vacancies) is known to be present in grain boundaries of a polycrystalline sample [161, 184, 34], making grain-boundary conduction a non-negligible transport mechanism [265, 2, 27, 161]. There are also reports that these defect concentrations are hugely affected by thermal annealing, electron, and ion impact [214, 171]. Lastly, it has also been shown recently that conduction in NiO is exclusively p-type [133, ?]. Thus, it is likely that older reports of n-type conduction [225] might also be attributed to sample imperfections.

Optical properties of NiO are similarly complex, even in its epitaxial form, with fine structures across the whole E_g [166]. Proper optical band-gap of NiO films have been reported to be between $3 - 4.3 \text{ eV}$, depending on the details of sample preparation [166, 207]. Yet, stoichiometric NiO has a green hue due to strong absorption in the red (1.75 eV) and violet ($2.75 - 2.95 \text{ eV}$), and low absorption in between (Fig. 4.7). Oxidized Ni, whether directly by oxygen or by incorporation of Li^+ in the lattice, increases the broadband absorption between (1.75 eV) and (2.75 eV), lending the material a more black appearance.

Numerous photoemission and inverse photoemission studies have been done [216, 145, 152, 211, 214] to understand its electronic structure. The theoretical spectra have also been calculated

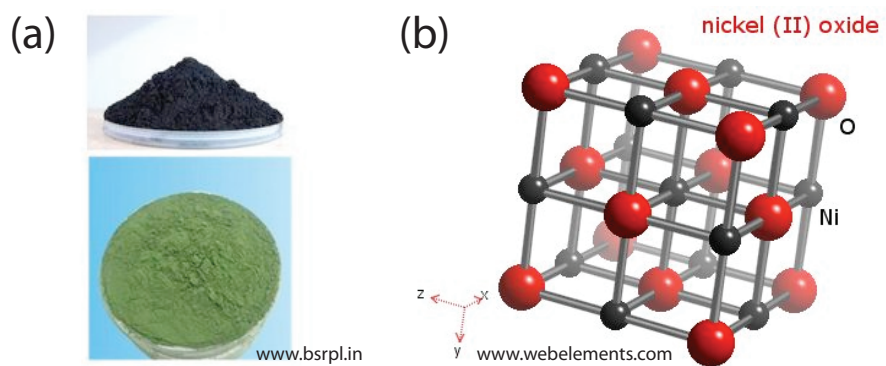


Figure 4.7: (a) Nickel oxide powder. NiO has greenish hue when close to stoichiometry and black when oxidized. (b) The cubic rock-salt structure of stoichiometric NiO.

[65]. However, most if not all of these studies do not focus on the electronics structure within $\pm 1.5 eV$ from E_F , which is the range we are mostly interested in. Still, a few points are worth noting:

- The prominent structure at the valence band edge is dominated by Ni 3d states [145, 211, 214]
- The prominent structure at the conduction band edge is the Ni 4s. However, a small structure at the shoulder ($(E_c - E) \sim 0.8 eV$) is observed and understood to be due to localized Ni states [214].
- The gap is inherently clean [211], but mid-gap structures are extremely sensitive to defects and film preparation [211, 214]. This, contradicts the optical data [166]. However, it is possible that Newman and Chrenko’s observation of low mid-gap structures might be due to the (low amount of) defects in the epitaxial film.

XPS has been used extensively to characterize nickel oxide and similar species. Biesinger et al. and Uhlenbrock et al. wrote recent and comprehensive reports on the XPS spectra of nickel metal, oxide, and hydroxides with focus on the Ni2p spectra [23, 249]. Kim and Winograd also reported a thorough study; however, their results are shifted from other reports [112]. For non-monocrystalline samples, Ratcliff et al. have studied nickel oxide thin films deposited by solution processing [190], while Sasi and Gopachandran nanostructured mesoporous films [207].

A peak at low binding energy of $842.6 eV$ is a characteristic of metallic nickel species, and a peak at $852.7 eV$ is attributed to Ni^{2+} of the stoichiometric NiO [23, 249]. The peak at $855.6 eV$ is related to Ni^{3+} and is surface sensitive [23, 249], while the very broad peak at $861 eV$ that is commonly found has been attributed to a “shake-up” in the NiO structure [112].

O1s spectra of these films are dominated by broad peaks ($FWHM \gtrsim 1.0 eV$). The main peak at $529.3 eV$ is characteristic of stoichiometric nickel oxide and tend to be quite separable [23, 249], while the peaks above $530 eV$ tend to overlap and are attributed to various surface species. The

peak at 530.9 eV is ascribed to Ni(OH)₂, while those at 531.1 eV and 532.8 eV are most possibly due to, respectively, defective sites and various hydroxyls or adsorbed O₂ [23].

Stoichiometric NiO is antiferromagnetic with Néel temperature, T_N , of 525 K (252° C) [216, 145, 117, 29]. Crystallographically, it is a rocksalt above the T_N (Fig. 4.7), but is rhombohedral below T_N because the alternating (111) ferromagnetic planes caused a slight distortion in the rock-salt structure⁴ [60, 198, 204]. Nevertheless, this deviation from rock-salt structure to rhombohedral is too fine for practical XRD purposes.

Nickel oxide films have found applications in solid-state chemical sensors [100, 51], and electrochromic windows [239, 168, 11, 265]. The (111) crystal facets of the largely rock-salt structure are purely oxygen- or purely nickel-terminated. This lends nickel oxide polycrystals a catalytic nature, making NiO_x widely used as catalysts [274, 89, 36, 54]. These have led to a wealth of electrochemical studies of this material and its derivative [272, 38, 40, 208, 41, 39, 184, 247, 266, 26, 251].

Contrary to a comment by Morin that conduction properties are insensitive to impurities $\lesssim 10^{18} \text{ cm}^{-3}$ [161], doping in nickel oxides have been done with various degree of success. Other than nickel vacancies (oxygen “doping”) that have been discussed earlier, doping with Li is probably the most common [56, 247], although Ga, In, Cr, Mg, Zn, Na, Ag have also been used as dopants [217, 179].

In this work, nickel oxide ultra-thin films ($t < 15 \text{ nm}$) are grown by PLD and magnetron sputtering. Nickel oxide films grown from nickel formate and nickel nitrite solution precursors have also been done and discussed elsewhere [232]. When using the optimum deposition parameters, nickel oxide films deposited by any means perform uniformly well in OPV devices. However, the physical vapor deposition route give the researcher a flexibility over the material characteristics by controlling deposition parameters.

⁴ Roth and Glens [204] referred this as “**superexchange coupling**” among the nickel ions. Newman and Chrenko [166] have shown that this has negligible effect on the optical properties.

4.2.1.1 NiO_x ultra-thin films by PLD

Due to the ability to tightly control the deposition parameters, PLD is our primary choice for NiO_x deposition method in this study. All NiO_x samples are deposited by PLD on commercial ITO on glass (Thin Film Devices or Colorado Concept). ITO is prepared by cleaning in ultrasonic bath of acetone and isopropanol for 10 minutes each, followed by 20 minutes of UV-ozone treatment [259]. Pulsed laser deposition is done at varying $p(O_2)$ and T_{sub} . In the case of high-temperature depositions, the samples are cooled down by ramping down heater temperature by 150°C every 30 minutes under the deposition $p(O_2)$.

Irrespective of the deposition parameters, DC conductivity of the films deposited on glass is not reliably measurable even after using a differential method employing electrometers. The high resistivity of the films also renders us unable to reliably perform Hall effect or Seebeck measurements. Similarly, attempts to get carrier concentration through capacitance-voltage measurement with Hg probe did not give reliable results. The only reliably measurable quantities are then the film's work-function, optical properties, structural properties from XRD, and electronic structures from photoemission studies.

Work-function has been shown to be the leading feature of an HTL, and is thus of primary interest to us. Work-function measurements are mostly done using the Kelvin method, with photoemission measurement done only on a few select samples. Work-functions of the films are tuned by varying $p(O_2)$. When changes in surface chemistry as a function of deposition parameter are negligible, the work-function is proportional to $E_F \sim kT \ln |p_v|$. Since nickel deficiency (excess oxygen) acts as an electron acceptor in the material [133], we expect that h^+ population in the film to vary as $p(O_2)$ and, consequently, the work-function of the NiO_x film increases linearly in $\ln |p(O_2)|$. Our measurement result, shown in Fig. 4.8, largely agrees with this expectation. Here we have demonstrated the ability to systematically engineer the work-function of the films by ~ 0.5 eV by spanning 4 decades of $p(O_2)$ (in unit of Torr). To increase our confidence in the measurement results, we have also included the data points from UPS from which it is also clear that

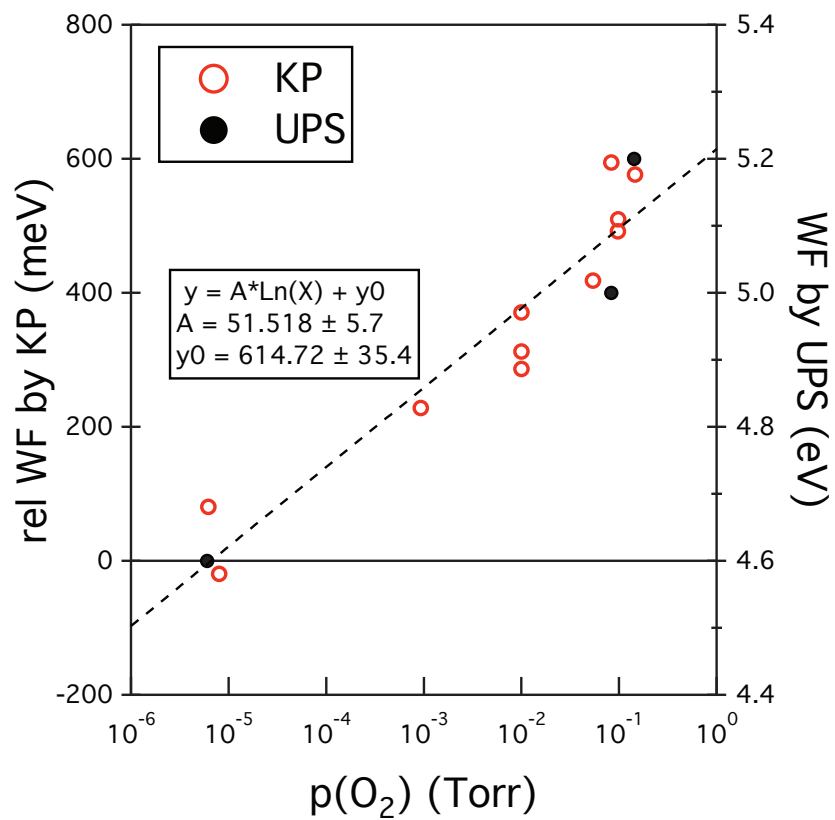


Figure 4.8: Work-function of the PLD NiO films as measured using the Kelvin method and UPS. Precision of KP data is less than 5 meV, UPS is 0.1 eV.

the work-function measured by UPS and the Kelvin method differs only by an offset, as expected. Increasing the substrate temperature, on the other hand, tend to reduce the work-functions of the films (Fig. 4.8). This is understood to be due to degassing of oxygen into the chamber atmosphere, mostly during sample cooling [27].

Select film optical absorbances ($t = 10 \text{ nm}$) are shown in Fig. 4.9. $E_g \sim 3.0 \pm 0.2 \text{ eV}$ for samples grown at room temperature as approximated by both Tauc-method and from UPS / IPES. With large band-gap and very low film thickness, the films are very transparent. Nevertheless, it is readily visible that films deposited under low $p(O_2)$ tends to appear more metallic. This is also evident in the increase of absorbance below E_g , especially for samples grown in vacuum at high temperature, which is usually an indication of the presence of localized mid-gap states.

The presence of mid-gap states is confirmed by the photoemission data. As shown in Fig. 4.10, Although the gap is mostly clean below E_F , the conduction band-tail extends slowly in an exponential manner to $\sim 0.5 \text{ eV}$ above E_F , the degree of which is also a function of $p(O_2)$. The valence band, on the other hand is relatively abrupt, albeit the presence of a shoulder at $\sim (E_F + 2.0 \text{ eV})$. Upon O_2 -plasma cleaning, the density of these states above E_F increase.

The systematic change in doping as a function of $p(O_2)$ is evident from the displacement of the E_F within the gap. As we increase $p(O_2)$, the E_F moves closer towards E_v and the film becomes more p-doped. E_g also increases but remains relatively constant at $3.0 \pm 0.2 \text{ eV}$ at higher $p(O_2)$. A systematic shift in E_{vac} is also observed.

Film structural properties may be significantly altered when in the ultra-thin limit. For example, it has been shown that a columnar structure may develop on NiO_x films grown on glass [144]; however, we observed that this only happens at thicker films $t \gtrsim 30 \text{ nm}$. Directly measuring the XRD pattern from the actual sample, however, is challenging due to 2 reasons:

- Extremely thin film samples greatly reduces signal
- The ITO substrate, which is thicker by an order of magnitude, returns a much stronger background signal comprising of a multitude of peaks, some of which overlaps with the NiO

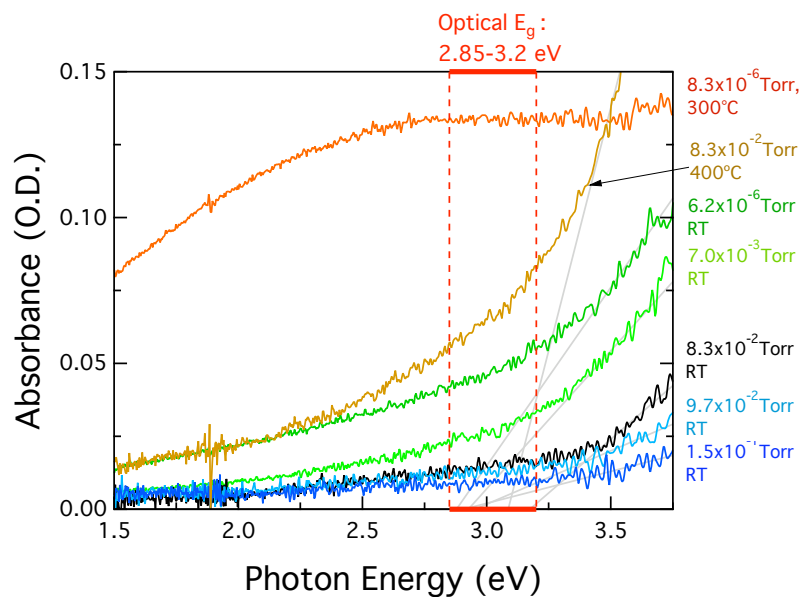


Figure 4.9: Optical absorbance of PLD NiO_x films. Dotted line indicates E_g from photoemission.

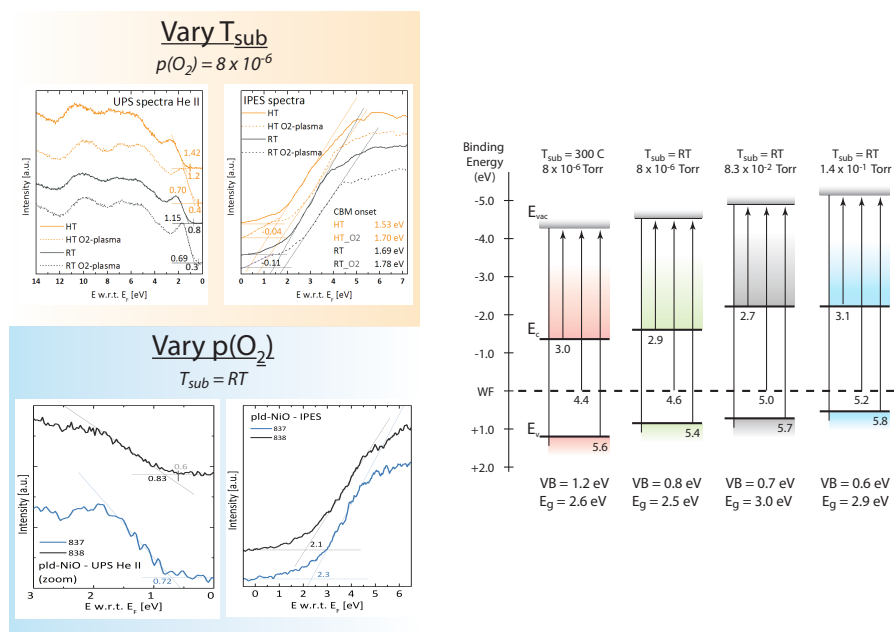


Figure 4.10: UPS / IPES spectra of select PLD NiO_x films and the extracted energy levels.

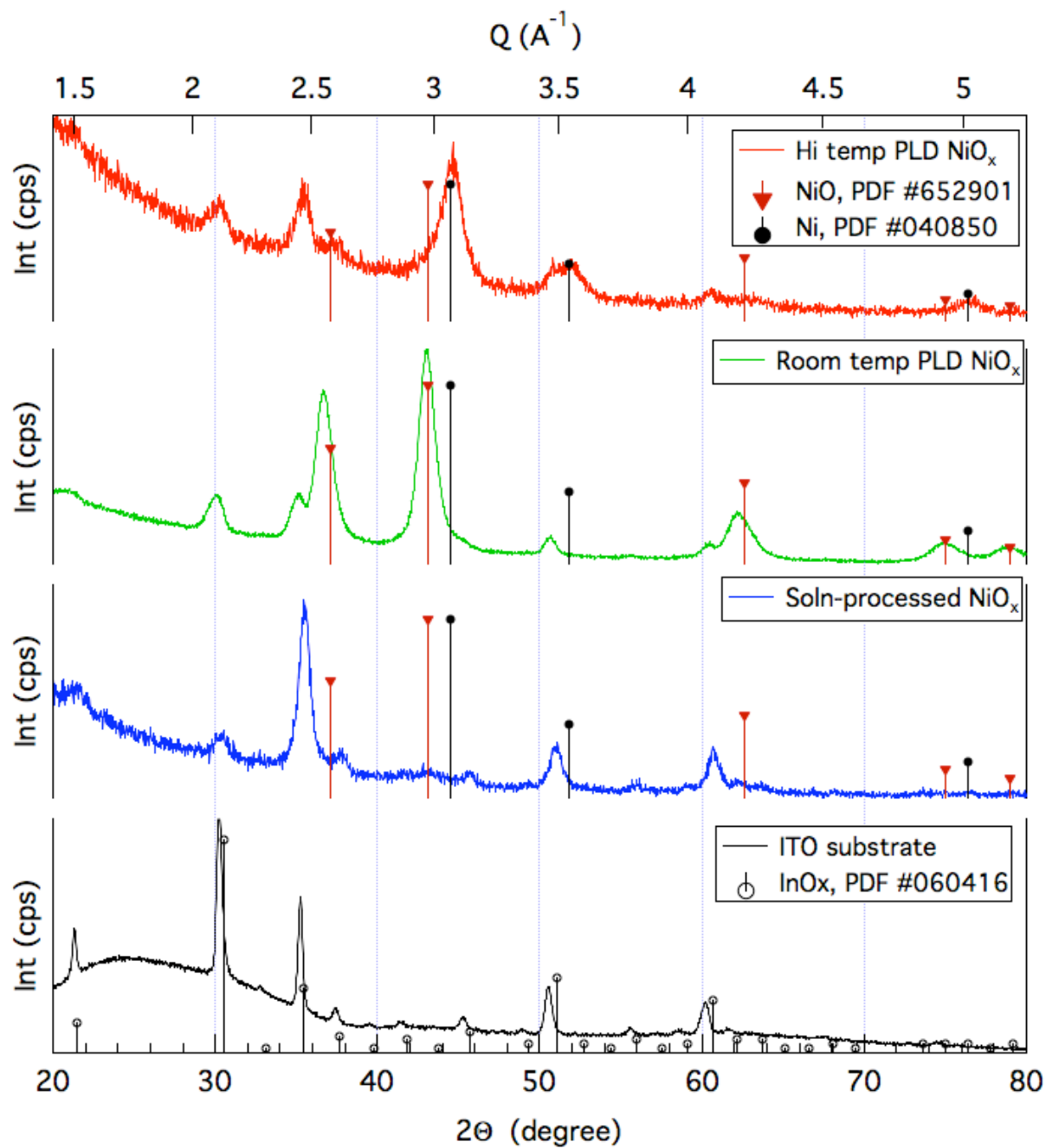


Figure 4.11: GIXD of select PLD NiO_x films, showing the different structural property. Also shown for comparison is the data for solution-processed NiO_x and the data for the ITO substrate. The data for ITO is taken in $\theta - 2\theta$ geometry.

signal (Fig. 4.11).

To overcome these problems, we perform XRD at grazing incidence between $\alpha = 0.15^\circ - 0.30^\circ$, practically increasing the illuminated sample volume while decreasing the illuminated substrate volume. Fig 4.11 shows the measurement result where the result from grazing-incidence measurement geometry –ITO background signal diminished while the NiO signal enhanced – is clearly visible ⁵. As a comparison, XRD signal from ITO taken in traditional $\theta - 2\theta$ geometry is also shown. From this data, it can be inferred that the shifts in the ITO peak locations are due to strains within the film. The analysis of ITO strain is not a primary focus of this work and is omitted. From these results, it is apparent that films grown at room temperature are composed of poly-crystalline NiO, in contrast to films by spin-casting from nickel formate [269]. On the other hand, XRD signal of polycrystalline NiO is weak in films grown at high temperature. Instead, the signal is dominated by metallic nickel peak, from which we infer the presence of some degree of phase segregation.

The nature of the surface states is further elucidated by the XPS spectra of the two samples, as-deposited and with O_2 -plasma treatment, which are shown in Fig. 4.12. The O1s data is composed of two overlapping peaks. Peak P1 at 529.5 eV of the O1s spectra has been related to stoichiometric NiO, confirming the presence of NiO in all films, including in those that do not return XRD peak. The shift of this peak to lower binding energy upon oxygen plasma cleaning suggests the formation of unstable non-stoichiometric surface species, consistent with the observation that the advantageous properties induced by the plasma treatment (improved wetting, increased work-function, etc.) is temporary.

Ratcliff et al. have attributed the broad peak P2 at 531.0 eV to surface hydroxyls and noted that this peak increases as a function of oxygen plasma-cleaning [190]. The increase of hydroxyl species in response to an oxygen plasma treatment may sound counter intuitive. However, Langell and Nassir have shown evidence that a sub-monolayer of surface hydroxyls adsorbed from ambient atmosphere passivates the thermodynamically unstable polar NiO(111) surfaces [132]. Therefore,

⁵ Small correction ($\lesssim 0.15^\circ$) to the Bragg reflection angle is applicable for small incidence angle due to refraction of X-ray in the material [242]. This, although is readily visible in the experiment, is only tangential to our study.

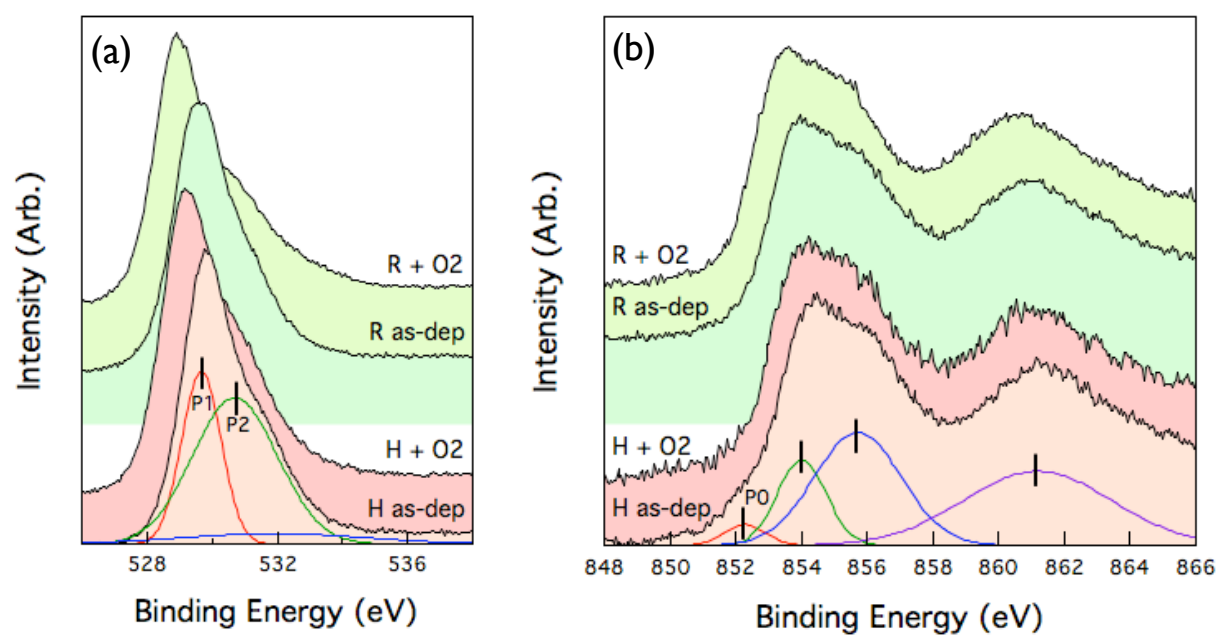


Figure 4.12: XPS (a) O1s and (b) Ni2p spectra of select PLD NiO_x films.

we postulate that the oxygen plasma treatment initially increases surface oxygen, producing essentially NiO(111) facets. This is then passivated by water from the atmosphere upon exposure. This conjecture is a topic of ongoing research.

Upon closer inspection of the UPS spectra, we also found that for the sample grown at high temperature, $g_e(E_F) \neq 0$, indicating a metallic surface states. This is corroborated by the presence of a small peak (P0) at $E_B = 852.3 \text{ eV}$ in the XPS Ni2p spectra which is a signature of metallic Nickel. This is in line with the XRD result and with the observation that the film is visibly more metallic. Upon O_2 -plasma treatment, the material returns to having a proper E_g , and the XPS peak disappear. However, its XRD data is largely unchanged, suggesting that O_2 -plasma treatment alters only the topmost surface of the film.

The ability to tune the electronic levels of NiO_x by PLD makes it the system of choice for studying band alignment in an actual device, which will be covered in §7.

4.2.1.2 NiO_x ultra-thin films by RF magnetron sputtering

NiO_x HTL was also deposited by sputtering. This will pave the way for scaling up the deposition to accommodate for larger area devices. In this study, nickel oxide samples are deposited on a pre-patterned ITO substrate (Thin Film Devices) and a witness glass substrate (Eagle Corning 2000) simultaneously. Glass substrates are first scrubbed in critical cleaner detergent to remove residual industrial grease. Both ITO and glass substrates are then cleaned in the same way as those for PLD. Right before deposition, the substrates are oxygen-plasma treated at $152 \pm 5 \text{ W}$, $0.70 \pm 0.10 \text{ Torr}$ for 5 minutes to remove residual organic molecules.

Sputtering is done using a stoichiometric 3"-diameter NiO target at RF (13.9 MHz) power of 109 Watt, at room temperature. The thickness of the films is estimated from stylus profilometry (Veeco DEKTAK 8 Advanced Development Profiler) of calibration samples deposited on glass, and close monitoring of the deposition rate using a quartz crystal microbalance. Film thicknesses were later confirmed using transmission electron microscopy (TEM). We vary the Ar: O_2 flow ratio from 1:10 to 1:45 while keeping the total chamber pressure constant at 12 mTorr. A witness sample on

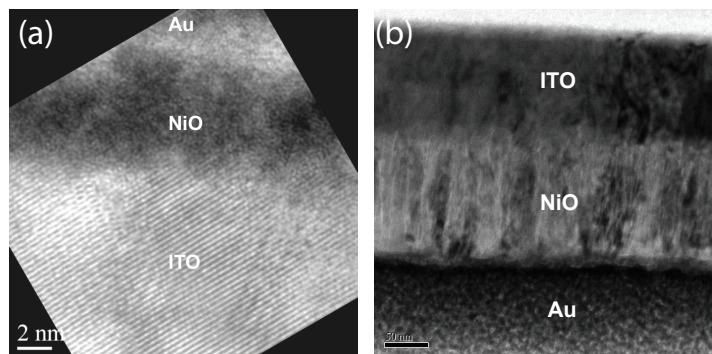


Figure 4.13: TEM of sputtered NiO films on ITO. (a) $t = 5$ nm, (b) $t = 150$ nm.

glass substrate accompanies all deposition.

Fig. 4.13 shows the TEM pictograph of a thin and a thick NiO_x sample, with thickness setpoint set to be 5.0 nm and 150.0 nm, respectively. As shown in the picture, the use of crystal microbalance during deposition have greatly assisted tight control of film thickness. The thickness of the thin film is close to 5.0 nm. Thickness of the thicker film is estimated to be 144.66 nm from the pictograph. The data also shows very different film structure at very low film thickness. The 5 nm-film appears to be amorphous, while the 150 nm-film is crystalline and suggestive of columnar growth. The latter is consistent with previous reports: nickel oxide grown by sputtering have been reported to have an inclined columnar structure [144, 265], possibly related to the angle at which flux is incident on the substrate [77].

The largely amorphous structure of the thin film is confirmed by XRD. Shown in Fig. 4.14a-c are the XRD data for the witness samples on glass after background subtraction, showing no sign of crystallinity. As a comparison, XRD of a 5-nm crystalline NiO_x sample grown on glass by PLD is measured using the same equipment and measurement geometry. The result is shown in Fig. 4.14d.

Unlike the films deposited by PLD, these films have measurable conductivities (Table 4.1). Conductivity increases as a function of oxygen mixing in the process gas, consistent with increased p-doping of the film by oxygen. WF also shows the expected trend (Table 4.2). Unfortunately,

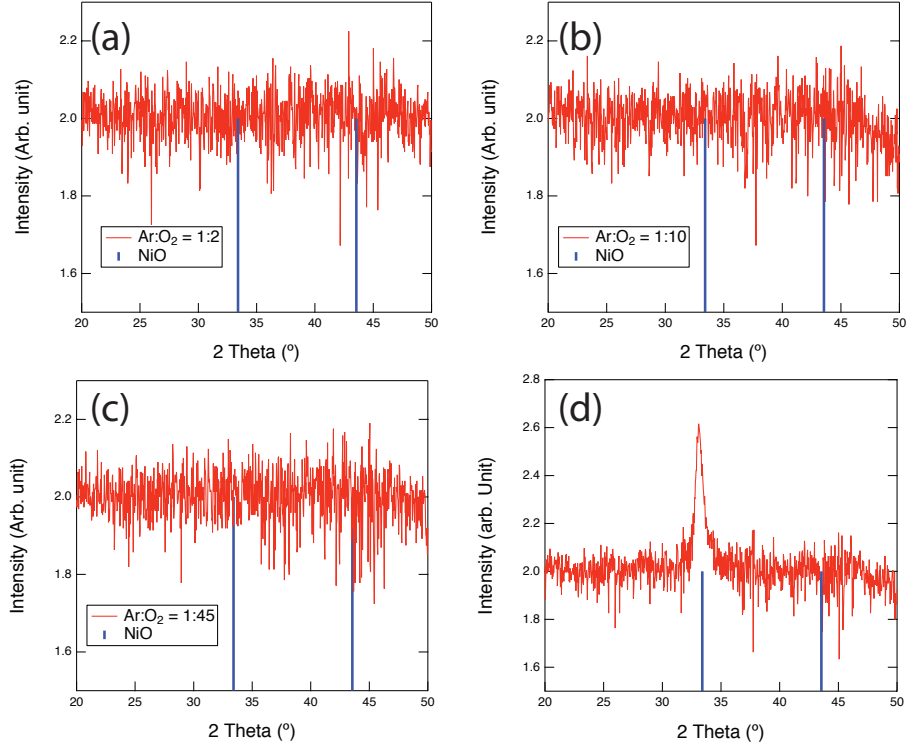


Figure 4.14: XRD of sputtered NiO_x grown at different Ar: O_2 ratio: (a) 1:2, (b) 1:10, and (c) 1:45. Also shown in (d) is the XRD data taken with the same instrument and measurement geometry for a crystalline NiO film grown by PLD. Data are background-subtracted

Deposition Ar : O_2 Ratio	Resistance (Ω)	Resistivity ($\Omega \text{ cm}$)	Conductivity (S cm^{-1})
1 : 2	5.0×10^5	2.5×10^{-1}	4.0×10^0
1 : 10	1.0×10^5	5.0×10^{-2}	2.0×10^1
1 : 45	8.0×10^4	4.0×10^{-2}	2.5×10^1

Table 4.1: Electrical properties of NiO_x films with different Ar: O_2 ratio during deposition.

Deposition Ar : O_2 Ratio	ϕ (eV)		
	As Deposited	After 2 Days	O_2 Plasma Clean
1 : 2	5.1	4.8	5.2
1 : 10	5.4	4.8	5.1
1 : 45	5.8	5.0	5.1

Table 4.2: Work-function of sputtered NiO_x films with different Ar: O_2 ratio during deposition. O_2 plasma clean done at 155 W, 0.80 torr for 5 minutes.

measurement of Seebeck coefficient still did not yield reliable results.

WF of these films were measured using Monroe electrostatic voltmeter with inconel-x as the reference standard (work-function of inconel-x standard was measured to be 4.33 eV by UPS). Of importance is the observation that although we were able to engineer the WF of the film, the WF decays to a similar value after two days storage in an inert N_2 atmosphere. Further, O_2 plasma treatment does not restore the surface condition of the film to the as-deposited state. This highlights the importance to know the time constant for the decay of the NiO_x .

Film transparency is also excellent, with absorbances of less than O.D. 0.10 (Fig. 4.15), comparable with samples grown by PLD. Since the glass substrate starts to absorb around 3.70 eV, we interpret the inability to see the proper absorption edge of the film as the band-gap being more than 3.70 eV.

Time-resolved work-function decay measurement was done on a fresh sample grown at $Ar:O_2 = 1:2$ with a KP Technologies Kelvin probe system with a gold reference standard. This is shown in Fig. 4.16. The data shows a very fast initial decay followed by slower decay and is best fit with a double exponential function. We believe the first fast decay may be an artifact of the set-up in the form of heating of a resistor, which can be seen in the raw data using an oscilloscope. The time offset in the measurement is due to the time required to unload the sample from the sputter chamber and Ar glovebox, sample transport, and equipment set-up. The difference between the initial measured WF (821.2 meV) and the final value from the fit (516.5 meV) agrees well with the 0.3 eV difference observed from the earlier measurement. More importantly, the data gives an estimate on the time constant of the decay, $\tau \approx 82.7 min$.

UPS was done twice on these samples to gain confidence on the observed data. These are shown in Fig. 4.17 and 4.18. Both measurements indicate that the samples grown at different oxygen contents are nearly identical. The two sets of data also yield different WF and E_v . We believe this is related to the different sample travel time and equipment. More importantly, on the second set (Fig. 4.18c), the sample is visibly decaying while being measured, leading to a 0.5 eV shift in WF , confirming our earlier observation.

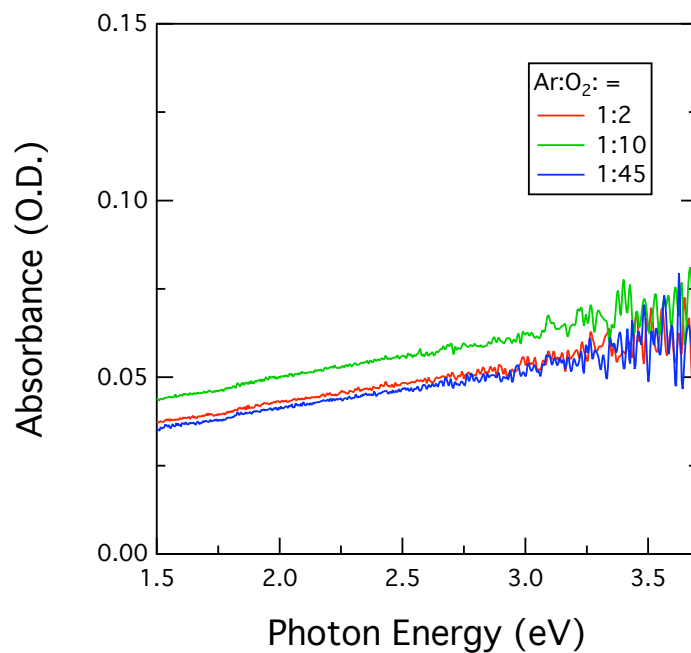


Figure 4.15: Absorbance of sputtered NiO_x films grown at different oxygen condition.

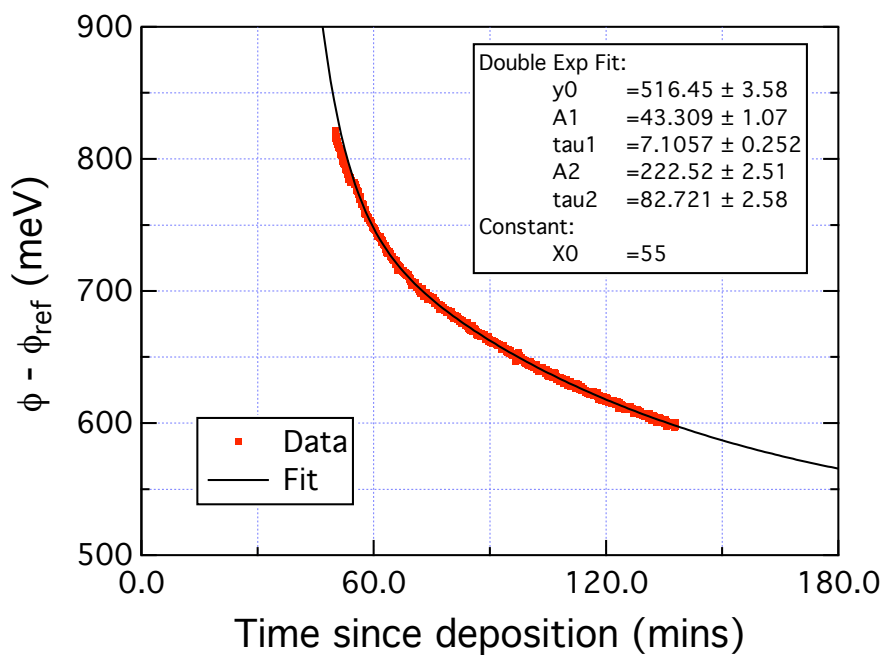


Figure 4.16: Work-function decay of sputtered NiO grown at $\text{Ar}:\text{O}_2 = 1:2$.

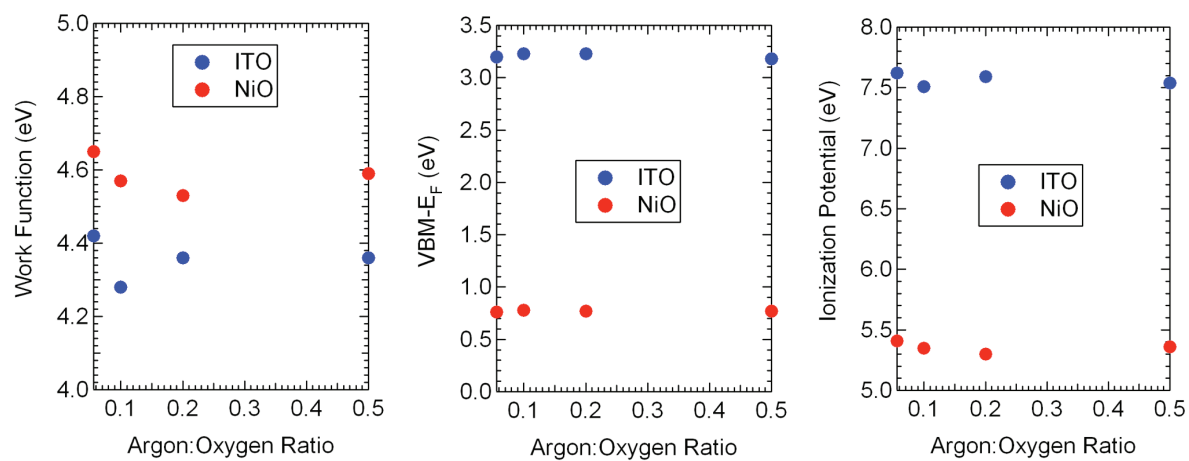


Figure 4.17: Photoemission study of sputtered NiO_2 , set 1. WF and E_v of the sputtered NiO_x as a function of Ar: O_2 ratio.

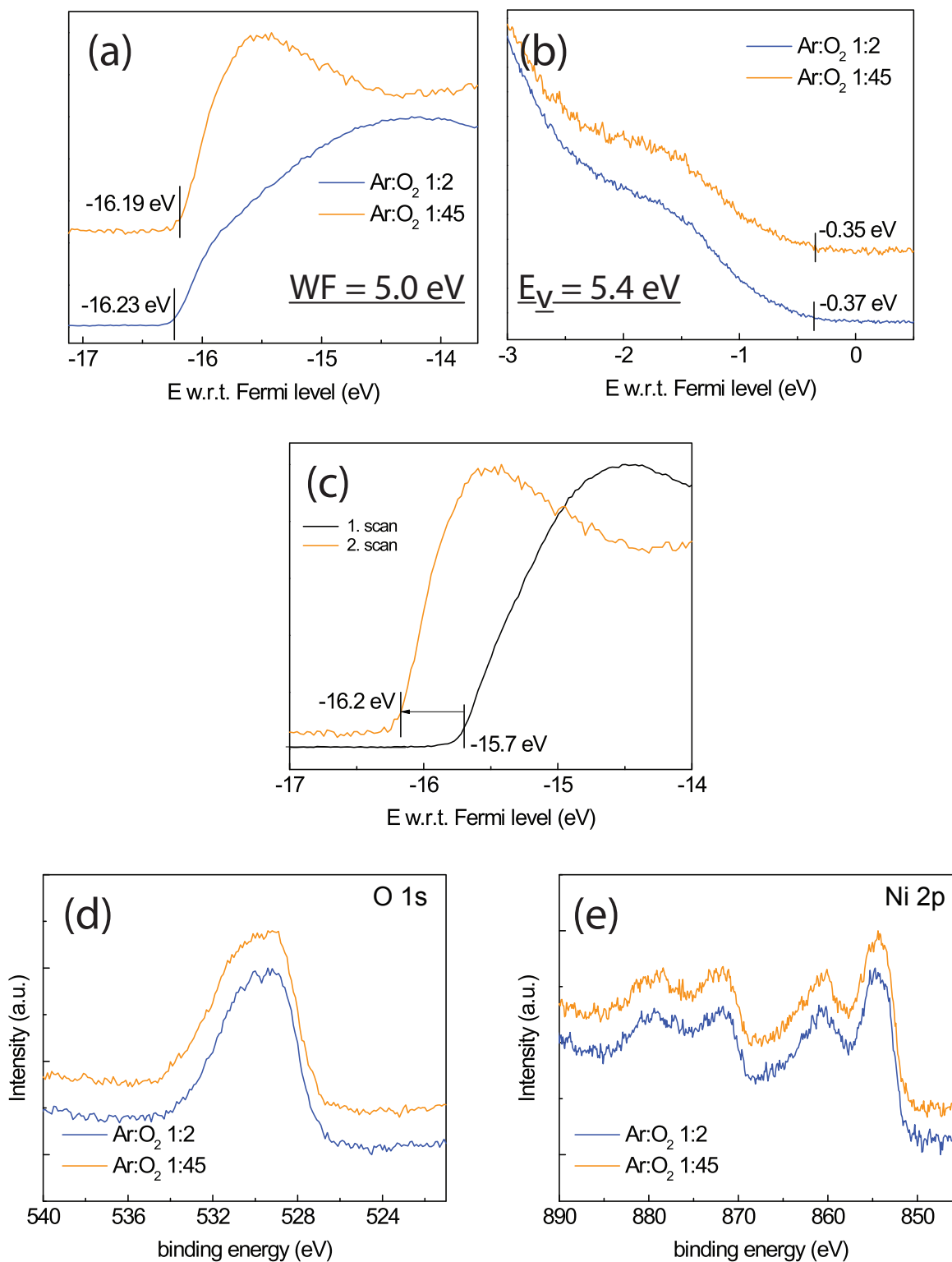


Figure 4.18: Photoemission study of sputtered NiO₂, set 2. (a) Photoemission onset, showing similar $WF = 5.0$ eV, (b) near gap structure, showing $E_v = 5.4$ eV, (c) changes in photoemission onset of the Ar:O₂=1:45 sample, (d) O1s XPS spectra, (e) Ni2p XPS spectra.

XPS was also done on these samples (Fig. 4.18d-e). Spectra from the two films are strikingly similar, confirming that the similar energy levels are due to their composition being the same. Although the O1s peaks are so overlapped, it can be argued that the peak at 529.3 eV characteristic of stoichiometric NiO still make up for a large fraction of the spectra. The large contribution of the Ni2p peak at ~ 855 eV is consistent with our expectation that the films are highly p-doped.

One of the consequences of the observed decay is that it poses a challenge for repeatable device processing or careful study on band-offsets using these films. Nevertheless, as we shall see in §5, these films still perform as an excellent HTL, paving a way for larger-scale production of NiO_x HTL.

4.2.2 P3HT, PCBM and P3HT:PCBM

P3HT:PCBM is a mixture of poly(3-hexylthiophene) (P3HT) and phenyl-C₆₁-butyric acid methyl ester (PCBM). It is perhaps the most ubiquitous polymer-fullerene photoactive material being used in organic photovoltaics up to date, and have been reported to have *PCE* up to $\sim 4.0\%$ ⁶, albeit the large scatters in the reported data [46]. As a photo-active layer, P3HT:PCBM is most commonly employed as a bulk-heterojunction, although P3HT/oxide hybrid devices have also been demonstrated [174, 143]. The use of P3HT:PCBM in our works largely stems from the wealth of material studies that have been done and its commercial availability.

P3HT belongs to the family of polythiophenes, which is one of the archetypical conducting polymers. It serves as the donor material and the optical absorber in the blend due to its strong absorption in the visible spectrum. They tend to stack in lamella as shown in Fig. 4.19, forming a quasi-2D semiconducting crystallites, with conduction being mostly along the polymer backbone and across the $\pi - \pi$ stacking [80, 224]. Carrier concentration is $\sim 10^{15} \text{ cm}^{-3}$, while mobility ranges between $10^{-5} - 10^{-4} \text{ cm}^2 \text{ V}^{-2} \text{ s}^{-2}$ [154, 139]. This is known to be sensitive to molecular weight and solvent [160]. For this reason, we keep reagent batch the same for every given experiment.

⁶ Higher *PCE* can be achieved by employing extremely small device area. See Ref. [222] for an in-depth discussion on the subtleties involved in accurately measuring organic solar cell efficiency.

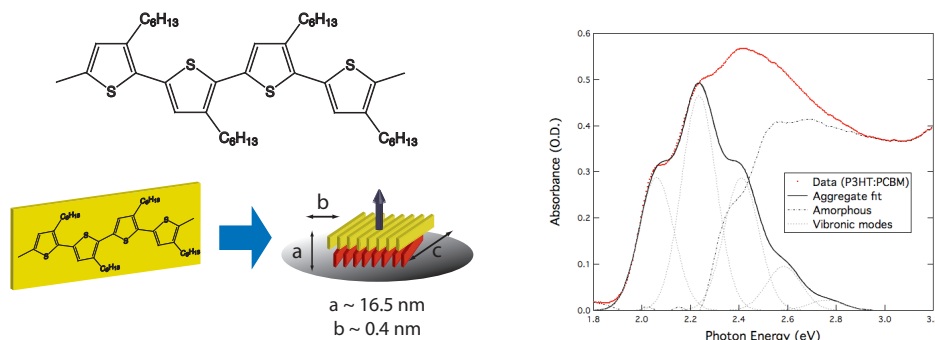


Figure 4.19: Illustration of P3HT, its lamellar structure in crystallites, and its optical absorbance.

P3HT absorbs mainly in the optical band and acts as the primary absorber material in the bulk heterojunction. Its optical absorption, profile shown in Fig. 4.19 is known to follow that of H-aggregates [37, 226, 228, 169]. Absorption at $\sim 2.0\text{ eV}$ has been used to gauge the degree of ordering in the film. However, more precisely, it only measures short-range orders [55], and not necessarily be correlated with medium to long-range orders measured by XRD. P3HT returns XRD signal at $Q \approx 0.39\text{ \AA}^{-1}$ corresponding to the inter-lamellar distance of 16.5 \AA and at $Q \approx 1.6\text{ \AA}^{-1}$ corresponding to the $\pi - \pi$ distance of 4.0 \AA [185, 59, 55, 106, 224].

Most relevant to this work, the electronic structure of P3HT have also been studied theoretically [170] and experimentally [82, 270, 240]. The combined UPS / IPES data from Ref. [82] is reproduced in Fig. 4.20. An interesting observation is that the proper electronic band-gap of P3HT is 2.52 eV , corresponding to 492 nm (green-blue) which suggests that the absorption of the lower optical wavelength is assisted by mid-gap states.

PCBM (Fig. 4.21) is a fullerene derivative that is widely used as an acceptor material in organic solar cells. The ester group serves to increase its solubility in chlorobenzene, allowing for solution processing. Due to the spherical symmetry of fullerenes, it has been argued that PCBM is the only 3-D organic semiconductor [80]. Carrier mobility, reported to be $10^{-4} - 10^{-3}\text{ cm}^2\text{V}^{-2}\text{s}^{-2}$, is higher than that of P3HT [154, 255, 155]. PCBM returns XRD signal at $Q \approx 0.65\text{ \AA}^{-1}$ corresponding to $d \approx 9.6\text{ \AA}$ [59]. However, PCBM in the BHJ film tend to be amorphous and does not crystallize

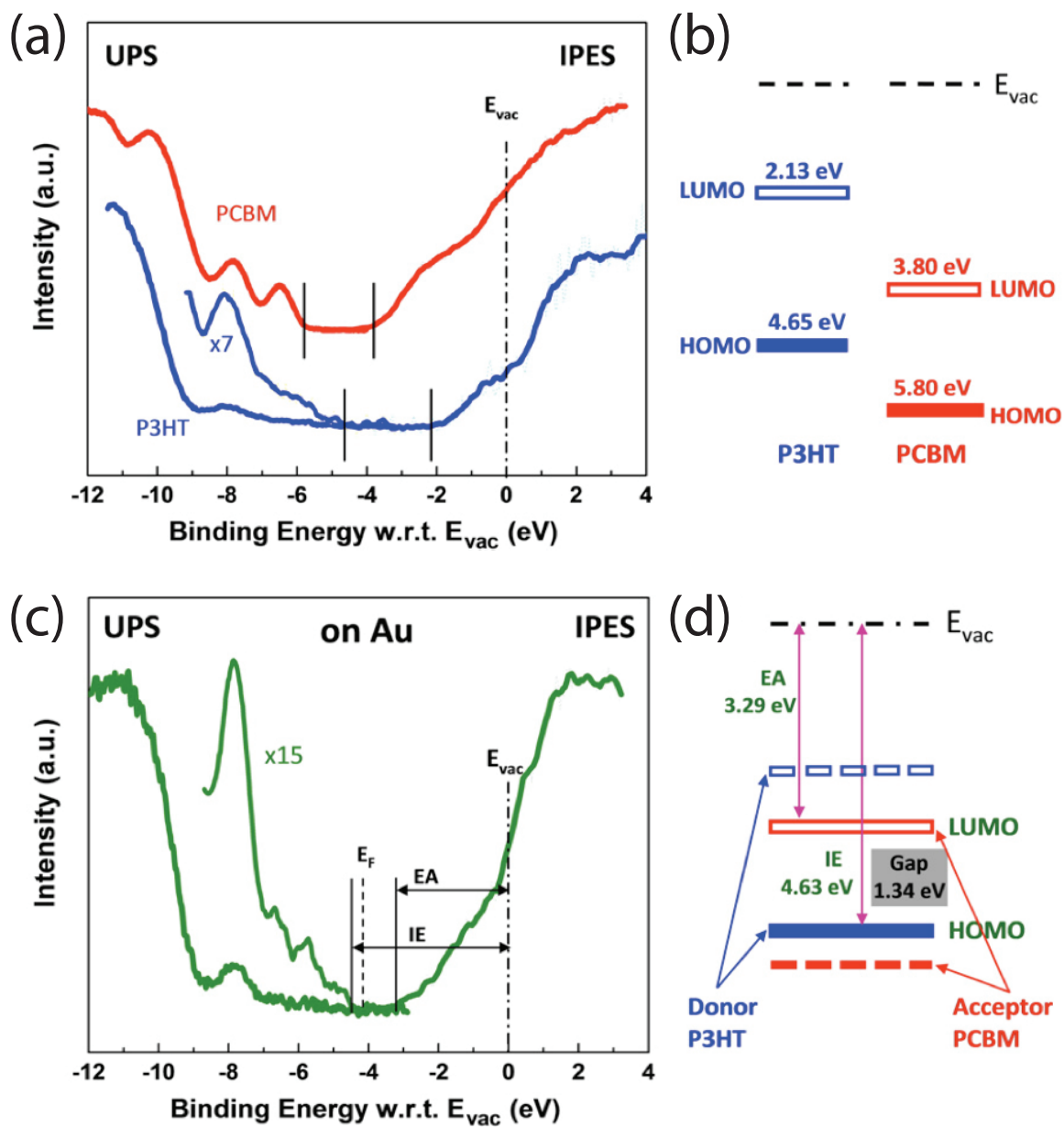
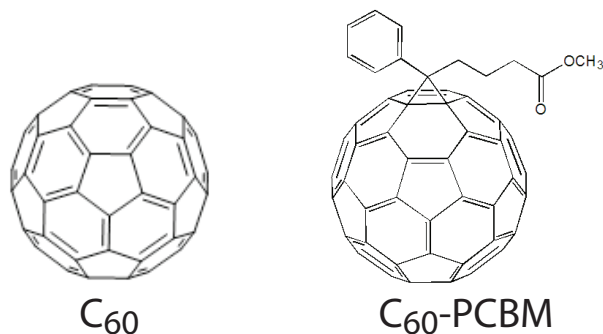


Figure 4.20: UPS and IPES spectra of (a)-(b) neat P3HT and PCBM films, (c)-(d) P3HT:PCBM bulk heterojunction film. From Ref. [82].

Figure 4.21: C_{60} and C_{60} -PCBM

until $\gtrsim 160^\circ C$ [273].

PCBM mainly absorbs in the ultraviolet (Fig. ??) [223], and its main role in the blend is to assist exciton splitting [24]. The electronic levels of PCBM and P3HT:PCBM blends are shown in Fig. 4.20, and is proposed to form a $0.4 - 0.6 eV$ interfacial dipole with P3HT that help exciton splitting [270, 82]. As excitons have to diffuse to the P3HT/PCBM interface to dissociate, BHJ morphology has been a topic of intense studies. Focus has been given to, for example, the effect of annealing [180, 273, 257, 210, 154], molecular packing and intercalation [156], and vertical phase segregation [68, 271, 248, 193, 243, 175]. Charge transport in the blend has also been done extensively [183, 255, 139], and the success of the slow-dry (solvent annealing) process has been attributed to the large increase in hole mobility in the blend [154]. Lastly, the two most prominent degradation paths which needs to be aware of during device processing and measurement are degradation of the top metallic contact and oxygen doping of the organics [192, 74, 212, 33].

4.2.2.1 P3HT:PCBM spin-casting recipes

3 different spin-casting recipes for P3HT:PCBM OPV devices are used at NREL. For this work, we are using exclusively the first recipe (“slow dry”), unless specified. Every step described herein, except for weighing the solutes, are done in a nitrogen glovebox.

In the slow dry recipe [137], P3HT and PCBM solids are mixed 1:1 by weight ratio and

dissolved in ortho-dichlorobenzene to form a 50 mg/mL solution by total solute weight. The solution is stirred for at least overnight at 60°C to ensure complete mixing. Before spin-coating, the solution is cooled down to room temperature. P3HT:PCBM films are spin-cast on the substrates under nitrogen atmosphere at 600 rpm, 600 rpm/s for 60 s. The wet films are then left to dry in a closed petri dish. The completely dried films are then thermal annealed for 10 minutes at 120°C on a hot plate and the contact regions scraped. As a top contact, Ca (20 nm) / Al (100 nm) bilayer is thermally evaporated through a shadow mask.

The second recipe (“dry-on-the-chuck”), by Dr. Andres Garcia, was developed to reduce the non-uniformity of device performances due to uncertainties in the solvent annealing process. In this recipe, the films are spun until dry. P3HT:PCBM solids are mixed in 1.5:1 by weight ratio and dissolved in ortho-dichlorobenzene to form a 35 mg/mL solution by total solute weight. The solution is stirred for at least overnight at 60°C to ensure complete mixing. Before spin-coating, the solution is cooled down to room temperature. P3HT:PCBM films are spin-cast on the substrates under nitrogen atmosphere at 500 rpm, 500 rpm/s for 200 s or until the film is dry. The films are then thermal annealed for 10 minutes at 120°C on a hot plate and the contact regions scraped. As a top contact, Ca (20 nm) / Al (100 nm) bilayer is thermally evaporated through a shadow mask. It was noted for this recipe that annealing at higher temperature tends to improve V_{oc} while reducing j_{sc} . Compared with conventional devices, typical dry-on-the-chuck devices have higher V_{oc} , lower j_{sc} , lower FF , but the same PCE . Dr. Garcia has claimed improved reproducibility; however, the recipe is still rarely used.

The third recipe, was built up by the current author on the second recipe and on a recipe by Orimo et al [175]. It was designed to be used with larger area samples, particularly combinatorial device libraries. Dr. Alexandre Nardes has provided helpful insights during the development process. Two issues needed to be addressed:

- Reduce processing time (solvent annealing time for a $2'' \times 2''$ sample took more than overnight)

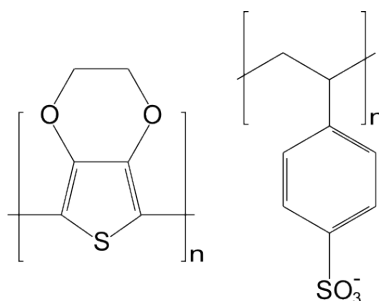


Figure 4.22: PEDOT:PSS

- Completely avoid the use of Ca in the top contact because of its fast degradation.

In this recipe, we follow spin-casting procedure of the dry-on-the-chuck recipe, with spin-casting time increased to 300 s to ensure complete dryness of the film (films are usually dry in 250 s). However, Al contacts are thermally evaporated onto the films without a thermal annealing step in-between. Thermal anneal is done on the whole structure after the top contact is deposited at 170°C for 30 minutes. The resulting device efficiency employing PEDOT:PSS is 2.5% as opposed to 2.7% of the control Ca/Al device.

4.2.3 PEDOT:PSS

Poly(3,4-ethylenedioxythiophene):poly(styrenesulfonate) (PEDOT:PSS) is a mixture of two conducting polymers, and is deposited from an acidic suspension in water [164, 163]. It is the most commonly used HTL in OPV applications. The film surface is PSS-terminated. Due to the ease of increasing its conductivity by post-treatment, PEDOT:PSS has also found applications as flexible transparent conducting electrodes [114].

As-deposited, its work function ranges between 4.8 - 5.1 eV [164]. However, after gentle sputtering to remove the PSS layer, the work function increases to 5.1 eV, and the UPS spectra becomes more metallic-like.

4.2.3.1 PEDOT:PSS spin-casting recipe

PEDOT:PSS is spin-cast in twice at 6000 rpm, 6000 rpm/s for 45 s in air. The contact regions are then cleaned using wet cotton swab, and the film thermally annealed on a hot plate at $130^{\circ}C$ for 1 hr. This yields a film thickness of $\sim 20 - 30 \text{ nm}$.

4.2.4 Indium Tin Oxide

Indium tin oxide (ITO) is the most prevalently used transparent conducting oxide [71, 77, 219]. It is a polycrystalline mixture of indium oxide with tin oxide, with usually 80 – 90% indium content. It is a degenerately doped semiconductor with band-gap of $3.5 - 4.0 \text{ eV}$, and conductivity of $10^3 - 10^4 \text{ S cm}^{-1}$ [86]. Optical transparency of commercial ITO on glass typically range between 85-95% in the optical regime.

Chapter 5

Sputtered Nickel Oxide as an Efficient Hole Transport Layer in P3HT:PCBM Organic Solar Cell

We begin our discussion with the work done on developing NiO_x HTL by RF sputtering. This chapter is a modified version of an article that we published in a peer-reviewed journal (Ref. [261]). Although we mentioned earlier in §4 that the instability of the sputtered film makes it not ideal for our study, this study has a historical significance. When the study was done, there was only one empirical design rule for an HTL: its WF has to be as high as possible. Additionally, it was also empirically found that O_2 plasma treatment on the HTL always improve device performance [21, 20]. In some cases, O_2 plasma treatment is so crucial that the device won't work without it [232, 269]. The contemporary conjecture was that O_2 plasma treatment serves to increase the WF even further. This study convinced us that the situation is not as simple.

We shall see in this study that: (1) V_{oc} does not always grow as a function of WF . (2) The active layer properties (in this case thickness) may be affected by the HTL, resulting in unintended smear in the data. (3) O_2 plasma treatment does not always improve device performance. These observations hint at the details that we need to address in order to do a careful study and help shape our subsequent investigation strategies.

Additionally, although further studies on these sputtered films are not preferable, the NiO_x HTL's perform very well in devices. This study is therefore a demonstration that such high-performance HTL can be deposited by an easily scalable deposition technology.

This chapter contains an expanded discussion of a peer-reviewed journal article that has been

published by the author [261].

5.1 Experimental

In this study, all of our NiO_x samples were deposited on a pre-patterned ITO substrate (Thin Film Devices) and a reference glass substrate (Eagle Corning 2000) simultaneously. After a standard substrate cleaning process [259], sputtering was done using a stoichiometric 3"-diameter NiO target at RF (13.9 MHz) power of 109 Watt, at room temperature. The thickness of the films was estimated to be 5 nm based on optical ellipsometry (J.A. Woolam M-2000), stylus profilometry (Veeco DEKTAK 8 Advanced Development Profiler) of calibration samples deposited on glass, and close monitoring of the deposition rate using a quartz crystal microbalance. Film thicknesses were later confirmed using transmission electron microscopy (TEM). X-ray diffraction (Bruker D8) was used to investigate the film structural properties. Ultraviolet - visible transmission measurements were done with Ocean Optics spectrometers.

Excess oxygen was expected to generate holes and thus make the NiO_x system p-type conductive [161]. Thus, the doping level and work-function of the film can be tuned by controlling the O_2 partial pressure during deposition. We investigated this by varying the Ar: O_2 flow ratio from 1:10 to 1:45 while keeping the total chamber pressure constant at 1.6 Pa. Work-function of these films were measured by the Kelvin probe method and by ultraviolet photoemission spectroscopy (UPS).

UPS of the NiO_x film on ITO was performed at NREL, during which nominally "clean" samples were exposed to air in the same manner as during device preparation. The NREL instrument has been described previously [181]. Briefly, a non-monochromatic He(I) excitation source was used. Satellites in the resulting spectra were numerically subtracted assuming contributions of 2% at 23.087 eV and 0.5% at 23.742eV to the principal resonance line at 21.218 eV, which was taken to be 100% [186]. A -45 V bias was used on the sample to assure that the secondary electron cut-offs were due to the material being studied rather than the spectrometer. The binding energy scale was calibrated using sputter-cleaned molybdenum foil.

UPS of the organic blends on top of the HTL was performed with a Kratos Axis Ultra X-ray photoelectron spectrometer with a He(I) excitation source (21.22 eV) at the University of Arizona. In these UPS experiments, a -9.00 V bias was applied to the sample to further enhance the collection of the lowest kinetic energy electrons. A separate UPS spectrum was measured for a sputter-etched, atomically clean gold sample before characterization of the sample to ensure accurate values for the low and high kinetic edges relative to the Fermi edge.

Kelvin probe measurements were performed using a Monroe electrostatic voltmeter with inconel-x as the reference standard (work-function of inconel-x standard was measured to be 4.33 eV by UPS). Transient work-function decay measurement was done with a KP-technologies Kelvin probe system with a gold reference standard. It is important to note that the Kelvin probe method spatially averages the work-function over the probed area, while UPS measures the lowest work-function within the area. It is also important to stress that although the absolute work-function values obtained from this method are highly dependent on the condition of the reference sample and may not be as accurate as ones obtained by UPS, the values for work-function differences should be precise to roughly ± 0.1 eV.

P3HT:PCBM active layer was deposited by spin-coating from 50 mg total per mL total solution of P3HT (Plextronix) and PCBM (Nano-C) in dichlorobenzene (1:1 blend ratio) using the procedure outlined by Li *et al.* [137]. In the case of aged NiO_x films, oxygen plasma treatment is done at 152 Watt, 107 Pa average pressure of ultra-high purity O₂ prior to active layer deposition. Finally, 20 nm of Ca followed by 100 nm of Al is thermally evaporated as the top contact.

P3HT:PCBM solutions for UPS experiments were made according to the details outlined by Xu *et al.* [270] using the reagents specified above. As a control, we prepared a comparable P3HT:PCBM device which incorporates a standard PEDOT:PSS (Baryon Clevios 4018) HTL layer alongside the NiO_x HTL devices. PEDOT:PSS is spin-coated at room temperature in air at 6000 rpm for 45 seconds twice. The films are then baked at 130°C for 1 hour in air before active layer deposition.

J-V characteristics of the devices are measured using Keithley 238 High Current Source

HTL	Ar:O ₂	O ₂ plasma?	ϕ (eV)	j_{sc} (mA/cm ²)	V_{oc} (mV)	R_s (Ω)	R_{shunt} (k Ω)	η (%)	t_{BHJ} (nm)
NiO _x	1:2	Fresh	5.1	9.83 ± 0.19	575 ± 2	11.1 ± 0.0	6.2 ± 0.1	3.52 ± 0.08	304 ± 1
	1:10	Fresh	5.4	9.98 ± 0.09	573 ± 3	10.6 ± 0.0	5.5 ± 0.1	3.61 ± 0.05	310 ± 10
	1:45	Fresh	5.8	10.48 ± 0.09	585 ± 2	11.3 ± 0.0	7.1 ± 0.1	3.84 ± 0.03	337 ± 28
PEDOT	N/A	No	4.8	10.39 ± 0.32	591 ± 2	13.0 ± 0.0	19.3 ± 0.3	3.69 ± 0.12	326 ± 8
NiO _x	1 : 2	No	4.8	8.38 ± 0.20	581 ± 4	10.9 ± 0.0	12.8 ± 0.2	3.43 ± 0.07	285 ± 2
	1 : 10	No	4.8	8.15 ± 0.19	588 ± 3	10.7 ± 0.0	17.7 ± 0.2	3.36 ± 0.07	276 ± 15
	1 : 45	No	5.0	8.22 ± 0.08	581 ± 3	10.8 ± 0.0	13.4 ± 0.1	3.39 ± 0.04	277 ± 2
NiO _x	1 : 2	Yes	5.2	6.63 ± 0.21	551 ± 7	11.1 ± 0.0	8.3 ± 0.1	2.47 ± 0.06	267 ± 4
	1 : 10	Yes	5.1	7.29 ± 0.28	554 ± 3	11.1 ± 0.0	6.1 ± 0.1	2.66 ± 0.06	284 ± 4
	1 : 45	Yes	5.1	7.21 ± 0.33	560 ± 3	11.2 ± 0.0	7.2 ± 0.1	2.68 ± 0.09	270 ± 7
PEDOT	N/A	No	4.8	8.96 ± 0.15	590 ± 2	11.4 ± 0.0	36.3 ± 0.5	3.73 ± 0.04	331 ± 4

Table 5.1: Summary of NiO_x HTL deposition condition, surface treatment, work-function, and their corresponding average device performance indicators.

Measure Unit under one sun intensity in nitrogen atmosphere. Device temperature is not controlled, but is approximated to be near room temperature.

5.2 Results and Discussions

A TEM image of the sputtered NiO_x film is shown in Fig. 5.1a, which indicates film thickness of roughly 5 nm. It is also evident from these data that, unlike the PLD NiO_x reported earlier by Irwin et al.[104], our films appear amorphous and consistent with our previous studies on PLD and solution-deposited NiO_x films [20, 232]. X-ray diffraction data also showed no sign of crystallinity; however, the columnar structures of NiO_x films that has been previously reported [144, 265], were observed under TEM but only in thicker films of approximately 150 nm. The NiO_x films also demonstrate high transmittance of greater than 90% in the optical region (Fig. 5.1b), owing mostly to the film thinness. A positive correlation between the film transmittance and the Ar:O₂ ratio during deposition is also observed, although, statistically, the differences are not very significant. This transparency is favorable in for incorporation in standard device architecture, where light passes through both the transparent contact and the HTL before reaching the photo-active BHJ layer.

Table 5.1 summarizes the work-function of the NiO_x films as measured by Kelvin probe as a function of Ar:O₂ ratios, and their average performance as HTLs in P3HT:PCBM OPV devices. The work-functions of the as-deposited films spans a range of 0.7 eV by systematically varying the Ar:O₂ ratio from 1:2 to 1:45. Moreover, the trend in work-function of these films when measured

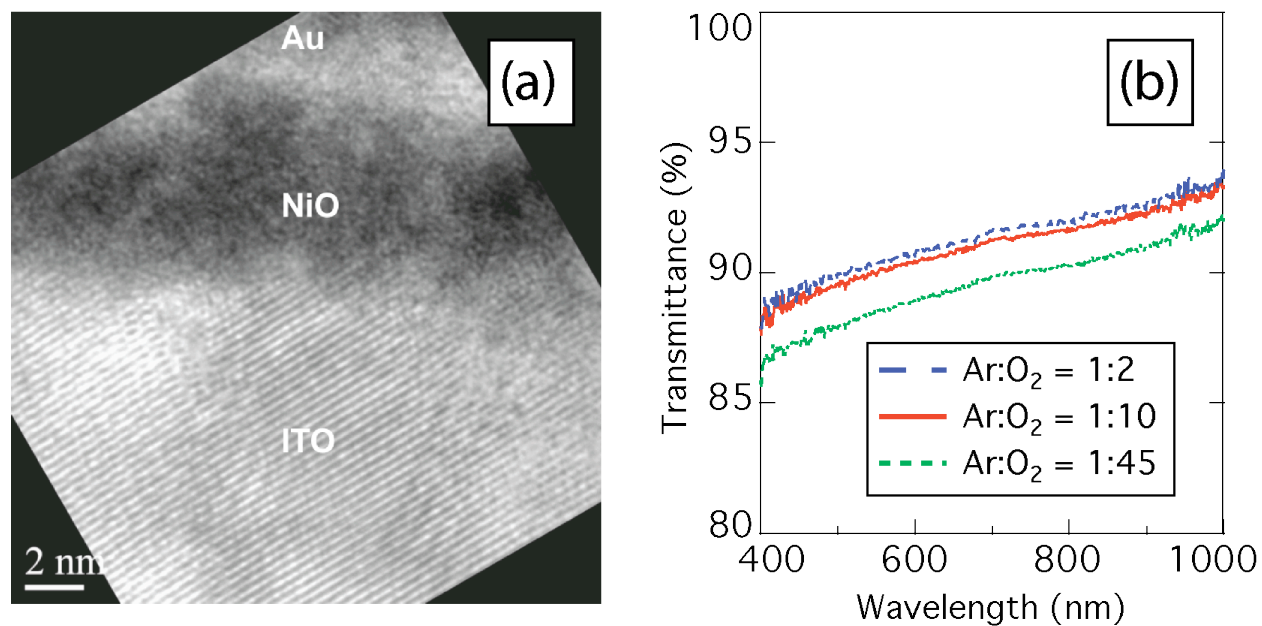


Figure 5.1: (a) TEM data of the sputtered NiO_x film, showing the lack of crystallinity and the 5 nm thickness. (b) Transmittance of sputtered NiO_x films with different deposition atmosphere.

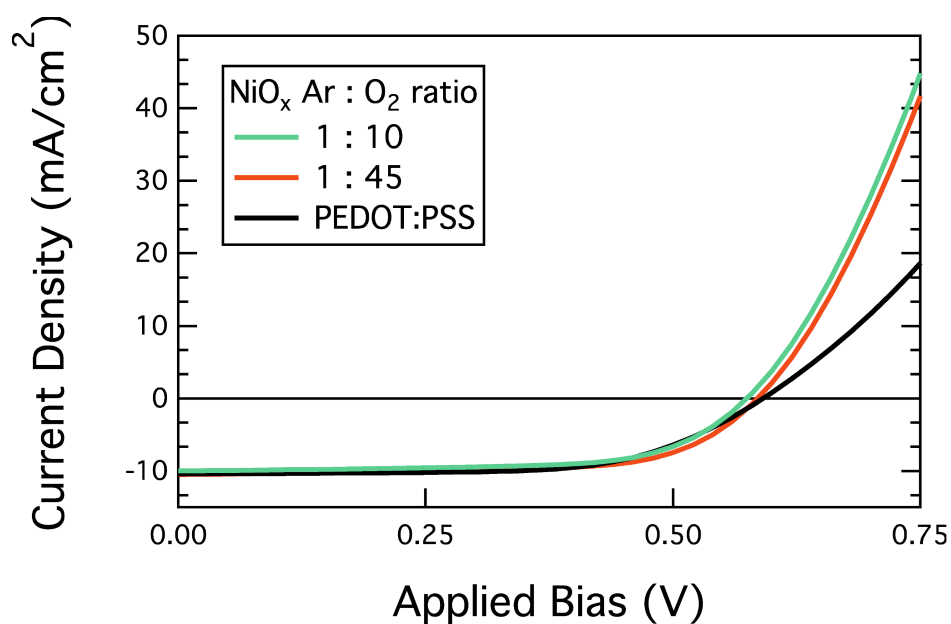


Figure 5.2: J-V characteristics of the best P3HT:PCBM devices employing as-deposited NiO_x HTLs and PEDOT:PSS.

in air is commensurate with the expected trend from p-doping of the film.

Work-function of a freshly sputtered NiO_x sample ($\text{Ar}:\text{O}_2 = 1:45$) followed by a brief exposure to ambient atmosphere during sample transport is measured to be 4.8 eV by UPS and is presented as the top spectrum in Figure 5.4. There is a feature at ~ 1.5 eV below the Fermi level, indicative of Ni 3d states, suggesting that the surface of the NiO_x film composed partially of Ni^{2+} oxidation states. The feature with the onset at ~ 3.0 eV below the Fermi is attributed to the O 2p orbital.

The work-function of the NiO_x film as measured by UPS differed by about 1 eV from the result measured from immediate post-fabrication films using Kelvin probe. This discrepancy is attributed not only to the inherent differences between UPS and the Kelvin Probe method discussed earlier, but also to the different species suspected to be present on the surfaces of the different samples, as shown by XPS (Fig. 5.3): (1) The surface species of the NiO_x films were found to contain a significant of $\text{Ni}(\text{OH})_2$ and hydrous species, which may result in a vacuum level shift and a decrease in overall work function. This contamination is expected to have been acquired during sample transfer in air. (2) Later films were also shown to have sulfur, indium, and tin impurities totaling about 5 at. %, of which tin and indium signals might be attributed to signal from ITO as the NiO_x is both thin enough to be penetrated by the X-ray and is only about twice as thick as the ITO surface roughness. The estimated 0.5% sulphur contamination is commonly found from air exposure.

We also found that the work-function of the as-deposited RF-sputtered NiO_x films is not as stable as NiO_x films deposited by PLD and solution process. The work-function of the RF-sputtered NiO_x films, as measured using Kelvin probe, decay with time constant on the order of tens of minutes to a stable value of roughly 4.8 eV when stored in N_2 environment. Oxygen plasma treatment of the films increases the work-function, but does not restore the as-deposited work-function (Table 5.1). For comparison, the work-function of the PEDOT:PSS control films were measured to be 4.8 eV by Kelvin probe, a value that is within the reported range of 4.7 - 5.4 eV [163].

The energetic alignments between the NiO_x film and the active layer blends were determined

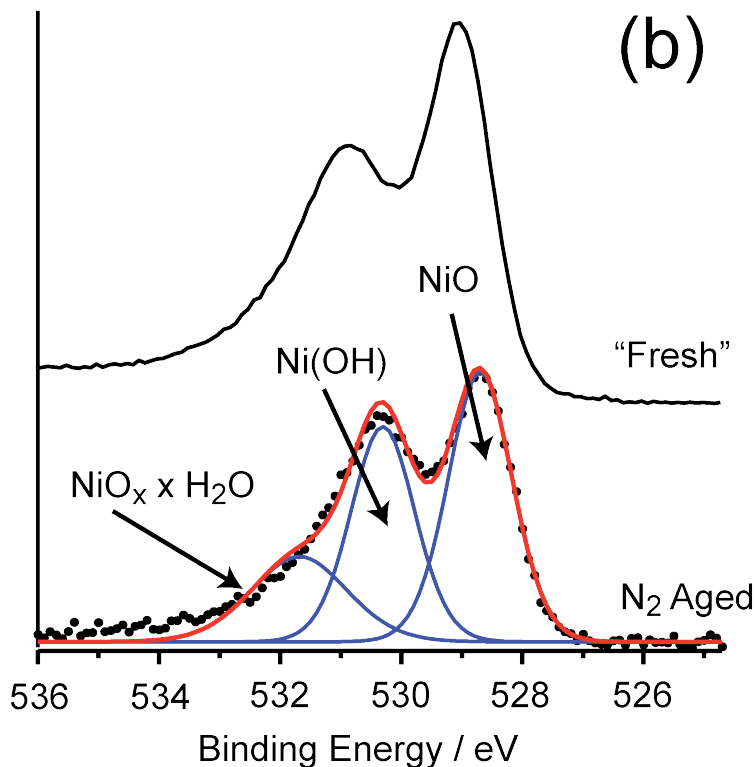
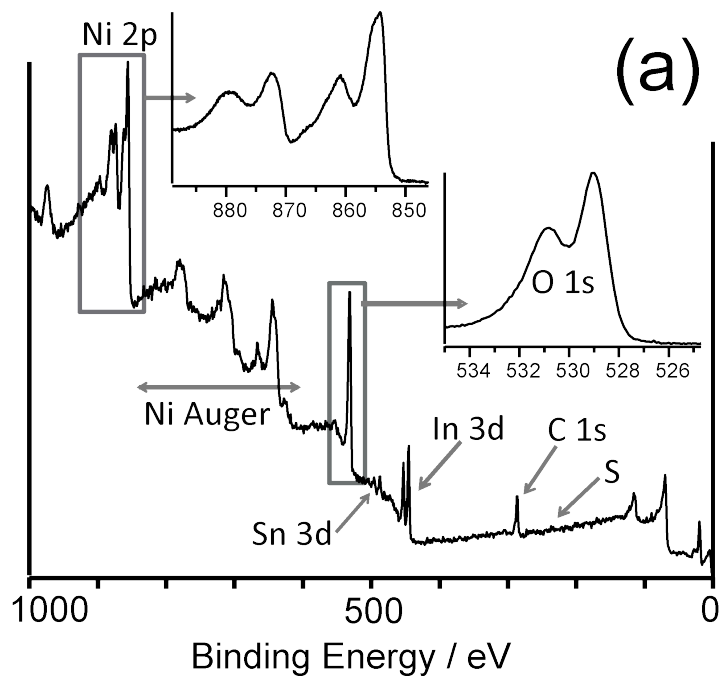


Figure 5.3: (a) XPS survey data of a sputtered NiO_x film, showing peaks from the various elements. (b) Comparison of the O 1s peaks of the different NiO_x films, showing the presence of Ni(OH) and hydrous oxides at different amounts. The “fresh” sample has been briefly exposed to air during sample transport.

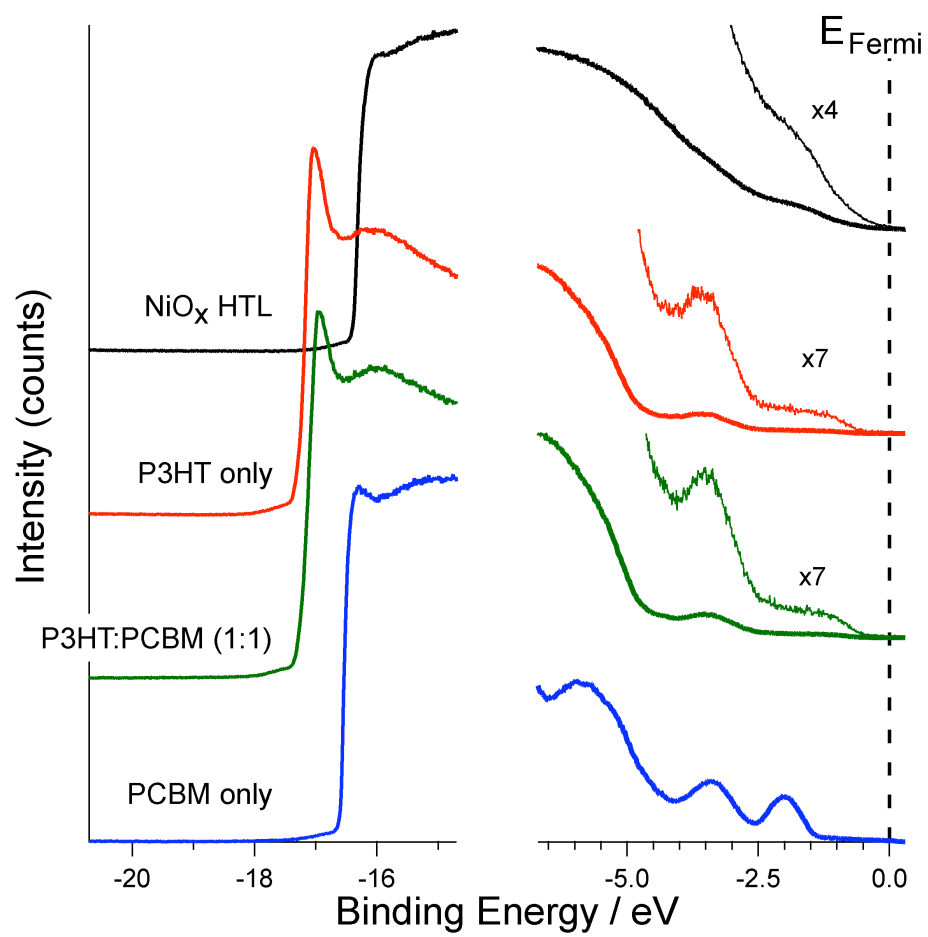


Figure 5.4: UPS data on different blends of P3HT:PCBM on NiO_x HTL.

using UPS for different blend ratios, analogous to a previous study performed by Xu **et al.** The results were found to be in agreement with previous reports, with the migration of the P3HT layer to the top of the blend, as indicated by the presence of the density of states nearest the Fermi level being P3HT-like in character. The result for blend ratios 1:0, 1:1, and 0:1 are shown in Fig. 5.4.

The onset of the density of states at ~ 1.0 eV below the Fermi level is associated with the sp^2 hybridization of the polymer and has found to vary with the oxidation state of the polymer [189]. No change in polymer oxidation state was observed upon formation of the NiO_x - P3HT interface. Given that the P3HT film measured was thicker than 5 nm and UPS measurements are consistent with the top two nanometers of the film, the energetics close to, but not at, the interface are consistent with bulk P3HT.

In the 1:1 blend of the P3HT:PCBM, the film is determined to be predominantly P3HT-like. P3HT-like character, even at high fullerene to polymer ratios, is consistent with previous reports of migration of the polymer to the top of the blend [270]. The second feature of the pure P3HT film at ~ 3.5 eV from the Fermi level also decreases in binding energy, becoming more fullerene-like with increasing fullerene concentration. Again, this is consistent with the report that the HOMO of the blend is dominated by that of P3HT [82].

For the pure PCBM on NiO_x , a Schottky-like interface was observed, with the work function of the PCBM found to be slightly different from that of the NiO_x substrate. This suggests a favorable formation of electron barrier at the interface. However, unlike the results previously reported by Xu **et al.**, a small shift in the vacuum level was observed for the pure PCBM film on the NiO_x , consistent with the change in the surface dipole upon addition of the organic fullerene to the oxide film.

Hence, these results indicate that while this vacuum level shift does occur upon formation of the oxide/blend interface, the energetics of the blend are not directly impacted and are consistent with previous results for P3HT:PCBM energetic alignment. In particular, the effective gap of the active layer at this interface: $E_{gap} = LUMO_{acceptor} - HOMO_{donor} \approx 1.4eV$ is similar to the previously reported bulk values [82]. This indicates that any change in device open circuit voltage

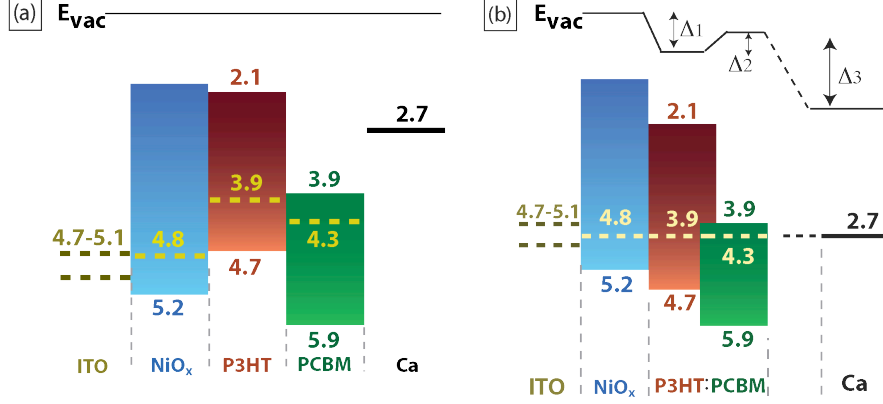


Figure 5.5: The energy level alignments of the OPV layers used in this study: (a) before equilibration (Vacuum level aligned), and (b) after equilibration (Fermi level aligned) showing vacuum level shifts. The valence bands (LUMO) levels are taken from Ref. [82]

(V_{oc}) is not due to direct modification of the effective gap of the active layer due to the HTL.

The most efficient device ($\text{Ar}:\text{O}_2 = 1:45$, fresh film) has $\eta = 3.84 \pm 0.03\%$ as compared to $\eta = 3.69 \pm 0.12\%$ of the PEDOT:PSS control device. Although the PEDOT:PSS device has higher V_{oc} and shunt resistance (R_{shunt}), our best sputtered NiO_x-employing device has superior current extraction and sharper diode turn-on, i.e. fill-factor, leading to higher device performance (Fig. 7.10). The trends in V_{oc} correlate well with the trend in short circuit current (j_{sc}) and active layer thicknesses, with the exception for the last data set where the correlation with active layer thicknesses is not as clear.

To explain the trend in the data, we first note that the potential between the contacts is approximately equal to the difference of their stand-alone work-functions ($\sim 2.0eV$), modified by interfacial dipoles that form when the various layers are brought into contact together. For active layer thicknesses of $\sim 100nm$ under normal operating bias of $\sim 1V$ this corresponds to an electric field of the order of 10^7Vm^{-1} . This, combined with relatively high carrier mobilities ($\sim 10^{-8}m^2V^{-1}s^{-1}$) and lifetimes ($\sim 10^{-3}s$) in both P3HT and PCBM [35, 101, 66], leads to long carrier drift lengths of $\sim 100\mu m$. It is therefore reasonable to postulate that almost all photo-generated carriers are extracted in all of our samples ($t_{BHJ} \sim 300nm$). Thus, the thicker the

active layer, the more carrier being generated, explaining the proportionality of j_{sc} and active layer thicknesses.

We also note that none of our V_{oc} comes close to the theoretical limit of $\sim 1.4eV$ as defined by the effective gap of the active layer. In this regime, V_{oc} is expected to be proportional to j_{sc} , consistent with our data:

$$V_{oc} \approx \frac{nkT}{e} \text{Ln} \left(\frac{j_{sc}}{j_0} \right) \quad (5.1)$$

where n is the diode ideality factor, k_B is the Boltzmann constant, T is temperature in Kelvin, e is the unit charge, and j_0 is the diode saturation current. Since the active layer is solution deposited from the same stock solution, the differences in thicknesses must be the result of different surface properties of the NiO_x films alone. Nevertheless, investigations on how the surface properties of the HTL influence BHJ thickness and morphology is beyond the scope of this chapter.

Lastly, it is worthwhile to note the lack of correlation between V_{oc} of the devices and the work-function of the HTL. Although this is in contrast to popular postulate that the two are correlated, it is actually consistent with the energy alignment determined from UPS. The reason for this apparent discrepancy is that our energy level alignment is such that no hole barrier is formed between the HTL and the active layer; hence no extra energy is expended in passing through the interface. Such Fermi level alignment of P3HT by an underlying substrate of deeper work-function has also been previously reported [270, 20].

5.3 Summary

We investigated RF sputtered NiO_x HTLs in P3HT:PCBM BHJ devices. Work-function of the oxide layer changes within a range of ~ 0.7 eV by varying the Ar: O_2 ratio during deposition. The ability to tune the work-function is crucial if one is considering use of NiO_x with other donor-acceptor materials with different energy levels. Unfortunately, we note that the work-function of the NiO_x thin film decays in N_2 atmosphere with a time constant in the order of tens of minutes to a common value of 4.8 eV regardless of the different as-deposited values. Oxygen plasma treatment

of the films increases the work-function of the aged films, but not to the initial work-function value.

Our best as-sputtered NiO_x device efficiency is $3.84 \pm 0.03\%$, better than that of our PEDOT:PSS control ($3.69 \pm 0.12\%$). Energetic alignment of the active layer on NiO_x was done using UPS, the result of which is consistent with previous reports. Additionally, the UPS data also suggests the formation of a favorable electron injection barrier between NiO_x and PCBM, and the absence of hole barrier with P3HT. The trends in j_{sc} stem from the differences in active layer thicknesses, which led to differences in photo-generated carriers. Differences in V_{oc} can similarly be related to differences in j_{sc} ¹.

From this study, we were convinced that the WF rule alone is not sufficient to yield a good HTL. We have also encountered a case where O_2 plasma treatment did not lead to an improved device performance. A more thorough investigation is therefore necessary. Lastly, we also learnt that photogeneration rate in the BHJ must be the same to be able to make a fair comparison across all samples. In retrospect, this can be likened to making sure that we are sourcing the same voltage when measuring a non-illuminated device.

We realized that the WF rule mostly stems from the works on metal / organic injecting interface in organic light emitting diodes (OLED) [48, 49, 47], in which case there is only a single salient level in the contact material, namely its E_F . The PEDOT:PSS that has been the de-facto HTL for OPV and OLED applications are very highly-doped [103] that its electronic properties are probably better approximated as a metal-like material than a non-degenerate semiconductor.

In contrast, the NiO_x employed here are expected to be non-degenerately doped. Therefore, its electronic properties must be described by 3 levels: E_F , E_v , and E_c . As a result, a complete investigation must involve not only UPS to get E_F and E_v of the material, but also *IPES* in order to get E_c . Lastly, we also need to know the final energy level alignment at the interface after contact.

¹ We note that the data presented here is not complete enough to be revisited under the light of the new analysis presented in §7.

Chapter 6

The Impact of Substrate Surface Properties on the Morphology of Polymer-Fullerene Bulk Heterojunction

Although our primary interest is the study of band alignment at the NiO_x / BHJ interface, our study on sputtered NiO_x revealed that the properties of the BHJ might be affected by the surface properties of the NiO_x. A careful study must include investigation on the morphology of the BHJ. This is because during device fabrication, the BHJ is spin-coated on the oxide. Film formation in spin-coating is affected by substrate properties and evaporation kinetics of the solvent [243, 84]. Since morphology of the BHJ impacts device performance, we have to be able to (1) show that the changes we engineer in the NiO_x energy levels do not indirectly impact the BHJ morphology in any significant way, or (2) if any BHJ morphology change occurs, we have to be able to deconvolve the contributions of the NiO properties from that of the BHJ morphology.

The umbrella term morphology in BHJ films can be categorized into: vertical and lateral phase segregation of the mixture and degree of structural / crystallographic disorders in the film. The latter can be further differentiated into long-range (inter-crystallite), medium-range (inter-diffracting planes), and short-range (intra-diffracting planes) disorders, and film texture [140]. In this study, we are going to assess two aspects: the vertical phase segregation and the crystallographic ordering. We assume that the film is quasi-homogenous in the lateral direction.

6.1 Vertical Phase Segregation of P3HT:PCBM

During design phase, the BHJ has been modeled as either a bilayer or a quasi-homogenous layer. Modeling the BHJ as a bilayer has been shown to be erroneous [244]. Modeling the BHJ layer as quasi-homogenous layer is an alternative because similarities with the concept of band-tails and Shockley-Read-Hall recombination is more readily made [244, 116]. Consequentially, this perspective is gaining wide acceptance in the community [50].

However, reports have indicated that vertical phase segregation of P3HT and PCBM may be precipitated at the interface with the substrate [270, 68, 135]. In these reports, top surface of the film is also reported to be extremely P3HT-rich, constituting a deviation from the assumption of a quasi-homogenous film, quasi-isotropic. We've observed this P3HT-rich top surface in the previous study on sputtered NiO_x HTL. Depending on the severity, vertical phase segregation has also been shown to affect device performance, both adversely and positively, and therefore is of direct interest [68, 271, 32].

Assessment of vertical phase segregation can be done by XPS combined with depth-profiling by sputtering or with film lift-off [68, 82], neutron-scattering [68], TEM and electron tomography [250, 138], or cross-sectional AFM [135]. XPS coupled with sputtering is the most straight-forward and available among all of the reported techniques. In XPS, sulphur signal is used as tags for P3HT, while the rest of the carbonaceous material is assumed to be composed of PCBM. Depth-profiling is facilitated by Ar-sputtering of the film. However, Ar-sputtering may result in unintended chemical mixing or preferential sputtering of sulphur. Film lift-off can only be done on unannealed film, and only provide an additional measurement of the buried interface. Neutron scattering experiment provides an excellent contrast between PCBM and P3HT but requires special sample preparations. In particular, to assess the buried interface it requires special substrate, which is incompatible with the goal of our experiment. Likewise, cross-sectional AFM requires sample cleaving and measurement at cryo-temperature, and has only been reported once. Here we investigate the degree of vertical phase segregation in the film by XPS combined with Ar-sputtering.

6.1.1 Assessing Vertical Phase Segregation by Depth-Profile XPS

The device architecture employed here is the same as before and is shown in Fig. 6.1a. Of course, the top metal contact is omitted in this study. In order to address the concerns about preferential sputtering and degradation due to X-ray exposure, two calibration runs involving pure P3HT film were done. In the first test, the sample is continuously exposed to X-ray while continually measure XPS spectra on the same spot. The result, shown in Fig. 6.1b, indicates that no significant degradation is incurred by prolonged X-ray exposure. Further, from this run, we also obtain a calibration signal for a pure P3HT film. Compared to the theoretical prediction, our “pure” P3HT film experimentally returns an apparent 90% P3HT by weight. This discrepancy is most probably related to differences in the details of reagent synthesis and sample preparations. In the second test, the neat P3HT film is depth-profiled by Ar-sputtering and its composition analyzed by XPS to assess the degree of sputter mixing (6.1b). The small reduction in apparent P3HT concentration, about 20% total, is an indication for sputtering damage / mixing.

Also shown in Fig. 6.1b is the vertical P3HT concentration profile of the actual P3HT:PCBM BHJ samples. While the calibration data displayed are raw data, data for the samples are already normalized with respect to the P3HT depth-profile calibration to take into account the impact of sputter mixing. The surfaces of our BHJ films are covered in almost pure, phase-segregated P3HT, consistent with previous reports employing similar sample preparation techniques [270, 68, 135]. As we sputter deeper into the film, P3HT concentration rapidly drops, to below 50% (dot-dash line), giving rise to a presumably more PCBM-rich region near the buried interface. This has also been reported [243, 271, 68].

6.1.2 Understanding the Physical Origin of Vertical Phase Segregation by 2-Component Surface Energy Measurement and XPS

Surface energy obtained via contact angle measurement has been shown to be correlated with the degree of phase segregation in organic materials, including P3HT:PCBM [88, 68, 271]. PCBM-

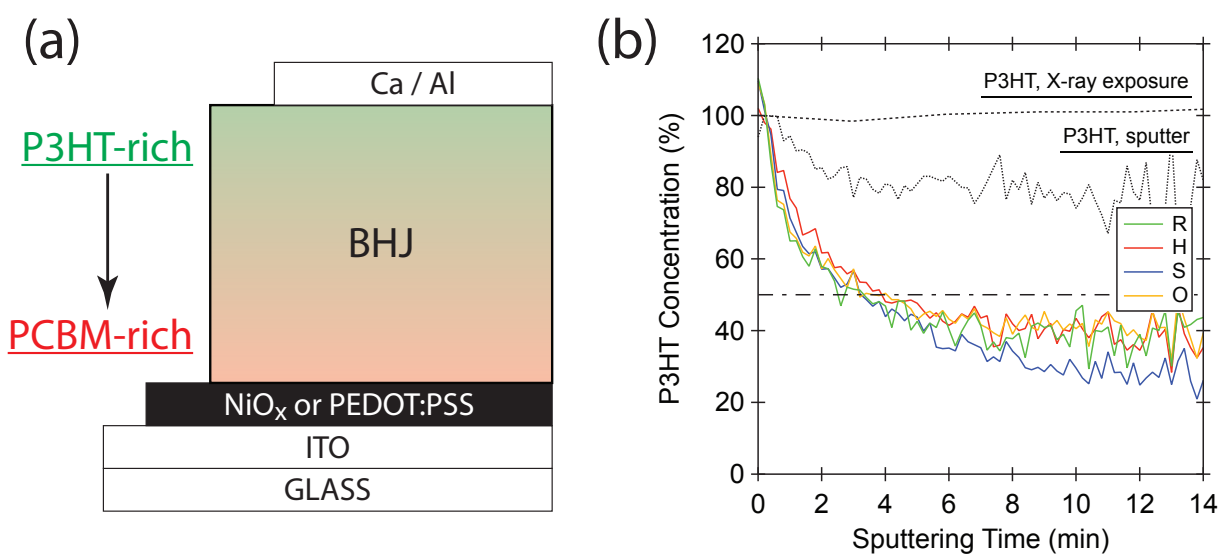


Figure 6.1: (a) Device structure. (b) P3HT concentration as a function of argon sputtering time, suggesting vertical phase segregation of the BHJ. Calibration data are displayed as-is, while sample data are normalized to the P3HT sputter calibration. Dot-dash line marks 50% P3HT by weight.

rich interface is commonly related to the high surface energy of the substrates surface. However, most of the reports perceive this result from an empirical point of view and little has been done to elucidate the physical mechanism. We suggest using the concept of surface polarity as a way to understand the physics that's being involved.

Surface polarity (hydrophobicity / hydrophilicity) is a familiar concept that has been successfully used to explain surface wettability and interfacial formation. Polarity is defined as the fraction of polar surface energy of the total surface energy:

$$Polarity = \frac{\gamma^p}{\gamma^p + \gamma^{np}} \times 100\% \quad (6.1)$$

where γ is the component of the surface energy, with superscripts indicating polar or non-polar. Materials with similar polarity tend to form a robust interface, while those with different polarity tend to phase separate. The underlying physics is that the enthalpy of interface formation, $\Delta G_{1,2}$, of materials 1 and 2 can be approximated from the components of the surface energies using the well-known Goussier equation [73, 75]:

$$\Delta G_{1,2} = -2 \left(\sqrt{\gamma_1^{np} \times \gamma_2^{np}} + \sqrt{\gamma_1^p \times \gamma_2^p} \right) \quad (6.2)$$

from which it is apparent that an interface is more favorably formed when (1) the surface energies of the two initial surfaces are high, and (2) the two surfaces have similar polarity. A reasoning based on interactions among chemical sites at the interface have also been explored and largely agree with the thermodynamical description [17].

The polarity of the substrate can be estimated from a 2-component (polar/non-polar) contact angle measurement, where contact angles of two or more liquids of known surface tension and polarity are measured on the sample surface. The components of the surface energy can then be calculated from simultaneously solving the Owens-Wendt equation with contact angles from the different liquids [176]:

$$\sqrt{\gamma_s^{np} \times \gamma_l^{np}} + \sqrt{\gamma_s^p \times \gamma_l^p} = \gamma_l^{tot} \frac{\cos \theta + 1}{2} \quad (6.3)$$

where the subscripts l and s refer to the probe liquid and the solid surface. The calculated surface energies from contact angle measurement for the surfaces of interest are summarized in Table 6.1.

Table 6.1: Polar and non-polar components of surface energies of the substrates and organics as calculated from contact angle measurement results.

Sample	O ₂ plasma	γ^p (mJ/m ²)	γ^{np} (mJ/m ²)	γ^{tot} (mJ/m ²)	Polarity (%)
H	as-dep	43.0	26.3	69.3	62.0
	treated	46.3	26.4	72.7	63.7
R	as-dep	43.7	26.7	70.3	62.1
	treated	46.3	26.4	72.7	63.7
S	as-dep	38.6	26.6	65.1	59.2
O	treated	45.8	26.6	72.3	63.3
P	N/A	30.6	42.3	72.88	42.0
P3HT	N/A	0.136	20.2	20.3	0.670
PCBM	N/A	8.68	18.7	27.4	31.7

The values for as-deposited PLD NiO_x films are also included in the table for completeness. Data for PEDOT:PSS is obtained from the literature [182] since we were unable to measure a reliable contact angle.

The surface energies of all substrates are very similar and polar regardless of the different processing methods, including O₂ plasma treatment. A difference within 5 mJ/m² is typically taken as not significant. Sample S, however, is the only one with significantly lower surface energy, mainly due to its lower polar component. In contrast to the oxides, both organic film surfaces, especially that of P3HT film, have low surface energy and is largely non-polar. PEDOT:PSS has very similar surface energy with the NiO_x films, but with much lower polarity.

Surface energy measures how favorable it is to form a surface. Therefore, the starkly P3HT-rich top surface is readily explained by P3HT having a lower total surface energy than PCBM. Unlike the case of a free surface (vacuum / material interface), surface polarities need to be taken into account when considering an (material / material) interface via the Goods equation (Eqn. 6.2). Comparing the polarities of the different materials (Table 6.1), we conclude that PCBM is more favorably deposited on the oxide surfaces than P3HT due to their more similar polarity / hydrophilicity, leading to a PCBM-rich interface. The report that PEDOT:PSS / P3HT:PCBM interface is only slightly PCBM-rich [68] is also consistent with this hypothesis since PEDOT:PSS

is much less polar than any of the NiO_x. Note that this is despite the total surface energy of PEDOT:PSS and NiO_x being almost identical, highlighting the improvement that 2-component contact angle measurement offers. The same can be said for the slightly lower P3HT concentration near the interface with sample S.

Although the surface energy is useful for understanding the physics of vertical phase segregation, in order to be directly relevant to the technological application, we also need to understand the physical mechanism that leads to these differences in surface energy. The non-polar surface of P3HT is readily explained by the tendency of P3HT to form lamellar structures with alkyl chains directed perpendicular to the substrate (Fig. 6.5a). In this configuration, we expect the top surface to be rich in the hydrophobic alkyl groups, leading to its non-polar nature. Similarly, from the symmetry of the system, we expect that the oxide / organic interface is also rich in alkyl chains. This has been shown to be the case for films grown on Si [55, 109].

AFM images of the substrates are shown in Fig. 6.2, where it can be seen that there is negligible differences among the NiO_x surface topologies, which mostly inherit the surface structure of the underlying ITO. In contrast, PEDOT:PSS surface is much smoother due to its thickness (last sub-figure). However, no obvious correlation exists between these trends in surface structures and the surface energy data.

On the other hand, our combined XPS and XRD data (Fig. 6.3 and 6.4) suggest that the differences in the surface energies of these films stem mostly from differences in the film surface composition. XPS O1s spectra of the PLD NiO_x are shown in Fig. 6.3a, while the data for samples S and O are already published elsewhere [190]. The data is composed of two overlapping peaks. Peak P1 at 529.5 eV of the O1s spectra has been related to stoichiometric NiO, confirming the presence of NiO in all films [190, 23, 165]. The shift of this peak to lower binding energy upon oxygen plasma cleaning indicates the formation of unstable non-stoichiometric surface species, consistent with the observation that the advantageous properties induced by the plasma treatment (improved wetting, increased work-function, etc.) is temporary [232, 20].

We reported earlier that O₂ plasma cleaning of the solution-processed NiO_x films (sample S)

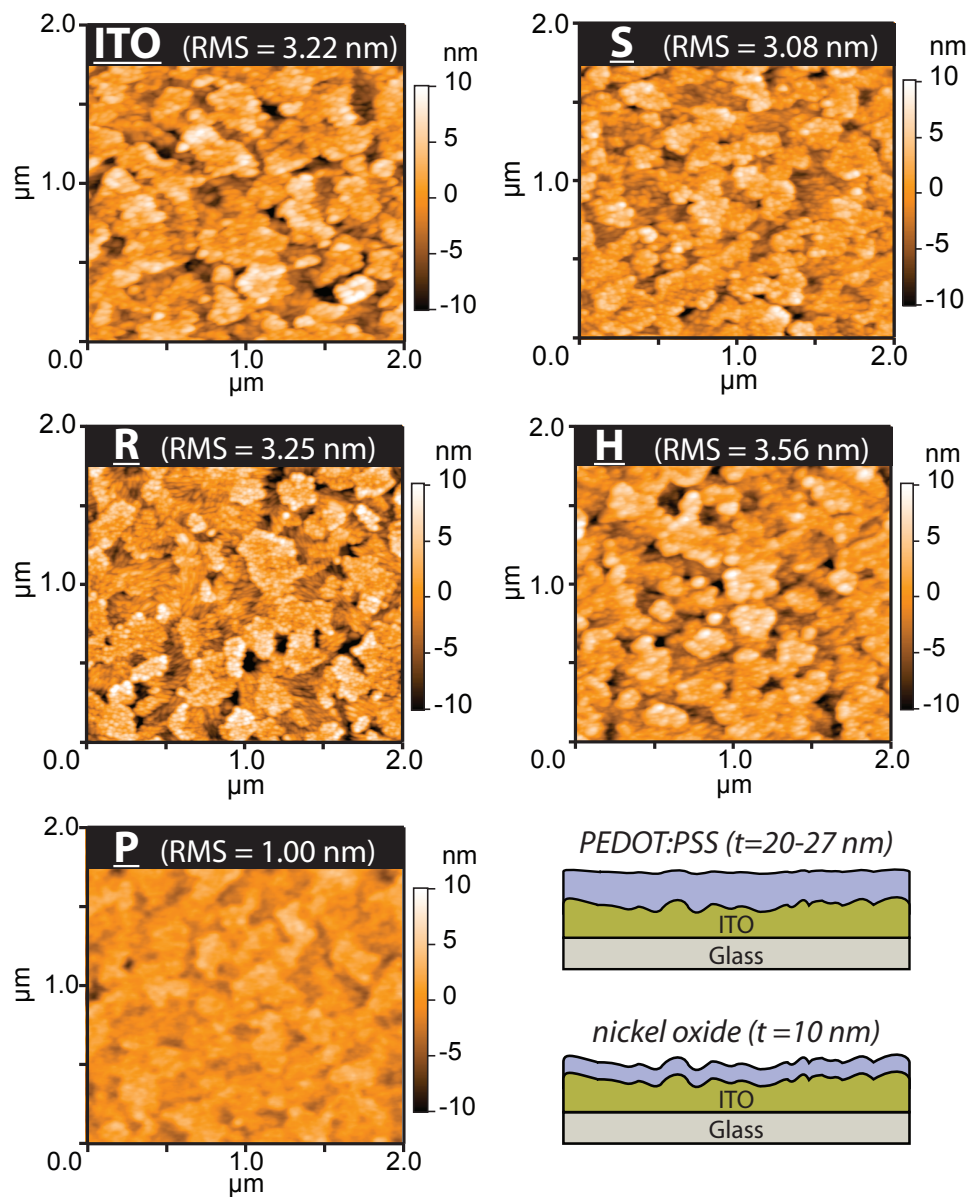


Figure 6.2: AFM images of nickel oxide (S, R, H) and PEDOT:PSS (P) substrates, all deposited on ITO. PEDOT:PSS surface roughness is lower due to its thickness.

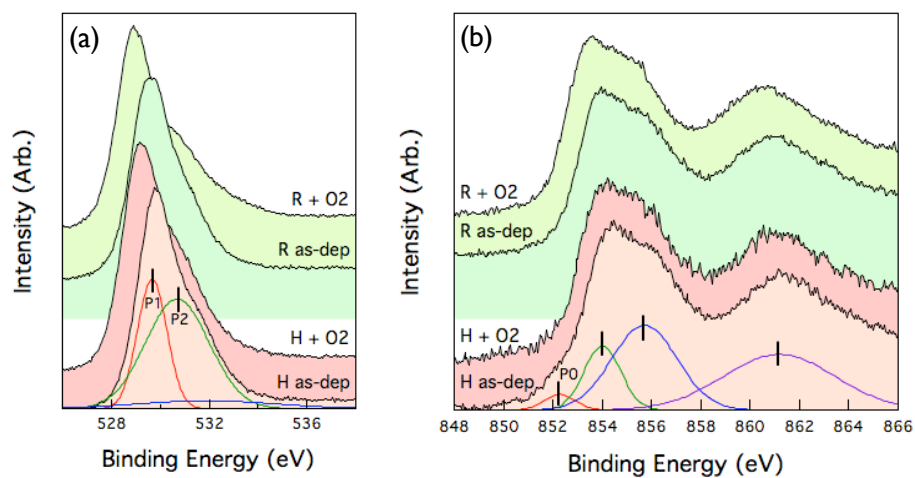


Figure 6.3: XPS (a) O1s and (b) Ni2p of the nickel oxide substrates, indicating the P0, P1, and P2 peaks. Spectra are offset for clarity.

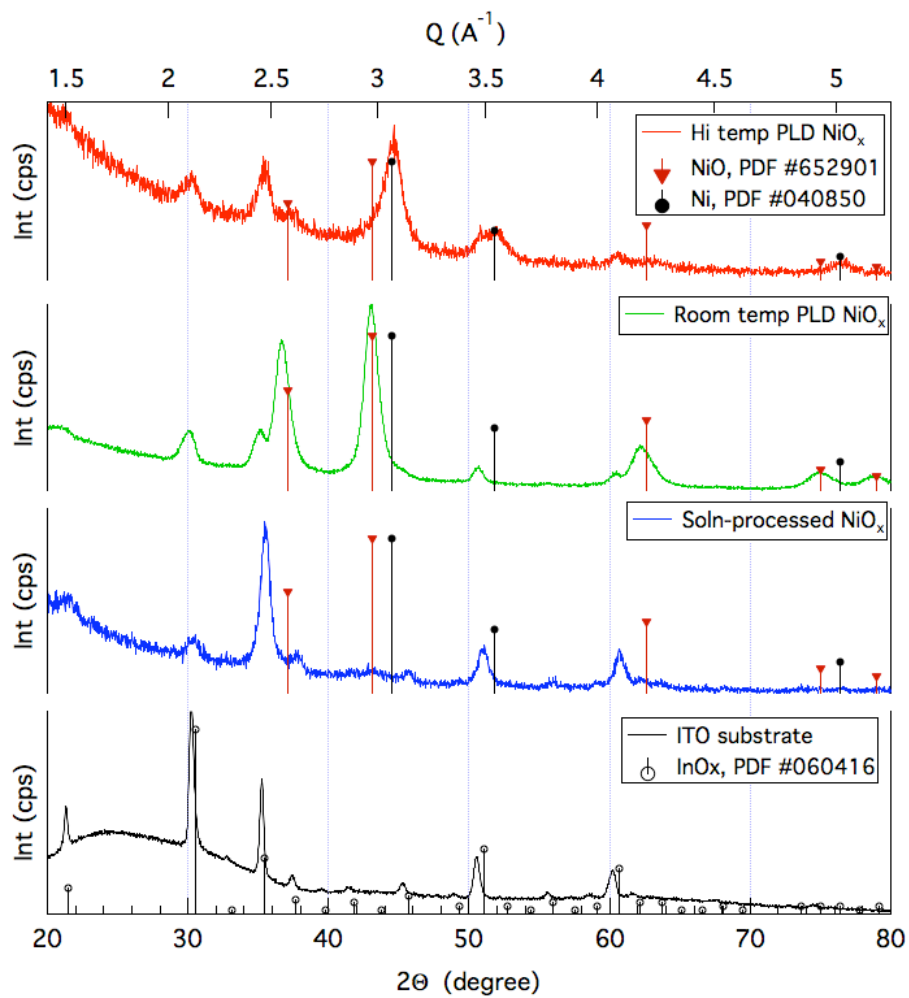


Figure 6.4: GIXD of the nickel oxide substrates. Also shown is the $\theta - 2\theta$ XRD of ITO for comparison.

result in an increase of surface hydroxyls [191], and the increase in contribution of Peak P2 at ca. 531.0 eV. In contrast, we observe in samples H and R that peak P2 does not significantly change upon plasma treatment. This trend correlates with the surface energy and polarity data (Table 6.1).

An earlier study by Langell and Nassir [132] provide us with a possible physical explanation. They have shown evidence that a sub-monolayer of surface hydroxyls adsorbed from ambient atmosphere passivates the thermodynamically unstable polar NiO(111) surfaces. NiO crystals have a mostly-rocksalt crystal structure [198], leading to its (111) facets being either fully oxygen- or nickel-terminated, and give rise to a highly polar but catalytic surface [274]. In contrast, the electrostatic interactions among the nickel and oxygen ions on the (100) facets are effectively balanced due to their inter-digitated arrangement. Therefore, the hydroxyl-rich surface may be an indication of largely NiO(111)-terminated surface.

To examine if this is the case, we performed grazing incidence XRD on the NiOx samples. GIXD (Fig. 6.4) reveals that the structure of NiO in these films differs from sample to sample. Sample R is evidently composed of polycrystalline NiO, while sample S and O lacks any sign of crystallinity. The lack of NiO XRD signal does not signify the absence of NiOx, as this has been confirmed by XPS. Rather, this signals that the NiO phase lacks any crystalline structure. Any possibility of samples S and O to be highly textured is ruled out because of the polycrystalline ITO substrates. Therefore, since our samples are either polycrystalline or amorphous, the film surfaces unavoidably contain a fraction of NiO(111) facets, possibly contributing to the high surface polarity.

Lastly, GIXD data for sample H only shows a weak NiO peak at $2\theta = 37^\circ, Q = 2.7\text{\AA}^{-1}$. Instead, the data is dominated by reflections from metallic Ni crystallites. The presence of metallic Ni is corroborated by the presence of an additional small peak at 852.3 eV in the XPS Ni 2p data (P0 in Fig. 6.3b). XPS peak P0 vanishes after O₂ plasma treatment of the sample; however, we found no change in XRD data from all samples after O₂-plasma treatment, including that of sample H, suggesting that the O₂-plasma treatment only alters the topmost surface of the film.

The results so far highlight that surface polarity of the substrate is better correlated with

the PCBM-rich interface. Although the high surface energies of the substrates correctly predict the PCBM-rich interface, the different degree of PCBM-richness of the interface is not able explicable without taking into account the different surface polarity. Variations in the crystal structure and composition of the NiO_x and PEDOT:PSS films may contribute to this quantity. This study shows that surface roughness of the substrates do not significantly impact its surface energy components. However, we expect that this is not universally true [22, 128].

6.2 Crystallographic Order and Texture

In addition to the composition gradient, BHJ film crystal structure may also be affected by the surface properties of the NiO. Medium and long range orders in the samples, encompassing inter-crystallite and inter-lamellar (inter-diffracting planes) orders are quantified using analysis of X-ray diffraction patterns. For completeness, in addition to the usual $\theta/2\theta$ specular XRD data, a pole-figure is obtained from patching two 2D-GIXD data with a rocking curve data done in specular geometry [12]. Qualitative analysis of organic materials using synchrotron-based 2D XRD is already widespread (Fig. 6.5). However, the analysis in this study looks beyond qualitative analysis, and aimed to actually **quantitatively** measure the texture, degree of crystallinity, and different kind of disorders in the materials.

The techniques employed here have been developed and discussed in the literature [12, 107, 109, 196, 195], and is briefly discussed in §3. The first part of the experiment consists of patching pole-figures from 2D GIXD data, 2D specular XRD data, and high-resolution rocking curves. This contain information about film textures and degree of crystallinity (amount of crystallites in the film) (Fig. 6.5d). We then fit the pole figure data with a Voigt function and extract its FWHM, which quantify the degree of texture in the film, and the area under the curve, which reflects the amount of crystallites in the film. The second part involves analyzing a high-resolution $\theta/2\theta$ data in order to gain insights on the nature of the crystallographic disorders in the film (Fig. 6.5c). The location of the peak is directly related to the inter-lamellar spacing of P3HT, while its FWHM measures the correlation lengths of the crystallites.

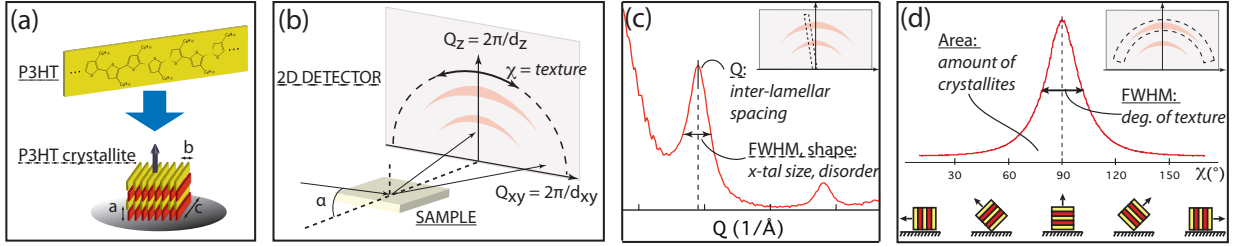


Figure 6.5: Illustration of the XRD data processing: (a) P3HT and its crystallite, (b) measurement geometry and principal axes, (c) specular Q -scan, equivalent to $\theta/2\theta$, (d) X -scan. Note that instead of taking a slice of the 2D scan, we took a high-resolution $\theta/2\theta$ scan

As we shall discuss in more details, the data (Fig. 6.6) collectively indicate that film morphologies are essentially the same at film thickness $> 20 \text{ nm}$, but is slightly different near the interlayer-BHJ interface. Since any structural disorder may alter the density of electronic states near the conduction / valence levels, substrate-induced structural differences may modify the conduction properties of the organics near the interface. Such modification will undoubtedly be important in any opto-electronic devices, especially those that employ ultra-thin film ($t < 50 \text{ nm}$) technologies.

Fig. 6.6a-6.6e show the trends in the various fit results to the XRD data as a function of film thickness as measured using AFM (t_{AFM}). Large scatters and error bars at low thicknesses are due to lower signal-to-noise and to larger uncertainty in the thickness measurements as we approach thicknesses close to substrate roughness (Fig. 6.2).

The amount of P3HT crystallites in the film is proportional to the weighted area under the pole figure:

$$I_{int} = \int_0^\pi I_{PF}(\chi) \times \sin(\chi) d\chi \quad (6.4)$$

where I_{int} is the weighted area, I_{PF} is the measured intensity of the pole figure, and χ is the crystallite orientation with 90° corresponding to the lamellae facing perpendicular to the substrate. In an ideal condition, we expect I_{int} to be linear in thickness. However, as shown in Fig. 6.6a, $I_{int} \propto t^{1.23}$. The supralinearity may be related to the fact that PCBM is more favorably deposited

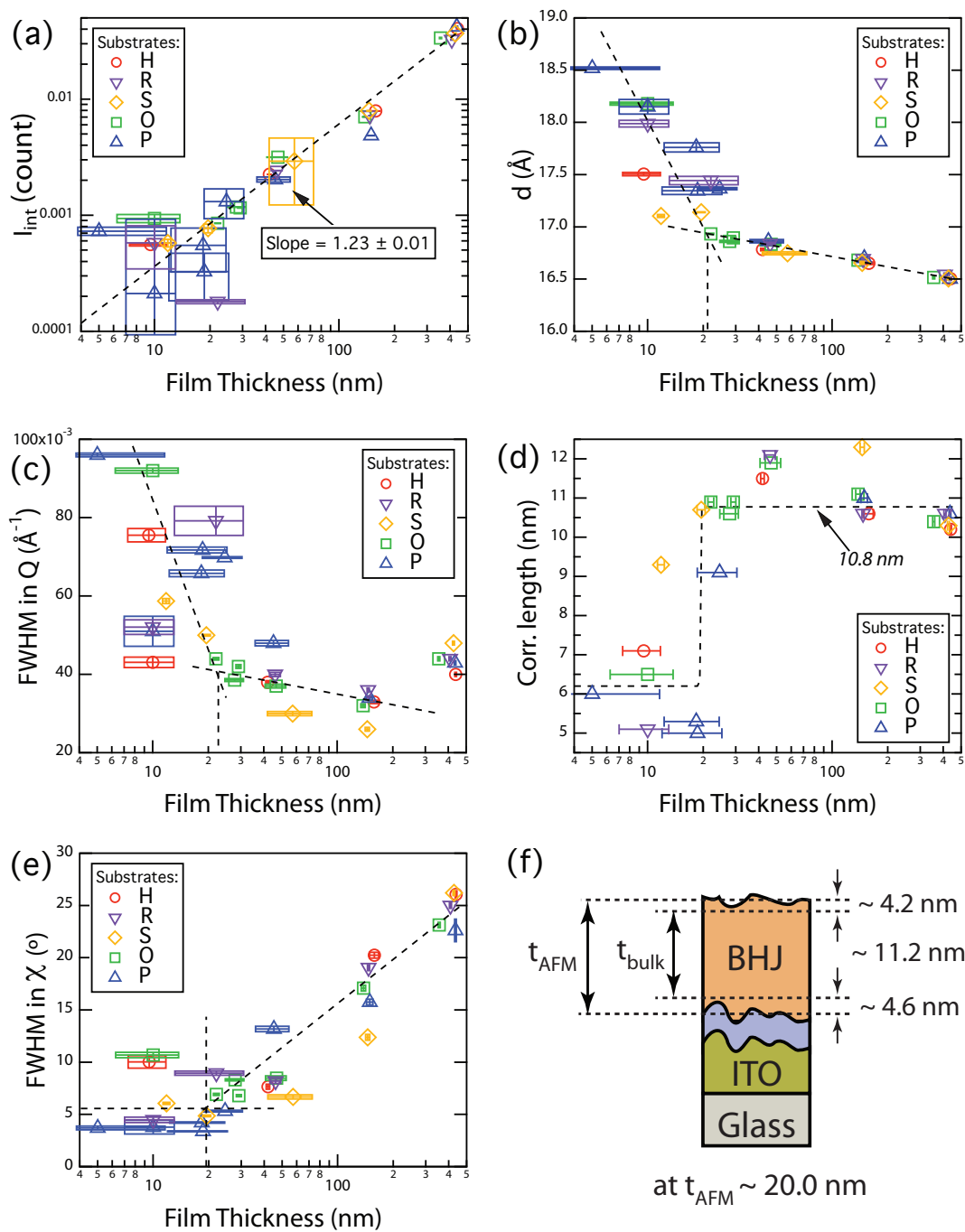


Figure 6.6: Fit results of the XRD data as a function of film thickness for P3HT:PCBM deposited on different NiO_x HTL. See text for details.

on the oxide.

The presence of PCBM-rich interface will also possibly disrupt the crystallinity of P3HT near the oxide interface and can be used to test this hypothesis. In polymeric systems, high inter-lamellar spacing is an indicator of a high degree of disorder in the film. This can be obtained from the position of the XRD peak in Q-space by the relation:

$$Q = \frac{2\pi}{d} \quad (6.5)$$

where d is the lattice spacing, which in the case of P3HT [100] reflections correspond to the inter-lamellar spacing.

d is found to be around 18.5 Å at extremely low film thicknesses (Fig. 6.6b), much higher than the reported value in the bulk pristine film of 16-17 Å, a sign of high degree of disorder. This is further confirmed by high Q-FWHM value at low thicknesses (Fig. 6.6c) which is inversely related to disorder in the film and crystallite size. Furthermore, as film thickness increases, d rapidly decreases to ~ 17 Å at $t \sim 20$ nm and decreases much more slowly at higher film thicknesses. Likewise, Q-FWHM follows a similar trend, except for the tendency to increase in the thickest films.

When multiple harmonics of the XRD peaks are separable from the background, Warren-Averbach analysis can be employed to gain insight on the nature of the observed disorder in the film. In particular, crystallite size distribution can be separated from paracrystallinity and strain [140, 196, 256, 53]. In this experiment, only the main peak is clearly separable from the background due to our extremely thin samples. However, a Warren-Averbach analysis is still informative with a caveat that the extracted correlation lengths are, strictly speaking, not crystallite sizes (only when analysis is done on multiple peaks, does correlation length equal crystallite size).

The extracted correlation lengths from Warren-Averbach analysis are shown in Fig. 6.6d. Correlation lengths tend to be low at $t < 20$ nm and rapidly increases to a relatively constant value of ~ 11 nm around $t = 20$ nm. The asymptotic value in crystallite size at higher film thickness has been observed in neat P3HT films grown on surface-treated Si [55, 107]. The full crystallite size was

found to be 10 nm, which is close to the value we extracted. In the above-mentioned references, the film thickness at which the full crystallite size is reached is equal to the actual asymptotic value of the crystallite size, leading to the conclusion that ultra-thin film results in spatial confinement on film growth. Physically, this film thickness is similar to the critical thickness for crystal growth in vacuum deposition. In contrast, in our case the full correlation length (~ 11 nm) does not equal the critical film thickness (~ 20 nm). We believe that this difference is because, unlike in the previous studies, the oxide substrates employed has a non-negligible surface roughness (Fig. 6.2). To test this hypothesis, we subtracted, from the critical film thickness of 20 nm, the oxide roughness amplitude of 4.6 nm (RMS = 3.3 nm) and the top surface amplitude of 4.2 nm (RMS = 3.0 nm) and arrive at film thickness that is free of surface roughness $t_{bulk} \sim 11.2$ nm, consistent with the measured correlation length (see Fig. 6.6f). Therefore, we conclude that the apparent disorder in the thinnest films is related to small crystallite size due to spatial constraint of crystal growth and possibly the high density of PCBM near the interface.

Determination of dominant disorder types via Warren-Averbach analysis are not possible with only a single peak. Therefore, we resort to using the Voigt curve shape analysis to semi-quantitatively examine the trends [196]. In this method, the peak is fit with a pseudo-Voigt function as a function of Q. The mixing parameter is thus a measure of how Lorentzian or Gaussian the peak is (Fig. 6.7). It can be shown that size and paracrystallinity disorder will lead to a Lorentzian shape ($\eta \rightarrow 1$), while micro-stress will lead to a Gaussian shape ($\eta \rightarrow 0$). The data, shown in Fig. 6.7, suggests that micro-stress dominates disorder at lower film thickness, while paracrystallinity / crystallite size is dominant at thicker samples.

In terms of film texture, the P3HT [100] reflection, which corresponds to diffraction from the lamella (Fig. 6.5), is found to always peak at $\chi = 90^\circ$ corresponding to lamella oriented parallel to the substrate, consistent with previous reports. The trend in full-width at χ -FWHM which reflects the degree of texture in the film is shown in Fig. 6.6e. The more textured the film is, the smaller the FWHM.

The degree of texture in the film is high at low film thicknesses, and it starts decreasing above

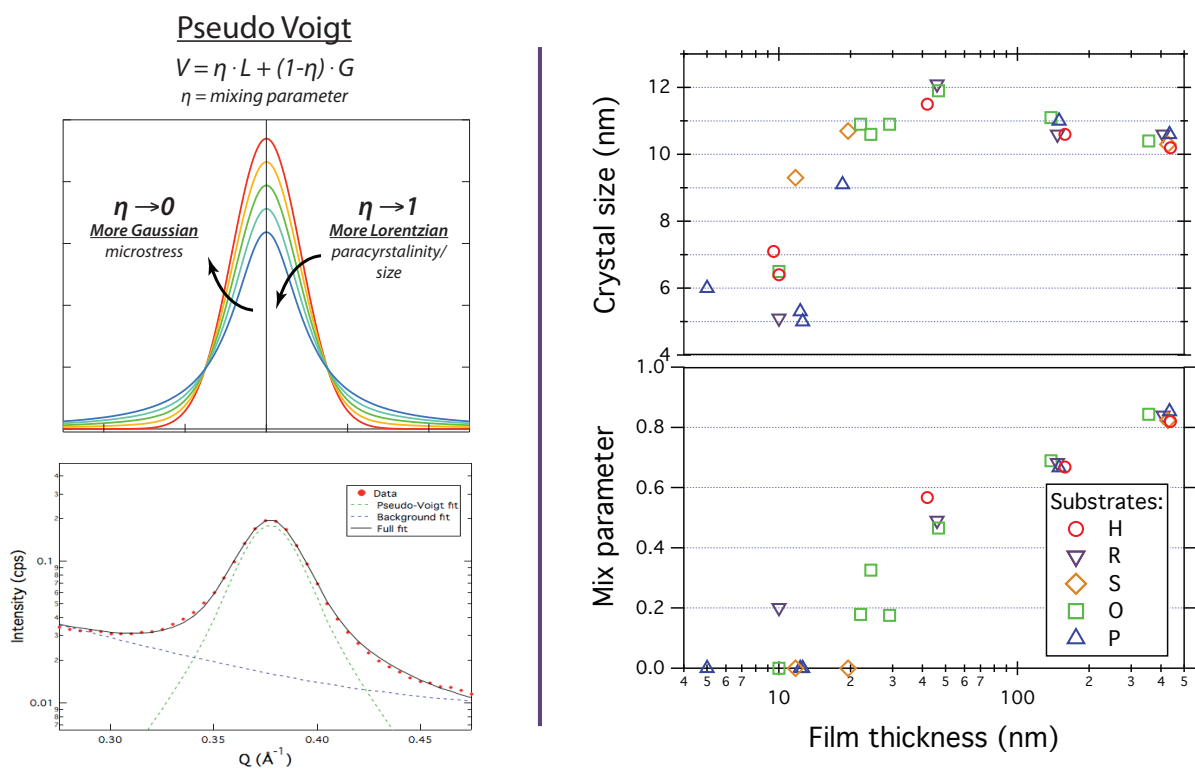


Figure 6.7: Pseudo-Voigt mixing parameter describing the XRD peak shape as a function of thickness. Also shown for comparison are the corresponding crystallite sizes.

$t > 20 \text{ nm}$. However, while the trends across different substrates tend to merge above $t = 20 \text{ nm}$, the BHJ film on PEDOT:PSS is consistently more textured at lower film thickness. In contrast, the data is rather scattered for films deposited on NiO_x. This is again consistent with the significantly lower surface roughness of the PEDOT:PSS films ($\sim 1 \text{ nm}$ RMS) compared to the NiO_x ones ($\sim 3.3 \text{ nm}$ RMS). As such, the high texture at low film thickness should not be taken as a sign of crystallographic templating by the substrate. Rather, this and the observation that film texture tends to be constant in the thinnest films corroborates the assertion that below $t < 20 \text{ nm}$, P3HT crystal growth is constrained by finite film thickness.

6.3 The Overall Picture

Comparing the data for BHJ films grown on different NiO_x HTL, one readily conclude that regardless of the HTL, the trends in the assessed metrics as a function of thickness are very similar. This assures us that changes in device performance that we are about to observe in the next chapter is due to mostly the NiO_x opto-electronic properties.

As we have stated earlier, for every metric that we assess $t \approx 20 \text{ nm}$, appears as a critical point when the trend as a function of thickness changes. It is also identified as the film thickness for the growth of natural-sized P3HT crystallite. More importantly, above this thickness, all observed structural trends are essentially uniform despite the different underlying substrates. Below $t = 20 \text{ nm}$, however, films grown on PEDOT:PSS tend to stand out in metrics such as d , texture, and correlation length. This leads us to conclude that on average, only growth of the crystallite nearest to the interface is influenced by the substrate surface properties. This might have stemmed from weak interactions between the predominantly alkyl chains in between the lamella.

Fig. 6.8 provides a summary of the film formation process. The highly non-polar nature of P3HT leads to PCBM being more favorably precipitated onto the substrates. Therefore, PCBM is precipitated first from the solution, resulting in a PCBM-rich interface. As more PCBM is precipitated and the solvent starts to dry from spin-casting process, P3HT starts to precipitate from the solution. At film $t \lesssim 20 \text{ nm}$, the film is highly textured due to spatial confinement, but

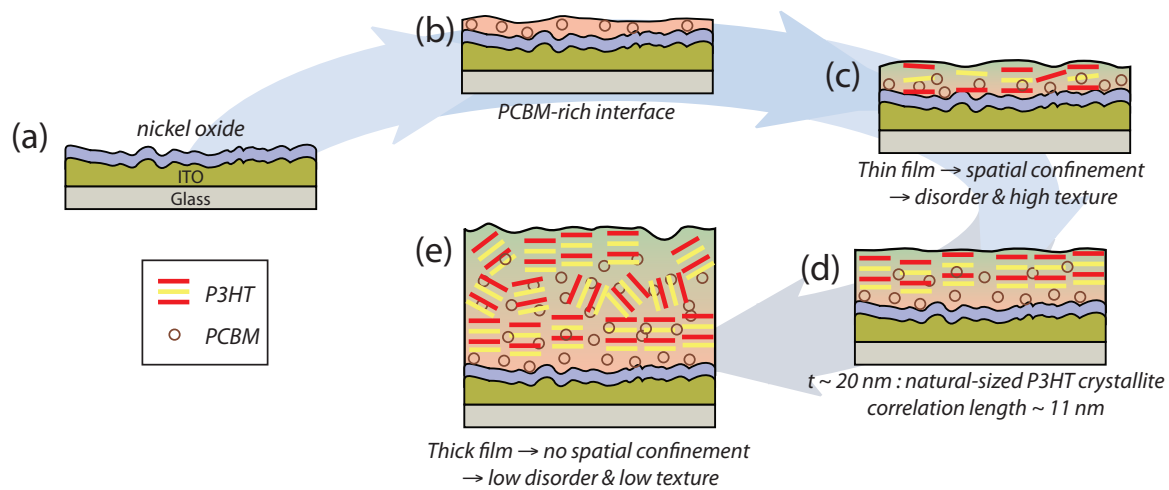


Figure 6.8: Illustration of P3HT:PCBM film formation process

otherwise is more disordered compared to thick films. This is probably related to high concentration of PCBM near the interface. Additionally, the polarity mismatch between P3HT and PCBM drives phase separation, resulting in the topmost surface being almost pure P3HT (i.e. the species with lower surface energy). At $t \sim 20 \text{ nm}$, P3HT forms natural-sized crystallites of $\sim 11.0 \text{ nm}$. In films thicker than $\sim 20 \text{ nm}$, film growth is no longer constrained by the low film thickness. This results in lower crystallographic disorder, but lower film texture. The final BHJ films display a vertical composition gradient, starting from PCBM-rich near the buried interface to pure P3HT at the top surface, with slightly different degree of film texture and composition near the interface, but otherwise similar despite the differences in the substrate surface properties.

Our result is very similar to that obtained by Duong et al [55] for the neat film on Si. The addition of PCBM into the system and the use of rough, high surface energy substrates impact the film morphology in the following ways:

- Vertical phase segregation of P3HT:PCBM due to preferential deposition of PCBM on the oxide surface
- Reduced texture near the interface due to surface roughness and possibly PCBM-rich interface

We do not observe any evidence of crystallographic templating of the organics by the substrate. We hypothesize that this is because of the weak interaction between P3HT and the substrate as elucidated by the surface energy calculation. Studies on substrate templating must therefore involve polar organic molecules that interact more strongly with the substrates, for example small, polar molecules.

6.4 Summary

A combination of X-ray diffraction techniques and depth-profile XPS have been used to explore the morphology of P3HT:PCBM films at different thicknesses in order to investigate the influence of substrate properties on the morphology. 2-components surface energy calculation from

contact angle measurement results are used to explain the observed trends, while XRD and XPS measurements provide insights into the physical causes for the observed differences in the surface energies. The PCBM-rich interface is related to the high surface polarity of the substrates.

On the other hand, differences in film texture near the interface are related to differences in substrate surface roughness. The influence of substrate surface properties, other than surface roughness, on the structure of the organics is weak. We propose that the reason for weak substrate influence on BHJ morphology stems from the weak interaction between P3HT and the substrates, which has been shown from the surface energy study above to be related to mismatch in molecular polarity / hydrophobicity. Such weak interaction with the substrate would have prevented any possibility of templating by the oxide surface, explaining the absence of any sign of templating by the substrate. Studies on substrate templating must therefore involve polar organic molecules that interact more strongly with the substrates, for example small, polar molecules.

In direct relevance to our interest of investigating the impact of NiO_x energy levels on OPV device performance, this study shows that there is negligible differences in morphology among the BHJ films grown on NiO_x processed by different methods. Therefore, we are confident that the differences in device performance are dominated by the NiO_x opto-electronic properties.

Chapter 7

The Impact of Band Offsets at Nickel Oxide - Bulk-Heterojunction Interface on OPV Performance

We are now standing on firm ground to study the impacts of NiO_x electronic properties to device performance. To recap, in §6 we have shown that morphology of the BHJ is largely unaffected by the surface properties of the NiO_x substrate, thus assuring that the differences in device performance is solely due to the differences in NiO_x / organic interfacial characteristics. Otherwise, differences in device performance might as well result from differences in, for example, charge dissociation efficiency due to differences in P3HT / PCBM domain sizes. On another front, in §4 we have demonstrated the ability to tune the position of E_v and WF of NiO_x films grown by PLD through varying PLD deposition parameters, which is necessary for a study of band alignments at the oxide / organic interface. Combined, these two studies provide a foundation for the study presented in this chapter on the effect of band-alignment in OPV devices.

More, we shall show that work-function is not the only parameter related to the electronic energy levels that is important in device performance. As has been shown for other inorganic semiconductor devices, band-offsets play an important role in OPV device performance. We focus on the tuning of E_v -offset. We conclude by proposing an update to the HTL / ETL design rules for OPV. Additionally, considering the results of this study in conjunction with two recent studies done by other groups [246, 81], we also propose that the use of the Anderson's rule for band alignment will allow an easy but powerful implementation of these rules.

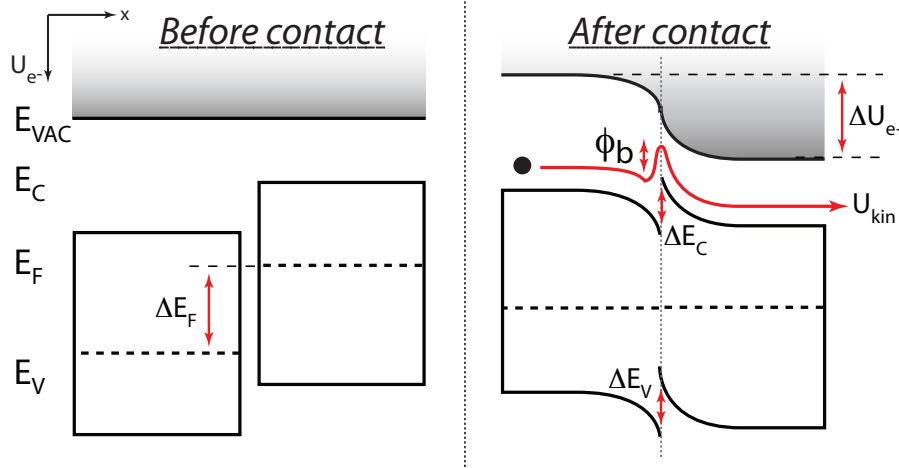


Figure 7.1: Energy levels of a heterojunction (a) before contact and (b) after contact, with an illustration of kinetic barrier experienced by an electron traveling along the conduction band edge.

7.1 Band Offsets and Kinetic Barriers: An Analogy

We found that the following analogy is helpful to illustrate the impact of band-offsets on carrier transport across an interface to experts with chemistry or material science background. It places the potential difference across the terminals in a similar place as the thermodynamic drive for chemical reaction and the band-offsets as the kinetic barrier for chemical reaction. The analogy is not mathematically precise, but qualitatively captures the essential physics.

Consider a heterojunction whose energy levels depicted in Fig. 7.1. After electrical contact, and in the absence of interfacial dipole, the electrostatic potential across the device, ΔU_{e^-} , is equal to the difference in the initial Fermi levels, ΔE_F . This built-in potential provides a drive for a test e^- to flow at the conduction band edge (E_C) from left to right, similar to the free energy in a chemical reaction. Band-offsets (ΔE_C , ΔE_V), on the other hand, are more similar to kinetic barriers. Since a test e^- is confined to travel at E_C , a discontinuity in E_C impacts the kinetics of current transport across the device. If ΔE_C is positive, it will reduce e^- current. On the other hand, a negative ΔE_C may result in thermal loss: an e^- traversing the interface must “drop” its energy by ΔE_C .

In a successful electronic device, it is thus of utmost importance to tailor, at every interface,

not only the work-function, but also the band-offsets.

7.2 Theory

We shall now consider transport of photogenerated electrons across the heterojunction over a barrier. Tunneling across the barrier, usually applicable only at high bias, is not considered here. The derivation follows that of Fonash's [63], which has been applied in, for example, CuInSe₂:CdS solar cells [205]. The treatment is an improvement over Anderson's work [7] where the barrier height was calculated from the band edges instead of from the quasi-Fermi levels. Additionally, we deviate from Fonash's derivation by utilizing the full Fermi-Dirac distribution function instead of the approximate Boltzmann form. The reason for this will be apparent will also be discussed.

Consider e^- transport¹ in three heterojunctions schematically illustrated in Fig. 7.2. The corresponding J-V characteristics is shown below the energy level diagrams. We assume idealized systems where mid-gap states and interfacial states are non-existent. The material on the left is the transport layer, the one to the right is the absorber. We consider cases when the gap of the transport layer remains constant but E_F (doping) are different. **Case 1** is when E_c of the transport layer perfectly matches that of the absorber. **Case 2** is when ΔE_c results an injection barrier for e^- from the transport layer to the absorber. **Case 3** is when ΔE_c results in an extraction barrier for e^- from the absorber to the transport layer. Lastly, in **Case 4**, the built-in potential V_{bi} is lower than that of **Case 1**, but otherwise they are the same.

The structure is uniformly illuminated such that E_{Fn} is raised uniformly in the bulk of the absorber. We assume that absorption in the transport layer is negligible, for example because of its large gap. On top of being under illumination, an external bias is applied across the device. Due to the transport layer's extreme thinness, we assume to the first order that almost all of the voltage is dropped in the active layer and negligible voltage is dropped in the transport layer.

We can approximate the extracted photocurrent with the help of the drift-diffusion formula

¹ Here we treat e^- transport because it is easier to visualize than h^+ . We still refer to the transport layer as "HTL".

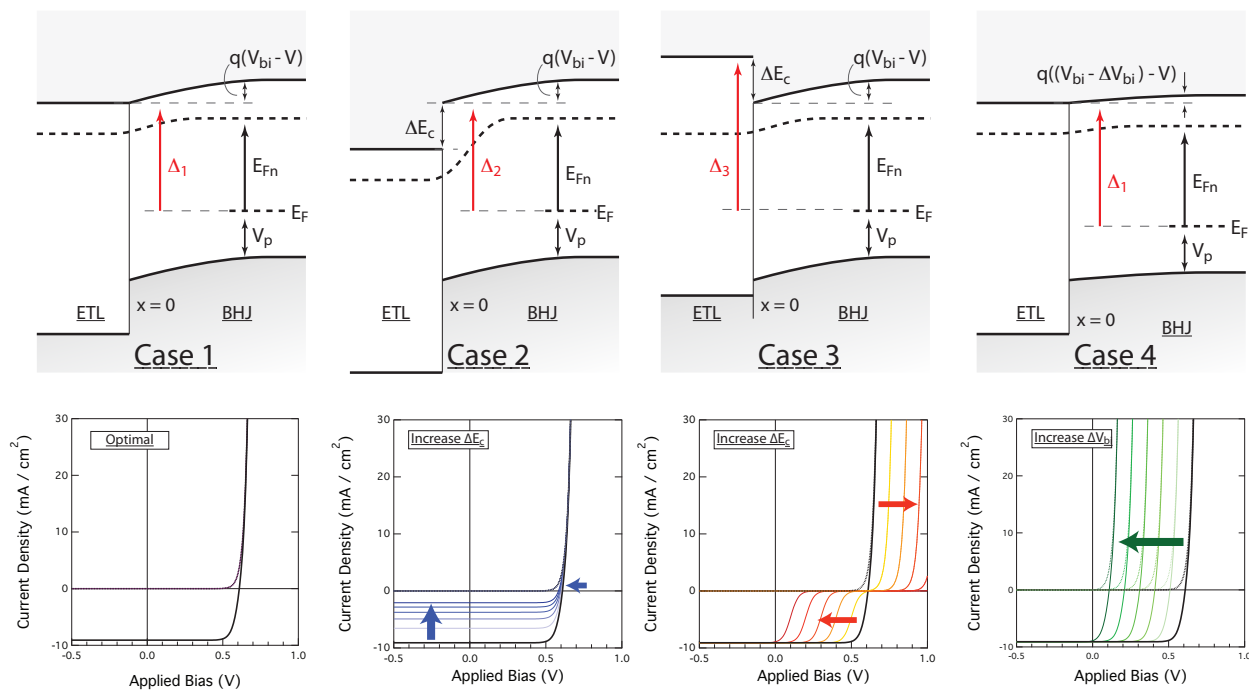


Figure 7.2: Energy levels in ideal heterojunctions with various band-offsets (Case 1 – 3) and reduced V_{bi} (Case 4). The devices are under illumination, resulting in splitting of E_{Fn} from E_F . For simplicity, only electron transport is considered. The corresponding JV curves are shown below each diagram, where the black curve is the best device. See text for details.

for current:

$$J = -q\mu n \left(\frac{d}{dx} \delta\varphi_n \right) \quad (7.1)$$

An appropriate location to evaluate the photocurrent is just to the left of the interface ($x = 0^-$), where almost all of the photocurrent is carrier by the electron photocurrent. Therefore, the electron photocurrent flowing across the HTL can be expressed as:

$$J_{ph} = -q\mu^{HTL} n_{ph}^{HTL} \left(\frac{d}{dx} \delta\varphi_n \right)^{HTL} \quad (7.2)$$

where q is the elementary charge, μ is the carrier mobility, n_{ph} is the photogenerated hole concentration. The last term, $\delta\varphi_n$, is the quasi-Fermi level splitting due to photovoltage and applied bias². Note that $\delta\varphi_n = E_{Fn}/q$. The superscript emphasizes that these quantities are evaluated at the HTL instead of at the BHJ.

Since q and μ are material properties, we only need to evaluate n_{ph}^{HTL} and $\delta\varphi_n^{HTL}$ in order to get J_{ph} for the various cases. Additionally, the constants of the system are the concentration of photogenerated carriers in the BHJ³, n_{ph}^{BHJ} , and the associated $\delta\varphi_n^{BHJ}$. Therefore, in order to understand the trends, we need to be able to relate n_{ph}^{HTL} , $\delta\varphi_n^{HTL}$ with those at the BHJ.

First, we shall discuss photocurrent extraction at the interface depicted in **Case 1**. Consider a photogenerated e^- traveling at E_c from the bulk of the absorber and reaching ($x = 0^+$) close to the metallurgical junction. From Fermi-Dirac statistics, the probability of an electron occupying this state is simply⁴:

$$\begin{aligned} f_1 &= \left(1 + e^{((\Delta_1+V)-E_{Fn}(0^+))/kT} \right)^{-1} \\ &\approx e^{(E_{Fn}(0^+)-(\Delta_1+V))/kT} \end{aligned} \quad (7.3)$$

where:

$$\Delta_1 = E_g^{BHJ} - qV_p - qV_{bi}$$

² In this treatment, $\delta\varphi$ is artificially independent of V because of our approximation that $\delta\varphi$ is uniform across the whole BHJ. This is expected to be a good approximation in the power-generating quadrant and is better in materials with very low imperfections.

³ This is one reason why it is crucial to keep the BHJ the same among the different samples.

⁴ This equation is presented in the fashion of Fonash's treatment in order to make easier connection with the literature. Eqn. 7.6 are more useful in illustrating the physics.

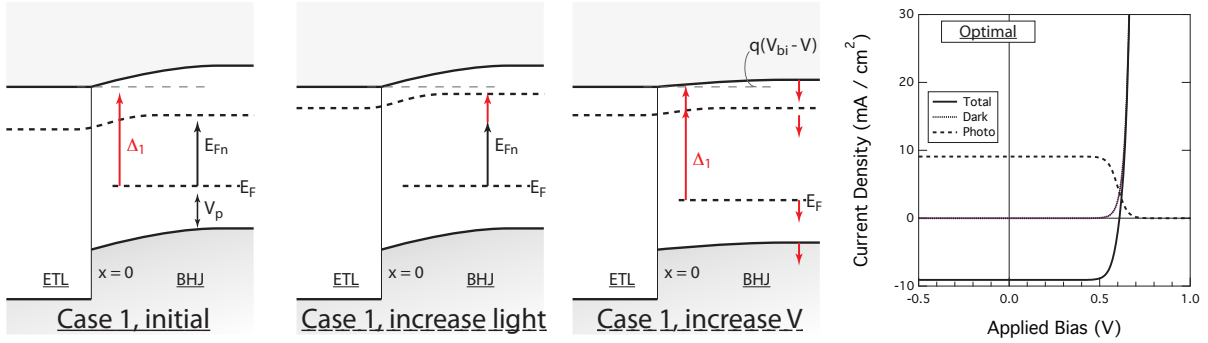


Figure 7.3: Case 1 under increasing illumination and forward bias. The calculated J-V characteristics using typical values from fits of actual devices is also shown.

where V is the applied bias, $E_{Fn}(0^+)$ is the quasi-Fermi level splitting in the absorber due to both the applied bias and photogeneration, Δ_1 is simply the location of E_c at the interface. The term in the exponent simply equals to the difference between E_c and E_{Fn} . The electron population at ($x = 0^+$) due to the illumination is thus simply:

$$\begin{aligned} n_{ph}^{BHJ} &= N_c f_1 \\ &\approx N_c e^{(E_{Fn}(0^+) - (\Delta_1 + V))/kT} \end{aligned} \quad (7.4)$$

It is important to note that the last approximation to the Fermi-Dirac distribution in Eqn. 7.3 is only valid when the exponent is large, i.e. when the photocurrent is small. **To evaluate conditions near J_{sc} , the full Fermi-Dirac form must be employed.** The approximate form, however, is useful when evaluating the behavior near V_{oc} .

To find out the relationship between n_{ph} at the two sides of the interface, we first note that an e^- reaching ($x = 0^+$) readily travels to the left of the interface since E_c is continuous. Therefore, for **Case 1**, $n_{ph}^{HTL} = n_{ph}^{BHJ}$.

To approximate $(\frac{d}{dx} \delta\varphi_n)^{HTL}$, we first note that E_F cannot split at the ITO / NiO_x interface due to the metallic-like property of ITO. Therefore, we approximate $(\frac{d}{dx} \delta\varphi_n)^{HTL}$ linearly by $\frac{\delta\varphi_n^{int}}{t}$ where $\delta\varphi_n^{int}$ is the quasi-Fermi level splitting at the NiO_x/BHJ interface and t is the thickness of the HTL. For this experiment t is constant at 10.0 nm. Since E_c is continuous at the interface,

$\varphi_n^{HTL} = \varphi_n^{BHJ}$. Incorporating these, Eqn. 7.2 becomes:

$$\begin{aligned} J_{ph,BEST} &= -q\mu^{HTL}n_{ph}^{BHJ} \left[\frac{\delta\varphi_n^{BHJ}}{t} \right] \\ &= -q\mu^{HTL} [N_c f_1(V)] \left[\frac{\delta\varphi_n^{BHJ}}{t} \right] \end{aligned} \quad (7.5)$$

where :

$$\begin{aligned} f_1(V) &= \left(1 + e^{(-q(V_p+V_{bi})+(E_g^{BHJ}-E_{Fn}(0^+))+V)/kT} \right)^{-1} \\ &\approx e^{(q(V_p+V_{bi})+(E_{Fn}(0^+)-E_g^{BHJ})-V)/kT} \end{aligned} \quad (7.6)$$

Eqn. 7.5 is the mathematical description that is of paramount interest in this study. **It relates the material properties of the HTL (μ^{HTL}), the photogeneration property of the absorber (n_{ph}^{BHJ} & $\delta\varphi_n^{BHJ}$), and the performance of the whole device.** It does not explicitly include the details of the photogeneration process in the BHJ. However, this is not the focus of our study on charge transport.

Eqn. 7.5 readily contain the expected behavior under different illumination and applied bias, mostly through the Fermi-Dirac distribution (Eqn. 7.6). The 1st term in the exponent of Eqn. 7.6 indicates that increasing V_{bi} improves current collection, as expected. Increasing light intensity increases n_{ph}^{BHJ} (2nd term in the exponent) and $\delta\varphi_n^{BHJ}$, resulting in higher photocurrent. On the other hand, raising the applied voltage tends to reduce photocurrent because it reduces the built-in potential which serves to drive the photocarriers across the volume of the absorber (3rd term in the exponent). The photocurrent thus have a Fermi-Dirac distribution shape, as shown in Fig. 7.3.

The relationship between V_{oc} and J_{sc} (§B, Eqn. 7) is often written as follows:

$$V_{oc} = \frac{kT}{q} \ln \left(\frac{J_{sc}}{J_0} + 1 \right) \quad (7.7)$$

However, we note that implicit in the derivation is the assumption that photocarrier transport efficiency is unity. Eqn. 7.3, on the other hand, is more accurate by partially taking into account that charge transport is dependent on, e.g. V_{bi} and V^5 . As Shockley and Queisser noted in their

⁵ A more complete treatment should also (1) considers the effect of carrier diffusion length in the BHJ, and (2) include the reverse current. The latter gives rise to the photoconductivity regime and explain the ‘‘crossover’’ of the photocurrent as seen in [167].

work [221], we need to revise Eqn. 7.7 by incorporating a voltage-dependent J_{ph} (Eqn. 7.5).

For simplicity, we assume the ideal diode rectification equation to describe the dark current:

$$\begin{aligned} J &= J_D - J_{ph} \\ &= J_{00} e^{-qV_{bi}/kT} \left(e^{qV/kT} - 1 \right) - J_{ph,0} e^{qV_{bi}/kT} e^{-qV/kT} \end{aligned} \quad (7.8)$$

where we have explicitly pull out the dependence on V and V_{bi} from both terms for purposes that will be clear later. We have also used the Boltzmann form of f_1 , which is valid near V_{oc} . J_{00} is a constant that is material dependent, while $J_{ph,0}$ also depends on light intensity as discussed before. To get V_{oc} , we set $J = 0$. This J-V characteristic is shown in Fig. 7.3. In the limit of high J_{ph} , we arrive at:

$$V_{oc} \approx \frac{kT}{2q} \text{Ln} \left(\frac{J_{ph,0} e^{qV_{bi}/kT}}{J_{00} e^{-qV_{bi}/kT}} \right) = V_{bi} + \frac{kT}{2q} \text{Ln} \left(\frac{J_{ph,0}}{J_{00}} \right) \quad (7.9)$$

Because the photogenerated carrier concentration is typically much lower than the equilibrium carrier concentration⁶, the logarithmic term is negative. This places V_{bi} as an upper boundary for V_{oc} , as usual. Therefore, the main difference between Eqn. 7.9 and Eqn. 7.7 is the factor of 2 in front of the logarithmic term.

We shall next discuss why **Case 2** and **Case 3** necessarily result in lower photovoltaic performance as compared to **Case 1**. In particular, we are interested in examining how J_{ph} and V_{oc} (Eqn. 7.5 & 7.9) are modified in the presence of ΔE_c . We shall start with **Case 3** which is more straight-forward. Fig. 7.4 provides the illustration for our discussion.

In **Case 3**, an e^- traveling at E_c of the absorber reaches ($x = 0^+$). Unlike in **Case 1**, ΔE_c is such that the e^- faces an energy barrier to travel across the interface. From Fermi-Dirac statistics, the probability that such an e^- having enough energy to travel across the barrier is:

$$\begin{aligned} f_3(x = 0^-) &= \left(1 + e^{((\Delta_3+V)-E_{Fn}(0^+))/kT} \right)^{-1} \\ &\approx e^{(E_{Fn}(0^+)-(\Delta_3+V))/kT} \end{aligned} \quad (7.10)$$

where:

⁶ in P3HT:PCBM, n_{ph} is estimated to be 1-2 order of magnitudes lower than n_0 .

$$\Delta_3 = E_{g2} - qV_p - qV_{bi} + \Delta E_c = \Delta_1 + \Delta E_c$$

We may rewrite Eqn. 7.10 as follows:

$$\begin{aligned} f_3(V) &= \left(1 + e^{((\Delta_1 + (V + \Delta E_c)) - E_{Fn}(0^+))/kT}\right)^{-1} \\ &= f_1(V + \Delta E_c) \end{aligned} \quad (7.11)$$

This is just a shift to lower V by ΔE_c . Consequently, we have for **Case 3**:

$$\begin{aligned} J_{ph,EXT} &= -q\mu^{HTL} (n_{ph}^{BHJ})_{(V+\Delta E_c)} \left[\frac{\delta\varphi_n^{BHJ} - V}{t} \right] \\ &\approx e^{-\Delta E_c/kT} J_{ph,BEST} \end{aligned} \quad (7.12)$$

where the subscript “EXT” refers to the extraction barrier for photocurrent. The last approximation is valid at low J_{ph}

To evaluate V_{oc} , we note that ΔE_c also results in an increased injection barrier from the HTL to the BHJ. This effectively reduces J_{00} by the same factor $e^{-\Delta E_c/kT}$. Therefore, V_{oc} is unaltered:

$$\begin{aligned} V_{oc,EXT} &\approx V_{bi} + \frac{kT}{2q} L n \left(\frac{J_{ph,0}}{J_{00}} \right) \\ &= V_{bi} + \frac{kT}{2q} L n \left(\frac{J_{ph,0,BEST} e^{-\Delta E_c/kT}}{J_{00,BEST} e^{-\Delta E_c/kT}} \right) \\ &= V_{oc,BEST} \end{aligned} \quad (7.13)$$

The fact that V_{oc} remains constant while the photocurrent is translated in V corresponds to a sigmoidal J-V characteristic, as shown in Fig. 7.4. Physically, this can be explained with the help of the energy level diagrams in Fig. 7.4 as follows:

Consider the case when $V_{bi}, E_{Fn} > \Delta E_c$. Initially, the exponent in Eqn. 7.10 will be positive, corresponding to the case where all photogenerated e^- will have enough energy to overcome the barrier. As we increase V , the built-in potential reduces to $V_{bi} - V$. As the reduced built-in potential falls below ΔE_c ($V = V_{bi} - \Delta E_c$), photocurrent starts to significantly falter.

Case 2 is unique from **Case 1** and **Case 3**. Here, $n_{ph}^{HTL} = n_{ph}^{BHJ}$ as before because there is no extraction barrier from the BHJ to the HTL. Additionally an injection barrier from the HTL

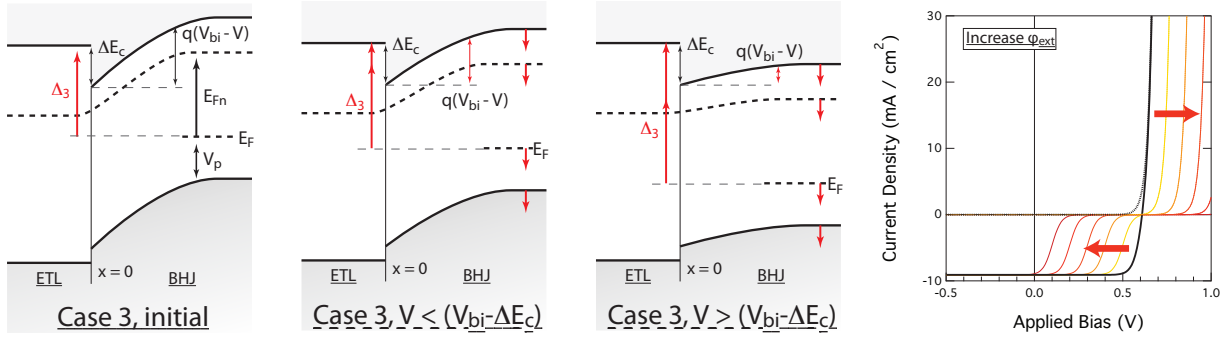


Figure 7.4: Case 3 under increasing forward bias. The calculated J-V characteristics under increasing ΔE_c are also shown.

to the BHJ is present. We shall show that although the number of carrier is conserved, ΔE_c now causes the photocurrent to be “clamped”⁷, effectively reducing J_{ph} :

The total carrier concentration, n , anywhere is given by:

$$n = n_0 + n_{ph} = N_c e^{-qV_n/kT} \quad (7.14)$$

where n denotes the total number of electrons, n_0 is the equilibrium population of electron and N_c is the effective density of states at the conduction band. $V_n = |E_c/q - \varphi_n|$ as indicated in Fig. 7.5. To reduce clutter in the subscripts, we shall denote the HTL by “1” and BHJ by “2” only in this derivation.

We assume that the photogenerated electrons do not recombine at the interface, thus their number is preserved across the interface. This leads to:

$$\begin{aligned} n_{ph,1} &= n_{ph,2} \\ n_H - n_{0,1} &= n_2 - n_{0,2} \\ N_{c,1} \left(e^{-qV_{n,1}/kT} - e^{-qV_{n0,1}/kT} \right) &= N_{c,2} \left(e^{-qV_{n,2}/kT} - e^{-qV_{n0,2}/kT} \right) \\ \frac{N_{c,1}}{N_{c,2}} &= \frac{e^{-qV_{n0,1}/kT} \left(1 - e^{-q(V_{n,1} - V_{n0,1})/kT} \right)}{e^{-qV_{n0,2}/kT} \left(1 - e^{-q(V_{n,2} - V_{n0,2})/kT} \right)} \\ &\approx \frac{e^{-qV_{n0,1}/kT} e^{-q(V_{n,1} - V_{n0,1})/kT}}{e^{-qV_{n0,2}/kT} e^{-q(V_{n,2} - V_{n0,2})/kT}} \end{aligned}$$

⁷ The case where a non-negligible potential is dropped across the HTL has been analytically treated in Ref. [205].

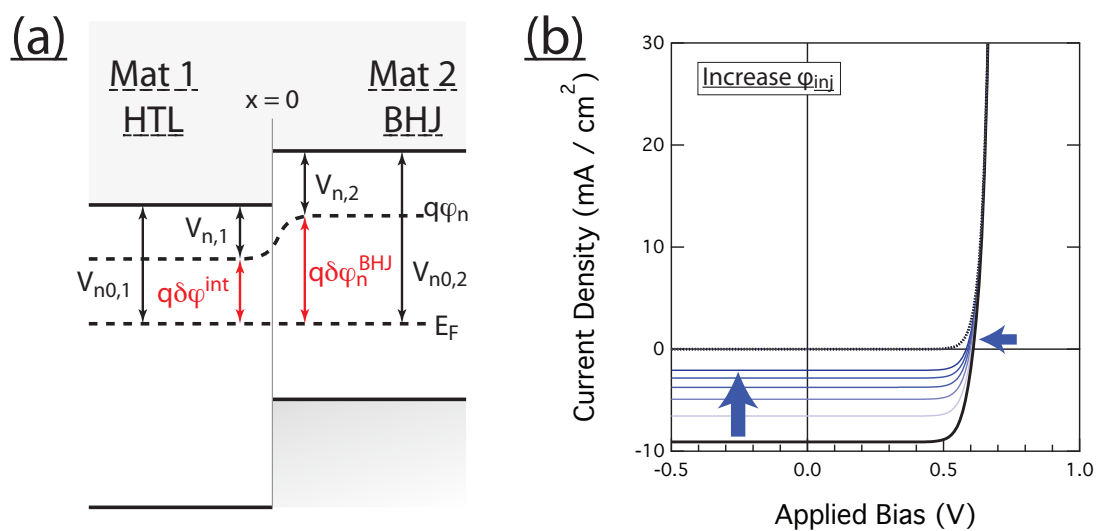


Figure 7.5: (a) Case 2 under illumination, illustrating the reduction in ϕ_n across the interface. (b) The calculated J-V characteristics with increasing ΔE_c .

$$= \frac{e^{-qV_{n0,1}/kT} e^{q\delta\varphi_1/kT}}{e^{-qV_{n0,2}/kT} e^{q\delta\varphi_2/kT}} \quad (7.15)$$

Hence,

$$\begin{aligned} e^{q\delta\varphi_1/kT} &\approx \frac{N_{c,2} e^{-qV_{n0,2}/kT}}{N_{c,1} e^{-qV_{n0,1}/kT}} e^{q\delta\varphi_2/kT} \\ &= \frac{n_{0,2}}{n_{0,1}} e^{q\delta\varphi_2/kT} \end{aligned} \quad (7.16)$$

Taking the logarithm of both sides, we arrive at the desired equation:

$$\delta\varphi_1 \approx \frac{Ln |n_{0,2}|}{Ln |n_{0,1}|} \delta\varphi_2 \quad (7.17)$$

In our case, material 1 is the HTL, while material 2 is the BHJ, thus we arrive at the final result:

$$\delta\varphi_{HTL} \approx \frac{Ln |n_{0,BHJ}|}{Ln |n_{0,HTL}|} \delta\varphi_{BHJ} \quad (7.18)$$

Therefore, for **Case 2**, Eqn. 7.2 becomes:

$$\begin{aligned} J_{ph,INJ} &= -q\mu^{HTL} n_{ph}^{BHJ} \frac{1}{t} \left[\left(\frac{Ln |n_{0,BHJ}|}{Ln |n_{0,HTL}|} \delta\varphi_n^{BHJ} \right) \right] \\ &= \left(\frac{Ln |n_{0,BHJ}|}{Ln |n_{0,HTL}|} \right) J_{ph,BEST} \end{aligned} \quad (7.19)$$

From Eqn. 7.19, it is apparent that the effect of ΔE_c here is to reduce the photocurrent at any given V (Fig. 7.5).

Compared to the best case, the total injection barrier remains the same. Therefore, the reduction in J_{ph} consequently results in slightly reduced V_{oc} :

$$\begin{aligned} V_{oc,EXT} &\approx V_{bi} + \frac{kT}{2q} Ln \left(\frac{J_{ph,0}}{J_{00}} \right) \\ &= V_{bi} + \frac{kT}{2q} Ln \left(\frac{\frac{Ln |n_{0,BHJ}|}{Ln |n_{0,HTL}|} J_{ph,0,BEST}}{J_{00,BEST}} \right) \\ &= V_{oc,BEST} - \frac{kT}{2q} Ln \left(\frac{Ln |n_{0,HTL}|}{Ln |n_{0,BHJ}|} \right) \end{aligned} \quad (7.20)$$

Intuitively, this behavior can be thought as follows: as a photogenerated carrier traverse through the interface, it has to drop in energy (thermalize) due to ΔE_c (for a direct connection with increased entropy, see Ref. [268]).

Another way to look at the situation is by realizing that the BHJ acts as a **current** source in the device. Therefore, the electron flow is limited by the rate of photogeneration in the BHJ. Consider a photocarrier current flow through the interface in the absence of any recombination mechanism. In this case, the photocarrier concentration at both sides of the interface has to be the same. However, since the HTL in this case is more heavily n-doped than the BHJ, the quasi-Fermi level splitting at the HTL has to be lower than that in the BHJ. Therefore, the photovoltage developed at the **external circuit** is reduced.

For completeness, we also would like to treat the case when V_{bi} is reduced (**Case 4**). It is evident from Eqn. 7.5 that reduced V_{bi} will shift J_{ph} in a similar fashion to device with extraction barrier:

$$\begin{aligned} J_{ph,VBI} &= -q\mu^{HTL} (n_{ph}^{BHJ})_{(V-\Delta V_{bi})} \left[\frac{\delta\varphi_n^{BHJ} - V}{t} \right] \\ &\approx e^{-\Delta V_{bi}/kT} J_{ph,BEST} \end{aligned} \quad (7.21)$$

where ΔV_{bi} is the change in the built-in potential. However, now we do not expect to observe a sigmoidal J-V characteristic because V_{oc} is also reduced:

$$\begin{aligned} V_{oc,VBI} &\approx V_{bi} + \frac{kT}{2q} \text{Ln} \left(\frac{J_{ph,0}}{J_{00}} \right) \\ &= V_{bi} - \Delta V_{bi} + \frac{kT}{2q} \text{Ln} \left(\frac{J_{ph,0}}{J_{00}} \right) \end{aligned} \quad (7.22)$$

The result is reduction of V_{oc} without any significant alteration in J_{sc} (Fig. 7.6).

In summary, we expect that the best device employs a transport layer whereby the transport band is continuous, while the to opposite band forming a blocking layer. A positive band-offset in the transport band leads to sigmoidal J-V characteristic, while a negative offset leads to reduction in J_{sc} and, to smaller extent, V_{oc} . Reduction in V_{bi} leads to linear reduction in V_{oc} .

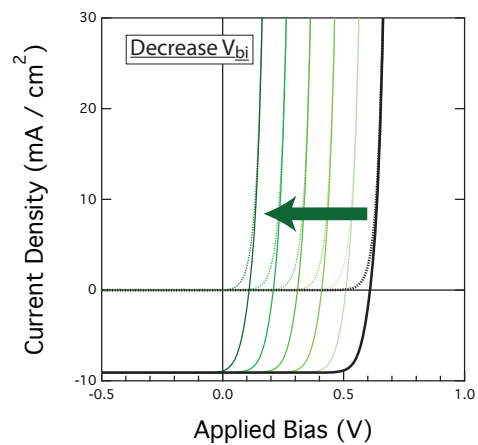


Figure 7.6: Calculated J-V characteristics for Case 4. The arrow indicates the direction for reduced V_{bi} .

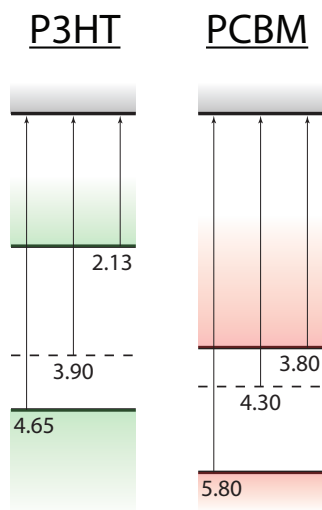


Figure 7.7: Energy levels of P3HT and PCBM from Ref. [82].

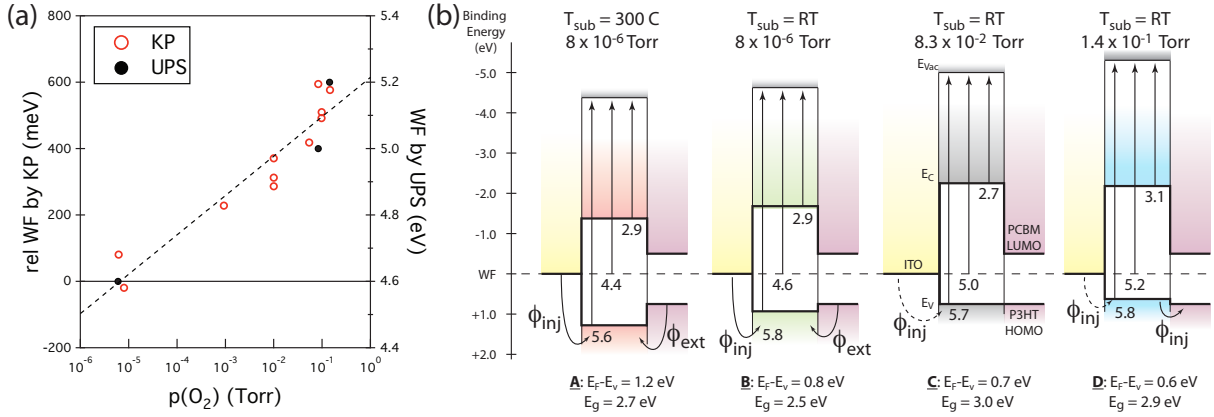


Figure 7.8: (a) WF of PLD NiO_x as a function of $p(O_2)$. (b) Energy levels for 4 samples in the set, together with the final band-alignment with P3HT:PCBM following Anderson's rules.

7.3 Experimental Results and Discussions

7.3.1 Band Alignment at the NiO_x / BHJ Interface

In order to get the band alignment at the interface, we need the initial energy levels of the two sides of the interface. P3HT:PCBM system is chosen for this study because of their status as de-facto standard for OPV devices. Its energy levels have been thoroughly investigated [82], and the results are shown in Fig. 7.7. The dashed lines are, strictly speaking, not E_F but the polaronic energies. This corresponds to polaron formation energy of 0.75 eV for P3HT and 0.50 eV for PCBM [270, 240].

WF of the NiO_x HTL grown by PLD for this study are presented again in Fig. 7.8a. The energy levels extracted from UPS / IPES for four select samples are shown in Fig. 7.8b. The details of material development and properties are discussed in §4.

Finding the final band-alignment after contact is a complex art (for reviews of the progress in inorganic materials over decades, we recommend Refs. [125, 119]). The most direct and trustworthy investigation method is arguably monolayer-by-monolayer deposition coupled with in-situ photoemission measurement, which is extremely challenging for polymer on oxide samples. However, recent reports suggest the validity of Anderson's rule (§D) for band alignment in many metal

oxide / organic interfaces [81, 7], with pinning occurring at the polaron energy of the organic material [240, 270, ?, 49]. Therefore, in this study we will approximate the band-alignment by employing the Anderson's rule.

Following Anderson's rules, we expect P3HT WF to be pinned by the NiO_x in all of the samples involved because WF of the NiO_x ($> 4.6 \text{ eV}$) are higher than the polaron energy in P3HT of 3.9 eV . This will lead to $(E_F - E_v)$ of 0.75 eV at the organic side. Similarly, energy levels of PCBM will be pinned by P3HT, leading to a constant $(E_c - E_F)$ of the organics to be 0.50 eV . Therefore, any kind of barriers for h^+ transport must arise from $(E_F - E_v)$ of the NiO_x , which can be engineered by varying $p(\text{O}_2)$ and T_{sub} .

Fig. 7.8b includes the proposed final band alignment on four select samples across a wide range of deposition parameters which readily span the three cases discussed in the theory section:

Sample A grown in vacuum, $T_{sub} = 300^\circ\text{C}$

- large extraction barrier from organic to NiO_x
- large injection barrier from ITO to NiO_x

Sample B grown in vacuum, $T_{sub} = 32^\circ\text{C}$

- smaller extraction barrier from organic to NiO_x
- smaller injection barrier from ITO to NiO_x

Sample C grown at $p(\text{O}_2) = 8.3 \times 10^{-2} \text{ Torr}$, $T_{sub} = 32^\circ\text{C}$

- negligible extraction barrier from organic to NiO_x
- injection barrier from ITO to $\text{NiO}_x = (E_F - E_v)$ of P3HT, no injection barrier from NiO_x to organic

Sample D grown at $p(\text{O}_2) = 1.4 \times 10^{-1} \text{ Torr}$, $T_{sub} = 32^\circ\text{C}$

- no extraction barrier from organic to NiO_x
- small injection barrier from NiO_x to organic

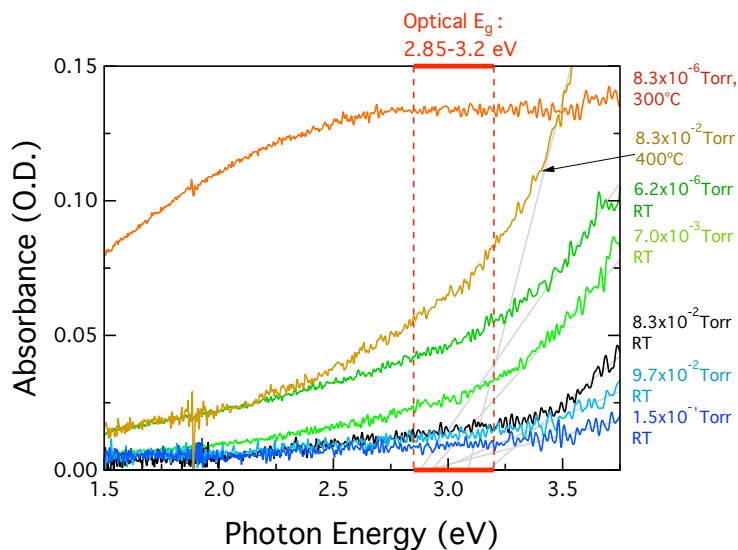


Figure 7.9: NiO_x film absorbances as a function of deposition parameters.

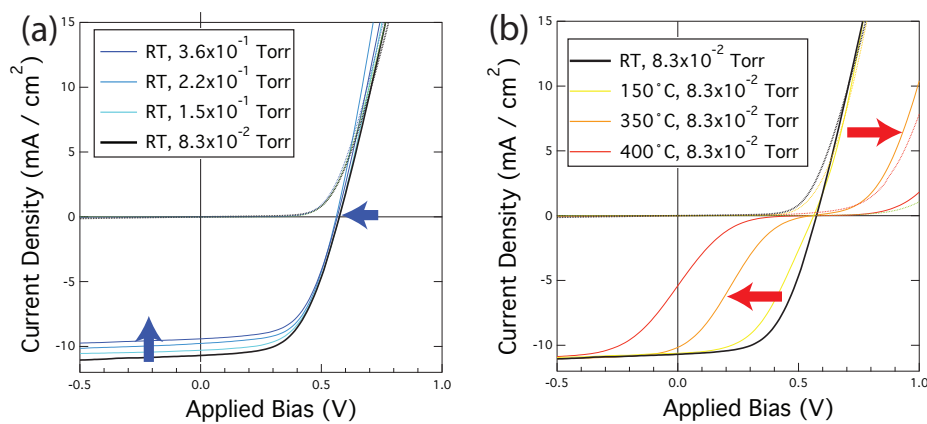


Figure 7.10: JV characteristics of P3HT:PCBM devices on NiO_x HTL's deposited under varying parameters. Black curve is the best device. (a) Blue curves uses NiO_x grown at higher $p(\text{O}_2)$, while (b) orange curves employ NiO_x grown at elevated temperature.

Device current-voltage (J-V) characteristics are shown in Fig. 7.10a and 7.10b, with the best device (black curve) employs sample C. The trends in the J-V characteristics as a function of deposition parameters are more correlated with the expected band-offsets than WF. Fig. 7.10a are from devices made with NiO_x layers grown at increasingly higher $p(\text{O}_2)$. It can be seen that the effect of increasing $p(\text{O}_2)$ too high is mainly to systematically lower J_{sc} and slightly reduce V_{oc} . Note that this is not due to lower HTL transmission (Fig. 7.9). Sample D belongs to this group. Hence, this corresponds to the situation when an injection barrier from the HTL to BHJ is present (**Case 2**).

On the other hand, Fig. 7.10b depicts the J-V characteristics of devices made with NiO_x layers grown at increasing T_{sub} . These are similar to sample A, except that we purposely keep $p(\text{O}_2)$ the same at $8 \times 10^{-2} \text{ Torr}$ to achieve similar film optical transmissions (Fig. 7.9). This is important because, since a photovoltaic cell is a current source, we need to keep photocurrent generation in the active layer to be the same to be able to fairly compare device performances. The sigmoidal J-V characteristics in these devices become more severe as T_{sub} is increased due to a growing barrier to photocurrent extraction (**Case 3**).

The observed J-V characteristics under illumination agree with theory. From the photoemission data (Fig. 7.8b), the shifts in J-V characteristics that causes the sigmoids are expected to be in the order of 0.1 eV . This is exactly what we observe in the actual data (Fig. 7.10b). The increased diode turn-on voltage, which sets this case apart from that of low E_{Fn} also appears in our data.

On the other hand, ΔE_v in the devices grown under high $p(\text{O}_2)$ is expected to be in the order of $0.05\text{-}0.1 \text{ eV}$. With P3HT polaron formation energy of 0.75 eV , we expect $\sim 10\% - 20\%$ reduction in J_{ph} , which agrees with Fig. 7.10a. The corresponding reduction in $V_{oc,INJ}$ is only in the order of a few mV . The observed reduction in $V_{oc,INJ}$ is less than 10 mV (inset of Fig. 7.10a), in line with the expected value.

Tress et al. have observed similar behaviors on organic HTL / organic BHJ interface, suggesting the universality of these results [244]. Through numerical simulations, the sigmoidal J-V

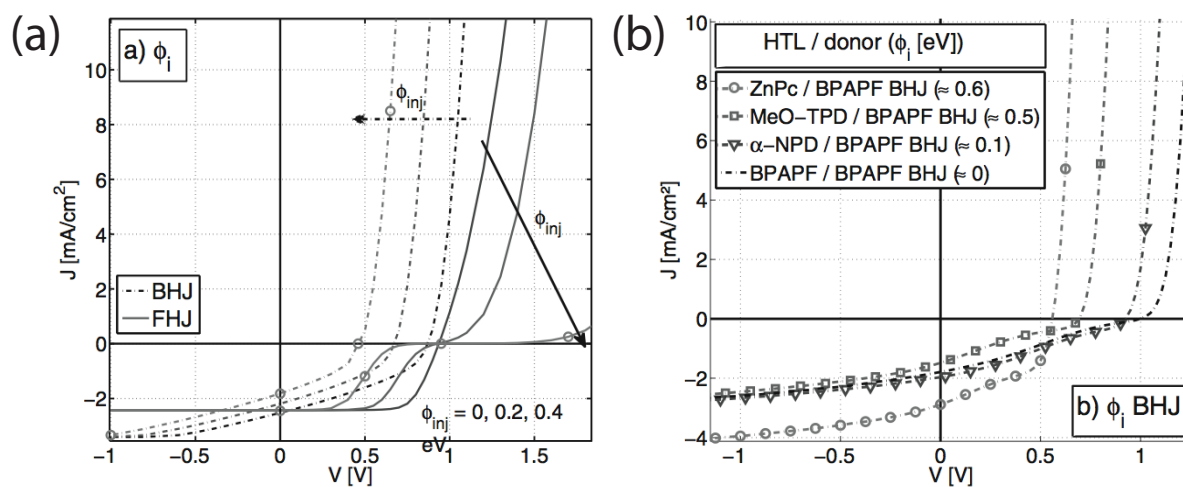


Figure 7.11: (a) Numerically simulated J - V characteristics for devices containing an injection barrier at an organic HTL / organic BHJ interface (dashed). The solid lines are for flat heterojunctions and are not relevant for our studies. (b) Experimentally measured J - V characteristics. Our analytical treatment is able to explain these observations by Tress et al. Reproduced from Ref. [244]

characteristics have also been attributed to the presence of extraction barrier. However, in their systems, the engineering of an injection barrier from the HTL to the BHJ also results in reduced V_{bi} as shown by the numerical simulations. Therefore, not only did they observe the reduced J_{ph} , their devices also have systematically reduced V_{oc} (Fig. 7.11a & 7.11b). The reason for reduction in V_{bi} observed by Tress et al might be due to the significant potential drop in the HTL. Although this is not explicitly mentioned in their work, it is suggested in their simulated energy-level diagram. The analytical treatment for the reduction in V_{bi} in such case has been done [205].

From this work, and taking into account the earlier work by Tress et al. [244], we propose to update the design rules for HTL in OPV devices by including the considerations related to band-offsets. The **final** alignment of the best HTL is depicted in Fig. 7.12. Additionally, when Anderson's rule can be applied, the energy levels of the layers **before** contact should follow:

- (1) High WF \rightarrow increase V_{bi} for extraction of photogenerated carriers
- (2) E_v of HTL = HOMO of donor \rightarrow no extraction / injection barrier
- (3) E_c of HTL < LUMO of acceptor \rightarrow reduce interfacial recombination near V_{oc}
- (4) Clean gap \rightarrow reduce recombination in the bulk of the HTL

Film transparency and carrier mobility are of course assumed to be superior.

We note for **Rule 3** that the electron-blocking property of the HTL is only important near V_{oc} , when V_{bi} is almost nulled by the applied bias. In fact, it has been shown that deep work-function n-type semiconductor with no electron blocking capability can be successfully used as an HTL [153, 85]. As a result, **Rule 3** is crucial in the last steps of device optimization and maximization of the fill-factor. **Rule 4** is not part of Anderson's rules but is readily understood via Shockley-Read-Hall formalism. Based on simple symmetry arguments these rules can be appropriately adjusted to apply to ETL layers.

Implicit in these design rules is a series of tradeoffs in the physical properties required to create an effective HTL / ETL. From this perspective it is crucial that the HTL / ETL be specifically

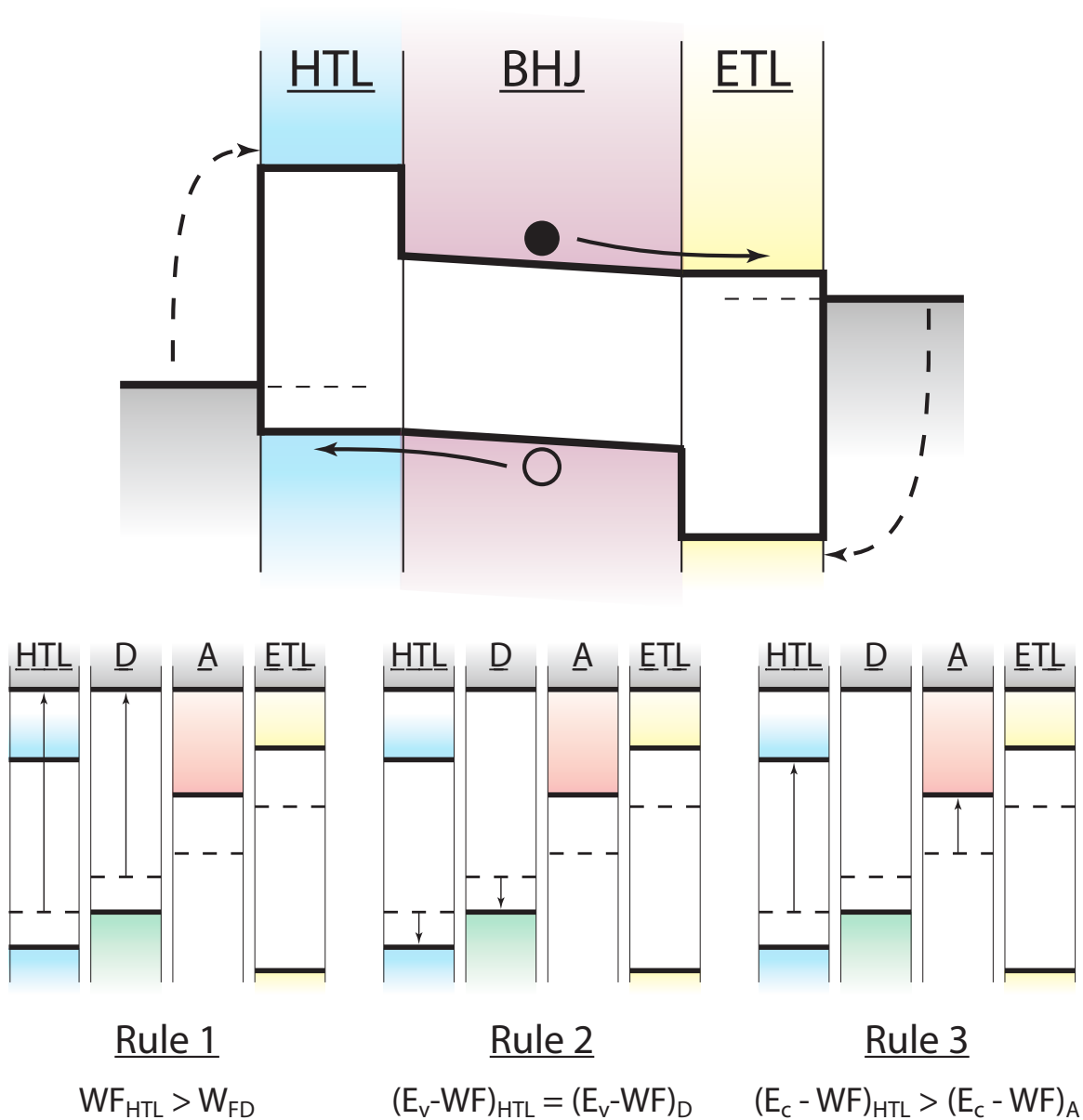


Figure 7.12: An illustration of the proposed optimal energy levels for HTL and ETL in a photovoltaic device after contact. Below, an illustration of the rules on how to achieve the final band alignment assuming the validity of Anderson's rules.

tailored to the active-layer in order to effectively extract the targeted carrier and maximize device performance. Furthermore, we expect the generality of these rules to hold as long as Anderson's rules are applicable, i.e. when no interfacial states develop as the two materials are put together. Greiner et al. have shown that many metal oxide/organic interfaces falls under this category [81]. As an example of a case when Anderson's rules are not expected to be valid is the metal / organic interfacial system that is studied by Winget et al in Ref. [263].

7.4 Summary

We first discussed the expected photocurrent extraction characteristics of a PV cell in the presence of band-offsets at the HTL / absorber interface. We saw that the best device employs a transport layer whereby the transport band is continuous, while the to opposite band forming a blocking layer. A positive band-offset in the transport band leads to sigmoidal J-V characteristic, while a negative offset leads to small reduction in photocurrent and photovoltage.

We then set to experimentally test this theory. PLD NiO_x is used as an HTL because of the ability to systematically tune its WF and $(E_F - E_v)$ by varying deposition parameters. The energy levels of the NiO_x are measured via UPS/IPS and the Kelvin probe, while that of the BHJ are taken from the literature. We use Anderson's rules for band alignment at an ideal interface to conjecture the final alignment after contact.

J-V characteristics of OPV devices employing these NiO_x films largely follow what we expect from theory. Additionally, a work by other group [244] have shown similar results on organic / organic interfaces, suggesting the universality of this observation. Based on the results, an update to the design rules for HTL is proposed. Similar rules for ETL are readily derived using the same arguments.

Because Anderson's rules have been suggested to universally apply to many of metal oxide / organic interfaces [81], we also propose the use of these rules to conjecture the energy levels of the materials **before contact**. These are readily measurable by, for example, photoemission measurements.

Combined, these rules will greatly benefit the development of OPV and organic electronic technologies in general because as OPV drives to maturity, there will be greater need to integrate contact design intimately with more focus on designing device interfaces and overall architecture rather than solely designing better photoactive molecules.

Chapter 8

Development of Laser-Induced Breakdown Spectroscopy for Stoichiometric Analysis of Compositionally-Graded Combinatorial Amorphous Thin Film Oxides

The growth of OPV has been astonishing. During the 5 years we spent on this project, OPV cell efficiency has boosted from $\sim 4\%$ to more than 12%. This rapid development has been primarily attributed to the prolific discoveries of novel, and better organic photo-active materials. However, as OPV drives to maturity, there will be an increasing focus on the engineering of other aspects of the device, such as the contact / photoactive layer heterojunction.

So far, we have discussed an in-depth study of a particular contact / organic system, namely nickel oxide / P3HT:PCBM. While the updated design rules that result from the study are relatively easy to follow, the implementation, namely finding the right material that satisfies the criteria for a given photoactive material, is not as straight-forward. Often, one has to spend a prohibitively long time to explore an immense deposition parameter space just to arrive at one suitable material composition. Sometimes, one gets a good candidate material, but the processing steps are not compatible with the rest of the device. To address this challenge, our group has started a high-throughput material development effort based on combinatorial approach, whereby a single sample with systematically varied deposition parameter across is (e.g. composition, T_{sub}) are prepared and thoroughly characterized in semi-automatic manner. The development is guided by the calculations done by the theory group at NREL. In this way, the time required for exploring the deposition parameter space can be greatly reduced.

In the work described here, we expose the work done in optimizing a laser-induced breakdown spectroscopy (LIBS) instrument as a quantitative analysis tool as a part of this combinatorial effort [260]. LIBS is an optical atomic emission spectroscopy that has begun to see use as a quantitative analysis tool for metals and alloys [1, 3, 4]. During the analysis, an intense laser pulse is focused onto the sample, ablating a tiny amount of the material into a plume of excited atoms. The atoms in this plume eventually relax to lower energy states and emit photons with characteristic wavelengths which can then be analyzed to determine the elemental content of the sample.

The intensity of the characteristic photon flux emitted from the plume is expected to be proportional to the number of atoms in the plume, which makes it possible to calculate the relative amount of constituent atoms in the sample. Because of the short analysis time (1 second per laser shot) and small sampling area (diameter ~ 1 mm) [235], LIBS is potentially suitable for combinatorial analysis. In addition, LIBS offers several appealing features for compositional analysis in general: it does only local damage, it is able to detect light elements [13], the analysis is independent of the physical state of the sample (see, for example, [42, 62, 187]), and no special sample preparation is needed.

Here we discuss our work in optimizing a commercial LIBS instrument as a quantitative analysis tool for determination of the metals ratio in combinatorial mixed-metal-oxide thin-film samples. Our results from LIBS analysis of amorphous indium zinc oxide (a-IZO) combinatorial thin-film samples are compared with analysis by Inductively Coupled Plasma Atomic Emission Spectroscopy (ICP-AES), an established analysis methodology. We also compared LIBS compositional mapping capability with X-Ray Fluorescence Spectroscopy (XRF).

8.1 Experimental Set Up

8.1.1 Equipment

A commercial LIBS system from NewWave Research equipped with CCD spectrometers from OceanOptics was used. The specifications are listed in Table 8.1. ICP-AES analysis was done with

a VARIAN Liberty 150 ICP Emission Spectrometer. The XRF analysis system, the Maxxi5/PIN, and the associated data acquisition software, XMasteR, was made by Roentgenanalytik Messtechnik GmbH. The analysis software for the XRF, called MTFFP, was developed by Matrix Metrologies and optimized for compositional analysis of multi-layer thin-films. Profilometry was done using a VEECO DEKTAK profilometer.

The schematic of the LIBS set-up is illustrated in Figure 8.1. The LIBS system was comprised of a separate laser, and the LIBS housing which contains the sample stage, the optics, and the spectrometers. The sample stage had software-controlled sample movement in the X-Y direction. Furthermore, the Z-position of the objective lens can be moved manually to change the depth of laser focus.

Throughout this study, we used 50% laser energy (~ 100 mJ per pulse) and a $200 \mu\text{s}$ Q-switch, as suggested by the laser manufacturer to ensure optimum laser stability. Under these conditions, the laser energy stability was specified to be about 2% shot-to-shot. The 1064 nm Nd:YAG infra-red laser was produced in the laser unit, and was passed to the LIBS system through fiber optics. Before reaching the sample, the laser pulse passed through a series of optics, including one collimating lens that can be moved along the beam line to adjust the laser spot size on the sample surface, and a shutter. After passing through the shutter, the laser pulse was reflected through a dichroic beam-splitter at the laser wavelength, and focused through an objective lens into the sample.

To help focus the laser onto the sample, the system was equipped with a video camera which shared the same objective lens. The afore-mentioned collimating lens is only movable through the software in which the user is given a discrete choices of laser spot sizes to be produced on the camera focus plane. The user is also given the option to have the laser focus above or below the camera focus to produce such spot size. Moving the objective lens position such that the camera is not in focus on the sample surface further changes the laser spot size on the sample.

A small amount of the sample was then ablated by the laser, and the characteristic spectral lines were emitted by the plume as it relaxes. Because the camera focus could not be moved all the way to the bottom of the ablation chamber, the sample was propped up on several stacked Corning

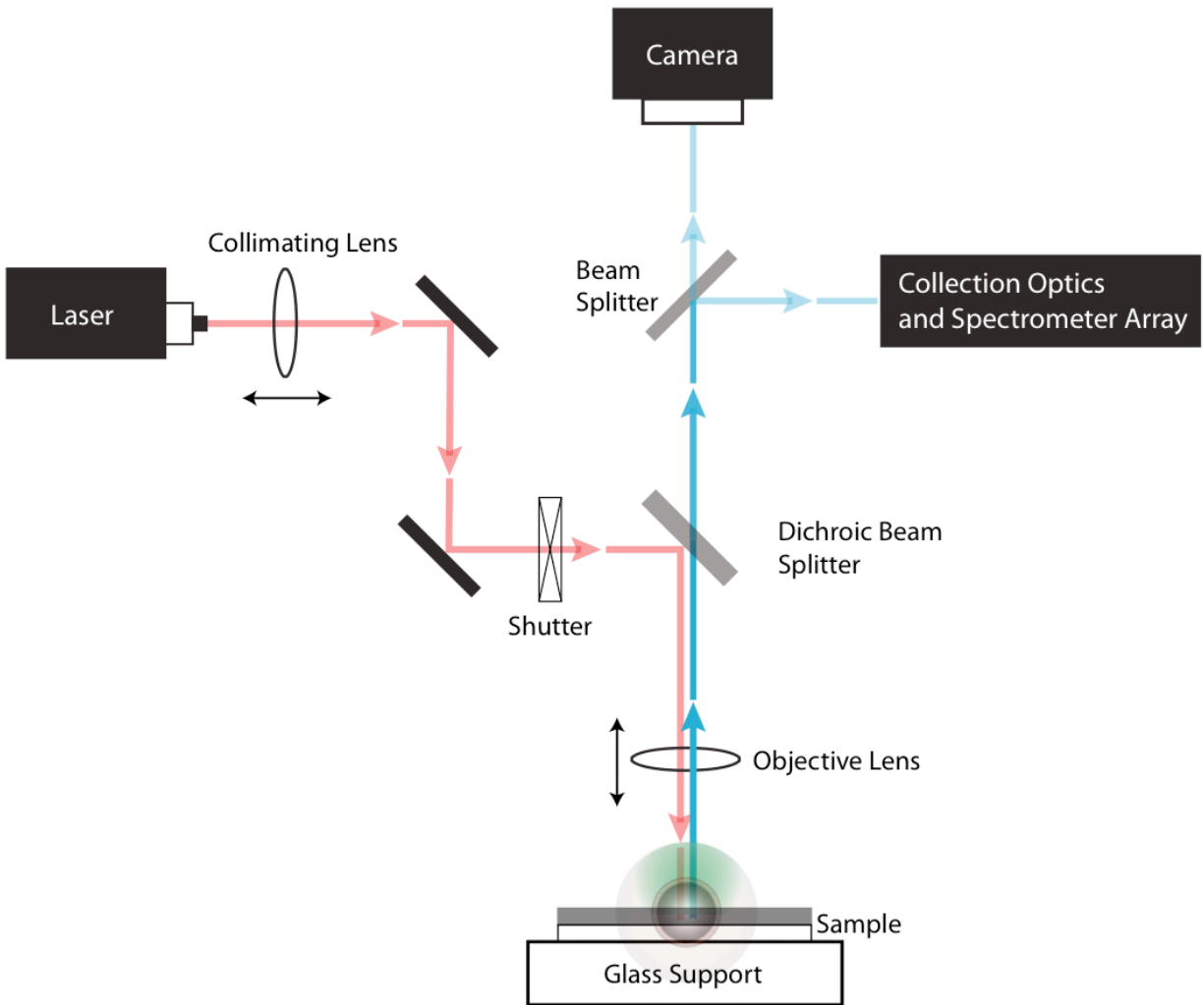


Figure 8.1: Diagrammatic representation of the LIBS system.

Laser	
Make, model	NewWave Research, Tempest
Type	Nd:YAG
Q-switch	155 or 200 μ s
Wavelength	1064 nm
Pulse FWHM	3-5 ns
Max pulse energy	200 mJ
Energy stability	$\pm 2\%$ pulse-to-pulse for 98% of shots after 30 min warm-up
Max rep rate	10 Hz
Spectrometers	
Make, model	OceanOptics, HR2000+
Focal length	101 mm
Total range	200 - 1100 nm
Individual range	198.14 - 301.69 nm 294.73 - 389.92 nm 383.28 - 512.81 nm 505.54 - 622.20 nm 615.97 - 719.30 nm 713.22 - 802.56 nm 795.03 - 968.24 nm
Filters	Longpass and bandpass
Integration time	1 ms to 65 s
Detector	
Make, model	Sony, ILX-511
Type	Linear silicon CCD array
Number of pixel	2048
Signal to noise ratio	250:1 at full signal
Dark noise	12 RMS count

Table 8.1: LIBS system specifications

Eagle 2000 glass slides. The Eagle 2000 glass slides do not contain amounts of indium or zinc, hence should not alter the signal received by the spectrometers. Since we do not know the exact composition of the chamber walls, this mounting scheme also reduces the chance of signal alteration caused by ablation of the chamber floor by the laser that was transmitted through the transparent sample. The ablation chamber was also continuously purged with argon during the experiment to reduce plume deposition on the objective lens. The emitted characteristic photons from the plume passed through the same objective lens as the excitation photons, after which they passed through a dichroic beam-splitter, and were split to the collection optics and the camera. The spectra were then simultaneously collected using seven parallel wavelength-dispersive spectrometers. Despite the low resolution of 0.05 nm per pixel, the use of these parallel spectrometers was essential because of its quick data collection, hence allowing us to get data across a wide spectrum with a single ablation. The spectrometers' wide total range (~ 200 nm to 970 nm) also made it possible to use multiple characteristic spectral lines for analysis if desired.

A representative of a LIBS raw spectrum from an a-IZO sample across the full spectrometer range is shown in Figure 8.2(B), while Figures 8.2(C) and 8.2(D) below it show the locations and the relative intensities of indium and zinc peaks across this range. It is evident from the three figures that LIBS spectra tend to be comprised of numerous overlapping spectral peaks. We chose to analyze the indium peak at 271 nm and zinc peak at 277 nm, which are shown in Figure 8.2(A). The choice of these particular lines was critical in the analysis for reasons that we will elaborate in detail after the discussion of the mathematical model (Section 8.2).

8.1.2 Sample Description

We used nine single-composition a-IZO thin films of different indium content to calibrate the system. The films were prepared by sputtering on 5 cm \times 5 cm engineered glass, and are all ≈ 200 nm-thick. All samples, except the one used for comparison with XRF, were deposited on Corning Eagle 2000 glass. Subsequent samples for combinatorial mapping were made through co-sputtering with two off-axis guns to produce a composition gradient along one direction (X-direction), re-

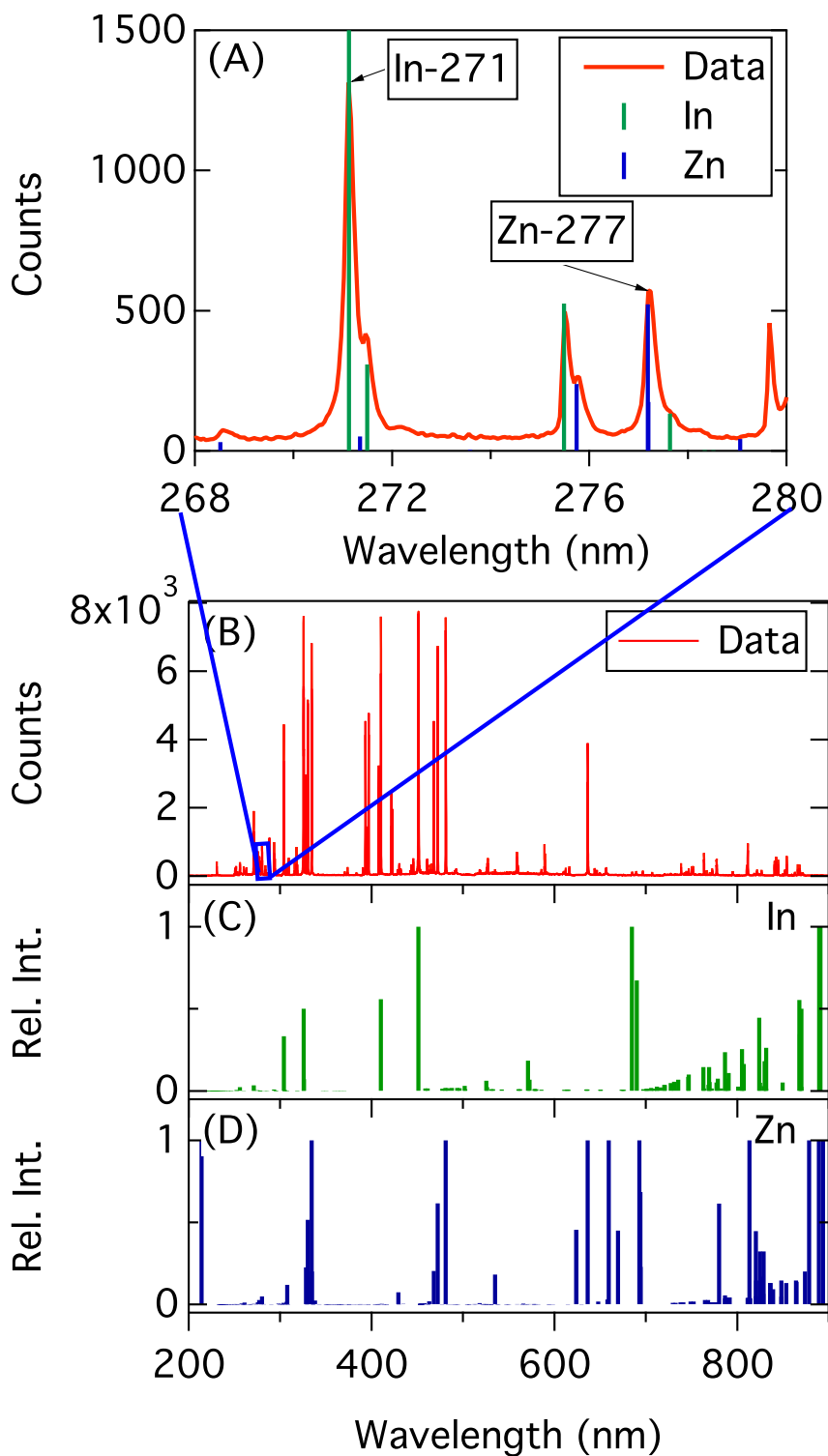


Figure 8.2: LIBS raw data and the position of Zn and In peaks. (A) is the zoom-in of the raw spectra between wavelengths = 268 and 280 nm, showing the data, and the positions of In and Zn lines, including the ones that we analyze. (B) is the full spectra that we obtain from the LIBS. (C) and (D) respectively shows the relative position of In and Zn peaks with normalized relative intensity.

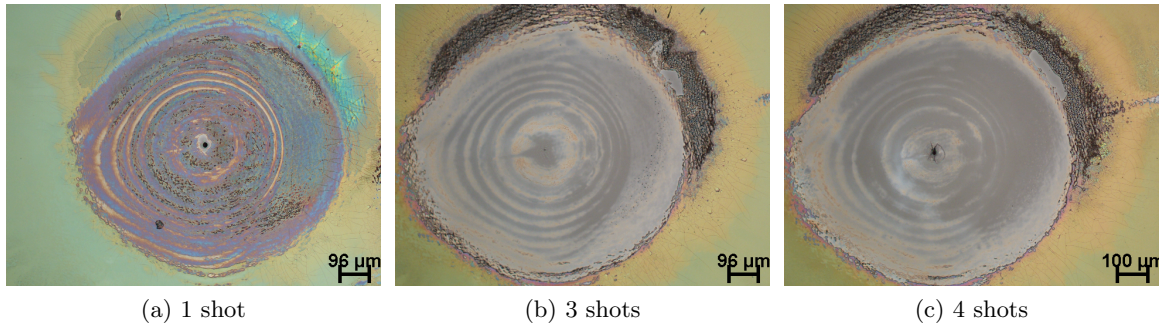


Figure 8.3: Microscope image of the laser-ablated spots on an a-IZO sample. The film was completely ablated after 3 laser shots.

maining relatively uniform along the other direction (Y-direction). The indium composition ranges across the X-direction of the three combinatorial samples were expected to be 15-50 at%, 35-70 at%, and 70-95 at% based on target composition, position, and orientation during deposition. For comparison with XRF, we used a combinatorial a-IZO library with expected indium content of 15-50 at%, deposited by sputtering on Corning 1737 engineered glass. The deposition details of these films are described in references [237] and [136].

Figures 8.3 show the microscope pictures of the LIBS ablation spot on an a-IZO sample after (A) 1 laser shot, (B) 3 shots, (C) 4 shots. These figures suggest that the film was completely ablated in 3 laser shots. Figure 8.4 shows the profilometry data taken across the diameter of the spot made by 3 laser shots which confirms both the large spot size on a-IZO and the claim that the 200 nm film has been completely ablated in 3 laser shots.

Generally, the ablation spot size on a sample is not only a function of laser diameter on the sample, but also a function of laser power density and the material that is being ablated. The collimating lens setting that was used to create the ablation spots in Figures 8.3 and 8.4 was factory-set to produce a spot with 220 μm diameter on stainless steel when the camera focus is on the sample surface. Additionally, the objective lens was also in the optimized position such that the camera focus, and hence the laser focus, is below the sample surface. Using this setting, our spot size on a-IZO is approximately 800 μm . The optimization process is the subject of the next

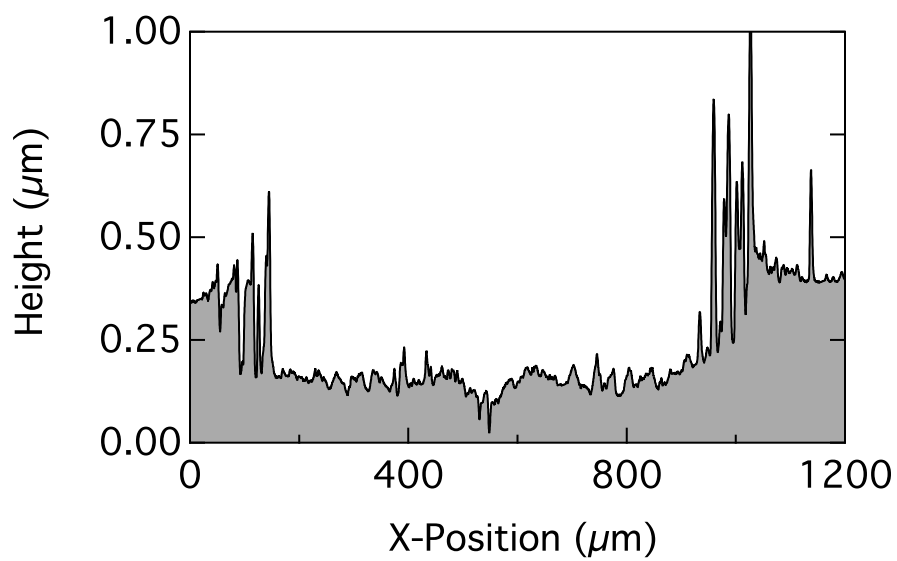


Figure 8.4: Cross section profile of LIBS laser-ablated spot on a 200 nm-thick a-IZO sample. Data was taken using stylus profilometer across the diameter of a spot created by 3 laser shots. Spot diameter was about 800 μm

sub-section.

8.1.3 Signal-to-Noise Optimizations

To ensure optimal signal-to-noise ratio and good precision, we had to adjust the laser intensity at the sample [8, 111], and the data acquisition time frame [8]. The intensity of the signal from the atomic transitions of the sample constituents is proportional to the power density of the excitation laser. Thus, it is important to have a sufficient laser intensity to generate a good signal-to-noise ratio. However, an overly-intense laser may lead to formation of optically dense plasma which may reabsorb the emitted characteristic light.

There were two ways to adjust the laser intensity on the sample in our system: (1) by adjusting the laser power, or (2) by changing the spot size on the sample. As mentioned earlier, the laser power was fixed at ≈ 100 mJ per pulse to maintain optimal stability; hence, we were left with the spot size as the only adjustable parameter to change the power density. This was done by changing the position of the objective lens with respect to the stage, or by moving the collimating lens through the software; the latter was a equivalent to a fine adjustment of the former. To determine the laser intensity that yields the optimum signal, we varied the distance between the objective lens and the sample while keeping the focusing lens setting through the software constant, and monitored the signal from the a-IZO sample. This focusing lens was initially set such that when the camera focuses on the sample surface, the laser focus was below the sample surface and the spot diameter on the surface was factory-calibrated to be $220 \mu\text{m}$.

Figure 8.5 shows the emission intensity of the analyzed peaks as a function of camera focus position (D). $D = 0 \mu\text{m}$ corresponds to camera focus on the sample surface, while positive and negative values of D corresponds to laser focus above and below the sample surface respectively. D is offset from the laser focus position as a function of the collimating lens position, which is left constant throughout the experiment; hence this offset is also a constant of the experiment. For the choice of zinc spectral line (at 277 nm), the number of counts increases dramatically by changing the focus position by a few hundred microns. This value maximizes when the camera focus is ≈ 400

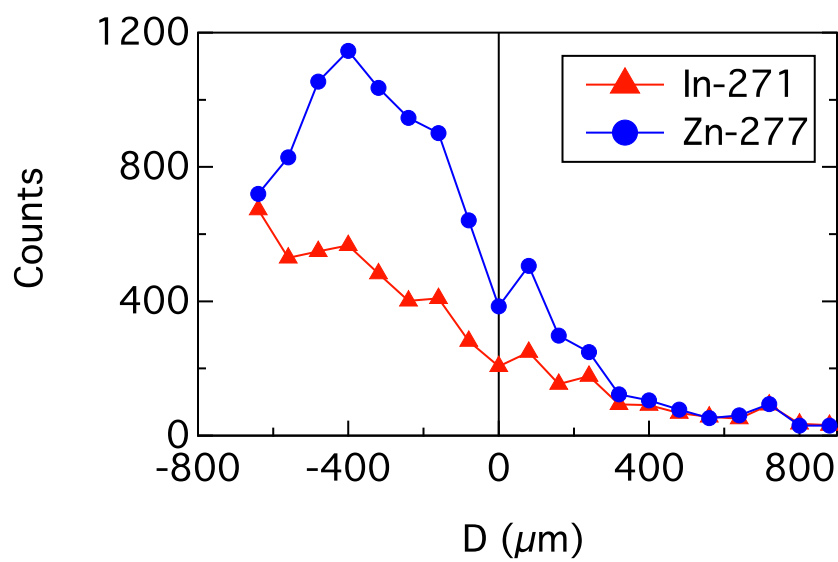


Figure 8.5: Signal count as a function of camera focus position relative to the sample surface. $D = 0 \mu\text{m}$ corresponds to camera focus on the sample surface, while negative value corresponds to camera focus below the sample surface. Based on the intensity of the Zn line, $D = -400 \mu\text{m}$ was used as the optimum position.

μm below the sample surface. In contrast, the indium line (at 271 nm) did not reach its maximum count rate within the range of the system. Consequently, we used the optimum setting for the Zn line during data acquisition. Using this setting, the spot diameter on the a-IZO sample was $\approx 800 \mu\text{m}$.

Each atomic excited state also has a unique lifetime, and thus a unique optimal time window for data collection [93]. Ideally, we would like to optimize both the time delay and the integration time as done by Aragon, et al. [8]; however for our system, the spectrometer integration time is fixed at 5 ms. The time delay between the laser fire and the start of measurement, however, can be adjusted between -50 and +50 μs in increments of 5 μs ; positive and negative time delay respectively means the start of data acquisition is after and before the laser fires. One would like to start data acquisition after the laser fires to avoid background scattered radiation. On the other hand, optical emission obeys an exponential decay law; hence starting data acquisition too late is not favorable for signal-to-noise ratio either. Clearly, for any peak, there exists an optimal time window for data collection, and if more than one peak is analyzed, then the lifetimes of all the different states need to be considered.

Figure 8.6(A) shows a LIBS spectrum as a function of the time delay (t_d), while Figure 8.6(B) shows the signal to noise ratio of the In-271 nm and Zn-277 nm lines. We used the following figure of merit to quantify the signal to noise ratio:

$$\text{S.T.N.} \approx \frac{P}{\sqrt{P+B}} = \frac{(P+B) - B}{\sqrt{P+B}} \quad (8.1)$$

where P is the peak count, and B is the baseline count. The quantity (P+B) is the total signal read by the spectrometers, and B is roughly approximated as the average of the baseline signal directly on the left and right of the peak. We chose $t_d = +5 \mu\text{s}$ because not only that the baseline due to scattered radiation had already become low, but also the signal to noise ratio was also maximized.

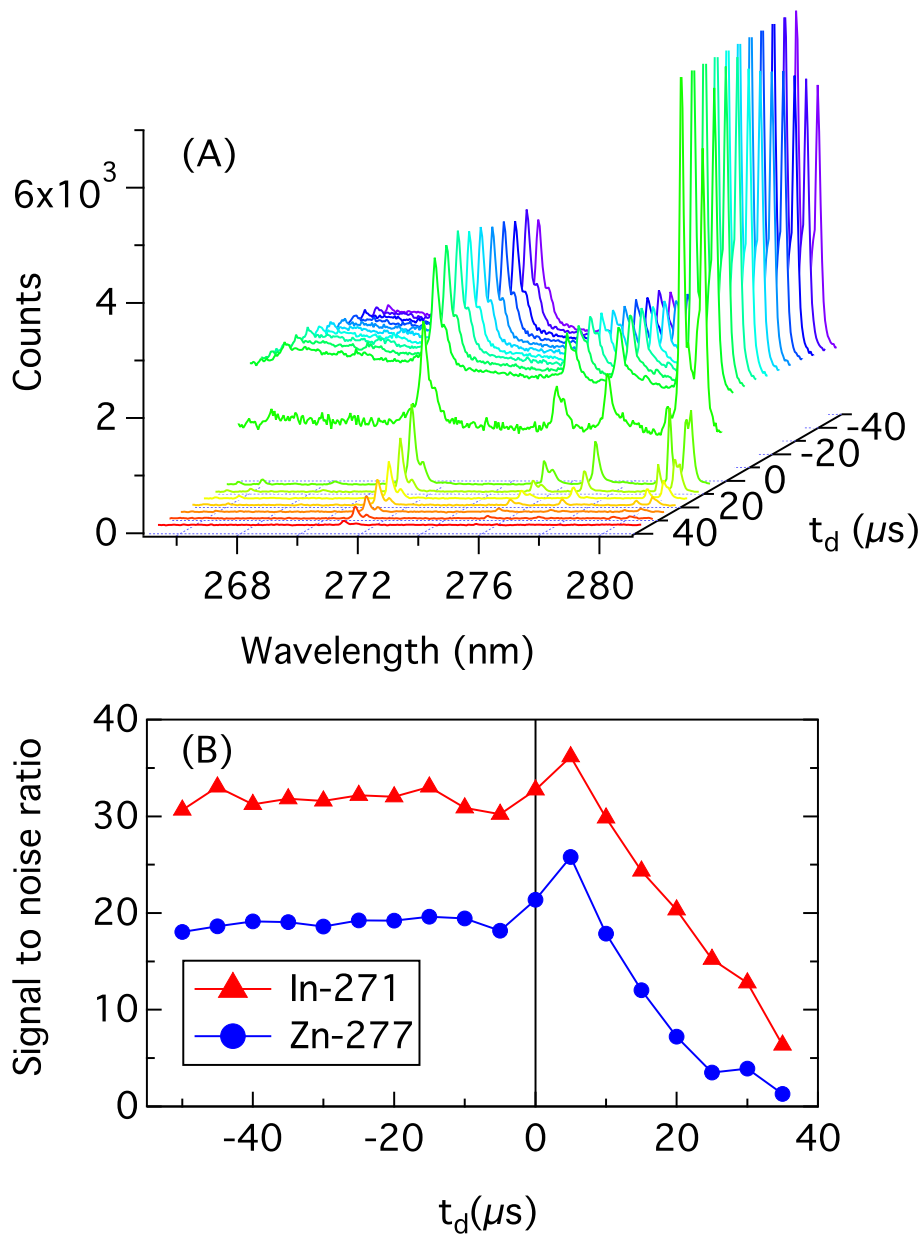


Figure 8.6: Figure 6(A) shows the LIBS spectra as a function of time delay between the start of data acquisition and the laser fire, t_d . $t_d = 0$ corresponds to starting data acquisition when the laser fires, while positive and negative t_d corresponds to starting data acquisition after and before the laser fires. Figure 6(B) shows the signal to noise ratio of Zn-277 nm and In-271 nm lines as a function of t_d as given in Equation 8.1. The optimum time delay is 5 μ s after the laser fires.

8.2 Assumptions and Mathematical Model for Analysis

In order for LIBS quantitative analysis to work, the number of collected characteristic photons must be proportional to the number atoms in the sample. This requirement can be further expanded into two sub-requirements: (1) that the number of characteristic photons emitted is proportional to the number of atoms in the plume, and (2) that the number of atoms in the plume must be proportional to the number of atoms in the sample.

The assumption that the number of detected characteristic photons is proportional to the number of atoms in the plume is reasonable and will be satisfied if the plasma is optically thin, and thus does not reabsorb part of the emitted light. This reabsorption is commonly known in optical spectroscopy as the “plasma shielding effect”, and is a complex function of material composition and plasma conditions [4, 8, 209]. Due to the complexity of plasma dynamics, the common solution to this possible problem is to avoid optically dense plasma by analyzing spectral peaks with lower transition probabilities [1]. Simulations by Riley et. al. [194] suggested lines with transition probability of $< \sim 10^{-7} \text{ s}^{-1}$. As a consequence, the lines are much less affected by reabsorption, but the photon counts will be much lower and signal-to-noise ratio worse. Choosing the right lines is thus very important in ensuring accurate LIBS quantitative analysis. This is the subject of the next section (Section 8.3).

Panne et. al. [177] modeled the characteristic line intensity emitted by the plume using Saha and Boltzmann relationships as follows:

$$\begin{aligned} {}^q\text{Peak Count}_{i,k}^A &= {}^qW^A(T, n_e) \times \frac{g_i^A \times e^{E_i^A/k_B T}}{{}^qZ^A(T)} \\ &\times A_{i,k}^A \times n^A \times \frac{hc}{4\lambda_{i,k}\pi} \end{aligned} \quad (8.2)$$

where ${}^q\text{Peak Count}_{i,k}^A$ is the total number of observed photons associated with a given spectral peak emitted by (ionic) species **A** with ionization state **q**, from upper energy level **i** to energy level **k**. The first term, ${}^qW^A(T, n_e)$ is the probability that the species **A** in the correct ionic state **q** as dictated by the Saha equation. The second term on the right hand side of Equation 8.2

describes the probability that the species \mathbf{A} is in the correct electronic state given that it is in the correct ionization state \mathbf{q} : ${}^qZ^A(T)$ is the electronic partition function of the species that emits the characteristic photon, E_i^A is the energy of the excited electronic state, g_i^A is the degeneracy of the excited electronic state, \mathbf{T} is the local temperature of the plume, and k_B is the Boltzmann constant. The third term, n_A is the number of atoms (ions) in the sample for species \mathbf{A} . Hence, the first three terms in the equation describes the number of particles of species \mathbf{A} in the plume that may produce excited state \mathbf{i} that will relax to produce the characteristic line. The fourth term, $A_{i,k}^A$, is the probability of the transition from excited state \mathbf{i} to lower state \mathbf{k} that produces the characteristic photons. This equation is valid as long as the plume is in local thermodynamic equilibrium (LTE), which is usually satisfied in a LIB plume. For extensive discussion about LTE in the context of LIBS analysis, the readers are referred to [158].

The requirement that the number of atoms in the plume is proportional to the number of atoms in the sample, commonly known as “stoichiometric ablation”, is satisfied as long as the laser energy density is much larger than the chemical bond energies inside the sample, which comprises both the heat of formation of the compounds and the inter-molecular interactions. Chan and Russo et. al. [150] have extensively studied stoichiometric ablation and demonstrated that an ablation is stoichiometric when the laser peak power density on the target exceeds $\sim 10^9 \text{ W cm}^{-2}$, a value that is lower than our laser power by at least an order of magnitude. Additionally, matrix effects, which have been demonstrated to be important for LIBS analysis of certain materials and in other laser-ablation related processes, may be a complex function of composition and structure of the sample [1, 3, 78, 230, 18] and must be taken into account in our analysis.

Additionally, in real experiments, there are other factors that might affect the signal. The equipment optics, in general, will reduce the the characteristic line intensity. In the case of LIBS analysis on thin film samples, film thickness and substrate composition may also be important. For example, if the sample is transparent or semi-transparent and if there are objects underneath the film that contain trace amount of the analyte, then one must worry about the possibility of laser ablation of objects underneath the sample which might alter the signal. An example of such

object is the film substrate itself. Similar concern also arises when the film is so thin that it will completely be ablated in a single laser shot, raising the possibility of ablating part of the substrate in that one shot. Explicitly incorporating these factors into our model, Equation 8.2 becomes:

$$\begin{aligned} {}^q\text{Peak Count}_{i,k}^A &= f(\text{Others}) \times {}^qW^A(T, n_e) \\ &\times \frac{g_i^A \times e^{E_i^A/k_B T}}{{}^qZ^A(T)} \times A_{i,k}^A \times n^A \times \frac{hc}{4\lambda_{i,k}\pi} R2 \end{aligned} \quad (8.3)$$

In general, it is preferred that the variable used in the analysis, usually referred as the “natural variable” of the system, is independent of all factors except the sought-after concentrations of the atomic species. Following a widely accepted approach in the LIBS analysis of bulk materials [1, 3, 8, 230], we will use the ratio of signals from two different species as the natural variable. Hence, in the case of a binary sample, the LIBS natural variable can be expressed as:

$$\begin{aligned} \text{Count Ratio} &= \frac{\text{Count}_{A_1}}{\text{Count}_{A_2}} = \frac{f(A_1)}{f(A_2)} \times \frac{n_{A_1}}{n_{A_2}} \\ &= C \times \frac{1-R_{A_2}}{R_{A_2}} \end{aligned} \quad (8.4)$$

where A_1 and A_2 denote the two species, and C is a calibration constant, and R_{A_2} is the atomic fraction of species A_2 in the sample:

$$R_{A_2} = \frac{n_{A_2}}{n_{A_1} + n_{A_2}} \quad (8.5)$$

In the case of a sample with more than 2 elements, we can choose one reference element to be used throughout the entire analysis as done by Aragon et. al. [8]. The justifications for this approach are as follows:

Following Panne et. al. [177], we shall assume constant and uniform temperature. This was, the temperature-dependent terms in Equation 8.3 will become constants. In practice, there will be some non-uniformity in temperature across the plume, and small differences in plume-to-plume temperature due to shot-to-shot difference in laser power; however, this can reduce

experimentally. Aragon et. al. [8] suggested carefully selecting the characteristic lines for the analysis to reduce sensitivity to these effects and other matrix effects. This will be elaborated in the next Section (Section 8.3). Lastly, taking a ratio also allows us to cancel the effects due to equipment optics.

8.3 Selecting Spectral Peaks for Analysis

There have been discussions on how to choose spectral peaks for analysis to reduce uncertainty due to the plasma dynamics, especially in the case where the LTE and optically thin plasma conditions are not completely satisfied [1, 8]. First, to reduce sensitivity in the Boltzmann term to small variations in the temperature of the plume, it is advised to choose peaks with similar excited energy level and similar wavelengths. Aragon et. al. [8] suggested to use lines whose difference in the excited level energy is less than $\sim 1.5\text{eV}$.

Lines with similar wavelengths will also have similar variations due to the equipment optics; hence, allowing us to cancel the optical effect term in the calculation by taking intensity ratio (Equations 8.3 - 8.4). It is also advantageous to analyze lines that come from the same spectrometer since slight differences in spectrometer performance, such as differences in baseline or CCD response, can also be neglected. This applies here as there are seven spectrometers to cover the entire spectrum.

Second, peaks with low transition probability are less affected by photon re-absorption; however, their intensity tends to be very low, leading to a poor signal-to-noise ratio. Hence, we need to choose a peak that balances the intensity and the uncertainty due to photon reabsorption. Choosing lines with low intensity also ensures that the detector response is still linear.

Another complication in selecting peaks is that most of the LIBS spectral peaks are severely broadened and overlap with one another as is seen in figures 8.2(A) and 8.2(B). Usually, this problem is readily solved using a robust multi-peak fitting routine to de-convolve the unresolved peaks. A recent empirical study by Aragon [8] suggested that Voigt fitting works the best for LIBS spectra. Unfortunately, our spectrometer resolution is only about 0.05 nm per pixel, which is not

Element	λ (nm) (nm)	Upper Lvl (cm^{-1})	Lower Lvl (cm^{-1})	Transition Prob. (s^{-1})
Indium	271	39048.53	2212.598	$\sim 10^{-7}$
Zinc	277	68579.141	32501.399	$< 10^{-7}$

Table 8.2: Energy levels and transition probabilities of In-271 nm and Zn-277 nm lines.

high enough to completely de-convolve most of the overlapping peaks using our Voigt multi-peak fitting routine. Instead, we chose resolvable peaks manually and determine the peak counts using the maximum peak height with baseline subtracted.

Based on these considerations, our choice of In-271 nm and Zn-277 nm lines, shown in figure 8.2(A), were the best candidates for analysis. Table 8.2 summarizes the energy levels and relative intensities of these two lines as found in NIST basic atomic spectroscopic database [188]. Although the energy levels of the upper states that produce these lines were not close together, calculation of the ratio of the Boltzmann terms for these lines shows that at the typical LIB plasma of $\sim 11 \times 10^3$ K [158], the intensity ratio is relatively insensitive to temperature change:

$$\left(\frac{\text{Count}_{\text{In-271}}}{\text{Count}_{\text{Zn-277}}} \right) \times \frac{\partial}{\partial T} \left(\frac{\text{Count}_{\text{In-271}}}{\text{Count}_{\text{Zn-277}}} \right) \sim 3 \times 10^{-3} K^{-1} \quad (8.6)$$

In-271 nm and Zn-277 nm lines were among the most resolvable lines and the neighboring lines have much weaker intensity. Moreover, these particular transitions have good signal-to-noise ratios from all of the calibration samples, whose indium contents ranged from 46 to 86 atomic percent.

8.4 Calibration and Combinatorial Mapping

Calibration was done using ICP-AES because we have extensive experience with calibration and measurement with this system. The calibration process was as follows: from each sample, LIBS spectra were taken from 25 different spots across the single-composition samples, 5 shots at each spot. About one-third of the sample was then dissolved in 0.5 mL of concentrated nitric acid,

the resulting solution was diluted with 5 mL of distilled water, and then analyzed using ICP-AES for indium and zinc content.

The first step of LIBS data processing involves averaging the collected spectra to reduce effects due to random noise. Of the 5 spectra from each spot, the first one was discarded due to possible surface contamination. Because the film was fully ablated and the fourth laser shot might begin to ablate the glass substrate (Figure 8.3), only the second and third spectra from each spot were integrated, and then the integrated spectra from the 25 spots were averaged. These integrated and averaged spectra were then used to get the corresponding In and Zn peak heights and calculate the Zn/In intensity ratios.

Using these ratios and the indium atomic fraction from ICP, we produced a one-to-one map of indium atomic fraction in the sample versus the Zn/In intensity ratio from the LIBS. We fit our mathematical model (Equation 8.4) to this map and extracted the calibration coefficient, which in our case turns out to be 0.390 ± 0.080 (Figure 8.7). The fit is done using an orthogonal distance regression (ODR) algorithm and took into account both the ICP and LIBS intensity ratio uncertainties. The error bar of the LIBS Zn/In intensity ratios were one standard deviation derived from the averaging statistics. The uncertainty from the ICP measurement includes uncertainties related to sample preparation, and were estimated to be roughly 5 at%. Given this estimate for the ICP error, these errors represent a significant contribution to the overall calibration fit, as can be seen in figure 8.7, and account for roughly half of the uncertainty in the calibration coefficient. We can then use this calibration coefficient to get the indium content of any a-IZO sample from Zn/In intensity ratio from the LIBS spectra taken under the same experimental conditions.

Knowing this calibration coefficient, compositional mapping of three combinatorial libraries was performed. Spectra from 20-30 spots were taken and processed in an identical way as we did for the calibration, along the direction where the composition gradient occurs. The process of recording data took about 45 minutes; however, this could easily be reduced to below 10 minutes with full automation. After the spectra were taken, the samples were cut into three parts along the Y direction (perpendicular to the composition gradient) and ICP analysis was done for comparison.

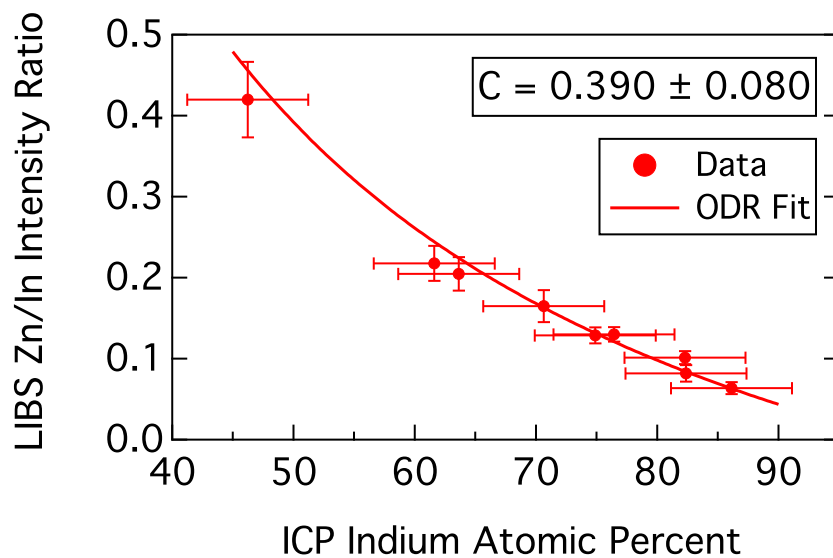


Figure 8.7: LIBS calibration curve. The ratios of the Zn-277nm to In-271nm characteristic lines against indium atomic percent from ICP-AES analysis. Equation 8.4 was fitted to the data and the calibration coefficient extracted. The uncertainty of the calibration coefficient is from orthogonal distance regression (ODR = 2) fit.

We also used one library to compare the LIBS and the more widely-used X-Ray Fluorescence Spectroscopy (XRF) in terms of combinatorial mapping capability. XRF spectra were taken from the combinatorial sample. LIBS spectra were then carefully taken from exactly the same spots on the sample as the XRF measurement. LIBS spectra were taken using the optimized hardware setting, while XRF spectra were acquired for 120 seconds per spot. LIBS compositional analysis was done using the same calibration coefficient as the original experiment. We used highly pure indium and zinc sputtering targets to calibrate the MTFPP software to ensure accurate XRF composition analysis. Lastly, ICP analysis was also done on the sample.

8.5 Results and Discussions

Since the ICP values are averaged over a larger section of film compared to the LIBS, we expect that the LIBS-determined composition will coincide with the ICP analysis result roughly in the middle of each ICP sample section (this is certainly true for a linear composition variation across any given section.) Figure 8.8 shows the result of LIBS compositional map for the three a-IZO combinatorial libraries. It is evident that the LIBS analysis result were not only consistent with ICP analysis, but also produced a finer compositional map, with the ability to resolve differences in composition down to around 1 at% (Figure 8.8). The slight deviations from the ICP results observed in samples L4 are considered insignificant, bearing in mind that the uncertainty associated with the ICP values is approximately ~ 5 at% when errors made during sample preparation are included. Lastly, both compositional analysis results gave indium contents that fall within the expected concentration range, affirming the validity of the analyses.

We noted that there are a few outliers in all samples around $X = 40$ mm and $X = 50$ mm. Although the cause for these outliers is still a subject for further investigation, we found that the glass slides that were used to mount the sample in the chamber were cracked around this X-position. To correct this possible problem, a better scheme for mounting would be to scaffold the sample up by the sample sides.

Figures 8.9 shows the compositional mapping using ICP-AES, LIBS, and XRF on the same

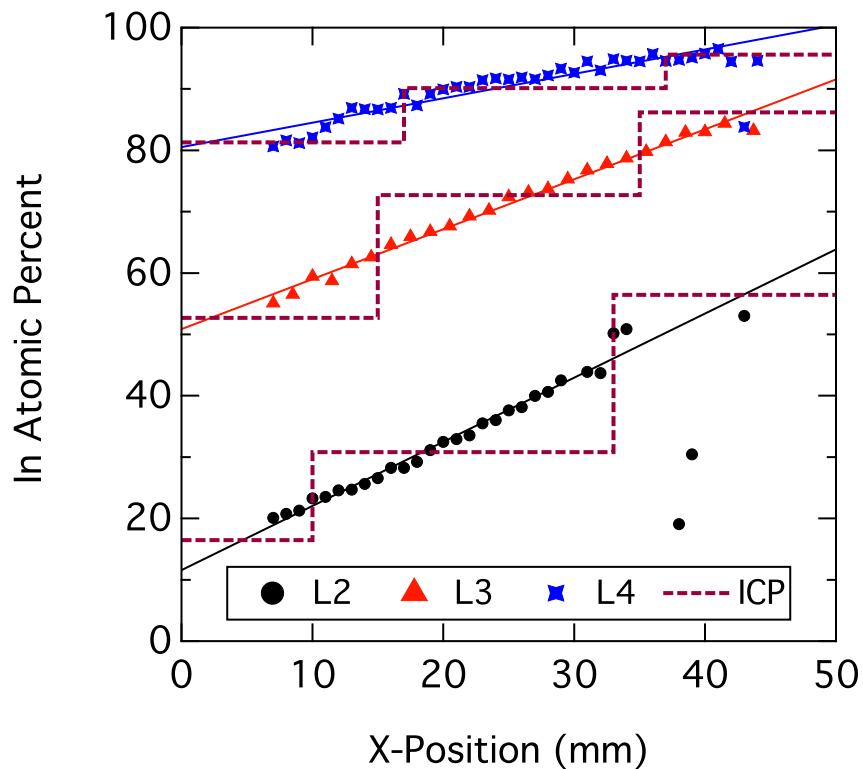


Figure 8.8: LIBS and ICP-AES combinatorial compositional analysis results as a function of position across the sample. Data is taken from 3 combinatorial libraries with different expected indium content. L2, L3 and L4 are expected to have indium content of 15-50 at%, 35-70 at%, and 70-95 at% respectively.

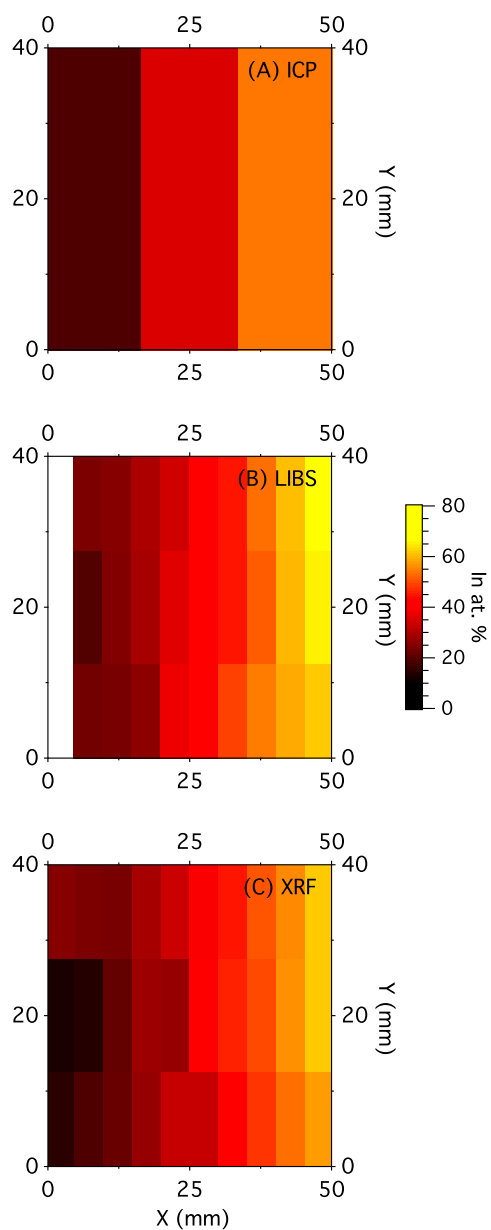


Figure 8.9: 2D Mapping of indium atomic percent in a combinatorial a-IZO sample using (A) ICP-AES, (B) LIBS, and (C) XRF. Note that LIBS mapping consists of 1 less column than the XRF.

sample. These figures clearly demonstrates the advantage of LIBS and XRF over ICP-AES in terms of finer mapping capability. Despite a slight systematic deviation between XRF and LIBS compositional analysis, they generally show similar trends in how the indium composition varied across the sample. At this time, we do not possess the capability to determine precisely whether this systematic difference was due to the LIBS or the XRF, or both.

One clear advantage of LIBS over XRF is the data acquisition time: a total of ~ 10 seconds per spot (for 5 shots per spot), is much shorter than the 120 seconds per spot required of the XRF. Moreover, unlike the XRF, LIBS is able to detect elements lighter than calcium in atmospheric conditions, and even small amount of hydrogen gas in hydrogen-nitrogen mixture [13]. On the other hand, XRF does not do any damage to the sample, while LIBS inflicts local damage. LIBS is therefore best employed in situations where localized damage to the sample can be tolerated, when data acquisition time is crucial, or when light elements are present in the analyte.

8.6 Summary

We have demonstrated that LIBS can be used as a versatile, albeit locally destructive compositional mapping tool for combinatorial thin-film samples, using a-IZO films as a case study. With proper optimization, LIBS can finely map an entire $5 \text{ cm} \times 5 \text{ cm}$ combinatorial library with 1 mm diameter laser spot resolution. The analysis result has been shown to be consistent with ICP and XRF compositional analyses. With data acquisition of about 10 seconds per spot, mapping can be extremely fast with full automation. Moreover, LIBS compositional analysis requires no specific sample preparation.

We also expect the mathematical model employed in this analysis to be largely material independent. However, care should be taken when using this method as it fails, for example, if an analyte-containing substrate is being ablated.

Selection process of the spectral lines for the analysis can be complicated and time-consuming. However, this step is crucial for an accurate analysis and needs to be done only once per material system. The analyzed lines should have similar wavelengths, relatively low intensity while main-

taining good signal-to-noise ratio over different material compositions, and relatively resolvable from neighboring peaks.

Chapter 9

Closing Remarks

Nickel oxide, regardless of its deposition method, can be used for a good hole transport layer for P3HT:PCBM, on par with the traditionally used PEDOT:PSS. Previous results have shown [269, 232] that NiO_x HTL deposited from nickel formate precursor can be superior to PEDOT:PSS, with improvement mainly in the fill factor. In the studies presented here, NiO_x HTL's are deposited by RF sputtering and PLD. Both results in comparable performance with the solution-processed NiO_x and better than PEDOT:PSS. The main improvement is also in fill factor.

Presented below are the key points that emerge from our studies on how the NiO_x HTL's help improve photocurrent extraction in these OPV cells.

9.1 Summary of Main Results

9.1.1 On Energy Level Alignment at HTL / BHJ Interface

HTL improves the device performance primarily through the band-alignment that favors photocurrent extraction and reduces injection / interfacial recombination. All three energy levels (WF, E_c , and E_v) have to be properly “matched” with the given BHJ in order to arrive at optimal photocurrent extraction (§7). For an HTL and after contact, E_v of the BHJ and of the HTL have to be continuous at the interface to ensure maximum photocurrent extraction at any bias, without losing energy to thermalization. E_g of the HTL must also be larger than that of the BHJ to reduce recombination at the interface near V_{oc} . This is equivalent to having E_c of HTL to be closer to vacuum than that of the BHJ. This is illustrated in Fig. 9.1.

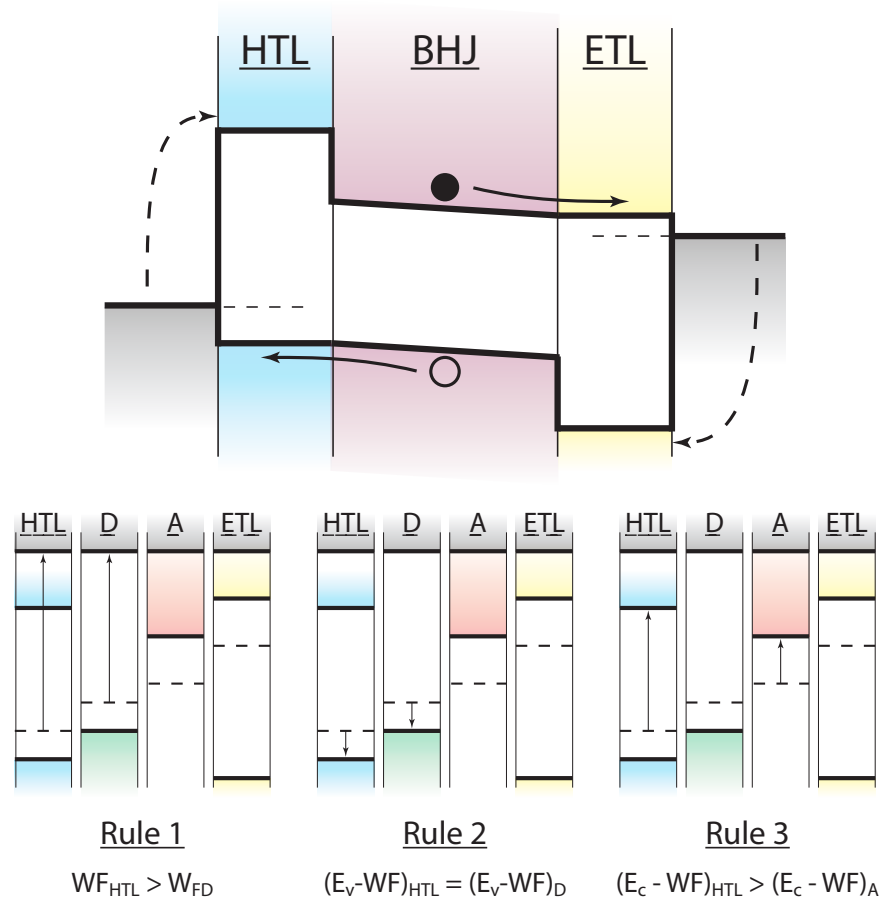


Figure 9.1: An illustration of the proposed optimal energy levels for HTL and ETL in a photovoltaic device after contact. Below, rules on how to achieve the final band alignment assuming the validity of Anderson's rule.

We additionally propose the use of Anderson's rules for band-alignment as recent reports suggest that its validity is quite broad in oxide / organic interfaces. Using the rules, device designers can conjecture what kind of energy levels of each material **before contact** will satisfy the criteria above **after contact**. For an HTL, these matching criteria are:

- (1) High WF \rightarrow increase V_{bi} for extraction of photogenerated carriers
- (2) E_v of HTL = HOMO of donor \rightarrow no extraction / injection barrier
- (3) E_c of HTL < LUMO of acceptor \rightarrow reduce interfacial recombination near V_{oc}
- (4) Clean gap \rightarrow reduce recombination in the bulk of the HTL

These rules are also illustrated in Fig. 9.1. Using simple symmetry argument, the rules for ETL can be derived in a straight-forward manner.

Increasing the WF has been understood to increase V_{bi} . This follows directly from Anderson's rules. Increased V_{bi} is beneficial to photocurrent extraction as it allows for more carrier to be extracted before it recombines [76]. In the case where the WF of the organic being pinned by that of the HTL, no appreciable improvements in device performance is seen (§5. We believe that this is because pinning essentially does not result in further increase in V_{bi} .

In Chp. §7, we saw that the optimal alignment for E_v , in the case for an HTL, is one that is continuous across the interface. If ΔE_v is present such that an extraction barrier evolves, the extracted photocurrent will be reduced, causing a sigmoidal J-V characteristics. On the other hand, if ΔE_v results in an injection barrier from the HTL to the BHJ, the device suffers from extra potential loss due to thermalization, resulting in lower J_{sc} and slightly lower V_{oc} .

The fill-factor improvement over PEDOT:PSS can be understood as due to the electron-blocking capability of the NiO_x . PEDOT:PSS energy levels has been shown to resemble that of a degenerately doped semiconductor, except for the first \AA of PSS top layer [103]. Therefore, near V_{oc} when the built-in field is very low, it is expected that e^-h^+ recombination near the hole collector interface is higher than it is for NiO_x . This results in reduced photocurrent near V_{oc} , and reduced

fill-factor compared to devices employing NiO_x .

Nevertheless, it is impossible to increase fill factor to reach unity. The main limiting factor in fill factor is the lower of the e^- or h^+ diffusion lengths in the active layer¹, which limit the probability that a photogenerated carrier in the volume of the bulk may reach the contact without recombining in the absence of electric field. The aim of using a transport layer is therefore only to **maximize the fill factor up to the value limited by the BHJ**. To obtain very high fill factor beyond this, it is necessary to either increase the absorber carrier diffusion lengths and / or to increase its optical absorbance to allow for thinner absorber layer.

9.1.2 On The Impact of HTL Surface Properties on BHJ Morphology

In order to be able to fairly investigate the effect of the HTL on solar cell performance, it is of utmost importance to make sure that the photogeneration rate over the whole volume of the BHJ is the same across different samples. The rate of carrier photogeneration is influenced by the optical absorption in the BHJ layer and the exciton dissociation efficiency. The first is affected by film thickness and HTL transparency, while the second is mainly affected by the BHJ morphology.

Film thickness and HTL transparency are easily measured. In §5, we see that variations in BHJ thickness has unintentionally led to challenges in data analysis in the study of sputtered NiO_x HTL's. Differences in device performance are eventually concluded to stem from differences in the photocurrent due to differences in the absorber thickness. In §7, we learnt from this experience and minimize the differences in photocarrier generation by making sure that HTL transparencies are similar. This, subsequently leads to clearer data set.

In §6, we assess differences in BHJ morphology through a combination of X-ray diffraction techniques and depth-profile XPS. Primarily, we found that although there are some differences in the BHJ morphology near the interface, there is negligible differences among the films deposited on NiO_x HTL's from different deposition methods / surface treatments. Additionally, all observed structural trends of the bulk of the film are essentially uniform despite the different underlying

¹ Equivalently, their lifetimes and mobilities combined

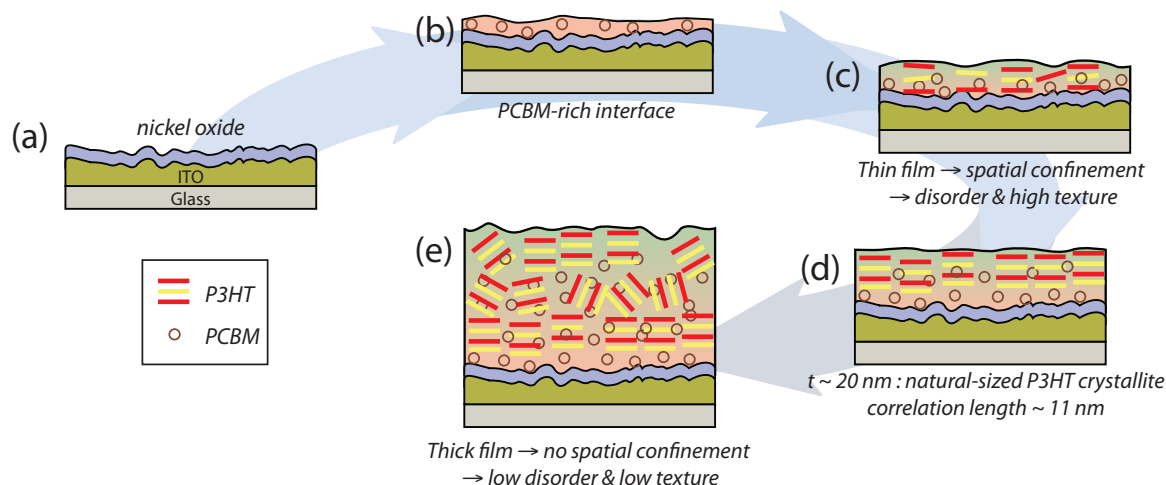


Figure 9.2: Illustration of P3HT:PCBM film formation process

substrates. The only possible outlier is the as-deposited solution-processed NiO_x . This gives us confidence that all of the differences in device performance we observe in §7 are purely due to the properties of the NiO_x themselves.

From this study on the BHJ, we also gather an insight to the film formation process (Fig. 9.2). The highly non-polar nature of P3HT leads to PCBM being more favorably precipitated onto the substrates. Therefore, PCBM is precipitated first from the solution, resulting in a PCBM-rich interface. As more PCBM is precipitated and the solvent starts to dry from the spin-casting process, P3HT starts to precipitate from the solution. At film thickness $t \lesssim 20 \text{ nm}$, the film is highly textured due to spatial confinement, but otherwise is more disordered compared to thick films. This is probably related to the high concentration of PCBM near the interface. Additionally, the polarity mismatch between P3HT and PCBM drives phase separation, resulting in the topmost surface being almost pure P3HT (i.e. the species with lower surface energy). At $t \sim 20 \text{ nm}$, P3HT forms natural-sized crystallites of $\sim 11.0 \text{ nm}$. In films thicker than $\sim 20 \text{ nm}$, film growth is no longer constrained by the low film thickness. This results in lower crystallographic disorder, but lower film texture. The final BHJ films display a vertical composition gradient, starting from PCBM-rich near the buried interface to pure P3HT at the top surface, with slightly different degrees of film texture and

composition near the interface, but otherwise similar despite the differences in the substrate surface properties.

Lastly, we note that our result is very similar to that obtained by Duong et al [55] for the neat P3HT film on Si. The addition of PCBM into the system and the use of rough, high surface energy substrates impact the film morphology in the following ways:

- Vertical phase segregation of P3HT:PCBM due to preferential deposition of PCBM on the oxide surface
- Reduced texture near the interface due to surface roughness and possibly PCBM-rich interface

9.2 Where Do We Go From Here

9.2.1 Optimization Process of Contact Materials for Photovoltaics by Physics-Driven Designs

One of the longer-term goal of this project is to come up with a systematic design and optimization process of contact materials for emerging photovoltaics applications, be it OPV or thin film inorganic. What can we learn from these studies on this front?

The studies presented here highlights the utmost importance of the knowledge of each layer's energy levels in guiding device design. This should be obvious since we achieve the desired control of opto-electronic processes by appropriately tailoring the these energy level profiles (See the introduction of §C, D or the appendices for more illustrative discussions).

We propose that despite their shortcomings, Anderson's rules should be used to get a first guess of contact energy levels in our optimization process. This amounts to start the optimization process by following the rules presented in §7. Fig. 9.3 helps illustrate the proposed design flow process.

We start from a given absorber layer that we would like to match to. The first step in the process is to characterize the energy levels of the absorber. Once this are known, §7 gives the

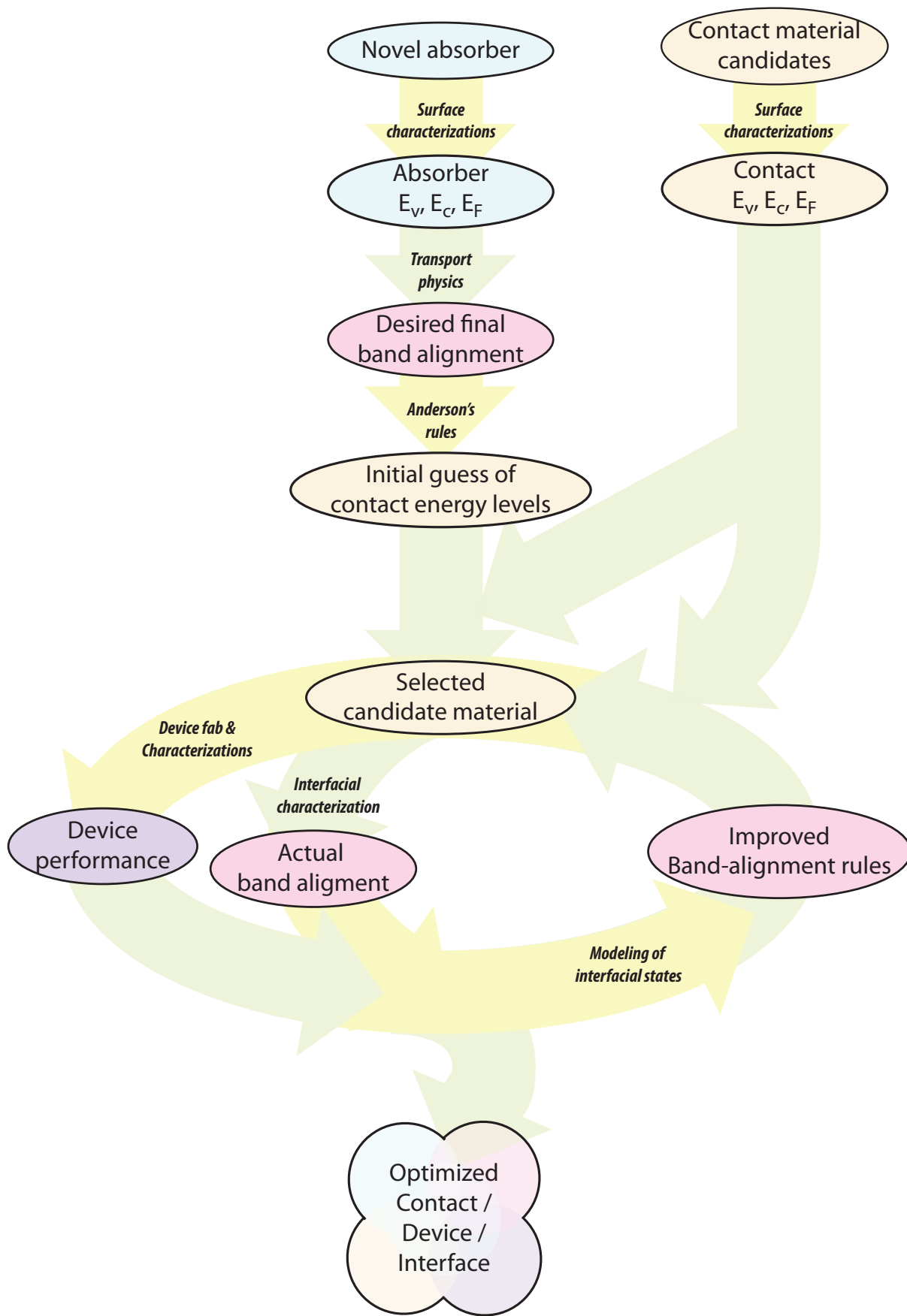


Figure 9.3: Proposed design phase flow for contact optimization.

final band alignment that gives optimal performance. We then use Anderson's rules to guess the appropriate energy levels of the contact materials (these are the enumerated rules presented in §7). We should then proceed to find materials with such properties. A library of candidate materials energy levels will prove to be invaluable.

Devices made with contacts with energy levels close to the desired values should then be fabricated and tested, in the fashion of the investigation in §7. This is to ensure that we really reach the optimal device performance and also serves as a way to test Anderson's rules, which are initially assumed to be valid. The samples can be chosen based on their J-V performance.

Measurements of device properties, such as V_{bi} or barrier height are not only useful, but may also serve as a consistency check. However, we note that for novel technologies, especially one that employs multi-layers, this is practically a mine field. For example, measurement of barrier height by capacitance techniques have been extremely useful in understanding Ga:As technologies. However, the success is based on decades of careful modeling. Obviously, the inputs for these models come from other direct measurements of energy levels, carrier concentrations, etc. Therefore, we cautioned against using capacitance techniques without the support of physical modeling and orthogonal measurement techniques. The use of formula for p-n homojunctions in these heterostructures should also be carefully reconsidered.

Direct measurement of the band-alignment by photoemission, is therefore possibly the most useful way to assess our devices. Whenever possible, it is desirable to perform on select samples the canonical layer-by-layer absorber material deposition with in-situ photoemission studies, especially in the case when validity of Anderson's rules were found to not hold. This type of studies easily reveals formation of interfacial states [263].

The study of such interfacial states is beyond the scope of our investigations. However, we note that these are often modeled as an interfacial electrostatic dipole layer. If one can assess and guess the appropriate magnitude of the dipoles based on the previous run of devices / samples, then one may arrive at an updated guess on the appropriate energy levels that will arrive at the **final** band alignment presented in §7.

The process can then be repeated and is expected to systematically converge to the optimal contact materials for the given absorber. In the process, one will also learn about the nature of band-alignments at these interfaces.

9.2.2 A High-Throughput Approach to Contact Optimizations for OPV

The highly accessible nature of OPV poses a unique challenge. Novel photoactive materials are produced literally every day, a fact which has been the major reason for the rapid increase in OPV PCE in the last decade. How may a device designer keep up with the rapid discoveries of photoactive materials?

High-throughput combinatorial approach to materials and device study may offer a solution to this challenge. At the most basic level, combinatorial material studies are able to efficiently generate vast amount of entries to the material properties database which have been identified as crucial to the device optimization process. A more interesting approach is to actually be able to integrate device characterization to the usual characterizations, i.e. by fabricating devices on these combinatorial samples and be able to measure them. On top of process efficiency, high-throughput approach also reduces experimental uncertainties because multiple samples are literally fabricated and measured simultaneously. The LIBS development presented in §8 is part of an effort to realize the ability to do this.

Fig. 9.4 illustrates the envisioned process. In the example shown, we are varying the film composition by co-sputtering / co-PLD from multiple targets in one direction. The sample is divided into 4 x 11 grids / pixels and shadow masks are used to pattern the films to conform to the device architecture. Film properties are then characterized for each pixel using measurement tools with mapping capability before the rest of the device is deposited to form a complete device. Device performance is consequently measured using appropriate equipment.

Fig. 9.5 will help illustrate the advantage the combinatorial approach. The data are from a preliminary study from 75 P3HT:PCBM devices fabricated on combinatorially grown Zn-Co-O and Ni-Co-O HTL's, at two different deposition temperatures, with and without O₂ plasma

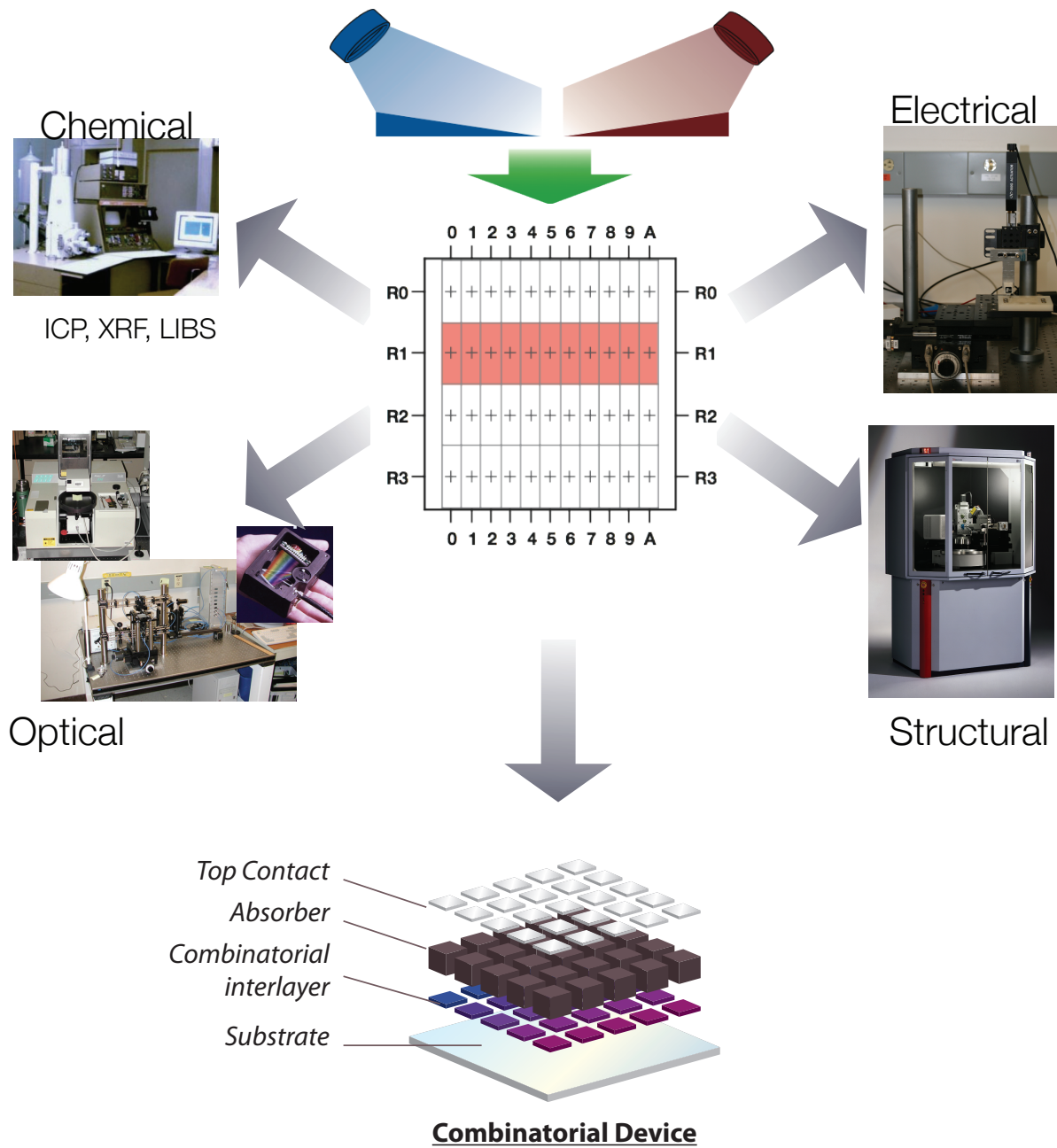


Figure 9.4: Illustration of the processes involved in a combinatorial device study. In the illustrated case, we vary the interlayer property.

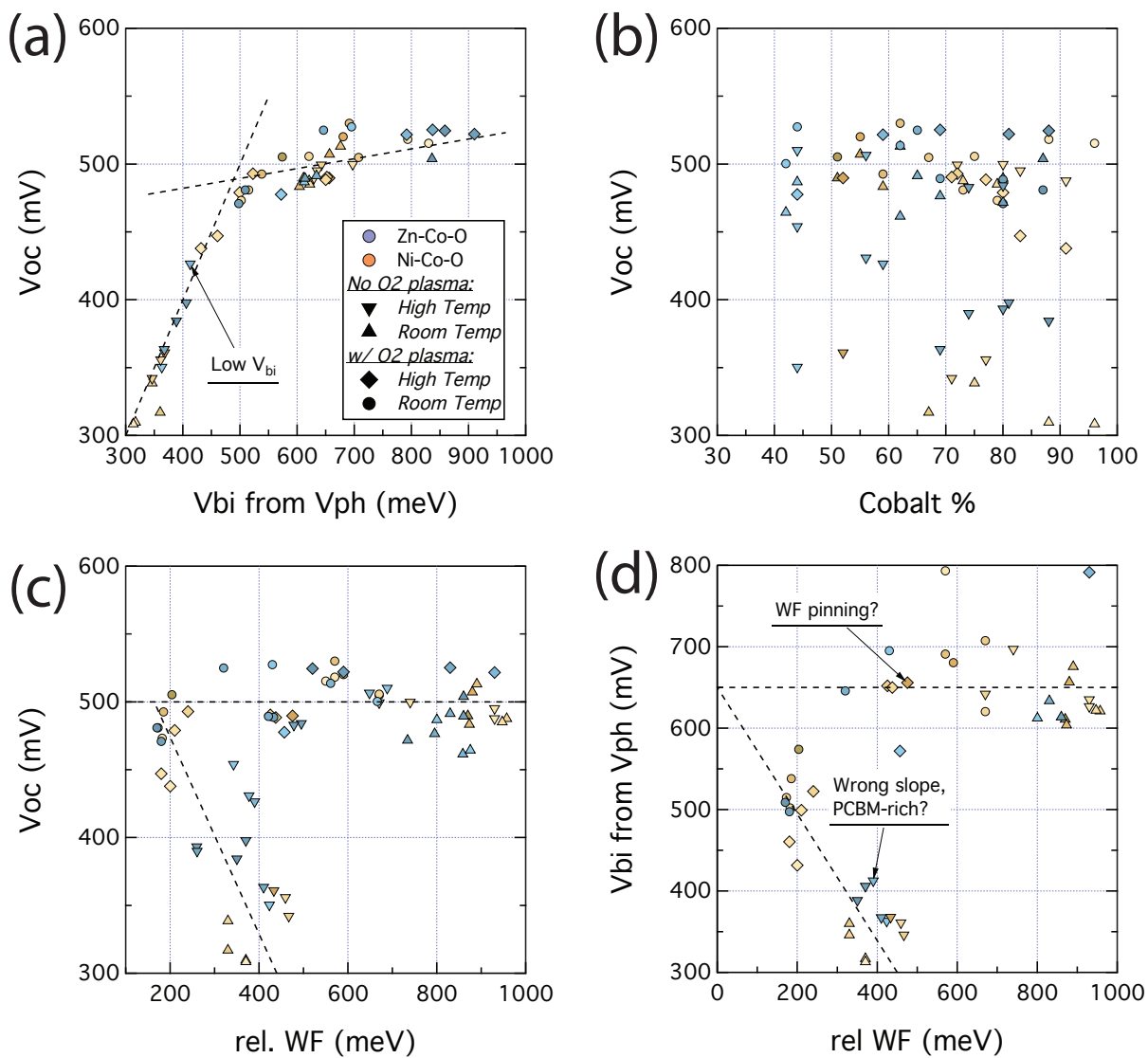


Figure 9.5: Preliminary combinatorial OPV device data. See text for details.

treatment. The 75 devices were fabricated in only 12 depositions in 4 days, demonstrating the high processing efficiency. When the data is plotted against the appropriate X-axis as guided by the design rules stated earlier, we arrive at a trend that is very clear, owing partly to the sheer number of data points. Data points from different material parameters (composition), deposition parameters (T_{sub}), post-treatment (O₂-plasma) that will otherwise seem scattered collapse to form these beautiful trends, underscoring the universality of the underlying physics.

For example, in Fig. 9.5a, we plot V_{oc} of the devices as a function of its V_{bi} as measured using the photovoltage saturation technique. The latter quantity has been suggested to closely approximate V_{bi} across the volume of the BHJ [148]. The correlation between the two quantities is irrevocably clear, in contrast to, say when we plot the data against composition (Fig. 9.5b). The first half where $V_{oc} = V_{bi}$ corresponds exclusively to devices that show sigmoidal J-V characteristics, while the rest are from devices lacking sigmoidal behavior.

From Anderson's rules, V_{oc} is expected to be related to WF . Plotting V_{oc} against WF of the samples (Fig. 9.5a) also produces a respectably clear trend. Again, the flat trend is from devices that does not show sigmoidal behavior. Plotting the V_{bi} against WF suggest that the flat trend is due to pinning. The negative slope of the other trend line is unexpected and demands further investigation. Unfortunately, we could not make any more solid conclusion from this data set alone due to the following technical reasons:

One of the main challenge is to be able to measure the energy levels in high-throughput manner. This can be done, for example, with a dedicated UPS / IPES system or a Kelvin probe/ photoemission set-up to get WF and E_v , and coupled with optical spectroscopy to approximate E_g . In our case, we could only get WF , and therefore did not have any insights into the band-offsets at the interface. We can guess that the sigmoidal J-V characteristics result from an extraction barrier such as that in the case of the NiO_x. However, this claim is never substantiated without any photoemission data.

Another challenge is the possible non-uniformity in the combinatorial samples. Although there are ways to correct for these, it is the author's opinion that it is better to minimize these non-

uniformities. This is because any uncontrolled changes in opto-electronic properties of the material often lead to compound effects. Take for example a difference in HTL optical transmittance. It has a direct effect of reducing the absorption in the BHJ, thus reducing photocurrent. However, if the reduced transmittance is due to increased mid-gap states, then we expect an increased recombination in the HTL, and thus a further decrease in photocurrent. More importantly, when we change the photogeneration rate, then the quasi-Fermi level splitting inside the BHJ is not the same from sample to sample. Therefore, we are not making a fair comparison among samples, and are prone to erroneous conclusion.

The last problem, specific to this sample set and has been addressed in the most current device architecture, is the possibility of cross-talk among device pixels. In the current device patterns, each device is completely isolated, and measurement is done through 40×1 -multiplexer. However, we strongly suggest to improve the measurement system further by incorporating a **true** 4-point sensing. This option is currently unavailable because the multiplexer in the measurement system built by the author supports only up to 80 inputs, while we need 160 inputs to do such measurement of a 40-pixel sample.

9.2.3 Studies on Material Disorders of Various Length Scales and Their Impact on Opto-Electronic Properties

Another topic of interest is a continuation to the studies presented in Chp. §6 related to investigations of material disorders at various length scales and their impact on opto-electronic properties. Disorder of any kind alters the opto-electronic properties of materials. They contribute to conduction in otherwise insulating materials [64, 130, 200], central in photoconductivity [200, 236], reduces the conductivity of crystalline semiconductor, etc. Likewise, disorders also affect opto-electronic properties of organic polymers [162, 197]. Being able to quantify these disorders in a systematic way is therefore of interest.

Lindenmeyer, Beumer, and Hosemann, in the light of the paracrystal theory, suggested that we divide the disorders in a mathematically systematic way into [140]:

- (1) inter-crystal disorder ($g^2(d_k)$)
- (2) inter-plane disorder ($g^2(d_j)$, part of intra-crystal disorder)
- (3) intra-plane disorder ($g^2(d_i)$, part of intra-crystal disorder)

where “planes” refer to be Bragg planes. Hosemann’s paracrystal theory is an attractive foundation for investigations on disorders because it is mathematically precise, it has successfully been applied to organic materials, and it readily connects with statistical mechanics² [97, 140, 95, 14, 98, 99, 96, 92]. The relationship among these disorder types are schematically illustrated in Fig. 9.6a.

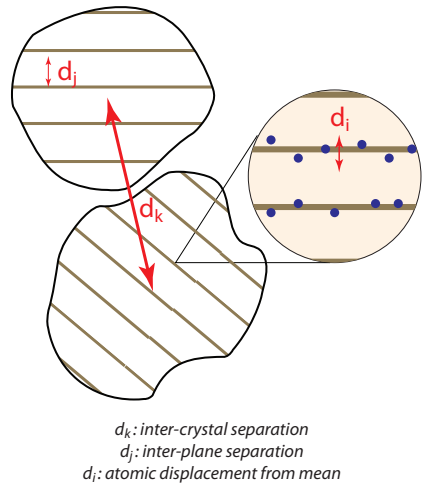
The first entry above is the micro-strain contribution to the disorder, while the combination of the first two terms form the total paracrystallinity in the absence of intra-plane disorders. These can be assessed by XRD and Warren-Averbach analysis [256, 53, 196]. The last term, on the other hand, is neglected in the ideal paracrystal theory. In polymeric systems such as P3HT, this is readily understood to be inter-atomic disorders within the polymer chain, which is very closely related to their optical absorption spectrum [120, 121, 16, 226, 37]. For the case of P3HT polymer, the author proposes to categorize the different types of aggregate disorders into building blocks schematically shown in Fig. 9.6b, where we also note some connections between the paracrystalline theory and the inter- and intra-aggregate disorders commonly discussed in literatures pertaining to optical absorption spectroscopy.

From this point of view, it should not be surprising if the disorder observed via XRD are not correlated with those observed via optical absorption spectroscopy: **although a crystalline material implies aggregation, the converse may not be true.** In the same light, we strongly agree with the suggestion made by Duong et al. to strictly differentiate “crystallite” from “aggregate”, and “crystalline” from “aggregated” [55].

In the course of the investigations that lead to Chp. §6, we have also measured the absorption spectra of P3HT:PCBM grown on the different NiO_x samples. Unfortunately, we had not been able to understand fully the trends (or lack of thereof) that we observe. We shall briefly describe the

² Hosemann treat disorders in a statistical way.

(a)



EQUATIONS RELATED TO THEORY OF PARACRYSTALS

* *Ideal paracrystal theory neglects intra-plane disorders:*

$$g_{tot}^2 = \frac{\langle d^2 \rangle_{ijk} - \langle d \rangle_{ijk}^2}{\langle d \rangle_{ijk}^2} \quad \langle d \rangle_{ijk} = \frac{1}{IJK} \sum_i \sum_j \sum_k d_{ijk}$$

$$g_{para}^2 = \frac{\langle d^2 \rangle_{jk} - \langle d \rangle_{jk}^2}{\langle d \rangle_{jk}^2} \quad \langle d \rangle_{ij} = \frac{1}{IJ} \sum_i \sum_j d_{ij}$$

$$\langle d \rangle_i = \frac{1}{I} \sum_i d_i$$

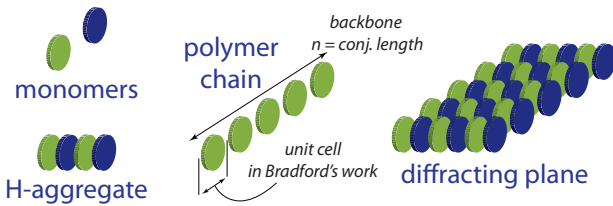
* *Disorders of different length-scales:*

$$g^2 = \frac{\langle d^2 \rangle_{ijk} - \langle \langle d \rangle_i^2 \rangle_{jk}}{\langle d \rangle_{ijk}^2} + \frac{\langle \langle d \rangle_i^2 \rangle_{jk} - \langle \langle d \rangle_{ij} \rangle_k}{\langle d \rangle_{ijk}^2} + \frac{\langle \langle d \rangle_{ij} \rangle_k - \langle d \rangle_{ijk}^2}{\langle d \rangle_{ijk}^2}$$

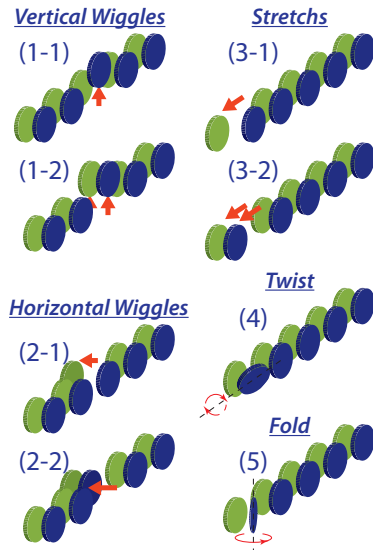
$$= g^2(d_i) + g^2(d_j) + g^2(d_k)$$

(Note that these are not equal to variances!)

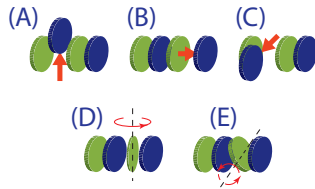
(b)



INTRA-PLANE DISORDER



INTRA-AGGREGATE DISORDER



NOTES:

- * (1-1) & (1-2) are also vertical folds
- * Some disorder types may not be physical
- * Other disorders are combo of these

INTRA-AGG. vs INTRA-PLANE

Connects paracrystalline theory with UV-Vis absorption spectroscopy

- (A) = (1-1) (D) = (4)
- (B) = (2-1) (E) = (5)
- (C) = (3-1)

(1-2), (2-2), (3-2) are inter-aggregate disorders

INTRA-PLANE vs INTER-PLANE

Intra-plane disorders that may result in {100} inter-plane disorders (lamellar structure assumed):

- (1-1), (1-2), (4)

Figure 9.6: (a) Illustration of the various distances in a material and the disorders related to them. (b) Building blocks of short-range disorders.

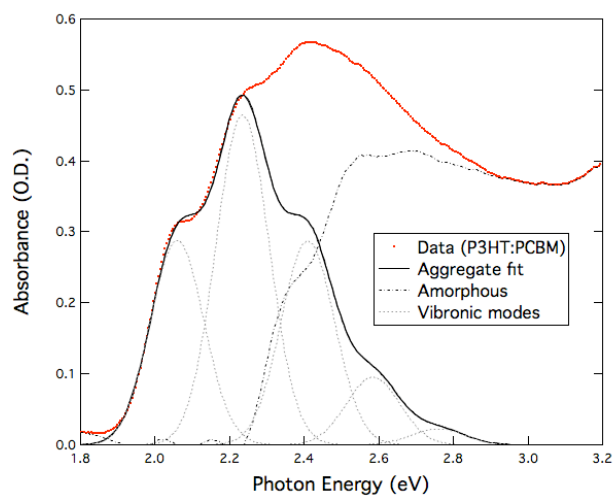


Figure 9.7: Spano fit of P3HT:PCBM data.

data analysis that we have done so far, as to help accelerate future research:

We followed the procedure suggested by Clark et al. to fit these data and extract information about P3HT aggregates in the film [37]. An example of such fit is shown in Fig. 9.7a. The extracted fit parameters of interest are:

- **Absorption amplitude**, C – amount of aggregates in the film
- **Exciton bandwidth**, W – conjugation length, inter-aggregate disorder [16, 19]
- **Electronic transition energy**, E_{0-0} – close to P3HT E_g
- **Linewidth**, σ – Standard deviation of distribution of E_{0-0}
- **Vibrational energy**, E_p – Held constant, close to $180 \pm 5 \text{ meV}$ for P3HT

C can be seen to be linearly dependent on film thickness, as expected. The area under the fitted curve has been used to estimate the amount of aggregates in the film [37, 55]. The procedure requires the additional knowledge of the difference in index of refraction of the aggregated vs. non-aggregated phase. The procedure to obtain this is outlined in the Supplementary Information for Ref. [37]. In our case, this cannot be done because of the presence of an additional broad PCBM peak at higher energy that is superimposed on the non-aggregated P3HT part of the spectrum and close to the absorption edge of the glass. This is unfortunate since the fraction aggregate might be a physical quantity that can be directly related to electrical properties of the film.

W has often been correlated with degree of crystallinity, but from the previous discussion this may not be true. Correlation with crystallite size from XRD is not expected either since the latter measures the correlation length in the direction perpendicular to the back-bone. Duong et al's interpretation as the average c-axis length of the crystalline is more correct, provided that termination of conjugation always happens at the edge of a crystallite. We do not see any clear correlation between W with any other fit parameters, including that from XRD.

At this point, we are not certain of the physical mechanisms related to the linewidth. However, it seems to be related to both inter-aggregate and intra-aggregate disorders through another

parameter l_0 [120, 121, 227]. Ref. [227], however, suggests that intra-aggregate disorders are more readily observed from changes in the emission spectra and is weak in absorption spectra.

An interesting study would have been to quantify these different disorders at different length scales to the electrical performance (conductivity, mobility, carrier concentration) and/or energy levels of the film. Since P3HT is essentially a 2D semiconductor, it would have been also be very interesting to investigate the degree of anisotropy of these electrical performance. The addition of PCBM is expected, to some degree, to add disorder into the P3HT system. Its impact may also be an interesting case study that may perhaps lead to a molecular-level device.

Bibliography

- [1] S Acquaviva, E D Anna, M L De Giorgi, and F Moro. Laser-induced breakdown spectroscopy for compositional analysis of multielemental thin films. Spectrochimica Acta Part B, 61:810 – 816, 2006.
- [2] D Adler and J Feinleib. Electrical and optical properties of narrow-band materials. Physical Review B, 2(8):3112–3134, 1970.
- [3] J A Aguilera, C Aragon, and J Campos. Determination of Carbon Content in Steel Using Laser-Induced Breakdown Spectroscopy. Applied Spectroscopy, 46(9):3–8, 1992.
- [4] J A Aguilera, C Aragon, and F Penalba. Plasma shielding effect in laser ablation of metallic samples and its influence on LIBS analysis. Applied Surface Science, pages 309–314, 1998.
- [5] ZI Alferov. Nobel Lecture : The double heterostructure concept and its applications in physics , electronics , and technology. Reviews of modern physics, 73(July):767–782, 2001.
- [6] J. S. Anderson and D. F. Klemperer. Photoelectric Measurements on Nickel and Nickel Oxide Films. Proceedings of the Royal Society A: Mathematical, Physical and Engineering Sciences, 258(1294):350–376, October 1960.
- [7] RL Anderson. Experiments on Ge-GaAs heterojunctions. Solid-State Electronics, 5:341–351, 1962.
- [8] C Aragon, J A Aguilera, and F Penalba. Improvements in Quantitative Analysis of Steel Composition by Laser-Induced Breakdown Spectroscopy at Atmospheric Pressure Using an Infrared Nd : YAG Laser. Applied Spectroscopy, 53(10):1259–1267, 1999.
- [9] Neal R Armstrong, P Alex Veneman, Erin Ratcliff, Diogenes Placencia, and Michael Brumbach. Oxide contacts in organic photovoltaics: characterization and control of near-surface composition in indium-tin oxide (ITO) electrodes. Accounts of chemical research, 42(11):1748–57, November 2009.
- [10] Neil W. Ashcroft and N. David Mermin. Solid State Physics. Saunders, 1976.
- [11] E. Avendano, A. Azens, G. a. Niklasson, and C. G. Granqvist. Proton Diffusion and Electrochromism in Hydrated NiOx and Ni[1x]VxOy Thin Films. Journal of The Electrochemical Society, 152(12):F203, 2005.

- [12] Jessy L Baker, Leslie H Jimison, Stefan Mannsfeld, Steven Volkman, Shong Yin, Vivek Subramanian, Alberto Salleo, A Paul Alivisatos, and Michael F Toney. Quantification of thin film crystallographic orientation using X-ray diffraction with an area detector. Langmuir, 26(11):9146–51, June 2010.
- [13] A J Ball, V Hohreiter, and D W Hahn. Hydrogen Leak Detection Using Laser-Induced Breakdown Spectroscopy. Applied Spectroscopy, 59(3):348–353, 2005.
- [14] FJ Baltá-Calleja and R Hosemann. The limiting size of natural paracrystals. Journal of Applied Crystallography, 13:521–523, 1980.
- [15] World Bank. Energy use (kg of oil equivalent per capita), 2012.
- [16] William Barford. Exciton transfer integrals between polymer chains. The Journal of chemical physics, 126(13):134905, April 2007.
- [17] A. Baszkin and L. Ter-Minassian-Saraga. Effect of surface polarity on self-adhesion of polymers. Polymer, 19(9):1083–1088, September 1978.
- [18] H E Bauer, F Leis, and K Niemax. Laser induced breakdown spectrometry with an echelle spectrometer and intensified charge coupled device detection. Spectrochimica Acta B, 53:1815–1825, 1998.
- [19] D. Beljonne, J. Cornil, R. Silbey, P. Millie, and J. L. Bredas. Interchain interactions in conjugated materials: The exciton model versus the supermolecular approach. The Journal of Chemical Physics, 112(10):4749, 2000.
- [20] Joseph J. Berry, N. Edwin Widjonarko, Brian A. Bailey, Ajaya K. Sigdel, David S. Ginley, and Dana C. Olson. Surface Treatment of NiO Hole Transport Layers for Organic Solar Cells. IEEE Journal of Selected Topics in Quantum Electronics, 16(6):1649–1655, November 2010.
- [21] Rafael Betancur, Marc Maymó, Xavier Elias, Luat T. Vuong, and Jordi Martorell. Sputtered NiO as electron blocking layer in P3HT:PCBM solar cells fabricated in ambient air. Solar Energy Materials and Solar Cells, 95(2):735–739, February 2011.
- [22] Bharat Bhushan and Yong Chae Jung. Wetting study of patterned surfaces for superhydrophobicity. Ultramicroscopy, 107(10-11):1033–41, October 2007.
- [23] Mark C. Biesinger, Brad P. Payne, Leo W. M. Lau, Andrea Gerson, and Roger St. C. Smart. X-ray photoelectron spectroscopic chemical state quantification of mixed nickel metal, oxide and hydroxide systems. Surface and Interface Analysis, 41(4):324–332, April 2009.
- [24] P. W. M. Blom, V. D. Mihailetschi, L. J. a. Koster, and D. E. Markov. Device Physics of Polymer:Fullerene Bulk Heterojunction Solar Cells. Advanced Materials, 19(12):1551–1566, June 2007.
- [25] Nicolas Blouin, Alexandre Michaud, David Gendron, Salem Wakim, Emily Blair, Rodica Neagu-plesu, Michel Belleste, Gilles Durocher, Ye Tao, and Mario Leclerc. Toward a Rational Design of Poly (2,7-Carbazole) Derivatives for Solar Cells. Journal of American Chemical Society, (130):732–742, 2008.

- [26] Gerrit Boschloo and Anders Hagfeldt. Spectroelectrochemistry of Nanostructured NiO. Journal of Physical Chemistry B, 105:3039–3044, 2001.
- [27] AJ Bosman and HJ Van Daal. Small-polaron versus band conduction in some transition-metal oxides. Advances in Physics, 19(77):1–117, 1970.
- [28] Christoph J. Brabec. Organic photovoltaics: technology and market. Solar Energy Materials and Solar Cells, 83(2-3):273–292, June 2004.
- [29] JC Bruyere and BK Chakraverty. Switching and negative resistance in thin films of nickel oxide. Applied Physics Letters, 16(1), 1970.
- [30] MJ Buerger. The correction of x-ray diffraction intensities for Lorentz and polarization factors. Proc. National Academy of Science of the National Academy of Sciences of the United States, 26:637–642, 1940.
- [31] D. Cahen and A. Kahn. Electron Energetics at Surfaces and Interfaces: Concepts and Experiments. Advanced Materials, 15(4):271–277, February 2003.
- [32] Mariano Campoy-Quiles, Toby Ferenczi, Tiziano Agostinelli, Pablo G Etchegoin, Youngkyoo Kim, Thomas D Anthopoulos, Paul N Stavrinou, Donal D C Bradley, and Jenny Nelson. Morphology evolution via self-organization and lateral and vertical diffusion in polymer:fullerene solar cell blends. Nature materials, 7(2):158–64, February 2008.
- [33] Michael L. Chabinyc, Robert A. Street, and John E. Northrup. Effects of molecular oxygen and ozone on polythiophene-based thin-film transistors. Applied Physics Letters, 90(12):123508, 2007.
- [34] HL Chang, TC Lu, HC Kuo, and SC Wang. Effect of oxygen on characteristics of nickel oxide indium tin oxide heterojunction diodes. Journal of Applied Physics, 100(124503):1–5, 2006.
- [35] S A Choulis, J Nelson, Y Kim, D Poplavskyy, T Kreouzis, J R Durrant, and D D C Bradley. Investigation of transport properties in polymer/fullerene blends using time-of-flight photocurrent measurements. Applied Physics Letters, 83(18):3812–3814, 2003.
- [36] St.G. Christoskova, N. Danova, M. Georgieva, O.K. Argirov, and D. Mehandzhiev. Investigation of a nickel oxide system for heterogeneous oxidation of organic compounds. Applied Catalysis A: General, 128(2):219–229, August 1995.
- [37] Jenny Clark, Jui-Fen Chang, Frank C. Spano, Richard H. Friend, and Carlos Silva. Determining exciton bandwidth and film microstructure in polythiophene films using linear absorption spectroscopy. Applied Physics Letters, 94(16):163306, 2009.
- [38] BE Conway and PL Bourgault. The electrochemical behavior of the nickel/nickel oxide electrode: part I. Kinetics of self-discharge. Canadian Journal of, 37, 1959.
- [39] BE Conway and MA Sattar. Electrochemistry of the nickel oxide electrode*: Part VIII. Stoichiometry of thin film oxide layers. Journal of Electroanalytical Chemistry, 19:351–364, 1968.
- [40] BE Conway, MA Sattar, and D Gilroy. Electrochemistry of the nickel-oxide electrode—V. Self-passivation effects in oxygen-evolution kinetics. Electrochimica Acta, 14(March 1968), 1969.

- [41] BE Conway, MA Sattar, and D Gilroy. Electrochemistry of the nickel-oxide electrode–VII. Potentiostatic step method for study of adsorbed intermediates. Electrochimica Acta, 14(March 1968):711–724, 1969.
- [42] David A Cremers and Leon J Radzlemekl. Detection of Chlorine and Fluorine in Air by Laser-Induced Breakdown Spectrometry. Analytical Chemistry, 55(8):1252–1256, 1983.
- [43] BD Cullity. Elements of X-ray Diffraction. 2nd edition, 1977.
- [44] Andrea Damascelli. Probing the Electronic Structure of Complex Systems by ARPES. Physica Scripta, T109:61, 2004.
- [45] Andrea Damascelli, Z Hussain, and ZX Shen. Angle-resolved photoemission studies of the cuprate superconductors. Reviews of Modern Physics, 75(April):473–541, 2003.
- [46] Minh Trung Dang, Lionel Hirsch, and Guillaume Wantz. P3HT:PCBM, Best Seller in Polymer Photovoltaic Research. Advanced Materials, 23(31):3597–3602, August 2011.
- [47] P. S. Davids, I. H. Campbell, and D. L. Smith. Device model for single carrier organic diodes. Journal of Applied Physics, 82(12):6319, 1997.
- [48] P. S. Davids, A. Saxena, and D. L. Smith. Nondegenerate continuum model for polymer light-emitting diodes. Journal of Applied Physics, 78(6):4244, 1995.
- [49] P. S. Davids, A. Saxena, and D. l. Smith. Bipolaron lattice formation at metal-polymer interfaces. Physical Review B, 53(8):4823–4833, February 1996.
- [50] Carsten Deibel and Vladimir Dyakonov. Polymerfullerene bulk heterojunction solar cells. Reports on Progress in Physics, 73(9):096401, September 2010.
- [51] RM Dell and FS Stone. The adsorption of gases on nickel oxide. Transactions of the Faraday Society, 50:501–510, 1954.
- [52] G Dennler, A Mozer, G Juska, A Pivrikas, R Osterbacka, A Fuchsbauer, and N Sariciftci. Charge carrier mobility and lifetime versus composition of conjugated polymer/fullerene bulk-heterojunction solar cells. Organic Electronics, 7(4):229–234, August 2006.
- [53] VA Drits, DD Eberl, and J Srodon. XRD measurement of mean thickness, thickness distribution and strain for illite and illite-smectite crystallites by the Bertaut-Warren-Averbach technique. Clays and Clay Minerals, 46:38–50, 1998.
- [54] M. E. Dry and F. S. Stone. Oxidation reactions catalyzed by doped nickel oxide. Discussions of the Faraday Society, 28:192, 1959.
- [55] Duc T. Duong, Michael F. Toney, and Alberto Salleo. Supporting info for: Role of confinement and aggregation in charge transport in semicrystalline polythiophene thin films. Physical Review B, 86(20):205205, November 2012.
- [56] Titas Dutta, P. Gupta, A. Gupta, and J. Narayan. Effect of Li doping in NiO thin films on its transparent and conducting properties and its application in heteroepitaxial p-n junctions. Journal of Applied Physics, 108(8):083715, 2010.

- [57] Klaus Ellmer. Transparent Conductive Zinc Oxide and Its Derivatives. In Handbook of Transparent Conductors, chapter 7. 2010.
- [58] Keith Emery. Measurement and Characterization of Solar Cells and Modules. In Steven S Hegedus and Antonio Luque, editors, Handbook of Photovoltaic Science and Engineering, chapter 16. 2003.
- [59] Tobias Erb, Uladzimir Zhokhavets, Gerhard Gobsch, Sofiya Raleva, Bernd Stühn, Pavel Schilinsky, Christoph Waldauf, and Christoph J Brabec. Correlation Between Structural and Optical Properties of Composite Polymer / Fullerene Films for Organic Solar Cells. Advanced Functional Materials, 15:1193–1196, 2005.
- [60] T. Eto, S. Endo, M. Imai, Y. Katayama, and T. Kikegawa. Crystal structure of NiO under high pressure. Physical Review B, 61(22):14984–14988, June 2000.
- [61] RB Fahim and AI Abu-Shady. Surface area and pore structure of nickel oxide. Journal of Catalysis, 17:10–17, 1970.
- [62] Pascal Fichet, Denis Menut, Evelyne Vors, and Annie Rivoallan. Analysis by laser-induced breakdown spectroscopy of complex solids , liquids , and powders with an echelle spectrometer. Applied Optics, 42(30):6029–6035, 2003.
- [63] S. J. Fonash and S. Ashok. An additional source of photovoltage in photoconductive materials. Applied Physics Letters, 35(7):535, 1979.
- [64] J. Frenkel. On pre-breakdown phenomena in insulators and electronic semi-conductors. Physical Review, 54(8):647–648, 1938.
- [65] Atsushi Fujimori and Fujio Minami. Valence-band photoemission and optical absorption in nickel compounds. Physical Review B, 30(2):957–971, 1984.
- [66] Germà Garcia-Belmonte, A Munar, E Barea, J Bisquert, I Ugarte, and R Pacios. Charge carrier mobility and lifetime of organic bulk heterojunctions analyzed by impedance spectroscopy. Organic Electronics, 9(5):847–851, October 2008.
- [67] Germà Garcia-Belmonte, Eduard V. Vakarin, Juan Bisquert, and J.P. Badiali. Doping-induced broadening of the hole density-of-states in conducting polymers. Electrochimica Acta, 55(21):6123–6127, August 2010.
- [68] David S. Germack, Calvin K. Chan, R. Joseph Kline, Daniel a. Fischer, David J. Gundlach, Michael F. Toney, Lee J. Richter, and Dean M. DeLongchamp. Interfacial Segregation in Polymer/Fullerene Blend Films for Photovoltaic Devices. Macromolecules, 43(8):3828–3836, April 2010.
- [69] N C Giebink, G P Wiederrecht, M R Wasielewski, and S R Forrest. Ideal diode equation for organic heterojunctions. I. Derivation and application. Physical Review B, 82(155305):1–12, 2010.
- [70] NC Giebink, BE Lassiter, GP Wiederrecht, MR Wasielewski, and SR Forrest. Ideal diode equation for organic heterojunctions. II. The role of polaron pair recombination. Physical Review B, 82(15):155306, 2010.

- [71] David S. Ginley. Preface and Table of Contents. In David S. Ginley, editor, Handbook of Transparent Conductors. Springer US, Boston, MA, 2011.
- [72] David S Ginley and John D Perkins. Transparent Conductors. In David S. Ginley, editor, Handbook of Transparent Conductors, chapter 1, pages 1–25. Springer US, Boston, MA, 2011.
- [73] L. A. Girifalco and Robert J. Good. A Theory for Estimation of Surface and Interfacial Energies. I: Derivation and Application to Interfacial Tension. Journal of Physical Chemistry, 61:904–909, May 1957.
- [74] M. Glatthaar, M. Riede, N. Keegan, K. Sylvester-Hvid, B. Zimmermann, M. Niggemann, A. Hinsch, and A. Gombert. Efficiency limiting factors of organic bulk heterojunction solar cells identified by electrical impedance spectroscopy. Solar Energy Materials and Solar Cells, 91(5):390–393, March 2007.
- [75] R.J. Good and LA Girifalco. A theory for estimation of surface and interfacial energies. III. Estimation of surface energies of solids from contact angle data. The Journal of Physical Chemistry, 64(5):561–565, 1960.
- [76] A.M. Goodman and A. Rose. Double Extraction of Uniformly Generated Electron-Hole Pairs from Insulators with Noninjecting Contacts. Journal of Applied Physics, 42(7):2823–2830, 1971.
- [77] Claes G Granqvist. Applications of Transparent Conductors to Solar Energy and Energy Efficiency. In David S. Ginley, editor, Handbook of Transparent Conductors, chapter 11. Springer US, Boston, MA, 2011.
- [78] Kenneth J Grant, George L Paul, and James O’Neill. Quantitative Elemental Analysis of Iron Ore by Laser-Induced Breakdown Spectroscopy. Applied Spectroscopy, 45(4):701–705, 1991.
- [79] B.A. Gregg. Excitonic solar cells. Journal of Physical Chemistry B, 107(20):4688–4698, March 2003.
- [80] Brian A. Gregg. Entropy of Charge Separation in Organic Photovoltaic Cells: The Benefit of Higher Dimensionality. The Journal of Physical Chemistry Letters, 2(24):3013–3015, December 2011.
- [81] Mark T. Greiner, Michael G. Helander, Wing-Man Tang, Zhi-Bin Wang, Jacky Qiu, and Zheng-Hong Lu. Universal energy-level alignment of molecules on metal oxides. Nature Materials, 10(11):1–6, November 2011.
- [82] Ze-Lei Guan, Jong Bok Kim, He Wang, Cherno Jaye, Daniel a. Fischer, Yueh-Lin Loo, and Antoine Kahn. Direct determination of the electronic structure of the poly(3-hexylthiophene):phenyl-[6,6]-C61 butyric acid methyl ester blend. Organic Electronics, 11(11):1779–1785, November 2010.
- [83] Serap Gunes, Helmut Neugebauer, and Niyazi Serdar Sariciftci. Conjugated Polymer-Based Organic Solar Cells. Chemical Reviews, 107:1324–1338, 2007.

- [84] David B. Hall, Patrick Underhill, and John M. Torkelson. Spin coating of thin and ultrathin polymer films. Polymer Engineering & Science, 38(12):2039–2045, December 1998.
- [85] Scott R. Hammond, Jens Meyer, N. Edwin Widjonarko, Paul F. Ndione, Ajaya K. Sigdel, Andrés Garcia, Alexander Miedaner, Matthew T. Lloyd, Antoine Kahn, David S. Ginley, Joseph J. Berry, and Dana C. Olson. Low-temperature, solution-processed molybdenum oxide hole-collection layer for organic photovoltaics. Journal of Materials Chemistry, 22(7):3249, 2012.
- [86] H. Hartnagel. Semiconducting transparent thin films. Institute of Physics Pubs., Philadelphia, 1995.
- [87] B.B. He, J.H. Reibenspies, and N. Bhuvanesh. Two-dimensional X-ray Diffraction. Powder Diffraction, 25:200, 2010.
- [88] Christine He, David S. Germack, R. Joseph Kline, Dean M. Delongchamp, Daniel a. Fischer, Chad R. Snyder, Michael F. Toney, James G. Kushmerick, and Lee J. Richter. Influence of substrate on crystallization in polythiophene/fullerene blends. Solar Energy Materials and Solar Cells, 95(5):1375–1381, May 2011.
- [89] Huan He, Shaogui Yang, Kai Yu, Yongming Ju, Cheng Sun, and Lianhong Wang. Microwave induced catalytic degradation of crystal violet in nano-nickel dioxide suspensions. Journal of Hazardous Materials, 173:393–400, 2010.
- [90] J J Heizmann, A Vadon, D Schlatter, and J Bessieres. Texture analysis of thin films and surface layers by low incidence angle X-ray diffraction. In GAPF, 1988.
- [91] C Herring and MH Nichols. Thermionic emission. Reviews of Modern Physics, 21(2), 1949.
- [92] AM Hindeleh and R Hosemann. Paracrystals representing the physical state of matter. Journal of Physics C: Solid State Physics, 21:4115–4170, 1988.
- [93] V Hohreiter, J E Carranza, and D W Hahn. Temporal analysis of laser-induced plasma properties as related to laser-induced breakdown spectroscopy. Spectrochimica Acta B, 59:327–333, 2004.
- [94] Tetsuro Hori, Takeshi Shibata, Varutt Kittichungchit, Hiroki Moritou, Jun Sakai, Hitoshi Kubo, Akihiko Fujii, and Masanori Ozaki. MoO₃ buffer layer effect on photovoltaic properties of interpenetrating heterojunction type organic solar cells. Thin Solid Films, 518(2):522–525, November 2009.
- [95] R Hosemann. Small-angle scattering of microparacrystallites (mPC's). Journal of applied crystallography, 11:540–541, 1978.
- [96] R Hosemann. The α^* -law in colloid and polymer science. Progress in Colloid & Polymer Science, 77:15–25, 1988.
- [97] R Hosemann and SN Bagchi. The interference theory of ideal paracrystals. Acta Crystallographica, 5:612–614, 1952.
- [98] R Hosemann and W Vogel. Novel aspects of the real paracrystal. Acta Crystallographica Section A: Foundations, A37:85–91, 1981.

- [99] Rolf Hosemann. Solid State Physics of Microparacrystals. Physica Scripta, T1:142–148, January 1982.
- [100] I Hotovy, V Rehacek, P Siciliano, S Capone, and L Spiess. Sensing characteristics of NiO thin films as NO₂ gas sensor. Thin Solid Films, 418:9–15, 2002.
- [101] Jinsong Huang, Gang Li, and Yang Yang. Influence of composition and heat-treatment on the charge transport properties of pol(3-hexylthiophene) and [6,6]-phenyl C61-butyric acid methyl ester blends. Applied Physics Letters, 87(12105):1–3, 2005.
- [102] J Hubbard. Exchange splitting in ferromagnetic nickel. Proceedings of the Physical Society, 84(4):455–464, October 1964.
- [103] Jaehyung Hwang, Fabrice Amy, and Antoine Kahn. Spectroscopic study on sputtered PEDOT:PSS: Role of surface PSS layer. Organic Electronics, 7(5):387–396, October 2006.
- [104] Michael D Irwin, D Bruce Buchholz, Alexander W Hains, Robert P H Chang, and Tobin J Marks. p-Type semiconducting nickel oxide as an efficiency-enhancing anode interfacial layer in polymer bulk-heterojunction solar cells. Proc. National Academy of Science, 105(8):2783–2787, 2007.
- [105] Thomas N Jackson, Yen-yi Lin, Student Member, and David J Gundlach. Organic Thin-Film Transistors for Organic Display Backplanes. Journal of Selected Topics in Quantum Electronics, 4(1):100–104, 1998.
- [106] Leslie Jimison. Understanding microstructure and charge transport in semicrystalline polythiophenes. PhD thesis, 2011.
- [107] Leslie Jimison, Alberto Salleo, Michael Chabiny, David Bernstein, and Michael Toney. Correlating the microstructure of thin films of poly[5,5-bis(3-dodecyl-2-thienyl)-2,2-bithiophene] with charge transport: Effect of dielectric surface energy and thermal annealing. Physical Review B, 78(12):1–18, September 2008.
- [108] PD Jones, DE Parker, TJ Osborn, and KR Briffa. Global and hemispheric temperature anomalies-land and marine instrumental records. Technical report, Carbon Dioxide Information Analysis Center, Oak Ridge National Laboratory, U.S. Department of Energy, Oak Ridge, Tenn., U.S.A, 2013.
- [109] R. Joseph Kline, Michael D. McGehee, and Michael F. Toney. Highly oriented crystals at the buried interface in polythiophene thin-film transistors. Nature Materials, 5(3):222–228, February 2006.
- [110] Jaewook Jung, Donghwan Kim, Won Suk Shin, Sang-Jin Moon, Changjin Lee, and Sung Cheol Yoon. Highly Efficient Organic Photovoltaic Cells with Molybdenum Oxide Buffer Layer. Japanese Journal of Applied Physics, 49(5):05EB05, May 2010.
- [111] A. Jurando-Lopez and M. D. Luque De Castro. Chemometric Approach to Laser- Induced Breakdown Analysis of Gold. Applied Spectroscopy, 57(3):349–352, 2003.
- [112] KS Kim and N Winograd. X-ray photoelectron spectroscopic studies of nickel-oxygen surfaces using oxygen and argon ion-bombardment. Surface Science, 43:625–643, 1974.

- [113] Myung-Gil Kim, Mercuri G Kanatzidis, Antonio Facchetti, and Tobin J Marks. Low-temperature fabrication of high-performance metal oxide thin-film electronics via combustion processing. Nature materials, 10(5):382–388, April 2011.
- [114] Yong Hyun Kim, Christoph Sachse, Michael L. Machala, Christian May, Lars Müller-Meskamp, and Karl Leo. Highly Conductive PEDOT:PSS Electrode with Optimized Solvent and Thermal Post-Treatment for ITO-Free Organic Solar Cells. Advanced Functional Materials, 21(6):1076–1081, March 2011.
- [115] Thomas Kirchartz, Wei Gong, Steven a Hawks, Tiziano Agostinelli, Roderick Charles Ian MacKenzie, Yang Yang, and Jenny Nelson. Sensitivity of the Mott-Schottky Analysis in Organic Solar Cells. The Journal of Physical Chemistry C, page 120315090401008, March 2012.
- [116] Thomas Kirchartz and Uwe Rau. Detailed balance and reciprocity in solar cells. Physica Status Solidi (a), 205(12):2737–2751, December 2008.
- [117] C. Kittel. Introduction to Solid State Physics. John Wiley & Sons, Toronto, 7th edition, 1996.
- [118] C. Kittel and H. Kroemer. Thermal Physics. Freeman, New York, 2 edition, 1980.
- [119] Andreas Klein. Energy band alignment at interfaces of semiconducting oxides: A review of experimental determination using photoelectron spectroscopy and comparison with theoretical predictions by the electron affinity rule, charge neutrality levels, and the common anion. Thin Solid Films, 520(10):3721–3728, March 2012.
- [120] E.W. Knapp. Lineshapes of molecular aggregates, exchange narrowing and intersite correlation. Chemical Physics, 85(1):73–82, March 1984.
- [121] Jasper Knoester. Nonlinear optical susceptibilities of disordered aggregates: A comparison of schemes to account for intermolecular interactions. Physical Review A, 47(3):2083–2098, March 1993.
- [122] H Kroemer. A proposed class of hetero-junction injection lasers. In Proceedings of the IEEE, volume 7, pages 178–179, 1963.
- [123] H Kroemer. HETEROSTRUCTURE DEVICES: A DEVICE PHYSICIST LOOKS AT INTERFACES. Surface Science, 132:543–576, 1983.
- [124] H. Kroemer, Wu-Yi Chien, J. S. Harris, and D. D. Edwall. Measurement of isotype hetero-junction barriers by C-V profiling. Applied Physics Letters, 36(4):295, 1980.
- [125] Herbert Kroemer. On the interface connection rules for effective mass wave functions at an abrupt heterojunction between two semiconductors with different effective mass. Journal of Vacuum Science & Technology, 21(2):551–553, 1982.
- [126] Herbert Kroemer. Heterostructure bipolar transistors: What should we build? Journal of Vacuum Science & Technology B: Microelectronics and Nanometer Structures, 1(2):126–130, 1983.

- [127] Herbert Kroemer. Nobel Lecture : Quasielectric fields and band offsets : teaching electrons new tricks. Reviews of Modern Physics, 73(July), 2001.
- [128] D.Y. Kwok and a.W. Neumann. Contact angle measurement and contact angle interpretation, volume 81. September 1999.
- [129] Robert Kykyneshi, Jin Zeng, and David P Cann. Transparent Conducting Oxides Based on Tin Oxide. In David S. Ginley, editor, Handbook of Transparent Conductors, chapter 6, pages 171–191. Springer US, Boston, MA, 2011.
- [130] MA Lampert. Incidence of an Electromagnetic Wave on a” ÄEerenkov Electron Gas”. Physical Review, 102(2):299–304, 1956.
- [131] L. D. Landau and E. M. Lifshitz. Statistical Physics. Pergammon, Exeter, 3 edition, 1982.
- [132] MA Langell and MH Nassir. Stabilization of NiO (111) thin films by surface hydroxyls. The Journal of Physical Chemistry, pages 4162–4169, 1995.
- [133] Stephan Lany, Jorge Osorio-guillén, and Alex Zunger. Origins of the doping asymmetry in oxides : Hole doping in NiO versus electron doping in ZnO. Physical Review B, 75(24120):1–4, 2007.
- [134] Mario Leclerc, Ahmed Najari, and Serge Beaupre. Macromolecular Science and Engineering Division Award Lecture Conjugated polymers : From micro-electronics to genomics. Canadian Journal of Chemistry, 87:1201–1208, 2009.
- [135] Jae-Hyun Lee, Hyun-Mi Kim, Ki-Bum Kim, Ryota Kabe, Pavel Anzenbacher, and Jang-Joo Kim. Homogeneous dispersion of organic p-dopants in an organic semiconductor as an origin of high charge generation efficiency. Applied Physics Letters, 98(17):173303, 2011.
- [136] Andrew J Leenheer, John D Perkins, Maikel F A M Van Hest, Joseph J Berry, Ryan P O Hayre, and David S Ginley. General mobility and carrier concentration relationship in transparent amorphous indium zinc oxide films. Physical Review B, 77(115215):1–5, 2008.
- [137] Gang Li, Vishal Shrotriya, Jinsong Huang, Yan Yao, Tom Moriarty, Keith Emery, and Yang Yang. High-efficiency solution processable self-organization of polymer blends. Nature Materials, 4(November):864–868, 2005.
- [138] Gang Li, Rui Zhu, and Yang Yang. Polymer solar cells. Nature Photonics, 6(3):153–161, February 2012.
- [139] J. V. Li, A. M. Nardes, Ziqi Liang, S. E. Shaheen, B. A. Gregg, and D. H. Levi. Simultaneous measurement of carrier density and mobility of organic semiconductors using capacitance techniques. Organic Electronics, 12:1879–1885, 2011.
- [140] P Lindenmeyer, H Beumer, and R Hosemann. The origin in thermodynamic stability of paracrystals. Progress in Colloid & Polymer Science, 64:232–237, 1978.
- [141] Matthew T. Lloyd, Dana C. Olson, Ping Lu, Erica Fang, Diana L. Moore, Matthew S. White, Matthew O. Reese, David S. Ginley, and Julia W. P. Hsu. Impact of contact evolution on the shelf life of organic solar cells. Journal of Materials Chemistry, 19(41):7638, 2009.

- [142] Matthew T. Lloyd, Craig H. Peters, Andres Garcia, Isaac V. Kauvar, Joseph J. Berry, Matthew O. Reese, Michael D. McGehee, David S. Ginley, and Dana C. Olson. Influence of the hole-transport layer on the initial behavior and lifetime of inverted organic photovoltaics. Solar Energy Materials and Solar Cells, pages 1–7, January 2011.
- [143] Matthew T. Lloyd, Rohit P. Prasankumar, Michael B. Sinclair, Alex C. Mayer, Dana C. Olson, and Julia W. P. Hsu. Impact of interfacial polymer morphology on photoexcitation dynamics and device performance in P3HT/ZnO heterojunctions. Journal of Materials Chemistry, 19(26):4609, 2009.
- [144] Y M Lu, W S Hwang, J S Yang, and H C Chuang. Properties of nickel oxide thin films deposited by RF reactive magnetron sputtering. Thin Solid Films, 421:54–61, 2002.
- [145] P Lunkenheimer, A Loidl, C R Ottermann, and K Bange. Correlated barrier hopping in NiO films. Physical Review B, 44(11):5927–5930, 1991.
- [146] Antonio Luque and Steven Hegedus. Front Cover, List of Contributors. In Antonio Luque and Steven Hegedus, editors, Handbook of Photovoltaic Science and Engineering. John Wiley & Sons, 2003.
- [147] RCI MacKenzie and Thomas Kirchartz. Modeling nongeminate recombination in P3HT:PCBM solar cells. The Journal of Physical Chemistry C, 115:9806–9813, 2011.
- [148] G. Malliaras, J. Salem, P. Brock, and C. Scott. Electrical characteristics and efficiency of single-layer organic light-emitting diodes. Physical Review B, 58(20):R13411–R13414, November 1998.
- [149] Stefan C. B. Mannsfeld, Ajay Virkar, Colin Reese, Michael F. Toney, and Zhenan Bao. Supplementary info for Precise Structure of Pentacene Monolayers on Amorphous Silicon Oxide and Relation to Charge Transport. Advanced Materials, 21(22):2294–2298, June 2009.
- [150] Xianglei Mao, Wing-tat Chan, Manuel Caetano, Mark A Shannon, and Richard E Russo. Preferential vaporization and plasma shielding during nano-second laser ablation. Applied Surface Science, 98:126–130, 1996.
- [151] Alex C Mayer, Shawn R Scully, Brian E Hardin, Michael W Rowell, and Michael D Mcgehee. Polymer-based solar cells. Materials Today, 10(11):28–33, 2007.
- [152] J.M. McKay and V.E. Henrich. Structure of valence and conduction levels in NiO. Physical Review Letters, 53(24):2343–2346, 1984.
- [153] Jens Meyer, Rebecca Khalandovsky, Patrick Görrn, and Antoine Kahn. MoO₃ films spin-coated from a nanoparticle suspension for efficient hole-injection in organic electronics. Advanced Materials, 23(1):70–3, January 2011.
- [154] By Valentin D Mihailetchi, Hangxing Xie, Bert De Boer, L Jan Anton Koster, and Paul W M Blom. Charge Transport and Photocurrent Generation in Poly (3-hexylthiophene): Methanofullerene Bulk-Heterojunction Solar Cells. Advanced Functional Materials, 16:699–708, 2006.

- [155] V.D. Mihailetchi, J.K.J. van Duren, P.W.M. Blom, J.C. Hummelen, R.a.J. Janssen, J.M. Kroon, M.T. Rispens, W.J.H. Verhees, and M.M. Wienk. Electron Transport in a Methanofullerene. Advanced Functional Materials, 13(1):43–46, January 2003.
- [156] Nichole Cates Miller, Eunkyung Cho, Matthias J N Junk, Roman Gysel, Chad Risko, Dongwook Kim, Sean Sweetnam, Chad E Miller, Lee J Richter, R Joseph Kline, Martin Heeney, Iain McCulloch, Aram Amassian, Daniel Acevedo-Feliz, Christopher Knox, Michael Ryan Hansen, Dmytro Dudenko, Bradley F Chmelka, Michael F Toney, Jean-Luc Brédas, and Michael D McGehee. Use of X-ray diffraction, molecular simulations, and spectroscopy to determine the molecular packing in a polymer-fullerene bimolecular crystal. Advanced materials (Deerfield Beach, Fla.), 24(45):6071–9, November 2012.
- [157] SP Mitoff. Electrical conductivity and thermodynamic equilibrium in nickel oxide. The Journal of Chemical Physics, 727:882–889, 1961.
- [158] Andrzej W. Miziolek, Vincenzo Palleschi, and Israel Schechter. Laser Induced Breakdown Spectroscopy (LIBS) Fundamentals and Applications. Cambridge University Press, New York, 2006.
- [159] Mamoru Mizuhashi. Process Technology and Industrial Processes. In David S. Ginley, editor, Handbook of Transparent Conductors, chapter 15, pages 5–10. Springer US, Boston, MA, 2011.
- [160] M. Morana, P. Koers, C. Waldauf, M. Koppe, D. Muehlbacher, P. Denk, M. Scharber, D. Waller, and C. Brabec. Organic Field-Effect Devices as Tool to Characterize the Bipolar Transport in Polymer-Fullerene Blends: The Case of P3HT-PCBM. Advanced Functional Materials, 17(16):3274–3283, November 2007.
- [161] F J Morin. Electrical Properties of NiO. Physical Review, 93(6):49–54, 1954.
- [162] J Mort. Conductive Polymers. Science, 208(May):819–825, 1980.
- [163] A M Nardes, M Kemerink, M M De Kok, E Vinken, K Maturova, and R A J Janssen. Conductivity , work function , and environmental stability of PEDOT:PSS thin films treated with sorbitol. Organic Electronics, 9:727–734, 2008.
- [164] Alexandre Mantovani Nardes. On the conductivity of PEDOT:PSS thin films. PhD thesis, Technische Universiteit Eindhoven, 2007.
- [165] Paul F. Ndione, Andres Garcia, N. Edwin Widjonarko, Ajaya K. Sigdel, K. Xerxes Steirer, Dana C. Olson, Philip a. Parilla, David S. Ginley, Neal R. Armstong, Robin E. Richards, Erin L. Ratcliff, and Joseph J. Berry. Highly-Tunable Nickel Cobalt Oxide as a Low-Temperature P-Type Contact in Organic Photovoltaic Devices. Advanced Energy Materials, 3(4):524–531, April 2013.
- [166] R. Newman and R. RM Chrenko. Optical Properties of Nickel Oxide. Physical Review, 114(6):1507–1513, June 1959.
- [167] Alex Niemegeers and Marc Burgelman. Effects of the Au/CdTe back contact on IV and CV characteristics of Au/CdTe/CdS/TCO solar cells. Journal of Applied Physics, 81(6):2881–2886, 1997.

- [168] GA Niklasson. Electrochromics for smart windows: thin films of tungsten oxide and nickel oxide, and devices based on these. J. Mater. Chem., 17:127–156, 2006.
- [169] Edwards T. Niles, John D. Roehling, Hajime Yamagata, Adam J. Wise, Frank C. Spano, Adam J. Moulé, and John K. Grey. J-Aggregate Behavior in Poly-3-hexylthiophene Nanofibers. The Journal of Physical Chemistry Letters, 3(2):259–263, January 2012.
- [170] John Northrup. Atomic and electronic structure of polymer organic semiconductors: P3HT, PQT, and PBTTT. Physical Review B, 76(24):1–6, December 2007.
- [171] PR Norton and RL Tapping. A photoemission study of the interaction of Ni (100),(110) and (111) surfaces with oxygen. Surface Science, 65, 1977.
- [172] M O’Keeffe and WJ Moore. Diffusion of oxygen in single crystals of nickel oxide. The Journal of Physical Chemistry, 65(4), 1961.
- [173] W G Oldham and A G Milnes. INTERFACE STATES IN ABRUPT SEMICONDUCTOR. Solid-State Electronics, 7(1963):153–165, 1964.
- [174] Dana C Olson, Yun-ju Lee, Matthew S White, Nikos Kopidakis, Sean E Shaheen, David S Ginley, James A Voigt, and Julia W P Hsu. Effect of ZnO Processing on the Photovoltage of ZnO / Poly(3-hexylthiophene) Solar Cells. Journal of Physical Chemistry C, 112:9544–9547, 2008.
- [175] Akiko Orimo, Kohji Masuda, Satoshi Honda, Hiroaki Benten, Shinzaburo Ito, Hideo Ohkita, and Hiroshi Tsuji. Surface segregation at the aluminum interface of poly(3-hexylthiophene)/fullerene solar cells. Applied Physics Letters, 96(4):043305, 2010.
- [176] DK Owens and RC Wendt. Estimation of the surface free energy of polymers. Journal of Applied Polymer Science, 13(8):1741–1747, 1969.
- [177] U Panne, C Haisch, M Clara, and R Niessner. Analysis of glass and glass melts during the vitrification process of fly and bottom ashes by laser-induced plasma spectroscopy. Part I : Normalization and plasma diagnostics. Spectrochimica Acta B, 53:1957–1968, 1998.
- [178] Sung Heum Park, Anshuman Roy, Serge Beaupre, Shinuk Cho, Nelson Coates, Ji Sun Moon, Daniel Moses, Mario Leclerc, Kwanghee Lee, and Alan J Heeger. Bulk heterojunction solar cells with internal quantum efficiency approaching 100 %. Nature Photonics, 3(May):297–303, 2009.
- [179] G. Parravano. Thermoelectric Behavior of Nickel Oxide. The Journal of Chemical Physics, 23(1949):5, 1955.
- [180] Andrew J Pearson, Tao Wang, Richard A L Jones, David G Lidzey, Paul A Staniec, Diamond Light Source, Harwell Science, Technology Campus, Didcot Oxfordshire, Paul E Hopkinson, and Athene M Donald. Rationalizing Phase Transitions with Thermal Annealing Temperatures for P3HT:PCBM Organic Photovoltaic Devices. Phase Transitions, 2012.
- [181] Craig L. Perkins and Falah S. Hasoon. Surfactant-assisted growth of CdS thin films for photovoltaic applications. Journal of Vacuum Science & Technology A: Vacuum, Surfaces, and Films, 24(3):497, 2006.

- [182] Mario Petrosino and Alfredo Rubino. The effect of the PEDOT:PSS surface energy on the interface potential barrier. Synthetic Metals, 161(23-24):2714–2717, January 2012.
- [183] A. Pivrikas, N. S. Sariciftci, G. Juska, and R. Osterbacka. A review of charge transport and recombination in polymer/fullerene organic solar cells. Progress in Photovoltaics: Research and Applications, 15:677–696, 2007.
- [184] S Pizzini and R Morlotti. Thermodynamic and transport properties of stoichiometric and nonstoichiometric nickel oxide. Journal of The Electrochemical Society, 114(11):2–4, 1967.
- [185] T J Prosa, M J Winokur, Jeff Moulton, Paul Smith, and A J Heeger. X-Ray Structural Studies of the Poly(3-alkylthiophenes): An Example of an Inverse Comb. Macromolecules, 25:4364–4372, 1992.
- [186] J W Rabalais. Principles of UltraViolet Photoelectron Spectroscopy. John Wiley & Sons, New York, 1977.
- [187] Leon J Radziemski, Thomas R Loree, David A Cremers, and Nelson M Hoffman. Time-Resolved Laser- Induced Breakdown Spectrometry of Aerosols. Analytical Chemistry, 55:1246–1252, 1983.
- [188] Y. Ralchenko, A. Kramdia, J. Reader, and N. A. Team. NIST atomic spectra database v.3.1.5, 2009.
- [189] Erin L Ratcliff, Paul A Lee, and Neal R Armstrong. Work function control of hole-selective polymer/ITO anode contacts: an electrochemical doping study. J. Mater. Chem., 20(13):2672–2679, 2010.
- [190] Erin L. Ratcliff, Jens Meyer, K. Xerxes Steirer, Neal R. Armstrong, Dana Olson, and Antoine Kahn. Energy level alignment in PCDTBT:PC70BM solar cells: Solution processed NiOx for improved hole collection and efficiency. Organic Electronics, 13(5):744–749, May 2012.
- [191] Erin L. Ratcliff, Jens Meyer, K. Xerxes Steirer, Andres Garcia, Joseph J. Berry, David S. Ginley, Dana C. Olson, Antoine Kahn, and Neal R. Armstrong. Evidence for near-Surface NiOOH Species in Solution-Processed NiO x Selective Interlayer Materials: Impact on Energetics and the Performance of Polymer Bulk Heterojunction Photovoltaics. Chemistry of Materials, 23(22):4988–5000, November 2011.
- [192] Matthew O. Reese, Anthony J. Morfa, Matthew S. White, Nikos Kopidakis, Sean E. Shaheen, Garry Rumbles, and David S. Ginley. Pathways for the degradation of organic photovoltaic P3HT:PCBM based devices. Solar Energy Materials and Solar Cells, 92(7):746–752, July 2008.
- [193] A.H. Rice, Rajiv Giridharagopal, S.X. Zheng, F.S. Ohuchi, D.S. Ginger, and C.K. Luscombe. Controlling Vertical Morphology Within the Active Layer of Organic Photovoltaics Using Poly (3-hexylthiophene) Nanowires and Phenyl-C61-butyric Acid Methyl Ester. ACS nano, (4):3132–3140, 2011.
- [194] D Riley, I Weaver, T Morrow, M J Lamb, G W Martin, L A Doyle, A Al-Khateeb, and C L S Lewis. Spectral simulation of laser ablated magnesium plasmas. Plasma Sources, Science, and Technology, 9:270–278, 2000.

- [195] Jonathan Rivnay, Stefan C B Mannsfeld, Chad E Miller, Alberto Salleo, and Michael F Toney. Quantitative determination of organic semiconductor microstructure from the molecular to device scale. Chemical reviews, 112(10):5488–519, October 2012.
- [196] Jonathan Rivnay, Rodrigo Noriega, R. Kline, Alberto Salleo, and Michael Toney. Quantitative analysis of lattice disorder and crystallite size in organic semiconductor thin films. Physical Review B, 84(4):1–20, July 2011.
- [197] Jonathan Rivnay, Rodrigo Noriega, John Northrup, R. Kline, Michael Toney, and Alberto Salleo. Structural origin of gap states in semicrystalline polymers and the implications for charge transport. Physical Review B, 83(12):1–4, March 2011.
- [198] HP Rooksby. A note on the structure of nickel oxide at subnormal and elevated temperatures. Acta Crystallographica, 1(4):226–226, 1948.
- [199] A. Rose. Photovoltaic Effect Derived from the Carnot Cycle. Journal of Applied Physics, 31(9):1640, 1960.
- [200] A. Rose. Concepts in photoconductivity and allied problems. Interscience, New York, 1963.
- [201] A. Rose. A global view of solar energy in rational units. Physica Status Solidi A, 56:11–26, 1979.
- [202] Robert T. Ross. Some Thermodynamics of Photochemical Systems. The Journal of Chemical Physics, 46(12):4590, 1967.
- [203] Robert T. Ross and Ta-Lee Hsiao. Limits on the yield of photochemical solar energy conversion. Journal of Applied Physics, 48(11):4783, 1977.
- [204] Walter L. Roth and Glen a. Slack. Antiferromagnetic Structure and Domains in Single Crystal NiO. Journal of Applied Physics, 31(5):S352, 1960.
- [205] A. Rothwarf. Polycrystalline thin films for terrestrial solar cells. Journal of Vacuum Science and Technology, 20(3):282, March 1982.
- [206] Anshuman Roy, Sung Heum Park, Sarah Cowan, Ming Hong Tong, Shinuk Cho, Kwanghee Lee, and Alan J Heeger. Titanium suboxide as an optical spacer in polymer solar cells. Applied Physics Letters, 95(013302):1–3, 2009.
- [207] B Sasi and K G Gopchandran. Nanostructured mesoporous nickel oxide thin films. Nanotechnology, 18(11):115613, March 2007.
- [208] MA Sattar and BE Conway. Electrochemistry of the nickel-oxide electrode–VI. Surface oxidation of nickel anodes in alkaline solution. Electrochimica Acta, (March 1968), 1969.
- [209] R Sattmann, V Sturm, and R Noll. Laser-induced breakdown spectroscopy of steel samples using multiple Q-switch Nd:YAG laser pulses. Journal of Physics D, pages 2181–2187, 1995.
- [210] Tom J. Savenije, Jessica E. Kroeze, Xiaoni Yang, and Joachim Loos. The formation of crystalline P3HT fibrils upon annealing of a PCBM:P3HT bulk heterojunction. Thin Solid Films, 511-512:2–6, July 2006.

- [211] G A Sawatzky and J W Allen. Magnitude and Origin of the band gap in NiO. Physical Review Letters, 53(24):2339–2342, 1984.
- [212] Julia Schafferhans, Andreas Baumann, Alexander Wagenpfahl, Carsten Deibel, and Vladimir Dyakonov. Oxygen doping of P3HT:PCBM blends: Influence on trap states, charge carrier mobility and solar cell performance. Organic Electronics, 11(10):1693–1700, October 2010.
- [213] Markus C Scharber, David Mühlbacher, Markus Koppe, Patrick Denk, Christoph Waldauf, Alan J Heeger, and Christoph J Brabec. Design Rules for Donors in Bulk-Heterojunction Solar Cells Towards 10 % Energy-Conversion Efficiency **. Advanced Materials, 18:789–794, 2006.
- [214] H. Scheidt, M. Globl, and V. DoseE. The oxidation of nickel: a study of empty electronic states by inverse photoemission and soft x-ray appearance potential microscopy. Surface Science, 12:97–110, 1981.
- [215] Pavel Schilinsky, Christoph Waldauf, and Christoph J. Brabec. Recombination and loss analysis in polythiophene based bulk heterojunction photodetectors. Applied Physics Letters, 81(20):3885, 2002.
- [216] T. Schuler, D. Ederer, S. Itza-Ortiz, G. Woods, T. Callcott, and J. Woicik. Character of the insulating state in NiO: A mixture of charge-transfer and Mott-Hubbard character. Physical Review B, 71(11):1–7, March 2005.
- [217] GM Schwab and H Schmid. Effect of Added Oxides on p Conducting Nickel Oxide. Journal of Applied Physics, pages 426–428, 1962.
- [218] Sean Shaheen. Inverted bulk-heterojunction plastic solar cells. SPIE Newsroom, pages 2–4, 2007.
- [219] Yuzo Shigesato. In Based TCOs. In David S. Ginley, editor, Handbook of Transparent Conductors, chapter 5, pages 5–10. Springer US, Boston, MA, 2011.
- [220] W. Shockley. The theory of pn junctions in semiconductors and pn junction transistors. Bell Syst. Tech. J, 28(3):435–489, 1949.
- [221] W Shockley and H J Queisser. Detailed Balance Limit of Efficiency of p-n Junction Solar Cells. Journal of Applied Physics, 32(3):510–509, 1961.
- [222] V Shrotriya, EHE Wu, G Li, Y Yao, and Y Yang. Efficient light harvesting in multiple-device stacked structure for polymer solar cells. Applied Physics Letters, 88(064104):1–3, 2006.
- [223] Vishal Shrotriya, Jianyong Ouyang, Ricky J. Tseng, Gang Li, and Yang Yang. Absorption spectra modification in poly(3-hexylthiophene):methanofullerene blend thin films. Chemical Physics Letters, 411(1-3):138–143, August 2005.
- [224] H. Sirringhaus. Integrated Optoelectronic Devices Based on Conjugated Polymers. Science, 280(5370):1741–1744, June 1998.
- [225] D P Snowden and H Saltsburg. Hopping conduction in NiO. Physical Review Letters, 14(13):497–499, 1965.

- [226] FC Spano. The spectral signatures of frenkel polarons in H-and J-aggregates. Accounts of chemical research, 43(3):429–439, 2009.
- [227] Frank C Spano. Modeling disorder in polymer aggregates: the optical spectroscopy of regioregular poly(3-hexylthiophene) thin films. The Journal of chemical physics, 122(23):234701, June 2005.
- [228] Frank C. Spano. Absorption in regio-regular poly(3-hexyl)thiophene thin films: Fermi resonances, interband coupling and disorder. Chemical Physics, 325(1):22–35, June 2006.
- [229] W E Spear and D S Tannhauser. Hole transport in pure NiO crystal. Physical Review B, 7(2):831–833, 1973.
- [230] L St-Onge and M Sabsabi. Towards quantitative depth-profile analysis using laser-induced plasma spectroscopy : investigation of galvannealed coatings on steel. Spectrochimica Acta B, 55:299–308, 2000.
- [231] P. Stallinga. Electronic Transport in Organic Materials: Comparison of Band Theory with Percolation/(Variable Range) Hopping Theory. Advanced Materials, pages n/a–n/a, June 2011.
- [232] K. Xerxes Steirer, Jordan P. Chesin, N. Edwin Widjonarko, Joseph J. Berry, Alex Miedaner, David S. Ginley, and Dana C. Olson. Solution deposited NiO thin-films as hole transport layers in organic photovoltaics. Organic Electronics, 11(8):1414–1418, August 2010.
- [233] X. W. Sun, D. W. Zhao, L. Ke, a. K. K. Kyaw, G. Q. Lo, and D. L. Kwong. Inverted tandem organic solar cells with a MoO₃/Ag/Al/Ca intermediate layer. Applied Physics Letters, 97(5):053303, 2010.
- [234] S. M. Sze. Physics of Semiconductor Devices. Wiley-Interscience, New York, 1969.
- [235] M T Taschuk, I V Cravetchi, Y Y Tsui, and R Fedosejevs. Laser-Induced Breakdown Spectroscopy for Two Dimensional Microanalysis of Surfaces. Technical report, University of Alberta, Edmonton.
- [236] G.W Taylor and J.G Simmons. Basic equations for statistics, recombination processes, and photoconductivity in amorphous insulators and semiconductors. Journal of Non-Crystalline Solids, 8-10:940–946, June 1972.
- [237] MP Taylor, DW Readey, CW Teplin, M.F.A.M. van Hest, J. A. L. Alleman, M.S. Dabney, L.M. Gedvilas, B.M. Keyes, B. To, J.D. Perkins, and D.S. Ginley. The electrical, optical and structural properties of In_xZn_{1-x}O_y (0 ≤ x ≤ 1) thin films by combinatorial techniques. Measurement Science and Technology, 16:90–94, 2004.
- [238] M.P. Taylor, D.W. Readey, C.W. Teplin, M.F.A.M. van Hest, J.L. Alleman, M.S. Dabney, L.M. Gedvilas, B.M. Keyes, B. To, P.A. Parilla, and Others. Combinatorial growth and analysis of the transparent conducting oxide ZnO/In (IZO). Macromolecular rapid communications, 25(1):344–347, 2003.
- [239] Robert C. Tenent, Dane T. Gillaspie, Alex Miedaner, Philip a. Parilla, Calvin J. Curtis, and Anne C. Dillon. Fast-Switching Electrochromic Li⁺-Doped NiO Films by Ultrasonic Spray Deposition. Journal of The Electrochemical Society, 157(3):H318, 2010.

- [240] Carl Tengstedt, Wojciech Osikowicz, William R. Salaneck, Ian D. Parker, Che-H. Hsu, and Mats Fahlman. Fermi-level pinning at conjugated polymer interfaces. Applied Physics Letters, 88(5):053502, 2006.
- [241] T Tiedje and A Rose. A physical interpretation of dispersive transport in disordered semiconductors. Solid State Communications, 37:49–52, 1981.
- [242] MF Toney and Sean Brennan. Observation of the effect of refraction on x rays diffracted in a grazing-incidence asymmetric Bragg geometry. Physical Review B, 39(11):7963–7966, 1989.
- [243] Bertrand Tremolet de Villers, Christopher J. Tassone, Sarah H. Tolbert, and Benjamin J. Schwartz. Improving the Reproducibility of P3HT:PCBM Solar Cells by Controlling the PCBM/Cathode Interface. The Journal of Physical Chemistry C, 113(44):18978–18982, November 2009.
- [244] W. Tress, K. Leo, and M. Riede. Influence of Hole-transport layers and donor materials on open-circuit voltage and shape of I-V curves of organic solar cells. Advanced Functional Materials, 21(11):1–10, 2011.
- [245] Wolfgang Tress. Device Physics of Organic Solar Cells. PhD thesis, Technische Universität Dresden, 2011.
- [246] Wolfgang Tress, Annette Petrich, Markus Hummert, Moritz Hein, Karl Leo, and Moritz Riede. Imbalanced mobilities causing S-shaped IV curves in planar heterojunction organic solar cells. Applied Physics Letters, 98(6):063301, 2011.
- [247] ACC Tseung, BS Hobbs, and ADS Tantram. The electrochemical reduction of oxygen on nickel oxide and its solid solutions with lithium and chromium oxides* 1. Electrochimica Acta, 15(October 1968):473–481, 1970.
- [248] Wing C. Tsoi, David T. James, Jong Soo Kim, Patrick G. Nicholson, Craig E. Murphy, Donal D. C. Bradley, Jenny Nelson, and Ji-Seon Kim. The Nature of In-Plane Skeleton Raman Modes of P3HT and Their Correlation to the Degree of Molecular Order in P3HT:PCBM Blend Thin Films. Journal of the American Chemical Society, 133(25):9834–9843, June 2011.
- [249] S Uhlenbrock. The influence of defects on the Ni 2p and O 1s XPS of NiO. Journal of Physics: Condensed Matter, 4:7973–7978, 1999.
- [250] Svetlana S. van Bavel, Maik Bärenklau, Gijsbertus de With, Harald Hoppe, and Joachim Loos. P3HT/PCBM Bulk Heterojunction Solar Cells: Impact of Blend Composition and 3D Morphology on Device Performance. Advanced Functional Materials, 20(9):1458–1463, April 2010.
- [251] A. Van der Ven, D. Morgan, Y. S. Meng, and G. Ceder. Phase Stability of Nickel Hydroxides and Oxyhydroxides. Journal of The Electrochemical Society, 153(2):A210, 2006.
- [252] J. A. Van Vechten. Ionization potentials, electron affinities, and band offsets. Journal of Vacuum Science & Technology B: Microelectronics and Nanometer Structures, 3(4):1240, July 1985.
- [253] T Venkatesan and SM Green. Pulsed laser deposition: Thin films in a flash. The Industrial Physicist, pages 22–24, 1996.

- [254] MW Vernon and MC Lovell. Anomalies in the electrical conductivity of nickel oxide above room temperature. Journal of Physics and Chemistry of Solids, 27(v):1125–1131, 1966.
- [255] Elizabeth von Hauff, Vladimir Dyakonov, and Jürgen Parisi. Study of field effect mobility in PCBM films and P3HT:PCBM blends. Solar Energy Materials and Solar Cells, 87(1-4):149–156, May 2005.
- [256] B. E. Warren and B. L. Averbach. The Separation of Cold-Work Distortion and Particle Size Broadening in X-Ray Patterns. Journal of Applied Physics, 23(4):497, January 1952.
- [257] Benjamin Watts, Warwick J. Belcher, Lars Thomsen, Harald Ade, and Paul C. Dastoor. A Quantitative Study of PCBM Diffusion during Annealing of P3HT:PCBM Blend Films. Macromolecules, 42(21):8392–8397, November 2009.
- [258] Matthew S. White. Effects of Charge Carrier Concentration in Hybrid Conjugated Polymer - Oxide Photovoltaic Devices. PhD thesis, University of Colorado, Boulder, 2009.
- [259] Matthew S White, Dana C Olson, Nikos Kopidakis, Alexandre M. Nardes, David S. Ginley, and Joseph J Berry. Control of Charge Separation by Electric Field Manipulation in Polymer-Oxide Hybrid Organic Photovoltaic Bilayer Devices. Physica Status Solidi A, pages 1–9, 2009.
- [260] N Edwin Widjonarko, John D Perkins, Jennifer E Leisch, Philip a Parilla, Calvin J Curtis, David S Ginley, and Joseph J Berry. Stoichiometric analysis of compositionally graded combinatorial amorphous thin film oxides using laser-induced breakdown spectroscopy. The Review of Scientific Instruments, 81(7):073103, July 2010.
- [261] N. Edwin Widjonarko, Erin L. Ratcliff, Craig L. Perkins, Ajaya K. Sigdel, Andriy Zakutayev, Paul F. Ndione, Dane T. Gillaspie, David S. Ginley, Dana C. Olson, and Joseph J. Berry. Sputtered nickel oxide thin film for efficient hole transport layer in polymer-fullerene bulk-heterojunction organic solar cell. Thin Solid Films, 520(10):3813–3818, March 2012.
- [262] Wikipedia. List of countries by energy consumption per capita, 2013.
- [263] Paul Winget, Paul F. Ndione, Joseph J. Berry, and Oliver Monti. In Progress, 2013.
- [264] RW Wright and JP Andrews. Temperature Variation of the Electrical Properties of Nickel Oxide. Proceedings of the Physical Society. Section A, 62:446, 1949.
- [265] DA Wruck and M. Rubin. Structure and electronic properties of electrochromic NiO films. Journal of The Electrochemical Society, 140:1097–1097, 1993.
- [266] Mengqiang Wu, Jiahui Gao, Shuren Zhang, and Ai Chen. Comparative studies of nickel oxide films on different substrates for electrochemical supercapacitors. Journal of Power Sources, 159:365–369, 2006.
- [267] P Wurfel. Physics of Solar Cells. Wiley-VCH Verlag GmbH, Weinheim, Germany, 2005.
- [268] P Wurfel and W Ruppel. Upper limit of thermophotovoltaic solar-energy conversion. Electron Devices, IEEE Transactions on, 33(4):790–793, 1980.

- [269] K. Xerxes Steirer, Paul F. Ndione, N. Edwin Widjonarko, Matthew T. Lloyd, Jens Meyer, Erin L. Ratcliff, Antoine Kahn, Neal R. Armstrong, Calvin J. Curtis, David S. Ginley, Joseph J. Berry, and Dana C. Olson. Enhanced Efficiency in Plastic Solar Cells via Energy Matched Solution Processed NiOx Interlayers. Advanced Energy Materials, pages 813–820, July 2011.
- [270] Zheng Xu, Li-min Chen, Mei-hsin Chen, Gang Li, and Yang Yang. Energy level alignment of poly- 3-hexylthiophene:[6,6]-phenyl C61 butyric acid methyl ester bulk heterojunction. Applied Physics Letters, 95:013301, 2009.
- [271] Zheng Xu, Li-Min Chen, Guanwen Yang, Chun-Hao Huang, Jianhui Hou, Yue Wu, Gang Li, Chain-Shu Hsu, and Yang Yang. Vertical Phase Separation in Poly(3-hexylthiophene): Fullerene Derivative Blends and its Advantage for Inverted Structure Solar Cells. Advanced Functional Materials, 19(8):1227–1234, April 2009.
- [272] D Yohe, A. Riga, R Greef, and E Yeager. Electrochemical properties of nickel oxide. Electrochimica Acta, 13(6):1351–1358, 1968.
- [273] Jun Zhao, Ann Swinnen, Guy Van Assche, Jean Manca, Dirk Vanderzande, and Bruno Van Mele. Phase Diagram of P3HT / PCBM Blends and Its Implication for the Stability of Morphology. Journal of Physical Chemistry B, 113:1587–1591, 2009.
- [274] Kake Zhu, Weiming Hua, and Xingyi Wang. A Facile Synthesis of NiO Nanosheet with High-energy (111) Surface. Chemistry Letters, (111):156–158, 2011.
- [275] A Zur and TC McGill. Dipoles, defects and interfaces. Surface Science, 132:456–464, 1983.

Appendix A

Symbols

A.1 Physical constants

For an extended list, consult physics.nist.gov/cuu/constants/

Symbol	Description	Value (S.I.)
q	Elementary charge (positive)	$1.602 \times 10^{19} C$
k, k_B	Boltzmann constant	$1.381 \times 10^{-23} J K^{-1} [m^2 kg s^{-2} K^{-1}]$
c	Speed of light in vacuum	$299792458 m s^{-1}$
ϵ_0	Permittivity of free space	$8.854 \times 10^{-12} F m^{-1} [m^{-3} kg^{-1} s^4 A^2]$
μ_0	Permeability of free space	$4\pi \times 10^{-7} = 1.257 \times 10^{-6} N A^{-2} [m kg s^{-2} A^{-2}]$
h	Planck constant	$6.626 \times 10^{-34} J s [m^2 kg s^{-1}]$
\hbar	Reduced Planck constant	$\frac{h}{2\pi} = 6.626 \times 10^{-34} J s [m^2 kg s^{-1}]$
m_e	Electron mass	$9.109 \times 10^{-31} kg$
m_p	Proton mass	$1.673 \times 10^{-27} kg$
m_n	Neutron mass	$1.675 \times 10^{-27} kg$
a_0	Bohr radius	$\frac{4\pi\epsilon_0\hbar^2}{m_e e^2} = 0.5292 \times 10^{-10} m$
μ_B	Bohr magneton	$\frac{4\pi\epsilon_0\hbar^2}{m_e e^2} = 927.4 \times 10^{-26} J T^{-1} [m^2 kg s^{-2} T^{-1}]$
N_A, L	Avogadro constant	$6.022 \times 10^{23} mol^{-1}$
σ	Stefan-Boltzmann constant	$\frac{\pi^2 k_B^4}{60\hbar^3 c^2} = 5.670 \times 10^{-8} W m^{-2} K^{-4} [kg s^{-3} K^{-4}]$

A.2 Energy levels and statistics of electron-hole population

Symbol	Description
e^-	Electron
h^+	Hole
μ_{ec}	Electrochemical energy of electrons in a material
E_F	μ_{ec} at thermodynamic equilibrium
E_{Fn}	Electron quasi-Fermi energy away from equilibrium
E_{Fp}	Hole quasi-Fermi energy away from equilibrium
E_g	Semiconductor band gap
E_v / E_c	Semiconductor valence / conduction band level
E_D / E_A	Electron donor / acceptor energy level
<i>HOMO</i>	Highest Occupied Molecular Orbital. Analogous to E_v
<i>LUMO</i>	Lowest Unoccupied Molecular Orbital. Analogous to E_c
χ	Electron affinity
φ	Fermi level = E_F/q
φ_n	quasi-Fermi level for electrons = E_{Fn}/q
φ_p	quasi-Fermi level for holes = E_{Fp}/q
ψ	Electrostatic potential in the material, referenced from ψ_0
ψ_0	The chemical potential corresponding to $n_i = p_i$
n_i/p_i	Intrinsic electron / hole population
n	Electron population in the conduction band
p	Hole population in the valence band
g_e	Electronic density of states
N_c/P_v	Effective density of states of E_c / E_v
N_D/N_A	e^- donor / acceptor concentration

A.3 Solar cell characterization

Symbol	Description
V_{oc}	Open-circuit voltage
J_{sc}	Short-circuit current density (normalized wrt. device area)
$J_{mpp}, V_{mpp}, P_{mpp}$	Current density, voltage, and power at maximum power point
PCE	Power conversion efficiency = $\frac{P_{mpp}}{\text{Irradiated power}}$
FF	Fill factor = $\frac{P_{mpp}}{V_{oc} \times J_{sc}}$

A.4 Charge transport

Symbol	Description
I, I_n, I_p	Total, electron, and hole current
j, j_n, j_p	Total, electron, and hole current densities per unit area
μ_0	The carrier mobility in thermal equilibrium
σ	DC conductivity, the inverse of resistivity
D	Carrier diffusivity = $\mu_0 kT/q$ if non-degenerate
m^*	Carrier effective mass in the medium

A.5 Photoelectric effect

Symbol	Description
A_c	Area of the photocell
Q_s	Photon flux from the sun with quantum energy higher than E_g
t_s	Probability of an incident solar photon is converted into a mobile charge
Q_c	Photon flux from the cell due to black-body radiation
t_c	Probability of an electron-hole pair recombine to produce a photon
F_s	Total rate of electron-hole pair generation due to solar irradiation
F_{c0}	Total rate of electron-hole pair recombination at thermodynamic equilibrium
F_c	Total rate of electron-hole pair recombination under external perturbation
f_{loss}	Fraction of the photogenerated carriers that does not result in external current
$f_{NR/R}$	Fraction of the non-radiative to radiative recombination

A.6 Deposition parameters

Symbol	Description
T_h	Heater temperature
T_{sub}	Substrate temperature
$p(\text{gas type})$	Working gas partial pressure
p_{tot}	Total working pressure
Z_{s-t}	Substrate to target distance

A.7 X-ray diffraction

Symbol	Description
θ	Bragg angle
\vec{q}	The smallest reciprocal lattice vector. $q = \frac{2\pi}{d}$
α	X-ray incidence angle
δ	X-ray exit angle in the direction \perp to sample surface
γ	X-ray exit angle in the direction \parallel to sample surface
χ	Orientation of the sample, with Euler axis \parallel to sample surface
ϕ	Orientation of the sample, with Euler axis \perp to sample surface

Appendix B

The Physics of Photovoltaic Conversion

At the heart of sunlight to electricity conversion is the photoelectric effect, first discovered by Heinrich Hertz in 1887 and explained by Albert Einstein in 1905, who was consequently awarded the Nobel Prize in physics in 1921. The photoelectric effect begins the light-to-electricity conversion.

In the photoelectric process, electrons in the idealized metal are modeled as a Fermi sea, with the highest occupied level denoted by the Fermi energy, E_F . E_F is negative since the electrons are bound to the metal cores, while positive energy denotes free electrons. When a photon of sufficient energy is incident on the metal surface, it is absorbed and excites the electron free from its bound state. This threshold energy to free an electron from a metal surface is called the **workfunction** of the metal. The workfunction is the same with E_F in the absence of any surface effects¹. Thus, in this way the energy contained in the incident photons is converted into kinetic energy of the electrons, which can be used to do work.

B.1 The Need for Semiconductors

In the real world, free electrons are of little practical utility. Rather, as the photoproduct, we are more interested in *mobile* electrons which are still confined within the interior of a conductor, much like electrical currents in wires. Additionally, we are interested in harvesting light in the visible spectrum ($\sim 1.7 - 3.1 eV$), in contrast to lights of shorter wavelengths corresponding to the typical metal work-functions (Fig. B.1).

¹ See for example the discussion in Chp. 13 of Ref [10], or Refs. [91, 252]

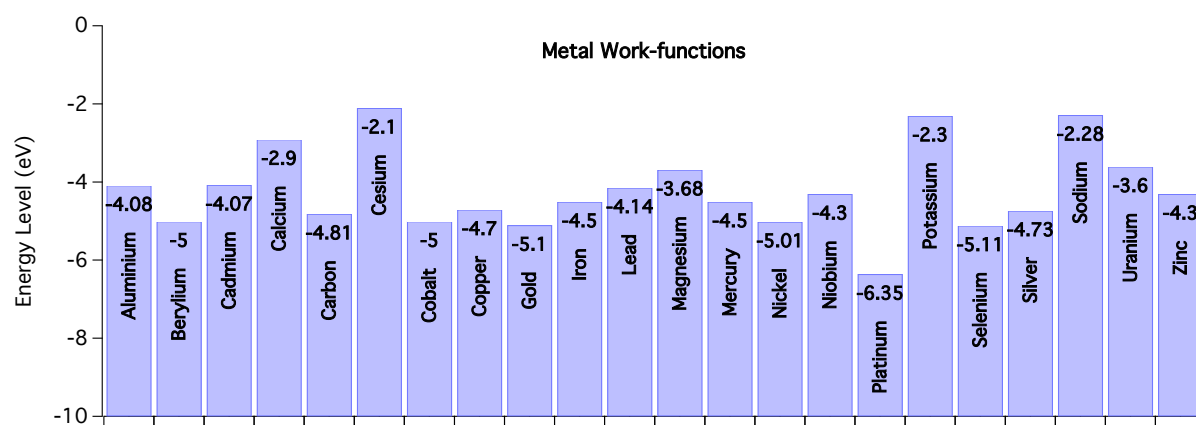


Figure B.1: Work-functions of select metals.

To achieve this, we turn to semiconductors, which are characterized by the presence of a finite band-gap, E_g . Unlike metal work-functions, the band-gap of semiconductors can be engineered to have values in the optical regime. Additionally, we can photo-excite electrons in the valence band to the conduction band instead of to vacuum. The electrons in the conduction band and holes in the valence band are also mobile, but are still confined to the material interior. Light of quantum energies higher than the band-gap energy (but lower than the ionization potential) is usually converted into electrons with energy equals to the conduction band edge, owing to the very fast thermalization process [10].

This description of the photovoltaic effect also holds for more general photochemical systems. For example, in molecular semiconductors, the “conduction band energy” is equivalent as the Lowest Unoccupied Molecular Orbital (LUMO) while the “valence band energy” is equivalent as the Highest Occupied Molecular Orbital (HOMO). Following the same logic, the population of carriers in the HOMO level is simply the population of molecules in the ground state, while the population of carriers in the LUMO level is simply the population of molecules in the excited state [202, 203]. The main difference between the crystalline inorganic semiconductor and molecular photochemical technologies lies in the details of charge transport and exciton splitting process, which will be briefly discussed in Chapter 2.

B.2 The ultimate efficiency of a photovoltaic cell

The ultimate photo-electric conversion efficiency that is allowed thermodynamically for such photovoltaic systems, called the detailed balance limit, has been discussed in great details by Shockley and Queisser [221], Rose[199], and Ross [202, 203]. In either work, a photovoltaic system under the following conditions is considered:

- (1) The semiconductor has a single cutoff frequency (absorption edge).
- (2) The density of mid-gap states in the semiconductor is negligible compared to the density of conduction / valence band states and the density of photo-excited carriers.

- (3) Each photon with energy greater than E_g produces one electronic charge at a voltage E_g/q . This is equivalent to having rapid carrier thermalization and 100% photon-to-electron conversion efficiency.
- (4) The semiconductor - sun - photon system is in a **steady-state** condition.

Note that the 2nd assumption implies that the only radiative recombination allowed is the band-to-band recombination. Five physical processes must be taken into account when carrying out the calculation for this ultimate efficiency, the sum of which must be zero at steady-state condition:

(1) **Radiative processes:**

Electron-hole pairs generation by incident radiation.

Radiative recombination of the electron-hole pairs.

(2) **Non-radiative processes:**

Non-radiative generation of electron-hole pairs.

Non-radiative recombination of electron-hole pairs.

(3) **Collection of electrons and holes which results in electrical currents available for doing external work.**

We shall now scrutinize each of these processes. In the following discussions, subscripts s denotes the sun, while subscripts c denotes the cell. The rate of electron-hole pairs generation by incident radiation is:

$$F_s = A_c f_{geo} Q_s t_s \quad (\text{B.1})$$

where A_c is the area of the cell, f_{geo} is a geometrical factor, Q_s is the photon flux from the sun with quantum energy higher than E_g , and t_s is the probability that such incident photon will produce an electron-hole pair.

The first two terms in Eqn. B.1 deals with the geometry of the solar cell itself. The factor f_{geo} takes into account the finite solid angle subtended by the captured solar radiation and the

effect of non-normal incidence [221]:

$$f_{geo} \approx 6.85 \times 10^{-5} \frac{\cos \theta}{\pi} \quad (\text{B.2})$$

where the constant is the fraction of the solid angle subtended by the Earth in Steradian and θ is the angle between normal incidence and the direction of the sun. Together with the third term, this takes into account the total number of photon flux with energy greater than E_g that is incident on the front side of the solar cell.

Lastly, t_s deals with the probability that an incident photon will eventually produce an electron-hole pair. This includes the material's absorption coefficient and photon-to-electron conversion efficiency. This term becomes extremely important, for example, in cases where the absorption spectrum of the material is not step-function-like, or when the photon-to-electron conversion efficiency is a function of applied bias such as in excitonic solar cells [69].

The rate of radiative recombination of electron-hole pairs in the cell of temperature T_c can be calculated in the following way: First consider the cell being completely surrounded by a blackbody of the same as the cell itself. In thermodynamic equilibrium, the rate of radiative recombination is exactly the same as the rate of electron-hole pair generation. This rate equals to:

$$F_{c0} = 2A_c Q_c t_c \quad (\text{B.3})$$

Here, unlike in Eqn. B.1, the geometrical factor equals 2 because the radiation from the cell points in all direction (including towards the back surface of the cell). Naturally, Q_c is different from Q_s due to temperature difference. Additionally, t_c may also be different from t_s due to difference in temperatures, difference in absorption / luminescence coefficients, and difference in photon densities of states outside and inside the cell surface due to the asymmetry in the refractive indices at the interface. In the following treatment, we assume $t_c = t_s$.

In steady state, but away from thermal equilibrium, the rate of electron-hole recombination may not equal F_{c0} . Rather, more generally it is proportional to the product of hole (p) and electron densities (n), np which may change as a function of, for example, applied bias. Since in thermal

equilibrium this product is equal n_i^2 and the recombination rate equals F_{c0} the rate of radiative recombination away from equilibrium equals:

$$F_c(V) = F_{c0} \frac{np}{n_i^2} = F_{c0} e^{V/V_{th}} \quad (\text{B.4})$$

where V_{th} stands for kT_c/q . V equals to the difference in quasi-Fermi levels for holes and electrons, which in a perfect system equals to the bias applied across the two terminals of the device [202, 220].

In the absence of non-radiative processes, radiative recombination becomes the only recombination mechanism, and it is straight-forward to calculate the maximum possible voltage difference that can be attained by this system. At steady state, the population of holes and electrons don't change as a function of time:

$$\frac{dn}{dt} = 0 = F_s - F_c(V) - I/q = F_s - F_{c0} e^{V/V_{th}} - I/q \quad (\text{B.5})$$

where I is the photocurrent drawn from the cell. Rearranging, we arrive at the potential difference in the absence of any non-radiative process:

$$V = V_{th} Ln \left| \frac{F_s}{F_{c0}} - \frac{I}{qF_{c0}} \right| \quad (\text{B.6})$$

Obviously, the previous equation reaches its maximum value when no current is drawn i.e. at open-circuit condition:

$$V_{oc,max} = V_{th} Ln \left| \frac{F_s}{F_{c0}} \right| \quad (\text{B.7})$$

It can be shown that Eqn. B.7 is simply a statement of conservation of energy [203]: the maximum energy that can be drawn from an engine equals to the difference between the higher and the lower potential energy that drives the it. In this case, the potential energies are related to the chemical potential energy related to the carrier population under illumination and the population without illumination. Similarly, Eqn. B.5 can also be solved for the maximum short-circuit current, attained when $V = 0$:

$$I_{sh,max} = q(F_s - F_{c0}) \quad (\text{B.8})$$

The maximum power than can be drawn from the system for doing external work, however, must be less than $V_{oc,max} \times I_{sh,max}$, simply from the definition of open- and short-circuit. In order

to extract the photogenerated carriers we need the photovoltaic system to push current to flow across the circuit at a non-zero external bias. The power generated can be expressed as:

$$P = I \times V \times (1 - f_{loss}(V)) \quad (\text{B.9})$$

where $f_{loss}(V)$ is the fraction of the photogenerated carriers that relax without yielding an external current. Obviously, $I < I_{sh,max}$ and $V < V_{oc,max}$. In the absence of non-radiative recombination, $f_{loss}(V)$ is necessarily the ratio of rate of emission to the rate of excitation at that particular bias, $F_c(V)/F_s$. Using Eqn. B.7, and the definitions for $F_c(V)$ and F_s (Eqns. B.4 and B.1), we find that

$$V = V_{oc,max} + V_{th}Ln |f_{loss}(V)| \quad (\text{B.10})$$

Note that the last term is negative. Eqn. B.9 then becomes:

$$P = I \times (V_{oc,max} + V_{th}Ln |f_{loss}(V)|) \times (1 - f_{loss}(V)) \quad (\text{B.11})$$

which has a maximum when:

$$\begin{aligned} f_{loss} &\approx \frac{V_{th}}{V_{oc,max}} \\ V_{mpp,max} &\approx V_{oc,max} - V_{th}Ln \left| \frac{V_{oc,max}}{V_{th}} \right| \end{aligned} \quad (\text{B.12})$$

The subscript *mpp* stands for “maximum power point”. Upon closer inspection of Eqns. B.12, B.3, and B.1, the maximum power is clearly dependent solely on light intensity and E_g ($t_s = t_c = 1$ under the assumption that every absorbed photon yield an electron). In other words, the problem of photovoltaic optimization is reduced to finding the optimum E_g for a given radiation. Fig. ?? shows the calculated theoretical maximum efficiency as a function of the E_g under 1-sun illumination, showing the optimum E_g of about 1.4 eV for photoelectric conversion efficiency, corresponding to that of Ga:As. Also shown are the E_g of a few other commonly used absorber materials.

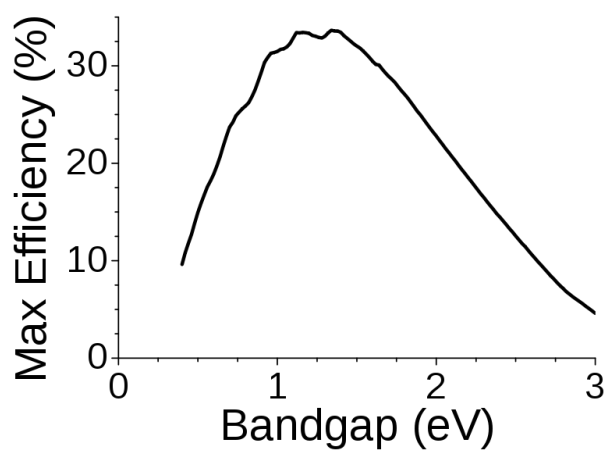


Figure B.2: The Shockley-Queisser thermodynamic limit for single E_g photovoltaic material.

B.3 Non-radiative recombination, losses during carrier transport

Non-radiative processes, such as carrier scattering during carrier transport, are almost always present in a real device. Adding $R(0)$, and non-radiative recombination, $R(V)$, to Eqn. B.5, we get:

$$0 = F_s - F_{c0}e^{V/V_{th}} + R(0) - R(V) - I/q \quad (\text{B.13})$$

Solving for V_{max} requires some knowledge of the functional form of $R(V)$ and $R(0)$. However, we can still learn something useful without this information. Let us define $f_{NR/R}$ as the ratio of non-radiative recombination to radiative recombination, i.e.:

$$f_{loss} = (1 + f_{NR/R}) \frac{F_c(V)}{F_s} \quad (\text{B.14})$$

If $f_{NR/R}$ is not a function of bias, Eqn. B.10 and B.12 then becomes:

$$V = V_{oc,max} + V_{th} \text{Ln} |f_{loss}(V)| - V_{th} \text{Ln} |1 + f_{NR/R}| \quad (\text{B.15})$$

$$f_{loss} \approx \frac{V_{th}}{V_{oc,max}}$$

$$V_{mpp,max} \approx V_{oc,max} - V_{th} \text{Ln} \left| \frac{V_{oc,max}}{V_{th}} \right| - V_{th} \text{Ln} |1 + f_{NR/R}| \quad (\text{B.16})$$

Therefore, non-radiative process serve as additional loss mechanisms. Physically, this can be thought as such: the treatment of the ideal case assumes that energy is shared only among three objects: the sun, the ideal absorber cell, and the external user. However, adding another process necessarily means that energy must be shared with another subsystem that causes the process. Thus, the external yield must go down in accordance to conservation of energy.

It is also instructional to show that there is a relationship between the current through the device with and without illumination. Eqn. B.13 can be rewritten as such:

$$0 = [F_s - F_{c0}] + [F_{c0} - F_{c0}e^{V/V_{th}} + R(0) - R(V)] - I/q \quad (\text{B.17})$$

The term in the first bracket is simply the rate of generation-recombination of carriers under illumination. The term inside the second bracket is also readily recognized as the total rate of generation-recombination of carriers in the dark.

Appendix C

Electrons and Holes in Semiconducting Materials

In §B we briefly described the photoelectric effect and the theoretical limit of photoconversion efficiency. In the discussions, we have assumed that each photon yield an e^- - h^+ pair in the external circuit. Practically, however, these photogenerated carriers have to be transported from the internal of the photovoltaic cell to the external circuit. Therefore, it is of importance to discuss the physics of carrier transport in semiconductors.

C.1 Statistics of Electrons and Holes in Semiconductors at Thermodynamic Equilibrium

Not detached from carrier transport is the carrier concentration in E_c and E_v at thermal equilibrium. From a physical point of view, the material provides an environment in which e^- can exist in a stable manner, called the electronic states. The details of atomic arrangement and composition inside the material dictates the distribution of density of states that are available to be populated by these e^- . Hence, the material is fully described by the distribution of its density of electronic states, $g_e(E)$. Since e^- are fermions, the probability of these states being occupied by an electron is described by the Fermi-Dirac statistics:

$$f(E) = \frac{1}{e^{(E-E_F)/kT} + 1} \quad (\text{C.1})$$

where E is the energy of the e^- , and E_F is the electrochemical potential of the e^- in the material. From a purely theoretical point of view, the material is fully described by its density of electronic

states, while the carrier population is described by the electrochemical potential of that carrier species.

To get the e^- population above E_c of the material, we simply need to count the number of occupied states, weighted by their probability of being occupied by an e^- . For holes below E_v , we simply change the integration limits and count the unoccupied states. Since e^- state occupation follows Fermi-Dirac statistics, these are:

$$\begin{aligned} n &= \int_{E_c}^{\infty} g_e(E) \frac{1}{e^{(E-E_F)/kT} + 1} dE \\ p &= \int_{-\infty}^{E_v} g_e(E) \left(1 - \frac{1}{e^{(E-E_F)/kT} + 1} \right) dE \\ &= \int_{-\infty}^{E_v} g_e(E) \frac{1}{e^{(E_F-E)/kT} + 1} dE \end{aligned} \quad (\text{C.2})$$

where n is e^- population in the conduction band E_c , p is h^+ population in the valence band E_v ¹. This is illustrated in Fig. C.1. We will discuss this the concept of doping and revisit Fig. C.1 in the next section. For the time being, we shall remain with the discussion of more general aspects of carrier population. One important consequence of Eqn. C.2 is that it states that the material restricts the equilibrium population of carriers through $g(E)$ and E_g alone (one may even argue that E_g is a subset of $g(E)$, thus the dependence is solely on $g(E)$). Further, we shall show that E_F can also be modulated by adding impurities or defects into the material (doping).

In the classical regime (**non-degenerate semiconductor**), defined as:

$$\begin{aligned} E_c - E_F &\gg kT \\ E_F - E_v &\gg kT \end{aligned} \quad (\text{C.3})$$

the Fermi-Dirac distribution function in Eqn. C.2 reduces to Boltzmann distribution function.

Thus, Eqn. C.2 can be simplified into:

$$\begin{aligned} n &\approx N_c e^{-(E_c-E_F)/kT} \\ p &\approx P_v e^{-(E_F-E_v)/kT} \end{aligned} \quad (\text{C.4})$$

¹ There is no h^+ density of states as h^+ are just a mathematical concept equivalent to an absence of e^- . See, for example Ref. [10]

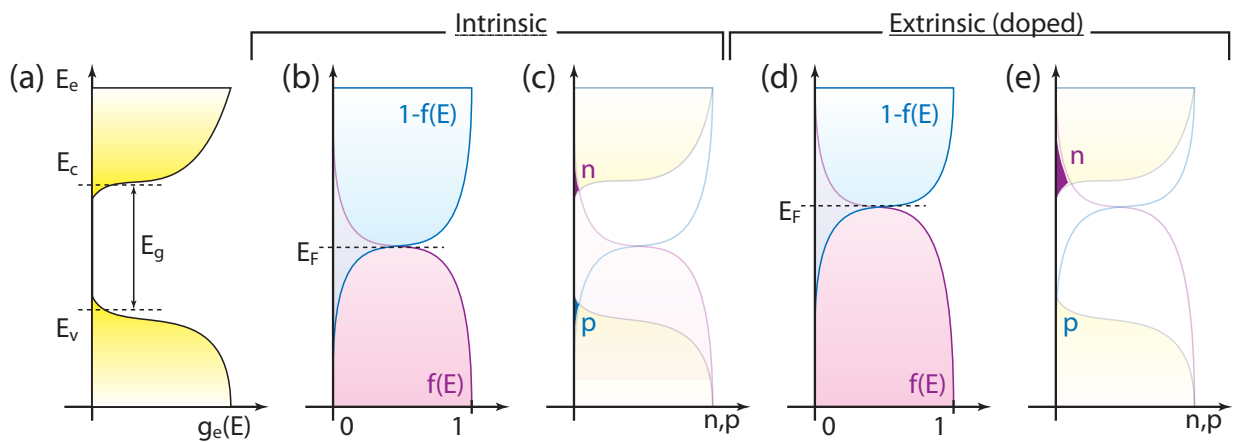


Figure C.1: n and p and their dependence on E_F and $g(E)$. (a) shows the e^- density of states as a function of energy. (b) is the Fermi-Dirac function describing the probability of such states being occupied by an e^- . (c) shows the actual e^- population, which is the product of $g_e(E)$ and $f(E)$. In an n-doped material, the dopant effectively raises the equilibrium Fermi level (d), resulting in an increased e^- population at the expense of h^+ population (e) as dictated by Eqn. C.6.

where

$$\begin{aligned} N_c &= \int_{E_c}^{\infty} g_e e^{-(E-E_c)/kT} dE \\ P_v &= \int_{-\infty}^{E_v} g_e e^{-(E_v-E)/kT} dE \end{aligned} \quad (\text{C.5})$$

are often referred to as the **effective density of electronic states of the conduction and valence bands** respectively. They are also known as the **quantum concentration of the conduction** e^- and h^+ . Most semiconductors that we are dealing with are non-degenerate. Notable exceptions are transparent conducting oxide such as ITO. Since this work focuses on non-degenerate semiconductors, the results discussed may not be applicable to transparent conducting oxides. Instead, transparent conducting oxides are modeled as a metal with finite, large E_g .

We shall start the discussion on dopants by examining the product of n and p :

$$\begin{aligned} n p &= N_c P_v e^{-(E_c-E_v)/kT} \\ &= N_c P_v e^{-E_g/kT} \end{aligned} \quad (\text{C.6})$$

The significance of Eqn. C.6 can be seen from the dependence of the product ($n p$) on solely E_g and $g(E)$ which are material-specific. It also means that for a given material and temperature, one may determine the population of one carrier type if the other is known because whenever one carrier type increases in population, it does so in the expense of the other carrier type (Fig. C.1). This is an important result, for it indicates that a carrier is physically produced by a dissociation of e^- and h^+ into the different bands². For this reason, Eqn. C.6 is known as the **Law of Mass Action**, emphasizing its precise analogy with a law of the same name in the study of chemical reactions.

C.1.1 Intrinsic Semiconductor

A semiconductor that is so pure so that impurities negligibly contribute to carrier concentration is called an **intrinsic semiconductor**. In this case, the equilibrium carrier concentration can

² Thurmond discussed the validity and caveats of treating e^- - h^+ dissociation as: $0 \rightleftharpoons e^- + h^+$

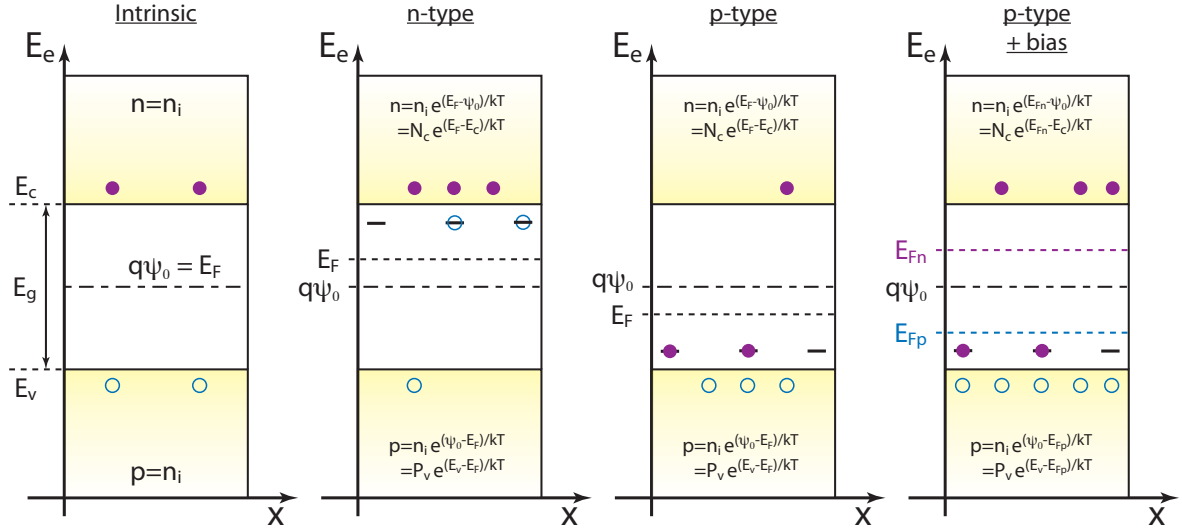


Figure C.2: Illustration of the doping process and carrier injection.

only be provided from dissociation of e^- and h^+ from E_v into E_c by the ambient thermal energy and consequently, their number must be the same (Fig. C.2). Hence, we can rewrite Eqn. C.6 as:

$$np = n_i^2 \quad (\text{C.7})$$

where n_i is the **intrinsic carrier concentration**. Consequently, for symmetric bands ($P_v = N_c$), the position of E_F is exactly in the middle of the gap. The deviation from mid-gap for non-symmetric bands is also small, in the order of kT . This can be seen by substituting Eqn. C.4 into Eqn. C.6, and using ($E_g = E_c - E_v$), yielding:

$$E_{F,i} = E_v + \frac{1}{2}E_g + \frac{1}{2}kT \ln \left| \frac{P_v}{N_c} \right| := q\psi_0 \quad (\text{C.8})$$

We also note this level as Shockley's choice for the reference level for electrostatic potential, ψ_0 [220]. We will follow this notation.

C.1.2 Extrinsic Semiconductor

We are now in the position to discuss doping in semiconductors. Semiconductors where impurities significantly contribute to its carrier concentration are called **extrinsic semiconductors**.

This is defined rigorously as:

$$|\Delta n| := |n - p| \gg n_i \quad (\text{C.9})$$

Additionally, if $n > p$ then the semiconductor is called **n-type semiconductor**. Conversely, it is called a **p-type semiconductor** if $p > n$.

How can doping achieve this? As an example, let us consider Si crystal as the host crystal and P and Al as dopant atoms. P atoms have one extra valence e^- than Si. When some Si atoms in the crystal are substituted by P atoms, these extra e^- don't fit into the already-full valence band. Hence, the P-doped Si crystal have more conduction e^- . Note that by law of mass action, it will also have fewer holes than the intrinsic Si crystal. This is because the positive P-ions also attract the thermal electrons, effectively reducing their population. P atoms in Si crystal is called **electron donor** and its concentration N_D . Al atoms, on the other hand, have one fewer valence e^- than Si. Hence, Al is a p-type dopant for Si and is called **electron acceptor** and its concentration N_A .

This process is illustrated in C.1 and Fig. C.2. Energetically, the addition of impurities introduces localized states in the gap near the band edge. The closer the state is to the band edge, the better the doping efficiency is. Consider again P as donors in a Si crystal. These states, when ionized and effectively increase n , will appear as a positively charged ion near E_c . The probability of ionization is given by [118]:

$$\begin{aligned} f_{D^+} &\approx \frac{1}{1 + 2 e^{(E_F - E_D)/kT}} \\ f_{A^-} &\approx \frac{1}{1 + 2 e^{(E_A - E_F)/kT}} \end{aligned} \quad (\text{C.10})$$

where the subscripts denote donors or acceptors. Conversely, the probability that positive ions attract and bind e^- is:

$$\begin{aligned} f_D &\approx \frac{1}{1 + 2 e^{(E_D - E_F)/kT}} \\ f_A &\approx \frac{1}{1 + 2 e^{(E_F - E_A)/kT}} \end{aligned} \quad (\text{C.11})$$

From Eqn. C.10 and C.11, it is evident that in order to be an efficient dopant, a prospective dopant

must introduce energy levels that is very close, within very few kT , to the band edges. In other words, the dopants must be in thermal equilibrium with the transport band.

C.1.3 Carrier Population in Non-Equilibrium Steady State

Another way we can increase carrier population in the material is by exerting external work to the system. However, we shall see that this is fundamentally different from the effect of doping.

Let us suppose that, for example, we apply an external bias or photoexcite the system. Upon receiving external energy, the bound e^- in E_v have higher probability of being excited to E_c . This leads to higher n , and can be described as increasing the Fermi-level for e^- . However, to conserve charge and particle number, this process necessarily leaves a h^+ in E_v , leading to also higher p , and should be described as decreasing the Fermi-level for h^+ . Hence, E_F is split into the **electron quasi-Fermi energy**, E_{Fn} , and **hole quasi-Fermi energy**, E_{Fp} , in non-equilibrium, describing their respective population:

$$\begin{aligned} n &= n_i e^{q(\psi_0 - \varphi_n)/kT} \\ p &= n_i e^{q(\varphi_p - \psi_0)/kT} \end{aligned} \quad (\text{C.12})$$

where

$$\begin{aligned} \varphi_n &:= E_{Fn}/q \\ \varphi_p &:= E_{Fp}/q \end{aligned} \quad (\text{C.13})$$

or equivalently

$$\begin{aligned} n &= N_c e^{(E_{Fn} - E_c)/kT} \\ p &= P_v e^{(E_v - E_{Fp})/kT} \end{aligned} \quad (\text{C.14})$$

This is in contrast to the earlier case of a doped semiconductor in equilibrium, where only one energy level E_F is sufficient to describe carrier population in the system (Fig. C.2, C.3). The law of mass action (Eqn. C.6) is consequently modified for cases away from thermodynamic equilibrium

to:

$$n p = n_i^2 e^{q(\varphi_n - \varphi_p)/kT} \quad (\text{C.15})$$

There is, however, a subtle difference between an external bias produced by a voltage source and by photoexcitation [200]. In the first, electric potentials $(E_{Fn} - E_F)$, $(E_{Fp} - E_F)$ are the controlled variable of the system, while in the latter, the photoexcited carrier $\delta n, \delta p$ are the variable of the system³. More physically, in the first case, a voltage source will supply however many carriers into the system to maintain a potential difference of, say 1.0 V, across the terminals. On the other hand, in photo-excitation process, the photovoltage across the terminals is determined by $\delta n, \delta p$, which in turn is determined by the light intensity, absorption profile of the material, and recombination inside the material. In a sense, the latter is better represented by a current source than a voltage source.

C.1.4 On Fermi Level, Quasi-Fermi Levels, Chemical Potential, and Electrochemical Potential

So far, the discussion have been based on population statistics of the carriers. Sometimes it is useful to establish connection with thermodynamics. Afterall, the two descriptions should agree because they are both based on statistical mechanics. An explicit connection with thermodynamics, however, will make it easier to draw connection with fields such as chemistry or electrochemistry, or even classical physics.

The potential energy experienced by a collection of charged particles in a material can be described in a statistical way⁴:

$$U = ST - PV + \sum_{\alpha} (n_{\alpha} \mu_{c,\alpha}^* - Q_{\alpha} \psi) \quad (\text{C.16})$$

³ We use δ to emphasize that we mean the increase in steady-state population of carrier by photoexcitation in contrast to Δn of Eqn. C.9.

⁴ The validity limit of such statistical / thermodynamical description is of utmost importance. However, it is not the objective of this work to go into such details. Instead, the readers are referred to, for example, Refs. [131, 10]. Herring and Nichols [91], and Ashcroft and Mermin [10] also discussed the validity limit in terms of spatial homogeneity. Jackson [105] has also touched upon similar validity limits in the light of classical electrodynamics theory.

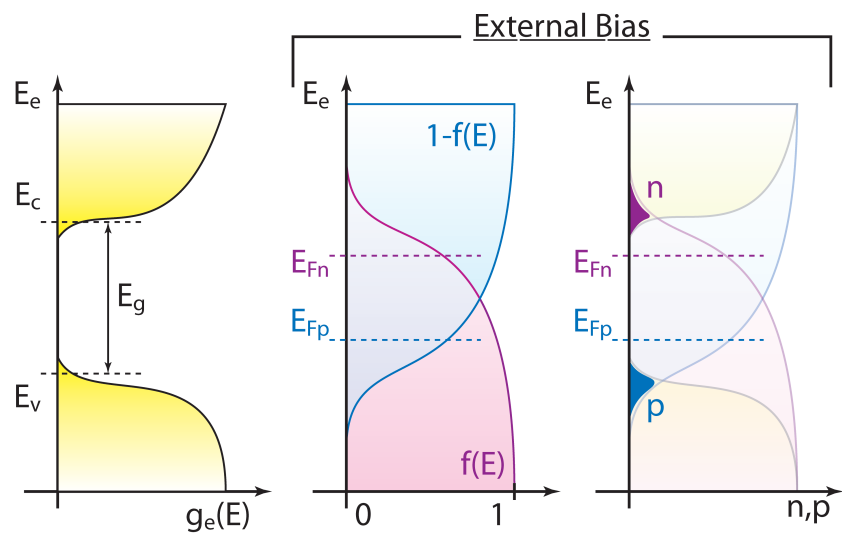


Figure C.3: n and p in the presence of external work, illustrating the quasi-Fermi level splitting. In non-equilibrium, the external energy supplied excites e^- into E_c , leaving h^+ in E_v . This increases n and p and, equivalently, splitting E_{Fn} and E_{Fp} away from E_F . Compare with Fig C.1.

where S is the system's entropy, T is its temperature, P is the pressure applied onto the system, V is the system volume, $\mu_{c,\alpha}^*$ is the chemical potential of species α in the system, n_α is the number of such species, Q_α is their total charge, and ψ is the electrostatic potential experienced by them. We stress that μ_c^* should not be confused with carrier mobility, hence the superscript. Note that in the last term we have also made an approximation that many-body correlation can be neglected.

For simplicity, we shall assume the particle being electrons for the following discussions. Q_α can then be decomposed into:

$$Q = -nq \quad (\text{C.17})$$

with which, Eqn. C.16 becomes:

$$U = ST - PV + n(\mu_c^* + q\psi) \quad (\text{C.18})$$

We note that the last term in Eqn. C.18 behaves like an intensive variable. We thus define the electrochemical potential for e^- as:

$$\mu_{ec}^* = \mu_c^* + q\psi \quad (\text{C.19})$$

In a solid state system, such as most solar cell devices, we often work under roughly constant temperature, volume, and number of particles. Additionally, we often have an experimental control over the Fermi level of the particle by doping. Hence, the most convenient thermodynamic potential to use in solid state is the Landau (Grand Canonical) Potential [146]:

$$\Omega = U - ST - (n\mu_c^*) \quad (\text{C.20})$$

whose differential under constant volume and temperature reduces to:

$$d\Omega = n(d\mu_c^* + q d\psi) \quad (\text{C.21})$$

To establish the connection between E_{Fn} and μ_{ec} , we are going to solve Eqn. C.18 for n and compare with the expression for n that we get from integrating $g_e(E)$ (Eqn. C.2). We shall first treat e^- in the material as an ideal Fermi gas, which satisfies:

$$pV = nkT \quad (\text{C.22})$$

The average total energy of ideal gas at E_c is simply:

$$U = n \left(E_c + \frac{3}{2} kT \right) \quad (\text{C.23})$$

where E_c is the potential energy experienced by e^- and the second term is due to their kinetic energy. We also note that the entropy for ideal gas of spin 1/2 due to Sackur and Tetrode is:

$$S = nk \left(\frac{5}{2} + Ln \left| \frac{N_c}{n} \right| \right) \quad (\text{C.24})$$

Combining Eqn. C.22, C.23, and C.24 with Eqn. C.18, we get:

$$\begin{aligned} U = n \left(E_c + \frac{3}{2} kT \right) &= n \left(kT \left(\frac{5}{2} + Ln \left| \frac{N_c}{n} \right| \right) - kT + \mu_{ec}^* \right) \\ E_c - \mu_{ec}^* &= kT Ln \left| \frac{N_c}{n} \right| \end{aligned} \quad (\text{C.25})$$

or equivalently:

$$n = N_c e^{(\mu_{ec}^* - E_c)/kT} \quad (\text{C.26})$$

Comparing this with Eqn. C.4 and, more generally, Eqn. C.14, we conclude that:

$$\begin{aligned} E_{Fn} &= \mu_{ec}^* \\ q \nabla \varphi_n &= \nabla \mu_{ec}^* \end{aligned} \quad (\text{C.27})$$

We can also similarly define the hole electrochemical potential.

C.2 Drift-Diffusion Model of Carrier Dynamics

In order to describe the physics of carrier dynamics in a material, we return to Eqn. C.18, which describes the state of the carriers in the system:

$$U = ST - PV + n(\mu_c^* + q\psi)$$

where variations in μ_c^* and ψ may be due the crystal potential or due to external work. to The force experienced by these particles is simply:

$$\vec{F} = -\vec{\nabla}U$$

Assuming that T and P are constant, the drive for carrier current are then the electrostatic field and gradient of carrier concentration in the material. Although these are usually treated separately, there are some caveats about the physical interpretation which need to be discussed at the end of this section.

C.2.1 Drift current

The **drift current** is the current due to electrostatic field in the material (Fig. C.4). For an e^- , this is simply:

$$\begin{aligned} j_{fe} &= -qn \langle v_e \rangle \\ j_{fh} &= qn \langle v_h \rangle \end{aligned} \tag{C.28}$$

where the subscript in j_f stands for “field” signifying the drift nature, and $\langle v_\alpha \rangle$ is the average velocity of the carriers. In the relaxation time approximation, $\langle v_\alpha \rangle$ is simply:

$$\langle v_\alpha \rangle = \mu_0 \mathcal{E} = -\mu_0 \nabla \psi \tag{C.29}$$

$$\mu_0 := \frac{q\tau}{m_\alpha^*} \tag{C.30}$$

where τ is the characteristic time between carrier scattering events in the material, \mathcal{E} is the local electric field, and m_α^* its effective mass in the material. The proportionality constant μ_0 is called the carrier’s **mobility** with the subscript “0” to emphasize that its value may change at high field. Eqn. C.28 then becomes the famous Ohm’s Law:

$$\begin{aligned} j_{fe} &= -\sigma_e \nabla \psi \\ j_{fh} &= \sigma_h \nabla \psi \\ \sigma_\alpha &:= qn \mu_0 \end{aligned} \tag{C.31}$$

where the proportionality constant σ_α is the **conductivity** of the carrier type in the material and is the inverse of resistivity.

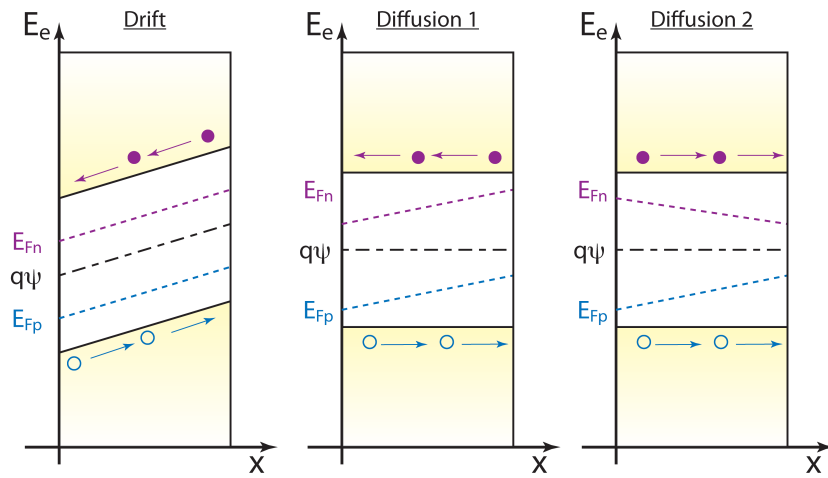


Figure C.4: Examples of energy levels for drift and diffusion currents. The last figure is for Dember effect in non-uniform illumination of photoactive layer at flat band, in this case the photons arrive from the left. The net current is zero.

C.2.2 Diffusion current

On the other hand, **diffusion current**, which is due to differences in particle concentrations (Fig. C.4), is governed by Fick's Law:

$$\begin{aligned} j_{de} &= -q D_e \nabla n \\ j_{dh} &= -q D_h \nabla p \end{aligned} \quad (\text{C.32})$$

where the subscript j_d stands for “diffusion”. The extra q -term is because we are calculating charge current, not particle current. The proportionality constant D_α is called the **diffusivity** which, for non-degenerate semiconductors, is related to the mobility by the **Einstein's relation**:

$$\mu_0 = qD/kT \quad (\text{C.33})$$

As a word of caution, note that unlike Ohm's Law, the sign for the diffusion of hole and currents in Eqn. C.34 are the same. This does not necessarily mean that they will always flow in the same direction. In fact, the diffusivity as dictated by μ_0 have different sign due to the different charge sign in Eqn. C.33. More generally, the sign of the gradients will also affect the direction of the diffusion currents, and either scenarios represented in Fig. C.4 are possible. Lastly, by recognizing that:

$$\frac{\nabla n_\alpha}{n_\alpha} = \nabla L n \left| \frac{n_\alpha}{N_\alpha} \right| = \frac{\nabla \mu_{c,\alpha}^*}{kT}$$

we can then recast Fick's Law in terms of the chemical potential:

$$\begin{aligned} j_{de} &= -q n \mu_{0,e} \nabla \mu_{c,e}^* \\ j_{dh} &= q p \mu_{0,h} \nabla \mu_{c,h}^* \end{aligned} \quad (\text{C.34})$$

The reason for doing this will be apparent soon.

C.2.3 Total drift-diffusion current

The total current is thus the sum of the two:

$$j_n = -q \mu_{0,e} n [\nabla \mu_{c,e}^* + \nabla \psi]$$

$$j_p = -q\mu_{0,h}p[\nabla\mu_{c,h}^* + \nabla\psi] \quad (\text{C.35})$$

With the help of Eqns. C.19 and C.27, the equations for current become very simple in terms of φ_n and φ_p ,

$$\begin{aligned} j_n &= -q\mu_{0,e}n\nabla\varphi_n \\ j_p &= -q\mu_{0,h}p\nabla\varphi_p \end{aligned} \quad (\text{C.36})$$

Eqn. C.36 is the central result in the classical drift-diffusion theory of current inside a homogenous material. This equation will be of utmost importance in our discussions about charge transport in OPV cells, as in any other semiconductor technologies.

We would like, however, to throw one cautionary remark on the use of Eqn. C.36. Although the separation of Eqn. C.36 into the drift and diffusion terms is commonly done and is mathematically correct, Würfel noted that this interpretation is not always physically correct [267]. The simplest but most convincing example is thermodynamic equilibrium of a junction. The energy levels are sketched in Fig. C.5. Here, total current is clearly non-existent despite the presence of the built-in electric field. One may then conclude that the diffusion current exactly opposes the drift current and correctly arrives at zero current. However, the drift and diffusion current each causes energy dissipation that is definite positive:

$$\begin{aligned} \frac{dU_f}{dt} &= \frac{j_{f,\alpha}^2}{\sigma_\alpha} \\ \frac{dU_d}{dt} &= \frac{j_{d,\alpha}^2}{\sigma_\alpha} \end{aligned} \quad (\text{C.37})$$

which is in contrast to the fact that there is no net energy dissipation at thermodynamic equilibrium! Therefore, the most correct interpretation is that the drive for motion of a charged particle is the gradient in its combined electrochemical potential.

Würfel proposed an analogy with microscopic motion of air particles in thermodynamic equilibrium. Two forces are acting on them: the gravity and pressure gradient due to changing density in the vertical direction. However, there is no real gravitational current falling down and a compen-

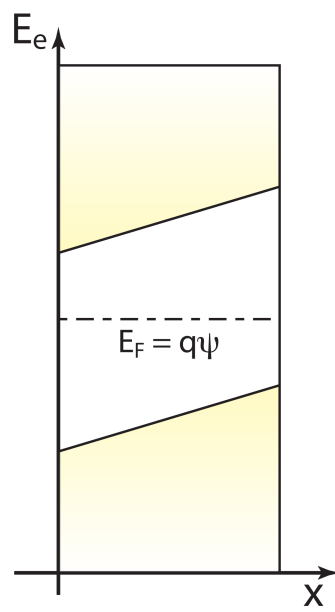


Figure C.5: Sketch of energy levels across a junction at thermodynamic equilibrium.

sating pressure current rising up. Indeed, the microscopic motions of the particles are Brownian and there is no net current.

Appendix D

Junctions

We have so far discussed the photogeneration process in an ideal solar cell and how carriers travel in a material. The remaining question is then: how can we tailor a device such that the photogenerated carriers are automatically extracted so that they can be utilized to do external work.

Macroscopic motion of any particle in the semi-classical limit is dictated by Newton's Second Law:

$$\sum_i \mathbf{F}_i = m^* \mathbf{a} \quad (\text{D.1})$$

Where \mathbf{F}_i is the force acting on the particle, m^* its effective mass, and \mathbf{a} its acceleration. The summation over index i is over the different forces that act on the particle. This law of motion still applies to particles confined to a media, such as e^- in a semiconductor. We use m^* to reflect that these e^- have apparent mass that's different than that of a free electron due to, for example, attractive potentials from the nuclei in the crystals. The value of m^* can be measured experimentally [10].

In terms of potential energy, the force experienced by a particle is simply:

$$\mathbf{F} = -\vec{\nabla}U + \vec{\nabla}W \quad (\text{D.2})$$

where U is the potential energy experienced by the particle, W is the work done onto the particle, and $\vec{\nabla}$ is the 3-dimensional gradient operator. In a one dimensional problem, this reduces to:

$$\mathbf{F} = -\frac{dU}{dx}\hat{x} + \frac{dW}{dx}\hat{x} \quad (\text{D.3})$$

From this perspective, such force can be achieved by **combination of tailoring an appropriate potential energy profile and exerting work**. Problems in device physics and engineering thus revolve around understanding how one can tailor the appropriate potential energy profile in the device structure to achieve the desired function.

In a solar cell, where **automatic** extraction of photo-generated charges is desired, $W = 0$. Thus, this is done by engineering the materials in the device such that potential energy experienced by e^- has the appropriate gradient. An analogy from mechanics: to make a ball roll, put it on a sloped ground and it will automatically roll downhill without any work from the experimenter. Alternatively, in the absence of any difference in potential energy such as on a flat ground, the experimenter may push the ball to make it roll. The combination of the two also applies.

D.1 Junctions

How can one engineer such potential gradient in our device structure? The potential energy experienced by a collection of charged particle in a material can be described in a statistical way ¹ :

$$U = ST - PV + \sum_{\alpha} N_{\alpha} (E_{F\alpha} + q_{\alpha}\psi) \quad (\text{D.4})$$

where S is the system's entropy, T is its temperature, P is the pressure applied onto the system, V is the system volume, $E_{F\alpha}$ is the chemical potential of species α in the system, N_{α} is the number of such species, q_{α} is their unit charge, and ψ is the electrostatic potential experienced by them. We have used E_F instead of the traditional μ to denote the Fermi level to avoid confusion with carrier mobility. Note that in the last term we have made an approximation that many-body correlation can be neglected.

For simplicity, we shall assume the particle being electrons for the following discussions. Since chemical potential for e^- (Fermi level) is a quantity that is material-specific, **a potential**

¹ The validity limit of such statistical / thermodynamical description is of utmost importance. However, it is not the objective of this work to go into such details. Instead, the readers are referred to, for example, Refs. [131, 10]. Herring and Nichols [91], and Ashcroft and Mermin [10] also discussed the validity limit in terms of spatial homogeneity. Jackson [105] has also touched upon similar validity limits in the light of classical electrodynamics theory.

gradient can be thus achieved by putting different materials intimately together so that electrons can be naturally exchanged among them, and the spatial symmetry breaking in the structure defines the direction of e^- flows in the device. Properties of the interface between the two material, referred to as the **junction**, are obviously central in device performance and is the focus of this section.

A junction can first be classified by the materials that are being electrically joined. These are illustrated in Fig. D.1, where the top figures represent the energy levels of the materials before contact, and the bottom after contact. The energy levels of the materials before contact are vacuum level-aligned and their bands “horizontal”, equivalent to assuming that charge neutrality is locally satisfied at every point in space. The bottom figures show the energy levels after electrical contact in equilibrium. As we shall see in more details, the different materials result in a non-constant energy levels that lend the devices its ability to do their designed function.

In a **homojunction**, the two sides are made of the same material with different doping level. Thus, essentially the only difference between the two is their E_F . An important example of this kind of device is the monocrystalline Si p-n junction [220]. More generally, if the two sides are composed of different materials, the junction is referred as a **heterojunction**. Heterostructures are further broadly categorized into three types based on the relative position and size of E_g of the materials before electrical contact (Fig. D.1).

D.1.1 Band Alignment at an Ideal Heterojunction

In the light of Eqn. D.4, we are mostly interested in the profile of $E_{F\alpha}(x)$ and $\psi(x)$ across the device. As an example, the case of a n-p staggered heterojunction at equilibrium is further elaborated in Fig. D.2 The final band-alignments depicted in Fig. D.1 and D.2a, following the Anderson’s Rule [6], are for the simplest cases where the two materials do not chemically interact strongly, leading to negligible density of interfacial states [119]. The cases for p-n, n-p, p-p, and n-n straddling heterojunctions are treated in Anderson’s original paper.

Upon contact and at thermodynamic equilibrium, there is no net movement of carriers leading

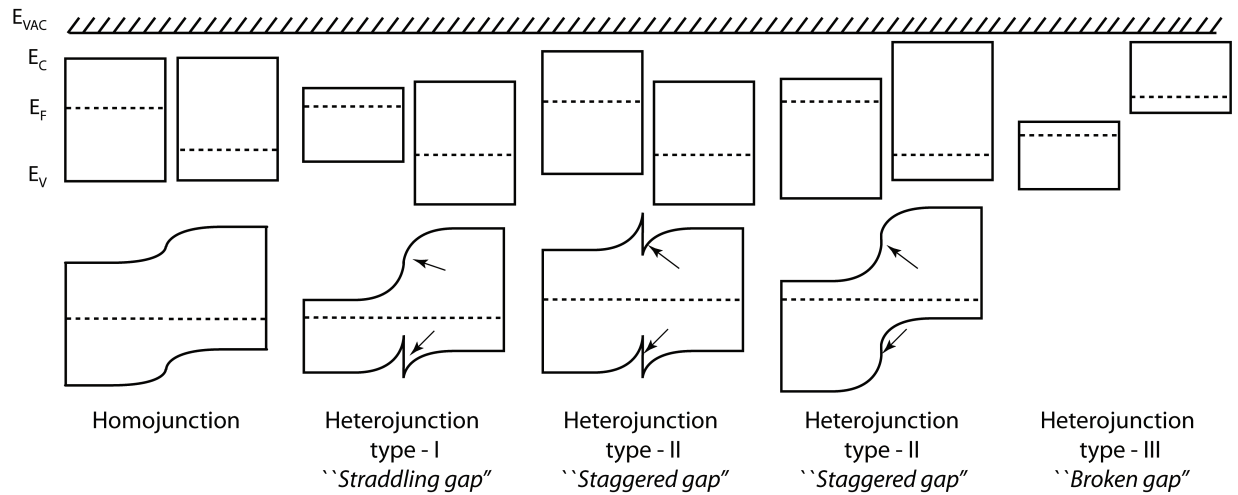


Figure D.1: Energy levels in a homojunction and heterojunctions. The top figures illustrate the materials before contact. The bottom figures depict the final band alignment following Anderson's rule. Arrows indicate the band-offsets.

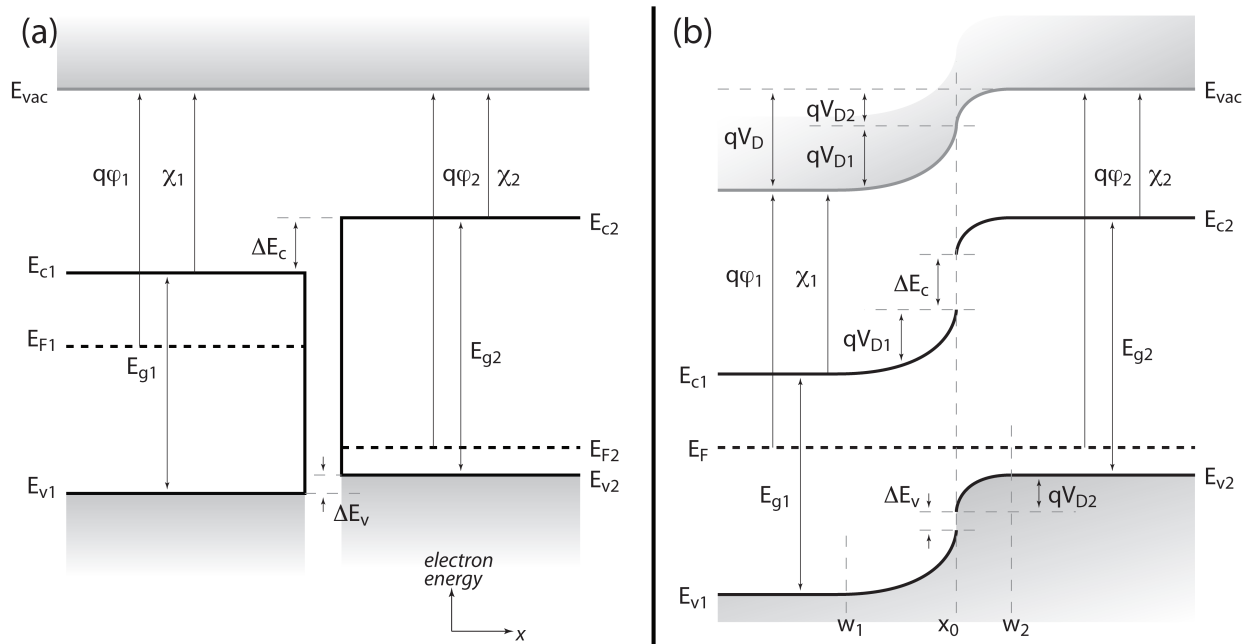


Figure D.2: Energy levels in a staggered n-p heterojunction before (a) and after (b) contact.

to a single, constant E_F throughout the device. This is achieved by rearrangement of carrier population near the interface: e^- from material 1, originally at higher E_{F1} than those at E_{F2} in material 2, starts to flow into the junction upon contact, a process known as **depletion** (Fig. D.3).

This causes a local imbalance of charges near the interface and, in accordance to Poisson's equation, results in a build-up of electrostatic potential. Since the electrostatic potential can be represented as the vertical displacement of the band edges [220], depletion is depicted as the band-bending in Fig. D.2b (the case when band bends the other way is referred as **accumulation**). The vacuum level must also bend parallel to the band edges since $q\varphi$ must remain constant for a given material ².

The **depletion width** in material 1 ($|w_1 - x_0|$) is a few L_D of the material, where L_D is defined as:

$$L_D = \sqrt{\frac{\epsilon_r \epsilon_0 kT}{8\pi q^2 n}} \quad (\text{D.5})$$

where ϵ_r is the relative permeability of the material and ϵ_0 is the permeability of free space. L_D is a characteristic length scale at which mobile charges screen an external electrostatic potential. It is called the **Debye length** to emphasize the similarity with the characteristic length in the Debye-Hückel theory of strong electrolytes. Similar analysis can be done on h^+ inside material 2.

In the absence of electrostatic poles, the electrostatic potential must be continuous. Consequently, the potential difference across any two points is simply the difference in the vertical displacement in the diagram. The total **diffusion potential** or **built-in potential** across the junction, V_D , due to the rearrangement of carrier concentrations is equal to $(V_{D1} + V_{D2})$, which respectively are the potentials sustained in materials 1 and 2. Because the rearrangement is to null the difference in E_{F1} and E_{F2} , V_D must also equal $|E_{F1} - E_{F2}|/q$. Additionally, V_{D1} and V_{D2} are related by:

$$\frac{V_{D1} - V_1}{V_{D2} - V_2} = \frac{N_{A2}\epsilon_2}{N_{D1}\epsilon_1} \quad (\text{D.6})$$

² A mathematically equivalent treatment is to set E_{vac} instead of E_F as the potential reference. From this perspective, the bands will remain flat, but E_F is continuously changing from E_{F1} inside material 1 to E_{F2} inside material 2. The interpretation of E_F is no longer the chemical potential, but rather the **electrochemical potential** [10].

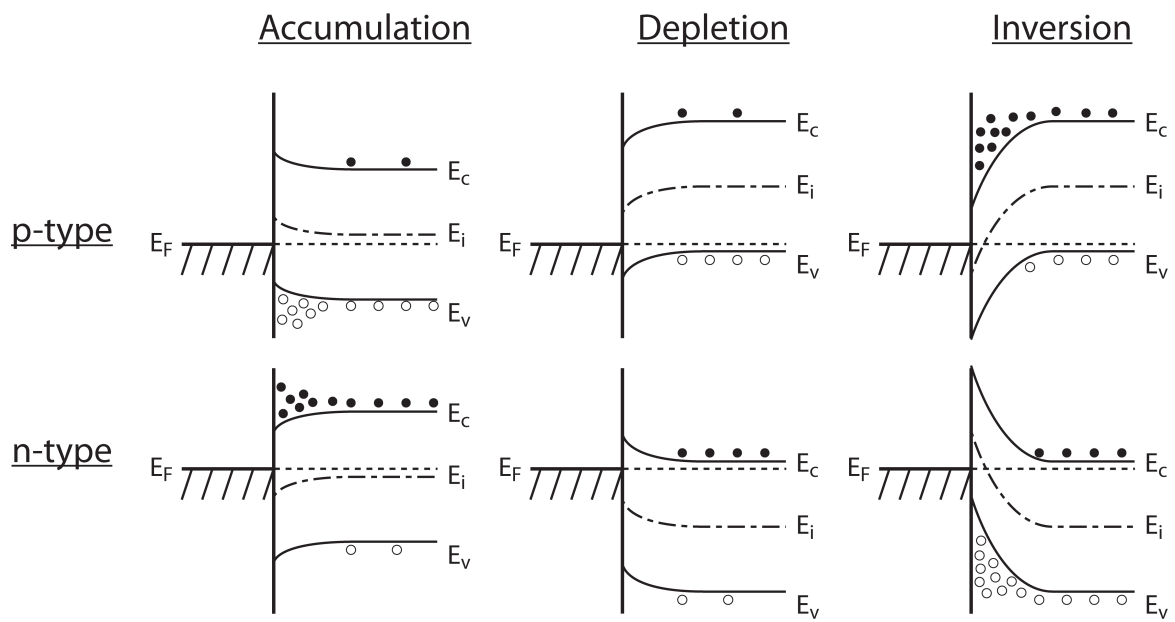


Figure D.3: Depletion, inversion, and accumulation

where V_1 and V_2 are parts of the applied bias that is dropped across material 1 and 2 respectively.

The quasi-electric field at any point in the device is simply the negative of the gradient of E_{vac} . Additionally, the boundary conditions for a dielectric interface from Maxwell's equation is:

$$\begin{aligned}\mathcal{E}_{\parallel 1} &= \mathcal{E}_{\parallel 2} \\ \epsilon_{r1} \mathcal{E}_{\perp 1} &= \epsilon_{r2} \mathcal{E}_{\perp 2}\end{aligned}\tag{D.7}$$

where \mathcal{E}_{\parallel} is the electric field in the direction parallel to the interface and \mathcal{E}_{\perp} in the direction normal to the interface. Since we are considering a 1-D problem, the parallel boundary condition is of no interest to us. The second condition, however, dictates that there is a discontinuity in the electric field whenever there is a mismatch in the dielectric constant. This is reflected in the different slopes of the bands across x_0 .

Another feature of extreme importance are the **band-offsets** at the interface. In general, there must be a discontinuity in the bands at the interface. Since E_{vac} is continuous and parallel to the band edges everywhere, the magnitude of the offsets must remain the same with prior to electrical contact (Fig. D.2a). In this respect, homojunctions are special cases where there exists no band-offset and no discontinuity in E-field at the interface.

D.1.2 Current Transport Across a Heterojunction

Current-voltage characteristic of an ideal heterojunction is of the form:

$$I(V) = I_{01}e^{-\frac{q}{kT}V_{B1}} - I_{02}e^{-\frac{q}{kT}V_{B2}}\tag{D.8}$$

where V_{B1} is the potential barrier for particle current from material 1 to 2, and V_{B2} from 2 to 1. The constants I_{01} and I_{02} are the reverse saturation currents of the two channels which depend on the respective carrier mobilities, doping levels, and the mechanism of current flows.

We shall again consider the condition depicted in Fig. D.2, with positive current at forward bias being defined to flow from material 2 to 1 (e^- current from material 1 to 2). Fig. D.4 will help navigate our discussion. To simplify the discussion without missing the essential physics, we neglect

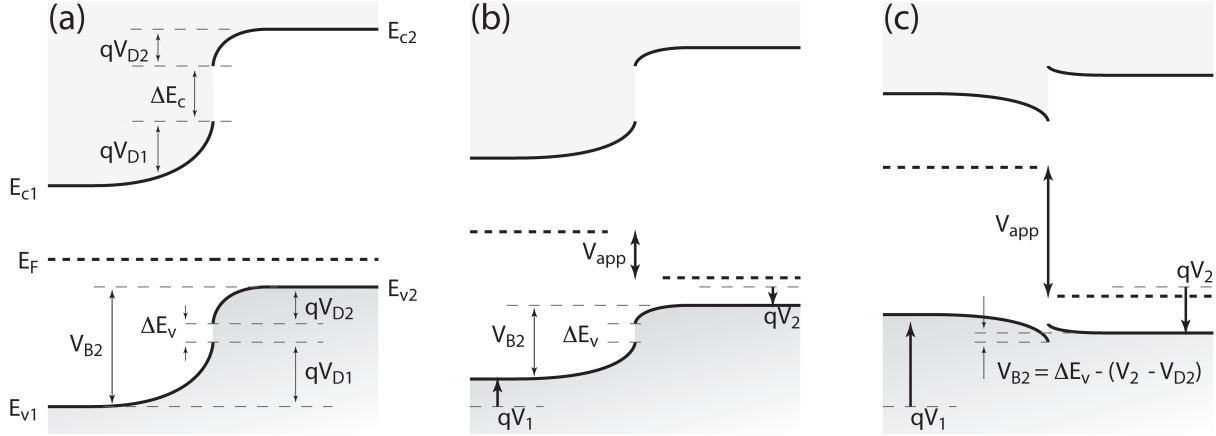


Figure D.4: Energy levels in a staggered n-p heterojunction at (a) equilibrium, (b) low forward bias, and (c) high forward bias. Positive current at forward bias is defined to flow from material 2 to 1 (e^- current from material 1 to 2)

the generation-recombination and tunneling terms. We also approximate the barrier heights $V_{B1,2}$ by the vertical displacement of the relevant bands. This approximation is generally good for ideal semiconductors with clean gap.

At $V_{app} = 0 V$ (Fig. D.4a), the barrier for e^- is simply $V_{B1} = (qV_D + \Delta E_c)$, and that for h^+ is $V_{B2} = (qV_D + \Delta E_v)$. Since $\Delta E_v < \Delta E_c$ and $I \sim e^{-\frac{V_B}{kT}}$, current across the junction is mostly carried by h^+ . Therefore, we make a simplification that the e^- current is negligible at low bias (Fig. D.4b), and Eqn. D.8 becomes:

$$I(V) \approx I_{02} e^{-\frac{q}{kT}(V_{D1}+V_{D2}+\Delta E_v)} e^{\frac{q}{kT}(V_1+V_2)} = I_{02} e^{-\frac{q}{kT}(V_D+\Delta E_v)} e^{\frac{q}{kT}V_{app}} \quad (\text{D.9})$$

which is reminiscent of Shockley's ideal diode equation, with the addition of ΔE_v -term³.

At higher bias, however, the characteristic deviates from that of an ideal homojunction diode. First, e^- current rises in importance but, as mentioned earlier and unlike in that of an ideal diode, its dependence on voltage is different than that of the h^+ current. Second, the constant band-offset reduces the efficiency of V_{app} in lowering the barrier.

³ It is interesting to compare current transport and rate of chemical reaction. V_D will be analogous to the thermodynamic / energetic barrier, while ΔE_v and ΔE_c will result in the equivalent of kinetic barriers. See §7

Consider, for example, the situation illustrated in Fig. D.4c, where $(V_{1,2} > V_{D1,2})$, $(V_1 - V_{D1} > \Delta E_v)$, but $(V_2 - V_{D2} < \Delta E_v)$. The barrier to h^+ conduction from right to left is now $V_{B2} = \Delta E_v - (V_2 - V_{D2})$. As we increase V_{app} , we still increase V_1 and V_2 . However, in this regime, the increase in V_1 does not lead to any decrease in V_{B2} . V_{B2} is reduced only by V_2 , and consequently the current will vary exponentially with V_2 instead of V_{app} .

Let us define a parameter η to be:

$$\eta(V_{app}) = -\frac{dV_{app}}{dV_B} \quad (\text{D.10})$$

Hence, η measures the fraction of V_{app} that effectively lowers V_B and is naturally a V_{app} -dependent quantity. For example, in our case, $\eta = 1$ at low V_{app} and increases to $\frac{V_{app}}{V_2}$ as the situation in Fig. D.4c is reached. η is known as the (V_{app} -dependent) **diode quality factor** or **diode ideality factor**.

Using η , we can describe the h^+ current across the heterojunction more generally as:

$$I(V) \approx I_{02} e^{-\frac{q}{kT}(V_D + \Delta E_v)} e^{\frac{q}{\eta(V)kT} V_{app}} \quad (\text{D.11})$$

In conclusion, the DC current characteristic of the heterojunction depicted in Fig. D.2-D.4 is described by Eqn. D.11, where $\eta = 1$ at low bias, and increases when V_{app} is such that $(V_1 - V_{D1} > \Delta E_v)$, but $(V_2 - V_{D2} < \Delta E_v)$. This characteristic is attributed to the resulting final band-alignment of the heterojunction as illustrated in Fig. D.2b.

The DC current characteristics of other heterostructures, such as the straddling type, can be very different. For example, the current of an ideal n-n straddling heterojunction does not saturate at large reverse bias [234]. Lastly, the topics of AC current and capacitance characteristics of the heterojunctions may also be derived. However, it is beyond the scope of this work; instead, the readers are referred to Refs. [220, 122, 124, ?, 123, ?] for detailed discussions.

D.1.3 Band-Offsets, Non-Ideal Interfaces, and Interfacial Dipoles

In the previous section, we have discussed the general properties of an ideal heterojunction. Here, “ideal” is not synonymous with “physically perfect”. By ideal we precisely mean that the

energy levels of the materials at the interface are the same with that in their respective bulk. This is rarely the case because of two reasons [10, 252]:

The first reason is practical and trivial. Any imperfections such as dislocations due to lattice mismatch, phase segregation, inter-diffusion, and adsorbate species will contribute to deviations from the predicted result. The second, however, is fundamental in nature. Band profiles in the bulk of the material, crystalline or amorphous, is a result of superposition of electrostatic potentials due to the nuclei which, to an excellent approximation, are infinitely extended in all three directions. At any surface, this is no longer true. The region near the surface may have a non-vanishing electric dipole (or higher) moment, of which the details is largely influenced by the crystallographic facet of the surface and its roughness. As a consequence, the potential energy and e^- wavefunction must extend slightly beyond the physical surface. Further, states that are forbidden in the bulk (within E_g) may actually be allowed. At buried interfaces, the details of orbital hybridization between the interfacial ions from the two species may also give rise to dipole moments and must be taken into account.

This is the primary reason why Anderson's Rule is valid mainly for materials that do not strongly interact chemically. The problem of finding the correct band alignment is still an active field of research even more than 50 years after Anderson [119]. Many theories are available to model the imperfections at the interface. The simplest and most useful is probably the concept of interfacial dipoles [275], where the imperfection is modeled as a dipole layer on top of an ideal interface. The magnitude and sign of the dipole must be measured or otherwise modeled based on empirical values.